



**HAL**  
open science

# A contribution to the vibroacoustic and psychoacoustic design of composite structures

Yahya Allah Tavakoli

► **To cite this version:**

Yahya Allah Tavakoli. A contribution to the vibroacoustic and psychoacoustic design of composite structures. Acoustics [physics.class-ph]. École Nationale des Travaux Publics de l'État [ENTPE], 2023. English. NNT: 2023ENTP0014 . tel-04659121

**HAL Id: tel-04659121**

**<https://theses.hal.science/tel-04659121>**

Submitted on 22 Jul 2024

**HAL** is a multi-disciplinary open access archive for the deposit and dissemination of scientific research documents, whether they are published or not. The documents may come from teaching and research institutions in France or abroad, or from public or private research centers.

L'archive ouverte pluridisciplinaire **HAL**, est destinée au dépôt et à la diffusion de documents scientifiques de niveau recherche, publiés ou non, émanant des établissements d'enseignement et de recherche français ou étrangers, des laboratoires publics ou privés.



Thesis National Number: **2023ENTP0014**

**A THESIS OF ENTPE**  
Member of the **UNIVERSITÉ DE LYON**

Doctoral school No. 162  
MEGA (MÉCANIQUE, ÉNERGÉTIQUE, GÉNIE CIVIL,  
ACOUSTIQUE)

To obtain the graduation of  
PhD in Acoustics

Defended on December 15, 2023, by

**Yahya AllahTavakoli**

---

**A Contribution to the  
Vibroacoustic and Psychoacoustic  
Design of Composite Structures**

---

In front of the following examination committee:

Altinsoy Ercan	Professor (Dresden University of Technology, Germany)	Reviewer
Duhamel Denis	Professor (École des Ponts ParisTech, France)	Reviewer
Meunier Sabine	Researcher, HDR (LMA, CNRS, France)	Examiner
Totaro Nicolas	Professor (INSA Lyon, France)	Comitee chair
Vicente Thibault	Assistant Professor (Le Mans Université, France)	Examiner
Hamzaoui Nacer	Emeritus Professor (INSA Lyon, France)	Supervisor
Ichchou Mohamed N.	Professor (Ecole Centrale de Lyon, France)	Supervisor
Marquis-Favre Catherine	Senior Researcher (ENTPE, France)	Supervisor

The thesis has been prepared at the LTDS (Laboratoire de Tribologie et Dynamique des Systèmes) at École Nationale des Travaux Publics de l'État (ENTPE) and École Centrale de Lyon, and at the LVA ( Laboratory of Vibration and Acoustics) at the National Institute of Applied Sciences (INSA Lyon), and financially funded by LABEX CELYA (Centre Lyonnais d'Acoustique)



**ENTPE**  
L'école de l'aménagement durable des territoires



ÉCOLE  
**CENTRALE LYON**

**INSA**

INSTITUT NATIONAL  
DES SCIENCES  
APPLIQUÉES  
LYON

Numéro national de thèse (NNT) : **2023ENTP0014**

# THÈSE DE DOCTORAT DE L'ENTPE

Membre de l' UNIVERSITÉ DE LYON

École Doctorale N° accréditation 162  
MEGA (MÉCANIQUE, ÉNERGÉTIQUE, GÉNIE CIVIL,  
ACOUSTIQUE)

Spécialité / discipline de doctorat :  
Acoustique

Soutenue publiquement le 15 décembre 2023, par

**Yahya AllahTavakoli**

---

## Une contribution à la conception vibroacoustique et psychoacoustique des structures composites

---

Devant le jury composé de :

Altinsoy Ercan	Professeur (Dresden University of Technology, Germany)	Rapporteur
Duhamel Denis	Professeur (École des Ponts ParisTech, France)	Rapporteur
Meunier Sabine	Chargée de Recherche, HDR (LMA, CNRS, France)	Examinatrice
Totaro Nicolas	Professeur (INSA Lyon, France)	Président du jury
Vicente Thibault	Maître de conférences (Le Mans Université, France)	Examinateur
Hamzaoui Nacer	Professeur émérite (INSA Lyon, France)	Codirecteur
Ichchou Mohamed N.	Professeur (Ecole Centrale de Lyon, France)	Codirecteur
Marquis-Favre Catherine	DR (ENTPE, France)	Codirectrice

La thèse a été préparée au LTDS (Laboratoire de Tribologie et Dynamique des Systèmes) de l'École Nationale des Travaux Publics de l'État (ENTPE) et de l'École Centrale de Lyon, et au LVA (Laboratoire Vibrations Acoustique) de L'Institut National des Sciences Appliquées de Lyon (INSA Lyon), et financée par LABEX CELYA (Centre Lyonnais d'Acoustique)

# Acknowledgement

First and foremost, I am deeply grateful to the enigmatic beauty behind science, drawing me further into this journey.

I would like to thank my three supervisors, Dr. Catherine Marquis-Favre, Prof. Nacer Hamzaoui, and Prof. Mohamed Ichchou, each an expert in distinct scientific domains. Our collaborative efforts led to numerous stimulating discussions and invaluable guidance. I extend my heartfelt appreciation to all three for their careful advice and unwavering support.

Throughout this endeavor, my wife, my dear friend Mina, has been my steadfast companion, as she has been in every stage of my life. Words fail to express the depth of my love for her. Mere gratitude cannot suffice, my dear Mina—thank you from the depths of my heart! Additionally, I am immensely grateful for the enduring presence and encouragement of two cherished women, my mother Soussan, and my sister Misagh, who have been vital parts of my life since my existence in this universe and childhood. Though words may seem inadequate again, I thank them wholeheartedly for their steadfast company.

Also, I express my gratitude to my father and other members of my family who consistently stand by me. To my dear friends who accompany me on this journey, I extend my sincere thanks and best wishes for success in both their personal and professional pursuits.

At the end, I would like to sincerely thank the esteemed jury members, Prof. Ercan Altinsoy, Prof. Denis Duhamel, Dr. Meunier Sabine, Prof. Nicolas Totaro, and Dr. Thibault Vicente, for meticulously reviewing my PhD thesis, attending the PhD defense, and dedicating their valuable time to enhancing my research. I wish all of them continued success in their outstanding scientific endeavors.

”We are as the flute, and the music in us is from thee  
We are as the mountain and the echo in us is from thee  
We are as pieces of chess engaged in victory and defeat  
Our victory and defeat is from thee, O thou whose qualities are comely!”  
*Rumi* (1207–1273 A.D.)

# Abstract

The development of lightweight structures is a significant trend across various engineering sectors, such as aerospace and mechanical engineering. The significant trade-off between weight and stiffness often leads to noise and vibration issues that need addressing. Lightweight structures face disadvantages in terms of noise emissions across a wide frequency range, necessitating optimization efforts. Composite sandwich panels represent typical lightweight structures and find extensive use in various industrial sectors. These panels consist of thin face sheets and a core, offering a wide range of choices in terms of materials and architectural configurations.

Recent research has demonstrated that the vibroacoustic properties of sandwich panels can be optimized and improved by manipulating their geometric architecture along with mechanical properties. Several ideas have been explored to validate the impact of geometric design on vibroacoustic indicators. This optimization step solely considers vibroacoustic characteristics and does not take into account auditory perception, i.e., psychoacoustic characteristics.

Some research studies have explored the connections between the physical parameters of radiating structures, particularly isotropic plates, and the auditory properties of the resulting radiated or transmitted sounds. These studies have focused on evaluating the effects of physical parameters on auditory perception, including structural parameters, excitation conditions, structural uncertainties, and simulation parameters used in vibroacoustic calculations for modeling structures. The outcomes have been valuable in providing recommendations for enhancing the quality of sounds emitted or transmitted by these structures from their design phase.

This thesis concentrates on both the psychoacoustic and vibroacoustic analysis of a sandwich structure, aiming to optimize the design of such a structure while considering its sound quality. Specifically, it addresses the following issues: reviewing the models for vibroacoustic modeling of composite panels, conducting laboratory measurements to assess the theoretical models from physical point of view, proposing a hybrid updating method for enhancing the models necessary for precisely vi-



broacoustic modeling of composite panels, auditory evaluation of the vibroacoustic simulation using recordings of the sounds emitted by the structure, determining the relevant structural parameters from a perceptual perspective, and optimizing the sound quality of sandwich structures through vibroacoustic simulations of different designs. To achieve these objectives, this research incorporates theoretical analyses, simulations, vibroacoustic laboratory measurements by considering both mechanical and acoustic excitations of the composite structures, and finally psychoacoustic tests and analyses.

# Résumé

Le développement de structures légères constitue une tendance importante dans divers secteurs de l'ingénierie, tels que l'aérospatiale et le génie mécanique. Le compromis important entre poids et rigidité entraîne souvent des problèmes de bruit et de vibrations qui doivent être résolus. Les structures légères sont confrontées à des inconvénients en termes d'émissions sonores sur une large gamme de fréquences, ce qui nécessite des efforts d'optimisation. Les panneaux sandwich composites représentent des structures légères typiques et sont largement utilisés dans divers secteurs industriels. Ces panneaux sont constitués de fines feuilles de face et d'un noyau, offrant un large éventail de choix en termes de matériaux et de configurations architecturales.

Des recherches récentes ont démontré que les propriétés vibroacoustiques des panneaux sandwich peuvent être optimisées et améliorées en manipulant leur architecture géométrique ainsi que leurs propriétés mécaniques. Plusieurs idées ont été explorées pour valider l'impact de la conception géométrique sur les indicateurs vibroacoustiques. Il est à noter que cette étape d'optimisation considère uniquement les caractéristiques vibroacoustiques et ne prend pas en compte la perception auditive, c'est-à-dire les caractéristiques psychoacoustiques.

Certaines recherches ont exploré les liens entre les paramètres physiques des structures rayonnantes, en particulier les plaques isotropes, et les propriétés auditives des sons rayonnés ou transmis qui en résultent. Ces études se sont concentrées sur l'évaluation des effets des paramètres physiques sur la perception auditive, notamment les paramètres structurels, les conditions d'excitation, les incertitudes structurelles et les paramètres de simulation utilisés dans les calculs vibroacoustiques pour la modélisation des structures. Les résultats ont été précieux en fournissant des recommandations pour améliorer la qualité des sons émis ou transmis par ces structures simples dès leur phase de conception.

Cette thèse se concentre à la fois sur l'analyse psychoacoustique et vibroacoustique d'une structure sandwich, visant à optimiser la conception d'une telle structure tout en considérant sa qualité sonore. Plus précisément, elle aborde les

problématiques suivantes : revoir les modèles de modélisation vibro-acoustique des panneaux composites, réaliser des mesures en laboratoire pour évaluer les modèles théoriques d'un point de vue physique, proposer une méthode de mise à jour hybride pour enrichir les modèles nécessaires à une modélisation vibro-acoustique précise des panneaux composites, évaluation auditive de la simulation vibroacoustique à l'aide d'enregistrements des sons émis par la structure, détermination des paramètres structuraux pertinents d'un point de vue perceptif et optimisation de la qualité sonore des structures sandwich grâce à des simulations vibroacoustiques de différentes conceptions. Pour atteindre ces objectifs, cette recherche intègre des analyses théoriques, des simulations, des mesures vibroacoustiques en laboratoire en considérant à la fois les excitations mécanique et acoustique des structures composites et enfin des tests psychoacoustiques et leurs analyses.

# Contents

<b>List of Figures</b>	<b>22</b>
<b>List of Tables</b>	<b>24</b>
<b>List of Acronyms</b>	<b>25</b>
<b>List of Symbols</b>	<b>27</b>
<b>1 Introduction and State of the art</b>	<b>29</b>
1.1 Motivation . . . . .	29
1.2 Literature review . . . . .	31
1.2.1 Vibroacoustic studies . . . . .	32
1.2.2 Psychoacoustic studies . . . . .	36
<b>2 Problem definition</b>	<b>47</b>
2.1 Vibration of composite panels . . . . .	47
2.2 6 <sup>th</sup> order problem . . . . .	48
2.3 4 <sup>th</sup> order problem . . . . .	50
2.3.1 Modal decomposition . . . . .	53
2.4 Radiation and Rayleigh integration . . . . .	53
2.5 Discussion . . . . .	54
<b>3 Modeling with diffuse acoustic excitation</b>	<b>57</b>
3.1 Methodology . . . . .	58
3.1.1 Diffuse acoustic excitation . . . . .	59

3.2	Numerical simulations . . . . .	61
3.3	Laboratory experiments . . . . .	63
3.4	Discussion and concluding remarks . . . . .	65
<b>4</b>	<b>Modeling with mechanical excitation</b>	<b>69</b>
4.1	Mechanical excitation . . . . .	69
4.2	Laboratory experiments . . . . .	70
4.2.1	Experimental set-up . . . . .	72
4.2.2	Characteristics of specimens . . . . .	72
4.2.3	Measurements . . . . .	75
4.3	Discussion . . . . .	76
<b>5</b>	<b>Updating models and parameters</b>	<b>79</b>
5.1	Introduction . . . . .	79
5.2	Hybrid Updating Method . . . . .	82
5.2.1	Hierarchical functions and formulations . . . . .	83
5.2.2	Inhomogeneous wave correlation technique . . . . .	87
5.2.3	Model updating . . . . .	88
5.2.4	Total least squares optimization . . . . .	89
5.3	Updating procedures . . . . .	91
5.3.1	Vibroacoustic comparisons . . . . .	95
5.3.2	Discussion of results . . . . .	100
5.4	Discussion and concluding remarks . . . . .	102
<b>6</b>	<b>Perceptual assessment</b>	<b>105</b>
6.1	Introduction . . . . .	105
6.2	Psychoacoustic test . . . . .	106
6.2.1	Participants . . . . .	106
6.2.2	Apparatus . . . . .	106
6.2.3	Stimuli . . . . .	106
6.2.4	Method . . . . .	108

<i>CONTENTS</i>	11
6.2.5 Preparing sound files . . . . .	110
6.3 Results . . . . .	112
6.3.1 Classification of participants . . . . .	112
6.3.2 Multidimensional scaling technique . . . . .	116
6.3.3 Perceptual space and model validation . . . . .	121
6.4 Summary and discussion . . . . .	126
<b>7 Design and optimization</b>	<b>129</b>
7.1 Composite panel design . . . . .	129
7.1.1 Vibroacoustic modeling . . . . .	133
7.2 Psychoacoustic tests . . . . .	134
7.2.1 Participants . . . . .	134
7.2.2 Test conditions . . . . .	134
7.2.3 Stimuli . . . . .	135
7.2.4 Method . . . . .	135
7.3 Results . . . . .	136
7.3.1 Classification and outliers detection . . . . .	136
7.3.2 Perceptual space . . . . .	139
7.3.3 Preference score . . . . .	141
7.3.4 Correlation of preference with perceptual dimensions . . . . .	145
7.3.5 Impression of stimuli ranked in perceptual space . . . . .	145
7.3.6 Psychoacoustic analysis . . . . .	146
7.3.7 Mechanical parameters . . . . .	148
7.3.8 Optimal designs . . . . .	154
7.4 Summary and discussion . . . . .	156
<b>8 General conclusion</b>	<b>159</b>
8.1 Mathematical model analysis . . . . .	159
8.2 Vibroacoustic modeling . . . . .	160
8.3 Hybrid updating method . . . . .	161
8.4 Psychoacoustic assessment . . . . .	162

8.5	Composite panel design . . . . .	163
8.6	Perspectives . . . . .	163
<b>A</b>	<b>Diverse applications of composite structures</b>	<b>181</b>
<b>B</b>	<b>Some results of updating</b>	<b>185</b>
<b>C</b>	<b>Statistical analysis of the design and optimization</b>	<b>191</b>

# List of Figures

1.1	a) Boeing 787, over 50% of the structural components made of composite materials Di Sante [2015] , b) The vertical composite tail plane of the first A350 XWB came out of the paint hall, Toulouse, France, in 2012, and c) A composite fuselage section produced by Spirit AeroSystems in North Carolina, USA, in 2011 Airbus© [2012] . . . . .	30
1.2	a) The full scale CCM primary structure (Kirsch [2011]), b) an analytical model for the CCM, illustrating the use of sandwich composite panels (green) and solid laminates (pink), c) the sandwich composite panel with an aluminium core, used in the CCM, under sandwich to solid laminate joint testing (Collier et al. [2008]) . . . . .	31
1.3	The four tested samples with different perforation configuration, used by Meng et al. [2017]: (a) sample with no perforation, (b) sample with perforation in the face sheet, (c) sample with perforation in the core, and (d) sample with perforation in both the face sheet and core . . .	34
1.4	The geometrical parameters of honeycomb sandwich panels analyzed by Zergoune et al. [2017], including cell angle ( $\alpha$ ) , wall thickness ( $t$ ), panel thickness ( $h_c$ ), vertical member length ( $h$ ) and angled member length ( $l$ ) . . . . .	35
1.5	The procedures employed by Trollé [2009], Trolle et al. [2012] : (a) the generation of the filtered stimulus, and (b) the synthesis of a stationary broadband noise up to the maximum frequency and with the specified frequency resolution . . . . .	40
1.6	The diagram providing an overview of the processes required for constructing the audio/visual model for an object, and subsequently generating sound and motion O'Brien et al. [2002] . . . . .	42
1.7	on overview on the approach to develop the psychoacoustic prediction model, presented by Duvingneau et al. [2015] . . . . .	43



2.1	The geometrical configuration for a composite sandwich plate . . . . .	51
2.2	The geometrical configuration corresponding to the Rayleigh integration and radiation of the vibrating composite panel embedded in a baffle . . . . .	54
2.3	Thesis scenario: From concepts of the 6th and 4th order problems, through modeling stimuli with acoustic and mechanical excitations, updating strategies, perceptual assessment, to composite panel designs and optimizations . . . . .	55
3.1	an overview of the strategy used in this chapter, required for vibro/psychoacoustically assessing and designing composite panels . . . . .	58
3.2	The DAF as a random pressure field excitation: the objective is to model the spectrum of the pressure level at an arbitrary receiver point, caused by the excited vibrating plate . . . . .	60
3.3	a comparison between the FEM and analytical approach for $f \in [0, 10\text{kHz}]$	62
3.4	the relative error associated with the integration approaches and different values of the mesh size . . . . .	63
3.5	a) Beta Cabin with the plate under study, b) inside Beta Cabin with microphones, c) four uncorrelated speakers required for generating an ideal DAF, d) a 4-microphones antenna for acquiring the DAF spectrum, e) the microphone system to record the sound radiated by the plate . . . . .	64
3.6	the spectrum $S_{p_e}(\omega)$ of the DAF excitation, measured during the experiments . . . . .	65
3.7	the measured and modeled SPL spectra radiated by the vibrating $61\text{cm} \times 61\text{cm}$ steel plate excited by the DAF . . . . .	66
3.8	the measured and modeled SPL spectra radiated by the vibrating $61\text{cm} \times 61\text{cm}$ aluminium plate excited by the DAF . . . . .	66
3.9	the measured and modeled SPL spectra radiated by the vibrating $33,9\text{cm} \times 29,2\text{cm}$ steel plate excited by the DAF . . . . .	67
3.10	the measured and modeled SPL spectra radiated by the vibrating $33,9\text{cm} \times 29,2\text{cm}$ aluminium plate excited by the DAF . . . . .	67
3.11	the measured and modeled SPL spectra radiated by the vibrating $33,9\text{cm} \times 29,2\text{cm}$ composite plate excited by the DAF . . . . .	68

4.1	The geometrical configuration associated with an example of a thick composite sandwich panel with a Nomex honeycomb core covered by CFRP face sheets subjected to point-force mechanical excitation $q = \tilde{q}(\omega)e^{i\omega t}$ . . . . .	71
4.2	The schematic diagram of the experimental set-up . . . . .	73
4.3	Some views of the configuration associated with the laboratory experiments: a) the PSV-300-F/S Scanning Vibrometer head, b) the clamped boundary condition performed with a torque equal to 30Nm for screws of the window frame, c) the shaker attached to the plate and connected to a piezoelectric sensor sending the force signal, d) the measuring window, and the floor covered by soundproofing forms e) the microphone recording the sound, f) the spectrum analyzer, g) the spectrum analyzer software . . . . .	73
4.4	The measured and simulated SPLs at 50cm distance for the sandwich plate . . . . .	77
4.5	The measured and simulated SPLs at 50cm distance for the composite laminate plate . . . . .	77
4.6	The measured and simulated SPLs at 50cm distance for the aluminium plate . . . . .	78
4.7	The measured and simulated SPLs at 50cm distance for the steel plate . . . . .	78
5.1	The schematic diagram illustrating the hybrid updating method . . . . .	83
5.2	The MAC corresponding to the composite sandwich specimen: a) a view of the elements of the MAC matrix before the updating, and b) after the updating . . . . .	93
5.3	The MAC corresponding to the composite laminate specimen: a) a view of the elements of the MAC matrix before the updating, and b) after the updating . . . . .	94
5.4	The MAC corresponding to the aluminium specimen: a) a view of the elements of the MAC matrix before the updating, and b) after the updating . . . . .	94
5.5	The MAC corresponding to the steel specimen: a) a view of the elements of the MAC matrix before the updating, and b) after the updating . . . . .	95

5.6	The average of the vibration field for the composite sandwich plate, measured by the LDV system (Laser), compared with the simulations done before and after the updating (Simu (before and after)) . . . . .	98
5.7	The SPL comparison corresponding to the composite sandwich plate, between the simulations (before and after updating) and microphone measurement; the small zoom window shows such SPL comparison for low frequencies . . . . .	98
5.8	The average of the vibration field for the composite laminate plate, measured by the LDV system (Laser), compared with the simulations done before and after the updating (Simu (before and after)) . . . . .	99
5.9	The SPL comparison corresponding to the composite laminate plate, between the simulations (before and after updating) and microphone measurement; the small zoom window shows such SPL comparison for low frequencies . . . . .	99
5.10	The average of the vibration field for the aluminium plate, measured by the LDV system (Laser), compared with the simulations done before and after the updating (Simu (before and after)) . . . . .	100
5.11	The SPL comparison corresponding to the aluminium plate, between the simulations (before and after updating) and microphone measurement . . . . .	101
5.12	The average of the vibration field for the steel plate, measured by the LDV system (Laser), compared with the simulations done before and after the updating (Simu (before and after)) . . . . .	101
5.13	The SPL comparison corresponding to the steel plate, between the simulations (before and after updating) and microphone measurement	102
6.1	The Cortex Manikin MK2 used before the psychoacoustic test. Before conducting the test, it was necessary to measure the sound pressure level, expected to be heard by participants, by means of the Cortex Manikin MK2 . . . . .	107
6.2	The first screen of the interface prompts participants to read the instruction for the test. Although the interface was designed in a way that is user-friendly and easy to understand for all the participants, before each test it was necessary to give the participants general tips about the test . . . . .	110

6.3	An screenshot of the interface presenting a listening panel for the three sessions accompanied by their learning (training) parts, which allowed participants to listen the paired sounds (paired stimuli) as many times as they want, and compare the sounds based on their dissimilarities . . . . .	111
6.4	The Dendrogram associated with the classification of participants and outlier detection in Session 1 associated with the stimuli produced by the mechanical excitation . . . . .	115
6.5	Weighted Silhouette values corresponding to the different classes of the participants in Session 1 associated with the stimuli produced by the mechanical excitation . . . . .	116
6.6	The Dendrogram associated with the classification of participants and outlier detection in Session 2 associated with the stimuli produced by the acoustic excitation . . . . .	116
6.7	Weighted Silhouette values corresponding to the different classes of the participants in Session 2 associated with the stimuli produced by the acoustic excitation . . . . .	117
6.8	The Dendrogram associated with the classification of participants and outlier detection in Session 3 associated with the simulated stimuli filtered with different values of the cutoff frequency . . . . .	117
6.9	Weighted Silhouette values corresponding to the different classes of the participants in Session 3 associated with the simulated stimuli filtered with different values of the cutoff frequency . . . . .	118
6.10	The L-curve (i.e. scree plot) between the distance between the calculated and measured dissimilarity matrices with respect to the number of dimensions in the perceptual space for Session 1 ( $r$ indicates the correlation between the measured and calculated dissimilarities) . . .	121
6.11	The L-curve (i.e. scree plot) between the distance between the calculated and measured dissimilarity matrices with respect to the number of dimensions in the perceptual space for Session 2 ( $r$ indicates the correlation between the measured and calculated dissimilarities) . . .	122
6.12	The L-curve (i.e. scree plot) between the distance between the calculated and measured dissimilarity matrices with respect to the number of dimensions in the perceptual space for Session 3 ( $r$ indicates the correlation between the measured and calculated dissimilarities) . . .	122

6.13	The perceptual space of the stimuli of Session 1, associated with the simulations and recordings of sounds radiated from the mechanically excited panels, including the positions of the stimuli and the ellipses representing the 95% confidence intervals for stimuli coordinates . . .	124
6.14	The perceptual space of the stimuli of Session 2, associated with the simulations and recordings of sounds radiated from the acoustically excited panels, including the positions of the stimuli and the ellipses representing the 95% confidence intervals for stimuli coordinates . . .	125
6.15	The perceptual space of the stimuli of Session 3, associated with the simulations with different cutoff frequencies, including the positions of the stimuli and the ellipses representing the 95% confidence intervals for the stimuli coordinates . . . . .	126
7.1	The designed composite sandwich panel with a hexagonal honeycomb core . . . . .	130
7.2	The English version of the initial interface: participants are guided with an instruction before the test . . . . .	137
7.3	The Dendrogram associated with the classification of participants and outlier detection in the mechanical session . . . . .	138
7.4	Weighted Silhouette values corresponding to the different classes of the participants in the mechanical session . . . . .	139
7.5	The Dendrogram associated with the classification of participants and outlier detection in the acoustic session . . . . .	139
7.6	Weighted Silhouette values corresponding to the different classes of the participants in the acoustic session . . . . .	140
7.7	The L-curve (i.e. scree plot) between the error of the calculation (the 2-norm distance between the measured and calculated dissimilarity), and the number of perceptual dimensions corresponding to the mechanical session . . . . .	141
7.8	The L-curve (i.e. scree plot) between the error of the calculation (the 2-norm distance between the measured and calculated dissimilarity), and the number of perceptual dimensions corresponding to the acoustic session . . . . .	142
7.9	The perceptual space and the coordinates of the stimuli, corresponding to the mechanical session . . . . .	142

7.10	The perceptual space and the coordinates of the stimuli, corresponding to the acoustic session . . . . .	143
7.11	The preference scores corresponding to the different designs in the mechanical session . . . . .	144
7.12	The preference scores corresponding to the different designs in the acoustic session . . . . .	144
7.13	Adjustment quality for the mechanical preference model: the comparison of the measured and calculated preference scores corresponding to the mechanical session, along with their respective 95% confidence intervals . . . . .	149
7.14	Adjustment quality for the acoustic preference model: the comparison of the measured and calculated preference scores corresponding to the acoustic session, along with their respective 95% confidence intervals .	149
7.15	Prediction quality of the acoustic preference model: the comparison of the measured preference scores of the mechanical session with the one predicted by the acoustic preference model, along with their respective 95% confidence intervals . . . . .	150
7.16	Prediction quality of the mechanical preference model: the comparison of the measured preference scores of the acoustic session with the one predicted by the mechanical preference model, along with their respective 95% confidence intervals . . . . .	150
7.17	The Pareto Front: the graph displays the Pareto optimal solutions (the solutions located on the red dash-dot line) in a 2D space of solutions, illustrating the preference scores for both mechanical and acoustic sessions, displaying the preference scores of the 10 designs accompanied by their respective 95% confidence intervals . . . . .	156
A.1	Many components of the A350 XWB, such as fuselage panels, wing, stabilizers and fin/rudder assembly, incorporate composite materials Hexcel© [2013] . . . . .	182
A.2	a) Geometry of a candidate CEV of the Apollo capsule, and b) its double-walled composite sandwich construction Ko et al. [2007] . . .	182
A.3	The structural model of composite floor in high-speed train with different components and different uses Zhang et al. [2021] . . . . .	183

B.1	Comparison of Sound Pressure Levels (SPL) for the composite sandwich plate: Simulations (before and after updating) vs. Microphone Measurements at a 20cm Distance . . . . .	186
B.2	Comparison of Sound Pressure Levels (SPL) for the composite sandwich plate: Simulations (before and after updating) vs. Microphone Measurements at a 100cm Distance . . . . .	186
B.3	Comparison of Sound Pressure Levels (SPL) for the composite laminate plate: Simulations (before and after updating) vs. Microphone Measurements at a 20cm Distance . . . . .	187
B.4	Comparison of Sound Pressure Levels (SPL) for the composite laminate plate: Simulations (before and after updating) vs. Microphone Measurements at a 100cm Distance . . . . .	187
B.5	Comparison of Sound Pressure Levels (SPL) for the Aluminium plate: Simulations (before and after updating) vs. Microphone Measurements at a 20cm Distance . . . . .	188
B.6	Comparison of Sound Pressure Levels (SPL) for the Aluminium plate: Simulations (before and after updating) vs. Microphone Measurements at a 100cm Distance . . . . .	188
B.7	Comparison of Sound Pressure Levels (SPL) for the steel plate: Simulations (before and after updating) vs. Microphone Measurements at a 20cm Distance . . . . .	189
B.8	Comparison of Sound Pressure Levels (SPL) for the steel plate: Simulations (before and after updating) vs. Microphone Measurements at a 100cm Distance . . . . .	189
C.1	The statistical analysis between the sharpness and dimension 1 of the perceptual space, corresponding to the session with the mechanical excitation . . . . .	192
C.2	The statistical analysis between the SC and dimension 1 of the perceptual space, corresponding to the session with the mechanical excitation	192
C.3	The statistical analysis between the stiffness-to-mass ratio and dimension 1 of the perceptual space, corresponding to the session with the mechanical excitation . . . . .	193

C.4	The statistical analysis between the loudness and dimension 2 of the perceptual space, corresponding to the session with the mechanical excitation . . . . .	193
C.5	The statistical analysis between the preference and dimension 2 of the perceptual space, corresponding to the session with the mechanical excitation . . . . .	194
C.6	The statistical analysis between the preference and loudness, corresponding to the session with the mechanical excitation . . . . .	194
C.7	The statistical analysis between the stiffness-to-mass ratio and dimension 1 of the perceptual space, corresponding to the session with the acoustic excitation . . . . .	195
C.8	The statistical analysis between the loudness and dimension 1 of the perceptual space, corresponding to the session with the acoustic excitation . . . . .	195
C.9	The statistical analysis between the preference and dimension 1 of the perceptual space, corresponding to the session with the acoustic excitation . . . . .	196
C.10	The statistical analysis between the sharpness and dimension 2 of the perceptual space, corresponding to the session with the acoustic excitation . . . . .	196
C.11	The statistical analysis between the preference and loudness, corresponding to the session with the acoustic excitation . . . . .	197
C.12	The statistical analysis between the preference and stiffness-to-mass ratio, corresponding to the session with the acoustic excitation . . . .	197
C.13	SPL associated with Designs 5, 8, and 9 in the session with mechanical excitation. Designs 8 and 9 exhibit the highest and lowest stiffness-to-mass ratios, respectively, while Design 5 falls in the middle. The transition from the lowest to highest stiffness-to-mass ratio corresponds to a shift from the lowest to highest values along the 1st dimension of the perceptual space (see Figure 7.9 and Table7.3) . . .	198



C.14 SPL associated with Designs 8, 9, and 10 in the session with acoustic excitation. Designs 8 and 9 exhibit the highest and lowest stiffness-to-mass ratios, respectively, while Design 10 falls in the middle. The transition from the lowest to highest stiffness-to-mass ratio corresponds to a shift from the lowest to highest values along the 1st dimension of the perceptual space (c.f. Figure 7.10 and Table 7.3) . . . 198

# List of Tables

3.1	the geometric and mechanical characteristics of the tested plates . . .	64
4.1	The initial information on the mechanical parameters. The mechanical properties of each CFRP ply with epoxy matrix after curing are based on the assessments of Shahdin et al. [2011], Qi et al. [2019], Zhou et al. [2021], and those of the Nomex core are based on the studies of Adams and Maheri [1993], Roy et al. [2014], Zhou et al. [2021]. The mass densities were measured in the laboratory experiments . . . . .	75
5.1	The coefficients $\{a_l, b_l, c_l, d_l\}$ required for defining the hierarchical functions . . . . .	84
5.2	The mechanical properties of the composite sandwich, laminate, aluminium, and steel plates, identified by the IWC technique . . . . .	92
5.3	The updated mechanical properties of the composite sandwich, laminate, aluminium, and steel plates . . . . .	95
6.1	The stimuli used in the psychoacoustic test, including the simulated sounds and ones recorded during the vibroacoustic laboratory experiments . . . . .	108
6.2	The series of aggregation methods, and the quantified level of adequacy, used for the three Sessions, corresponding to the stimuli produced with a mechanical excitation in Session 1, with an acoustic excitation in Session 2, and with different cutoff frequency values in Session 3 . . . . .	115

7.1	The geometrical and mechanical parameters associated with the composite sandwich panel tested in the laboratory experiments in Chapter 5 ( $a$ and $b$ : dimensions of panel, $h_f$ : thickness of face sheets, $h_c$ : thickness of core, $D_t$ : total bending stiffness, $E_f$ : Young modulus of face sheets, $G$ : shear modulus of core, and $\eta$ : loss damping factor) . . . . .	130
7.2	The parameters of the unit cell associated with the hexagonal honeycomb core of the sandwich panel ( $c$ : cell size, $l$ : angled member length, $h$ : vertical member length, $t$ : wall thickness, $\theta$ : cell angle, $G_s$ : shear modulus of material, $E_s$ : Young modulus of material, and $\rho_s$ : mass density of material) . . . . .	131
7.3	The geometrical, mechanical, and equivalent parameters associated with the composite sandwich panels designed for psychoacoustic tests ( $h_f$ : face sheet thickness, $h_c$ : core thickness, $E_f$ : Young modulus of face sheet, $G$ : shear modulus of core, $\eta$ : loss damping factor, $D_t$ : total bending stiffness, $E_{equi}$ : equivalent Young modulus, $M$ : surface mass density, and $D_t/M$ : stiffness-to-mass ratio) . . . . .	133
7.4	The sound pressure levels of the stimuli, associated with the different designs of the composite panel, excited by the mechanical and acoustic excitations, [unit: dB(A)] . . . . .	134
7.5	The series of aggregation methods and the quantified level of adequacy: : cophenetic and Goodman-Kruskal (e.g. see Sokal and Rohlf [1962], Farris [1969], Goodman et al. [1979]), used for the two Sessions	138
7.6	The statistical results associated with the regression model $P(s) = \alpha N(s) + \alpha_0$ between the preference and loudness for the mechanical session . . . . .	148
7.7	The statistical results associated with the regression model $P(s) = \alpha N(s) + \alpha_0$ between the preference and loudness for the acoustic session	148
7.8	The regression model for preference $P$ in the mechanical session in relation to the mechanical parameters $\eta$ , and $D_t/M$ , where $r$ is the correlation between the modeled and measured preference, and the model is defined as $P = \alpha_0 + \alpha_1\eta + \alpha_2D_t/M + \alpha_3(D_t/M)^2$ . . . . .	154
7.9	The regression model for preference $P$ in the acoustic session in relation to the mechanical parameters $\eta$ , and $D_t/M$ , where $r$ is the correlation between the modeled and measured preference, the regression model is defined as $P = \alpha_0 + \alpha_1\eta + \alpha_2D_t/M$ . . . . .	154

# List of Acronyms

**AHC** Ascending hierarchical classification

**ASD** Auto-spectral density

**CCM** Composite crew module

**CEV** Crew exploration vehicle

**CFRP** Carbon fiber-reinforced polymer

**DAF** Diffuse acoustic field

**FEM** Finite element method

**FGM** Functionally graded material

**FRF** Frequency response function

**INDSCAL** Individual differences scaling

**IWC** Inhomogeneous wave correlation

**LDV** Laser doppler vibrometer

**MAC** Modal assurance criterion

**MDS** Multidimensional scaling

**MLCTS** Multi-layer core topology system

**MOF** Modal overlap factor

**PDE** Partial differential equation

**PF** Pareto front

**PML** Perfectly matched layer

**RMS** Root mean square

**SAC** Sound absorption coefficient

**SCG** Spectral center of gravity

**SC** Spectral centroid

**SIMO** Single-input multiple-output

**SPL** Sound pressure level

**STL** Sound transmission loss

**TF** Transfer function

**TLS** Total least square

**WFEM** Wave finite element method

# List of Symbols

$w$  : transverse displacement

$\nabla$  : gradient operator

$\nabla^2$  : Laplacian operator

$a, b$  : panel dimensions in  $x$  and  $y$  directions

$G$  : shear modulus of viscoelastic core

$D_t$  : total flexural rigidity,

$M$  : mass per unit area

$E$  : Young's modulus

$\eta$  : loss damping factor

$\rho$  : total mass density

$h_1$  : thicknesses of face sheet

$h_2$  : thicknesses of core

$h$  : total thickness of composite

$q$  : external point force

$\acute{g}$  : shear parameter of core

$k_x, k_y$  : wave numbers in  $x$  and  $y$  directions

$D_{ij}$  : bending stiffness coefficient

$B_{ij}$  : coupling stiffness coefficient

$\psi_n$  : modal function

$\omega$  : angular frequency

$\omega_n$  : angular natural frequency

$p(x, y)$  : pressure field at  $(x, y)$

$v = \dot{w}$  : transverse vibration velocity

$c_0$  : sound speed in air

$Ray$  : Rayleigh integral operator

$[\bar{Q}_{ij}^k]$  : transformed reduced stiffness matrix

$\phi_n$  : hierarchical function

$\mathbf{K} = [K_{mn}]$  : stiffness matrix

$\mathbf{M} = [M_{mn}]$  : mass matrix

$\gamma(\theta)$  : wave attenuation

$r$  : linear Bravais-Pearson correlation coefficient

$p$  : p-value of statistical hypothesis test

$d_{ij}$  : dissimilarity distance between stimuli  $j$  and  $k$

$\mathbf{D}$  : dissimilarity matrix

$\mathbf{P}$  : preference matrix

$P(s)$  : preference score of stimulus  $s$

$N(s)$  : Zwicker loudness

$D_t/M$  : stiffness to mass ratio

# Chapter 1

## Introduction and State of the art

In this chapter, first, the motivation behind the research is discussed. Then the literature review focuses on the state of the art concerning vibroacoustic studies of composite sandwich structures, and psychoacoustic studies in related fields.

### 1.1 Motivation

Motivation stems from applications and usage of composite structures. In recent years, there has been a rapid and increasingly prominent trend in the utilization of composite materials across various industries such as aeronautics, space studies, and transportation. Such interest in composite materials can be attributed to their exceptional properties like their lighter weight, acceptable strength and stiffness, enhanced stability, corrosion resistance, sound baffling for a less noisy operating environment, and design flexibility for usage in complex designs, e.g., see Kaw [2005], Daniel et al. [2006].

In aeronautic industry, composite materials have experienced increasing acceptance in aeronautical construction over a period of four decades Giurgiutiu [2015]. Presently, new airframes, such as the Boeing 787 Dreamliner and Airbus A350 XWB (refer to Figure 1.1), are predominantly made of composites, with composites accounting for 80% of the volume Giurgiutiu [2015]. Aerospace giants like Airbus and Boeing have spearheaded the utilization of composite materials and other advanced materials in aircraft design and manufacturing Mrazova [2013].

In the field of space studies, significant advancements in composites have occurred since the historic Apollo moon landing in 1969, where they played a key role in constructing the Apollo crew exploration vehicle, e.g., see Ko et al. [2007]. Recently, NASA's Exploration Systems Mission Directorate performed certain projects like the



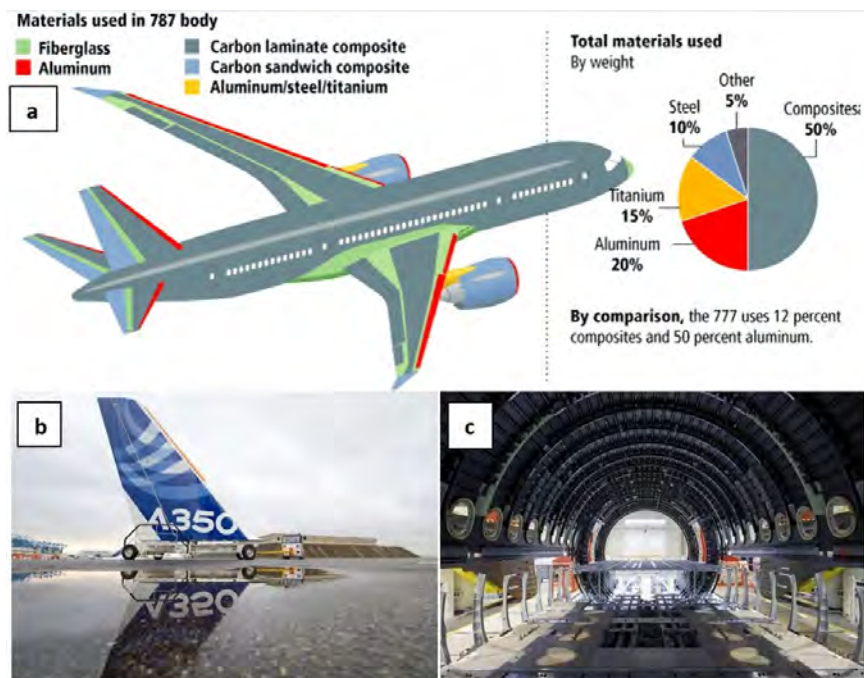


Figure 1.1: a) Boeing 787, over 50% of the structural components made of composite materials Di Sante [2015], b) The vertical composite tail plane of the first A350 XWB came out of the paint hall, Toulouse, France, in 2012, and c) A composite fuselage section produced by Spirit AeroSystems in North Carolina, USA, in 2011 Airbus© [2012]

Composite Crew Module (CCM) to develop a light-weight and durable crew module for future human spaceflight missions, particularly for deep space exploration Kirsch [2011] (see Figure 1.2). The goal of the CCM project was to investigate and evaluate the utilization of advanced composite materials, such as carbon fiber-reinforced polymers, in the construction of crew modules. The majority of the CCM structure was sandwich composites with unvented aluminum honeycomb core Collier et al. [2008], Kirsch [2011].

Similar to aerospace industries, in transportation, composite materials offer a range of advantages that have revolutionized the industry. The weight reduction, being one of the main benefits of composite materials, directly translates into improved fuel efficiency, as lighter vehicles require less energy to operate. By employing composite materials, the transportation industry can achieve substantial reductions in unnecessary fuel consumption, leading to greener future vehicles (e.g. see Koniuszewska and Kaczmar [2016], Sajan and Philip Selvaraj [2021]).

Furthermore, the increased stability provided by composites further contributes to lasting performance and safety in transportation. Another notable advantage of composite materials is their exceptional resistance to corrosion. Unlike traditional materials like metals, composites are highly resistant to deterioration caused by en-

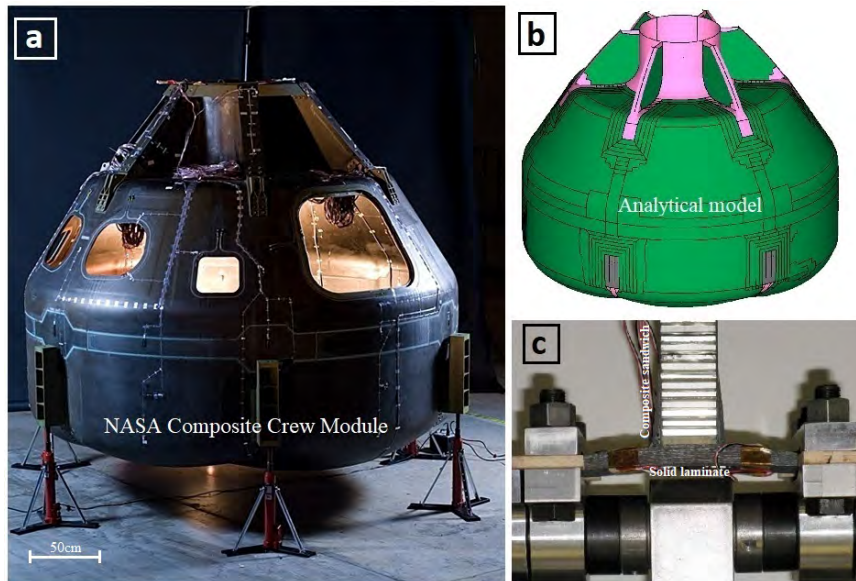


Figure 1.2: a) The full scale CCM primary structure (Kirsch [2011]), b) an analytical model for the CCM, illustrating the use of sandwich composite panels (green) and solid laminates (pink), c) the sandwich composite panel with an aluminium core, used in the CCM, under sandwich to solid laminate joint testing (Collier et al. [2008])

environmental factors such as moisture, chemicals, and temperature variations. This corrosion resistance ensures prolonged operation of vehicles without the need for extensive maintenance or frequent part replacements. In addition to these properties, composite materials also provide excellent sound baffling capabilities. The incorporation of composites in vehicle design can effectively reduce noise levels, creating a more pleasant and comfortable operating environment for drivers and passengers alike. Lastly, composites offer unparalleled design flexibility, enabling the construction of complex shapes and structures. This characteristic allows designers and engineers to optimize the aerodynamics and overall performance of vehicles, leading to increased efficiency and improved functionality (e.g. see Koniuszewska and Kaczmar [2016], Fan and Njuguna [2016], Sajan and Philip Selvaraj [2021]). For more details on various applications of composite structures, see Appendix A.

## 1.2 Literature review

As we discussed in the previous section, sandwich structures are common composite lightweight structures that are widely used in the different sectors of engineering industries like aerospace, mechanical, and transportation. The panels are constituted

from thin face sheets and a thick core offering a diversity of material choices and architectures. In some recent research, we can find that the vibroacoustic properties of sandwich panels can be improved playing with the geometrical architecture. Certain ideas have been explored to valid the impact of geometric design on the vibroacoustic indicators.

### 1.2.1 Vibroacoustic studies

In order to have the best design for composite sandwich structures, it is necessary to consider all possible states of their geometrical and physical parameters. Analytical models for vibroacoustic behavior of composite panels can allow to perform a large volume of analyses for large number of the geometrical and physical parameters with high speed and less time. Therefore, in recent years, numerous studies have emerged in the literature, examining the analytical modeling of dynamical behavior in sandwich panels.

#### Analytical models

The initial investigation into the analytical modeling of composite sandwich panels can be traced back to the early 1980s, when some scientists like Mead and Markus [1969], Narayanan and Shanbhag [1981, 1982] introduced and developed the 6<sup>th</sup> order problem for such modeling. Mead and Markus [1969] conducted a comprehensive review of all the assumptions underlying the problem and derived the sixth-order differential equation of motion for a sandwich rectangular plate with a viscoelastic core, considering the transverse displacement. Building upon the study of Mead and Markus [1969], Narayanan and Shanbhag [1981] analytically investigated the sound transmission through viscoelastic sandwich panels, specifically focusing on the low frequency range. Similarly, Narayanan and Shanbhag [1982] analytically studied the sound transmission through an infinite sandwich panel that incorporated a viscoelastic damping layer. They obtained expressions for the sound transmission loss and the coincidence frequency, which were based on the core parameters and the incidence pressure angle.

In the 1990s, Renji et al. [1996] presented an analytical expression that incorporated a core transverse shear stiffness and bending matrices in both directions for orthotropic panels. Their theoretical study resulted in the derivation of a governing partial differential equation, which took into account the shear flexibility of the core. Furthermore, Renji et al. [1996] conducted specific experiments on a representative panel to validate their theoretical findings. The experimental results demonstrated

a satisfactory alignment with the outcomes predicted by their theories.

The research done by Nilsson and Nilsson [2002] can be counted as another example for the analytical models of sandwich panels, which derived a six-order differential equation governing the apparent bending of sandwich beams, using Hamilton's principle. In this analytical modeling, bending, shear and rotation were considered and a method for the calculation of eigen frequencies and modes of vibration for rectangular orthotropic sandwich plates were presented.

### **Design and analyses**

During the design stage of sandwich panels, it is crucial to thoroughly evaluate various potential scenarios, considering both geometrical and physical parameters as well as configurations. For example, in a study conducted by Droz et al. [2016], diverse periodic cores were examined, aiming to enhance the transition frequency and decrease the modal density within a specific frequency range. The transition frequency occurs in a sandwich panel when the transverse shear stiffness significantly impacts the flexural motion, in contrast to the bending stiffness. Droz et al. [2016] utilized a wave/finite element method (WFEM) to compare different core constructions applicable to a given sandwich panel.

Similarly, Arunkumar et al. [2016] conducted a study to examine the impact of core geometry on the vibro-acoustic response characteristics of sandwich panels used in the aerospace industry. The researchers performed numerical analyses to investigate the vibro-acoustic behavior of sandwich panels with various cores. To reduce preprocessing time and computational effort, Arunkumar et al. [2016] first calculated the equivalent 2D elastic properties and utilized them to determine the vibration and acoustic response characteristics. Furthermore, this research ensured the accuracy of the results through validation studies on natural frequency and sound response evaluation. The comparison between the 2D FEM and 3D FEM models revealed a high level of agreement in their free vibration characteristics.

Meng et al. [2017] conducted a study to analyze the effects of a geometrical parameter on the vibro-acoustic indicators of sandwich panels. The authors performed numerical and experimental tests to evaluate the low-frequency sound absorption coefficient (SAC) and sound transmission loss (STL) of corrugated sandwich panels with various perforation configurations. The study employed Finite Element (FE) models that accounted for acoustic-structure interactions, as well as viscous and thermal energy dissipations within the perforations. The FE calculations were validated against experimental observations using additive manufacturing to produce the tested samples. The results presented by Meng et al. [2017] demonstrated that

compared to the traditional corrugated sandwich panels without perforations, the corrugated sandwich panels with perforated pores in one of their face sheets exhibited not only a higher SAC at low frequencies but also improved STL due to the increased SAC. Figure 1.3 illustrates the tested samples used in the study, which encompassed different configurations: (a) sample with no perforation, (b) sample with perforation in the face sheet, (c) sample with perforation in the core, and (d) sample with perforation in both the face sheet and core.

Also, in a study conducted by Zergoune et al. [2017], a modeling strategy was pro-

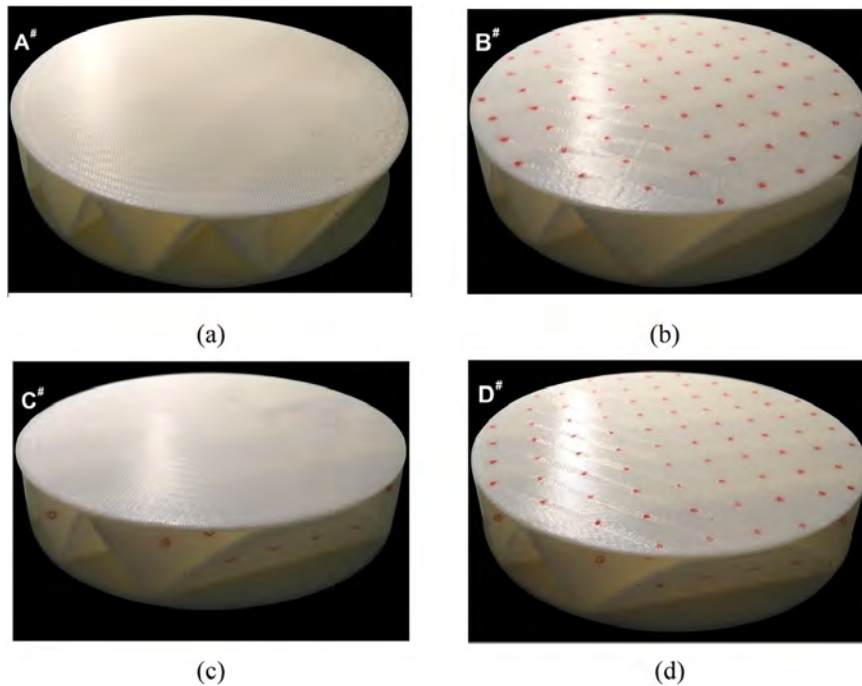


Figure 1.3: The four tested samples with different perforation configuration, used by Meng et al. [2017]: (a) sample with no perforation, (b) sample with perforation in the face sheet, (c) sample with perforation in the core, and (d) sample with perforation in both the face sheet and core

posed based on a two-scale method to analyze the flexural vibroacoustic behavior of sandwich panels. The primary vibroacoustic indicators investigated in this research were the sound transmission loss and the bending-shear transition frequency of the sandwich panels. The findings of Zergoune et al. [2017] revealed that these indicators are predominantly influenced by the geometrical and mechanical parameters. Through parametric analyses, the study highlighted the effects of various meso-scale parameters on the macro-scale responses of the sandwich panels, employing a three-dimensional model of a representative elementary cell.

Actually, the parametric analyses conducted by Zergoune et al. [2017] revealed several findings regarding the sound transmission loss (STL) of the sandwich panel.

Firstly, the cell angle ( $\alpha$ ) of the hexagonal core was found to have no influence on the STL. However, increasing the panel thickness ( $h_c$ ) was shown to significantly enhance the STL at mid frequencies and raise the transition frequency. Nonetheless, this increase in thickness may also lead to a notable decrease in the stiffness-weight ratio of the sandwich panel. Additionally, the research demonstrated that increasing the wall thickness ( $t$ ) in relation to the vertical member length ( $h$ ) resulted in a moderate improvement in the STL. Furthermore, increasing the angled member length ( $l$ ) in relation to the vertical member length ( $h$ ) was found to enhance the transmission loss in the mid frequency range. Moreover, the research showed that the overall increase in the transition frequency generally indicated an improvement in STL, particularly at the mid frequencies. Figure has illustrated the geometrical parameters of the composite sandwich panel analyzed in the study of Zergoune et al. [2017].

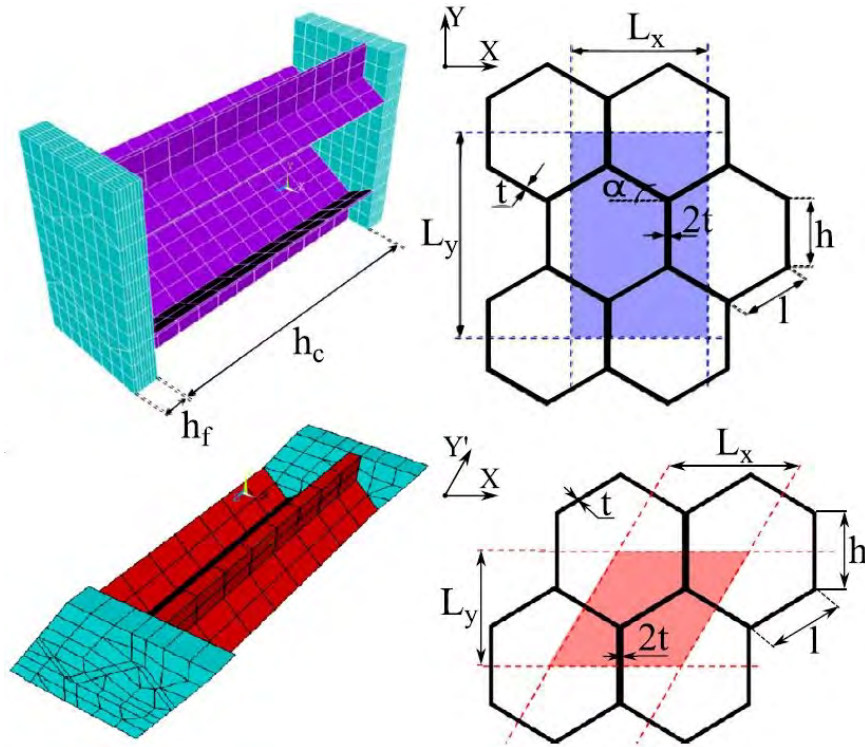


Figure 1.4: The geometrical parameters of honeycomb sandwich panels analyzed by Zergoune et al. [2017], including cell angle ( $\alpha$ ), wall thickness ( $t$ ), panel thickness ( $h_c$ ), vertical member length ( $h$ ) and angled member length ( $l$ )

Moreover, in recent years, other studies have been conducted. For instance, Errico et al. [2020] designed two types of sandwich panels using the periodic structure theory. In this study, a double-wall panel with mechanical links and a sandwich panel with a rectangular core were thoroughly examined. Moreover, the research

proposes a core optimization using shifted core walls. Additionally, Guenfoud et al. [2020] investigated multi-layer rectangular core topology systems that were constructed by stacking layers with various rectangular core geometries. This study has explored various models applied to a sandwich panel consisting of a rectangular core unit cell. Subsequently, Guenfoud et al. [2020] enhanced the panel's design to create a multi-layer rectangular core system. Traditionally, transition frequencies are studied as a consequence of the dynamic behavior of the structure. However, in this research, a novel approach was proposed to control the transition frequencies through Multi-layer core topology systems (MLCTS) designs. Lastly, Ntourmas et al. [2023] demonstrated a process for optimizing the stacking sequence of a composite aircraft wing skin. In this research, a two-stage approach is implemented to effectively meet all sizing requirements for an industrial-sized, medium-altitude, long-endurance drone. In the first gradient-based optimization stage, the structure's properties are modeled through generic stacks. The second optimization stage utilizes mathematical programming to solve a Mixed Integer Linear Programming formulation for stacking sequence optimization.

### 1.2.2 Psychoacoustic studies

As evident from the aforementioned studies, the primary emphasis lay on vibroacoustic modeling of composite panels and their associated vibroacoustic indicators, such as acoustic absorption, sound transmission loss, and transition frequency. However, these studies typically overlooked the impact of radiated sounds from vibrating composite panels on auditory perception. There are other types of research studies in the recent literature that have endeavored to optimize design by coupling vibroacoustics and auditory perception to enhance comfort. Although most of these recent studies have not specifically focused on composite panels, they have presented considerable knowledge regarding the connections between the physical parameters of radiating mechanical structures and the auditory characteristics of the emitted or transmitted sounds. They aimed to evaluate the influence of physical parameters on auditory perception. The findings of these studies can be used to offer valuable insights and recommendations during the design phase to enhance the quality of the sounds emitted or transmitted by the mechanical structures like composite panels.

#### Preliminary studies

For instance, Meunier et al. [2001] provided a combination of vibroacoustic and psychoacoustic investigations of sounds radiated by a vibrating structure excited either

by a force on the structure or by an incident sound pressure. The calculated sound field was the sound pressure radiated by a baffled thin-plate structure immersed in a fluid. In this research, various configurations were chosen for the experiments, each configuration leading to a particular acoustic signal. Then these signals were changed into sound files, which were used as test signals in corresponding psychoacoustic experiments for assessing their perceptual attributes and quality. Finally, based on the vibroacoustic and psychoacoustic investigations, overall, Meunier et al. [2001] could confirm an interest of extending vibroacoustic studies to a more complete psychomechanical investigation.

Another example is the study by Canévet et al. [2004] that focused on the auditory properties and quality of sounds generated by the vibrations of a fluid-loaded plate, which are excited by a transient point force. The researchers combined vibroacoustic and psychoacoustic tools to investigate how mechanical, acoustical, and auditory parameters interact and shape the perception of these sounds. To calculate the vibrations in the plate and the radiated acoustic field, Canévet et al. [2004] employed the method of resonance modes in the time domain and a Rayleigh-Kirchhoff formula. In this research, a series of sounds corresponding to various combinations of mechanical parameters was synthesized. Then a dissimilarity test was conducted to determine the auditory space in which these sounds are perceived. Finally, the main dimensions of this space were identified by analyzing acoustic and psychoacoustic properties of the sounds, primarily focusing on time-frequency patterns and the time course of specific loudness. Canévet et al. [2004] characterized the perceptual space by three dimensions and revealed that these dimensions, in the context of its associated case study, are primarily connected to psychoacoustic and physical properties. The first dimension was intricately connected to the time decay of signal amplitude, influenced by the mechanical damping of the structure, as well as the duration and position of the excitation. The second dimension was closely tied to the tonalness of sounds and was found to be influenced by the duration of transient excitation. Lastly, the third dimension was associated with the sharpness of sound onset, and its characteristics were linked to both the duration and location of the excitation.

### **Perceptual evaluations**

Demirdjian et al. [2004] conducted a psychomechanical investigation, combining vibroacoustic and psychoacoustic studies. The study focused on a fluid-loaded plate that was clamped and excited by a transient point force. The main objective was to determine whether a plate with varying thickness could be effectively modeled by a constant-thickness plate, yielding perceptually equivalent results. The researchers



employed psychoacoustic dissimilarity tests on synthesized sounds. The findings of the study suggested that the listeners relied on the pitch of the sounds as the perceptual attribute, enabling them to establish an equivalent thickness.

Faure and Marquis-Favre [2005] conducted a study on the coupling of vibro-acoustic and perceptual evaluations of sounds radiated from a steel plate, while varying the structural parameters. They proposed an approach that involves computing the sound pressure radiated from the plate at the listener's ears. The synthesized stimuli were then presented in pairs to participants, who provided dissimilarity and preference judgments as the structural parameters were varied. Furthermore, Faure and Marquis-Favre [2005] presented the results in terms of both vibro-acoustic indicators and preference and perceptual attributes for variations in the structural parameters. Finally, they investigated the effects of varying the structural damping factor, Young's modulus, thickness, density, and Poisson's ratio of a simply supported baffled steel plate on sound perception.

Also, Demirdjian et al. [2005] conducted a comparative study on the auditory properties of sounds emitted by a fluid-loaded vibrating plate when subjected to a transient point force excitation. The primary objective of this study was to assess the validity of a model developed to simulate the acoustic radiation. Specifically, Demirdjian et al. [2005] focused on a clamped steel plate excited by an impact hammer. From a physical point of view, they evaluated both recorded and synthesized sounds emitted by the vibrating plate. Furthermore, psychoacoustic tests were conducted to perceptually validate the simulations and determine the number of modes that needed to be considered in the calculations.

Another example of such research was Trollé et al. [2008] that concerned the effect of the independent variation of certain structural parameters on the auditory perception of environmental noises transmitted through a window. This research set out how some structural parameters, the structural damping factor and the mounting conditions, of a glass panel could affect the auditory perception of transmitted environmental noises. Trollé et al. [2008] highlighted that 1) only the use of the indicators of window acoustic performance does not provide a solution optimal from a qualitative point of view, and 2) so, performing an auditory evaluation of the transmitted noises, accompanying a physical analysis of the structure, proves to be profitable for improvement of acoustic comfort in houses.

Furthermore, the study conducted by Trollé [2009] focused on the auditory perception of sounds emitted from a vibrating plate within a damped cavity. The main objective was to optimize vibroacoustic computations in order to improve the quality of radiated sounds starting from the structural design phase. Within this study, the adjustment of vibroacoustic computation parameters proved crucial when

dealing with synthesized sounds, in order to be relevant from perceptual point of view. The study aimed to fine-tune the maximum limit frequency and the frequency step to a level that would ensure the preservation of perceptual outcomes related to an optimal structural design. These outcomes were initially obtained through auditory evaluations of a set of recorded sounds. To achieve this objective, Trollé [2009] obtained recorded sounds from an experimental system consisting of a cavity-backed plate. These sounds corresponded to the radiation of the plate inside the air cavity and were recorded for various structural configurations. The experimental configurations involved controlled variations of three structural parameters: the plate thickness, plate tightening conditions, and cavity sound absorption properties. For psychoacoustic assessments, Trollé [2009] subjected the recorded sounds to pairwise evaluations by a panel of listeners. The listeners were asked to provide dissimilarity and preference judgments. Reference perceptual results were then established, defining a perceptual space and preference ranking. Finally, utilizing the actual recorded sounds, Trollé [2009] aimed to accomplish two objectives: i) determine an appropriate cutoff frequency through lowpass filtering of the recorded sounds, allowing the retention of the reference perceptual results, and ii) identify an adjusted frequency step to be applied to the sound spectra during synthesis, ensuring the preservation of the previously established perceptual results. Building upon the research by Trollé et al. [2008], Trollé [2009], Trolle et al. [2012] further explored the optimization of vibro-acoustical computational expenses within the context of evaluating sound quality in a basic plate-cavity system. The authors aimed to identify simulation parameters that would minimize computational costs while adhering to perceptual constraints, in order to achieve perceptual outcomes of synthesized sounds that closely resemble the original real sounds. The diagram depicted in Figure 1 summarizes the procedures employed by Trollé [2009], Trolle et al. [2012]. Using vibroacoustic simulations, Trolle et al. [2012] focused on modifying the computational cost of vibroacoustic analysis to evaluate sound quality in a basic plate-cavity system. By concentrating on such a basic system, this study eventually aimed at reaching some recommendations useful for vibrating structures, made up of plane plates, in various environments like areas of transport and building.

McAdams et al. [2010] conducted a study on the psychomechanics associated with simulated sound sources and the material properties of impacted thin plates. The stimuli were synthesized using a computer model that simulated impacted plates with varying material properties, including viscoelastic and thermoelastic damping, as well as wave velocity related to elasticity and mass density. Based on psychoacoustic tests, they derived the perceptual structure from multidimensional scaling

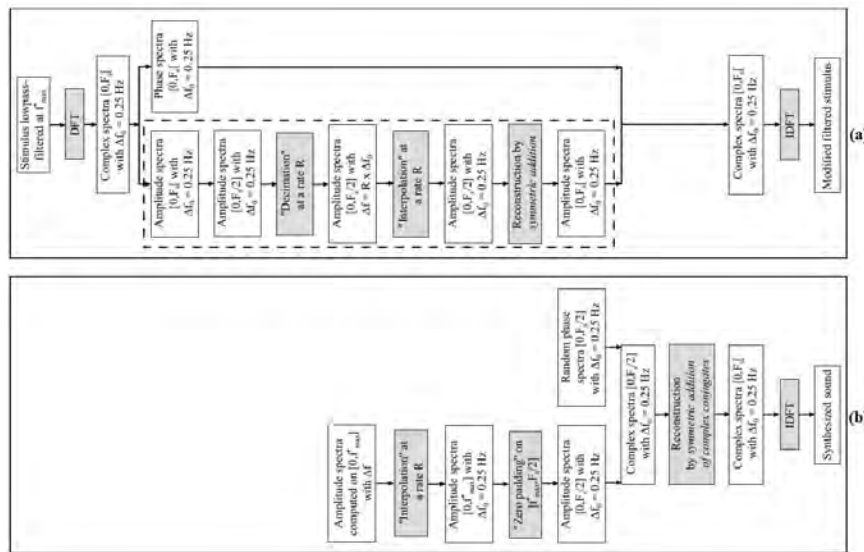


Figure 1.5: The procedures employed by Trollé [2009], Trolle et al. [2012] : (a) the generation of the filtered stimulus, and (b) the synthesis of a stationary broadband noise up to the maximum frequency and with the specified frequency resolution

of dissimilarity judgments and categorization responses. Then they could relate the perceptual dimensions to both physical and perceptual properties: one dimension linked to wave velocity and pitch, and another dimension tied to damping, timbre, and duration. However, McAdams et al. [2010] argued that despite this, when participants were tasked with categorizing the sounds, they tended to overlook cues related to wave velocity and instead focused on cues associated with damping. Furthermore, both the dissimilarity-rating and identification in their experiments consistently indicated that the findings were unaffected by the material of the mallet used to impact the plate.

Using recorded sounds radiated by impacted solid objects of varying shapes (rods, plates, and cylinders) made of aluminum, wood, or glass, Hjortkjær and McAdams [2016] examined similarity ratings and categorization performance in two psychoacoustic experiments. Regarding these experiments, sounds were recorded to represent different action categories (strike, rattle, drop) and material categories (wood, metal, glass). Rattle sounds originated from manually rattling these objects, drop sounds from releasing them onto a solid floor, and strike sounds from impacting objects within the same material category. For the first experiment, participants were tasked with rating the similarity between pairs of sounds. They achieved this by adjusting a continuous on-screen slider scale labeled "very similar" on one end and "very dissimilar" on the other. In the second experiment, participants were presented with sound stimuli during various trials. They were then asked to identify

either the material (wood, metal, or glass) or the action (drop, strike, or rattle) category.

Pulvirenti et al. [2023] conducted an analysis on the sensitivities of human perception regarding numerical parameters commonly found in Finite Element (FE) models used for exterior acoustic problems. The study considered the concept of adaptive mesh and employed the Perfectly Matched Layer (PML) technique to ensure the Sommerfeld radiation condition, thereby introducing a set of parameters for investigation. By convolving a source signal with various simulated Transfer Functions (TF), Pulvirenti et al. [2023] obtained multiple sound samples. These TFs represented the same acoustic path but were generated using FE models with different parameters. Psychoacoustic metrics were employed in this research to examine how changes in FE models affect sound properties, where jury tests were conducted to assess the modifications in human perception resulting from these differences. Regarding the FE models, based on the jury tests, the study found that a linear regression of loudness and sharpness has a high correlation with the perceived differences. Consequently, this research demonstrated the impact of numerical errors on these two metrics, establishing a connection between the accuracy of the FE models and the perception of the auralized sounds.

### **Auralization**

Meanwhile, when the aim is to investigate the psychoacoustics of sounds emitted by a vibrating structure, auralization plays a crucial role in the modeling and simulation of these sounds. Auralization, as defined by Kleiner et al. [1993], is the process of making the sound field of a source audible in a space by using physical or mathematical models. Its purpose is to predict and simulate the binaural listening experience at a specific position within the modeled space. Having the ability to predict the sound pressure emitted by the vibrating structure would greatly benefit the development of mechanical structures. Furthermore, being able to listen to the simulated radiated sound in a simulated environment would be useful at the design stage. Since the beginning of the 21st century, we can find various studies being interested in using auralization for different purposes. In 2001, O'Brien et al. [2001] proposed a general technique for approximating sounds that are generated by the motions of solid objects. O'Brien et al. [2001] also presented results achieved with a FEM-based method. Their method was a time domain version of FEM to compute the velocity of each node on a structure and just the pressure radiated from elements with an unobstructed line of sight are considered, i.e. in their technique, the reflected sound and diffractions are ignored for modeling the audio signals. Then

O'Brien et al. [2002] described a real-time method for producing sounds belonging to the motions of rigid objects. In this research, by numerically precomputing the shape and frequencies of an object's deformation modes, audio can be synthesized interactively directly from the force data produced by a standard rigid-body simulation. The majority of this research describes a FEM algorithm that calculates the required mode shapes and node displacements. The diagram illustrated by Figure 1.7 depicts the preprocessing steps used by this research to construct the audio/visual model for an object, and subsequently to generate sound and motion.

Continuing O'Brien et al. [2002], in 2006, James et al. [2006] described a fast tech-

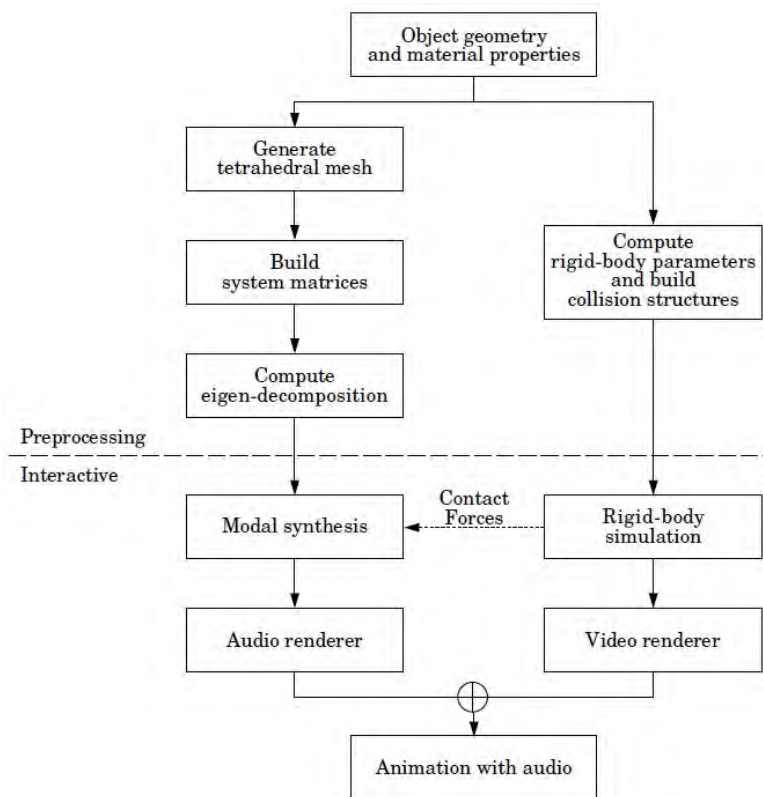


Figure 1.6: The diagram providing an overview of the processes required for constructing the audio/visual model for an object, and subsequently generating sound and motion O'Brien et al. [2002]

nique for synthesizing sound radiation from geometrically complex vibrating objects. Their technique and its corresponding precomputed acoustic transfer functions were founded on accurate approximations to Helmholtz equation solutions made by standard numerical methods. They introduced an algorithm for generating equivalent source approximations that provide real-time sound synthesis in physically based animation.

In addition to the above-mentioned studies, in the recent years, prediction of sound radiated from machinery such as cars has been of interest to engineers. The goal of such a prediction is to optimize sound parameters such as overall level or maybe even characteristics like harshness or sharpness. For instance, Duvigneau et al. [2015] presented a modeling approach of the acoustic behavior of engines including elastic multi-body simulation, vibration analysis, acoustic analysis, auralization and psychoacoustic modeling. The approach proposed by this research is utilized to produce audio signals which can be used in psychoacoustic tests and its target is to be able to design sound quality of a car engine in simulations. Figure illustrates a summary of the approach presented by this study. As seen in this figure, Duvigneau et al. [2015] employs a Finite Element Method (FEM) to predict the sound radiated from the source, where the authors also preferred to use the Sommerfeld radiation condition at the boundary of the meshed area (i.e. preferred to consider no reflections at the boundary points). Then the predicted sounds were utilized to conduct paired comparison listening tests, ultimately resulting in an interval-scaled ranking of the stimuli. A psychoacoustic model was constructed, demonstrating the strongest correlation with the subjective evaluation of engine sounds. This model was formulated as a function, comprising a weighted combination of carefully selected classical psychoacoustic indicators such as loudness and sharpness (see Duvigneau et al. [2015]).

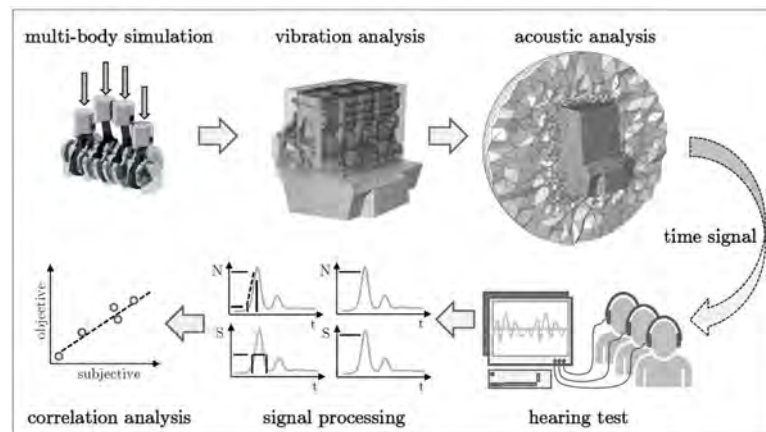


Figure 1.7: on overview on the approach to develop the psychoacoustic prediction model, presented by Duvigneau et al. [2015]

### Miscellaneous purposes

Also, in recent years some psychoacoustic studies have been conducted for applications of composite materials in miscellaneous fields like musical issues. Within

the recent literature, one can find certain evaluations of psychoacoustic aspects concerning composite materials employed in constructing and enhancing musical instruments. As an example in this regards, Roest [2016] conducted a study aiming to create a composite guitar with acoustic properties similar to a traditional wooden guitar. They developed a novel composite material composed of carbon fiber reinforced polyurethane foam, which successfully replaced wood in the key components of guitar. The acoustic response of this composite material was found to be comparable to that of high-quality tonewoods commonly used for guitar soundboards. Utilizing this new composite, a complete composite guitar was designed, manufactured, and tested. So, through certain psychoacoustic analyses, Roest [2016] claimed that when the newly developed composite was used in a complete composite guitar, the resulting instrument was extremely difficult to distinguish from a traditional wooden guitar. For this purpose, the study conducted psychoacoustic test with two goals: determining if the composite guitar was perceived as a wooden guitar and assessing its tonal qualities compared to other guitars. The test comprised a three-part setup. The first part introduced the research and gathered participant expertise. The second presented unique clips, followed by questions about identification, preference, and tone quality. The third involved matching sound clips to guitars, evaluating participants' ability to distinguish composite and carbon fiber guitars from traditional wooden ones.

Similarly, the study conducted by Duerinck et al. [2020] focused on evaluating the acoustic characteristics of six prototype violins. These violins were specifically manufactured in a controlled laboratory environment, with the only variable being the composite material used for the top plate. In this study, experienced listeners including instrument makers, musicians, music teachers and composers were invited to participate in psychoacoustic tests to assess the violins. For this purpose, two listening tests were carried out. In the initial listening test, participants provided individual ratings for the violins across various attributes. Each violin's attributes were presented using an eight-point Likert scale positioned between two contrasting adjectives. Additionally, the second listening test employed pairwise comparisons. This second test followed the ABAB format, as derived from the format used in Fritz et al. [2017]. This format enabled listeners to experience each violin twice: both before and after the other violin. Based on the psychoacoustic tests, contrary to popular belief that violins made from composite materials, as opposed to traditional tonewoods, possess a distinct sound quality or lack thereof, Duerinck et al. [2020] proved the quality of diverse sounds and timbres that can be achieved with fiber-reinforced polymer violins.

**Summarizing remark**

This chapter explored into the corresponding motivation and scientific literature behind the thesis. The motivation stemmed from the practical applications and critical requirements of composite structures. Then it provided a comprehensive literature review encompassing vibro-acoustic and psychoacoustic studies corresponding to the optimization of composite structures as well as other related research issues. Now, continuing with all the previous studies, the following chapters will concern the vibroacoustic modeling and psychoacoustic assessments of composite panels with the purpose of a conjoint psychoacoustic and vibroacoustic oriented design optimization of such composite structures. In Chapter 2, a comprehensive explanation of the problems associated with vibrating composite panels, and the technical scenario of the research is provided. Following that, Chapter 3 focuses on vibroacoustic modeling of panels excited by diffuse acoustic field. Similarly, Chapter 4 is centered around the modeling with mechanical excitation. Moving forward, Chapter 5 present a method for updating models and the parameters in the associated problems, necessary for the precise vibroacoustic modeling of composite panels. Chapter 6 addresses perceptual validation, while Chapter 7 presents psychoacoustic and vibroacoustic design optimizations of composite panels. Ultimately, Chapter 8 ends the thesis with general concluding remarks.





# Chapter 2

## Problem definition

In this Chapter, the vibration of composite panels is analytically investigated. For this purpose, governing partial differential equations (PDEs), called 6<sup>th</sup> and 4<sup>th</sup> order problems, which are able to model the vibration behavior of different composite panels including isotropic, laminate and sandwich composite panels, are discussed in detail. These problems will serve as the foundation for the simulations and mathematical modeling in the current thesis.

### 2.1 Vibration of composite panels

The vibration of composite panels is a complex field that requires the application of various theories and concepts from structural mechanics, materials science, and vibration analysis. The fundamental theory governing the behavior of composite panels arise from elasticity theory (e.g. see Gibson [2007]). Composite materials exhibit behavior that differs from isotropic panels due to their complex structures like the variety of materials and layers used in composite panels, layouts and geometrical arrangements of the layers, and orientations of reinforcing fibers within the matrix at each layer. For instance, the orientation affects the stiffness and compliance matrices, which describe how stress and strain vary in different directions (e.g. see Kaw [2005], Gibson [2007]). Meanwhile, Laminate theory can be helpful for investigating mechanical characteristics of composite panels, required for analyzing the vibration of composite panels. Laminate theory takes into account individual layers or laminae, and then the stiffness properties of each lamina, such as Young's modulus and Poisson's ratio, play a crucial role in predicting the overall panel's behavior. Laminate theory provides the means for performing analytical stress-strain assessments on various laminated structures under mechanical or acoustic loads. It allows

for the analysis of laminates with any number of layers, diverse layer thicknesses, and different material types. Classical laminate theory enables the computation of stresses and strains within individual layers, the determination of overall laminate properties, and the assessment of the total deformation experienced by the laminate (e.g. see Berthelot and Ling [1999]).

On the other hand, classical plate theory is often employed to model the deformation of composite panels under bending loads. The classical plate theory, also referred to as Kirchhoff–Love theory of plates, serves as a useful framework for depicting a three-dimensional plate in a simplified two-dimensional representation (Teotia and Soni [2018]). This theory operates under the fundamental assumption that the plate’s thickness remains constant throughout any deformation. This theory provides differential equations that describe how the panel’s mid-plane displacements and rotations change concerning the coordinates within the panel (e.g. see Barbero [2010]). Furthermore, natural frequencies and mode shapes describe how a composite panel or beam vibrates when subjected to external loads and various boundary conditions. Modal analysis entails solving eigenvalue problems to determine the panel’s natural frequencies and corresponding mode shapes (e.g. see Boudjemai et al. [2012]). So, considering laminate theory, plate theory, and modal analyses of composite panels, when these composite structures encounter external mechanical or acoustic forces or excitations, forced vibration analysis can be used for determining how the panel responds. This analysis considers solving dynamic equations of motion while considering damping effects, external loads, and boundary conditions. In recent years, from a vibroacoustic point of view, several studies have been conducted to examine and investigate composite panels, their vibroacoustic behaviors when subjected to various types of load, and the corresponding equations of motion governing them. In the meantime, the theoretical studies conducted in these fields can be summarized into two problems: 6th and 4th-order problems, which we will discuss in the following sections.

## 2.2 6<sup>th</sup> order problem

The 6<sup>th</sup> order problem refers to a sixth-order PDE for the vibroacoustic modeling of composite sandwich panels, which accounts for various factors including transverse shear deformation, normal deformation, and bending moments to accurately predict the response to external loads. This problem was originally proposed by Mead and Markus [1969] and subsequently developed further by other researchers such as Narayanan and Shanbhag [1981, 1982]. Today, the applications of this model

can be found in vibroacoustic studies of composite panels and beams. For instance, Alvelid [2013] developed the 6th order problem for a three-layer sandwich beam with a viscoelastic layer in the middle. In this study, the problem was solved in the case of a cantilever sandwich beam, and the results were compared with Finite Element Method (FEM) calculations. Also, Droz et al. [2017] derived analytical expressions for the equivalent bending and shear parameters by relating them to the transition frequency and the maximal group velocity, and this study employed the 6th order problem to investigate the group velocity. In a recent study by Kohsaka et al. [2021], the vibration characteristics of a sandwich beam with a lattice core were investigated using an analytical approach as well as finite element analyses. The analytical approach focused on solving the 6th order problem to express the motion in terms of the transverse displacement.

In practice, since the shear effects are not usually negligible for composite sandwich plates, the flexural vibrating motions of such panels are usually expected to satisfy high-order problems like the 6<sup>th</sup> order problem that can demonstrate the flexural motion in a spatial-time domain. For this purpose, one considers a vibrating composite sandwich panel with a  $a \times b$  rectangular shape (see Figure 4.1). The panel is excited by an external point force  $q(t, x, y) = q(t)\delta(x - x_0)\delta(y - y_0)$  exerted at point  $(x_0, y_0)$ .

For deriving the equations of motion for the three-layer sandwich panel, Mead [1965], Mead and Markus [1969], Mead [1972] proposed certain assumptions, including the following: 1) Negligible core bending stresses compared to the face sheet direct stresses, 2) Uniform plate motion in the transverse direction across all three layers, 3) Negligible shear strains in the face sheets within planes perpendicular to the panel's plane, and 4) Neglecting inertia forces in both the  $x$  and  $y$  directions. So, according to these assumptions, the equations of motion can be derived as follows (Mead [1972], Narayanan and Shanbhag [1981]):

$$\frac{E}{1-\nu^2} \frac{\partial^2 u}{\partial x^2} + \frac{E}{2(1+\nu)} \frac{\partial^2 u}{\partial y^2} + \frac{2G}{h_1 h_2} u + \frac{E}{2(1-\nu)} \frac{\partial^2 v}{\partial x \partial y} + \frac{G(h_1 + h_2)}{h_1 h_2} \frac{\partial w}{\partial x} = 0 \quad (2.2.1)$$

$$\frac{E}{1-\nu^2} \frac{\partial^2 v}{\partial y^2} + \frac{E}{2(1+\nu)} \frac{\partial^2 v}{\partial x^2} + \frac{2G}{h_1 h_2} v + \frac{E}{2(1-\nu)} \frac{\partial^2 u}{\partial x \partial y} + \frac{G(h_1 + h_2)}{h_1 h_2} \frac{\partial w}{\partial y} = 0 \quad (2.2.2)$$

$$D_t \nabla^4 w - \frac{G(h_1 + h_2)}{h_2} \left[ (h_1 + h_2) \nabla^2 w - 2 \left( \frac{\partial u}{\partial x} + \frac{\partial v}{\partial y} \right) \right] + M \frac{\partial^2 w}{\partial t^2} = q \quad (2.2.3)$$

where  $w(x, y, t)$  is the transverse displacement in z-direction,  $u(x, y, t)$  is the mid-plane displacement in x-direction,  $v(x, y, t)$  is the mid-plane displacement in y-direction,  $\nabla^4(\bullet) = \nabla^2(\nabla^2(\bullet))$ ,  $\nabla^2(\bullet) = \frac{\partial^2(\bullet)}{\partial x^2} + \frac{\partial^2(\bullet)}{\partial y^2}$  is the Laplacian operator,  $\nabla$  is the gradient operator,  $G$  is the shear modulus of the viscoelastic core,  $D_t$  is

the total flexural rigidity,  $E$  is Young's modulus of the face sheet,  $\nu$  is the Poisson's ratio of the plate material,  $M = \rho h$  is the mass per unit area of the entire sandwich,  $\rho$  is the total mass density of the composite panel,  $h_1$  and  $h_2$ , respectively, are the thicknesses of the face sheet and the constrained damping core,  $h = 2h_1 + h_2$  is the total thickness, and  $q$  is the external point force loading on the panel (Narayanan and Shanbhag [1982]). Figure 4.1 illustrates the geometrical configuration of the sandwich panel. Consequently, by eliminating the variables  $u$  and  $v$  in favor of  $w$  through a series of algebraic manipulations in Eq.(2.2.1) to Eq.(2.2.3), the 6<sup>th</sup> order problem can be introduced as follows (see Mead and Markus [1969], Narayanan and Shanbhag [1981, 1982]):

$$D_t \nabla^6 w - D_t \dot{g}(1 + Y) \nabla^4 w + M \frac{\partial^2}{\partial t^2} (\nabla^2 w - \dot{g} w) = \nabla^2 q - \dot{g} q \quad (2.2.4)$$

where  $\nabla^6(\bullet) = \nabla^2(\nabla^2(\nabla^2(\bullet)))$ ,  $\dot{g} = 2G(1 - \nu^2)/E_1 h_1 h_2$  as the shear parameter of the core is a function of the shear modulus and the thicknesses of the face sheets  $h_1$  and core  $h_2$ , and  $Y = 3(1 + h_2/h_1)^2$  is the geometric parameter of the sandwich panel (see Narayanan and Shanbhag [1982]).

If we consider the case of free vibration when  $q(t, x, y) = 0$ , and assume the plane wave  $e^{i(\omega t - k_x x - k_y y)}$  propagating within the plate, we can reach the 6<sup>th</sup> order dispersion relation via the six order problem defined by Eq.(2.2.4) as follows:

$$-D_t k^6 - D_t \dot{g}(1 + Y) k^4 + M \omega^2 (k^2 + \dot{g}) = 0 \quad (2.2.5)$$

where  $k = \sqrt{k_x^2 + k_y^2}$ , and  $k_x$  and  $k_y$  are the wave numbers in the  $x$  and  $y$  directions, respectively.

## 2.3 4<sup>th</sup> order problem

The hypotheses behind the 4<sup>th</sup> order problem can be traced back to the classical plate theory started by G. Kirchhoff around 1850 (Teotia and Soni [2018]). This problem originally emerges from the governing equations of the motion, and it is used for vibroacoustic modeling of thin composite plates (e.g. see Shimpi and Patel [2006], Guillaumie [2015], Berry et al. [2020], AllahTavakoli et al. [2023a,b]).

According to the classical laminate theory and Kirchhoff-Love hypotheses, the governing equations of composite laminates can be obtained through a constitutive equation, which establishes a connection between the mechanical properties of an individual lamina (a single layer within the panel) and the overall mechanical characteristics of the composite panel. This constitutive equation is represented by the

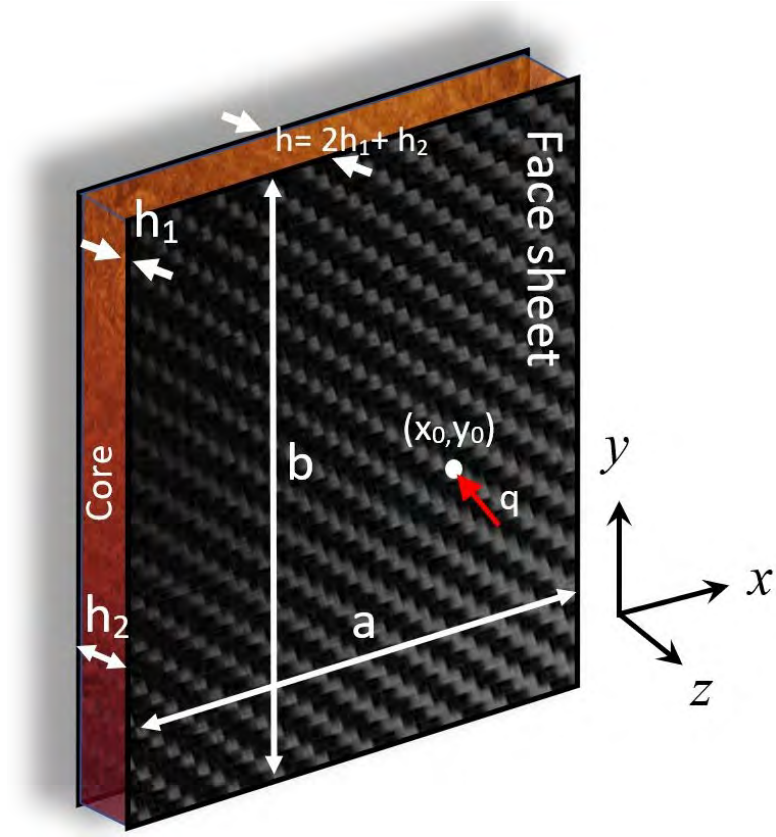


Figure 2.1: The geometrical configuration for a composite sandwich plate

stretching, coupling, and bending stiffness matrices (e.g. see Berthelot and Ling [1999]). In fact, this equation is employed to articulate the relationship between stress and strain within the laminate composite panel, and it serves as the foundation for the governing equations of motion. So, based on the constitutive equation, the following governing equation of motion in the  $z$ -direction concerning bending transverse displacement  $w$  can be derived for a thin laminate composite panel (Berthelot and Ling [1999]):

$$\begin{aligned}
 D_{11} \frac{\partial^4 w}{\partial x^4} + 4D_{16} \frac{\partial^4 w}{\partial x^3 \partial y} + 2(D_{12} + 2D_{66}) \frac{\partial^4 w}{\partial x^2 \partial y^2} + 4D_{26} \frac{\partial^4 w}{\partial x \partial y^3} + D_{22} \frac{\partial^4 w}{\partial y^4} \\
 - B_{11} \frac{\partial^3 u}{\partial x^3} - 3B_{16} \frac{\partial^3 u}{\partial x^2 \partial y} - (B_{12} + 2B_{66}) \frac{\partial^3 u}{\partial x \partial y^2} - B_{26} \frac{\partial^3 u}{\partial y^3} \\
 - B_{16} \frac{\partial^3 v}{\partial x^3} - 3B_{26} \frac{\partial^3 v}{\partial y^2 \partial x} - (B_{12} + 2B_{66}) \frac{\partial^3 v}{\partial y \partial x^2} - B_{22} \frac{\partial^3 v}{\partial y^3} \\
 + M \frac{\partial^2 w}{\partial t^2} = q(t, x, y)
 \end{aligned} \tag{2.3.1}$$

where  $u(x, y, t)$ ,  $v(x, y, t)$ , and  $w(x, y, t)$  are the mid-plane displacement in x-, y-, and z-directions respectively;  $(x, y) \in [0, a] \times [0, b]$ ,  $\{D_{ij}\}$  are the bending stiffness coefficients,  $\{B_{ij}\}$  are the coupling stiffness coefficients,  $\rho$  is the mass density,  $h$  is the thickness, and  $M = \rho h$  is the mass per unit area (herein, the geometrical configuration of the thin composite panel is the same as that of Figure 4.1, except for taking into account the core thickness).

For symmetric laminate panels with multiple orthotropic layers, we have  $B_{11} = B_{12} = B_{16} = B_{22} = B_{26} = B_{66} = 0$ , and  $D_{16} = D_{26} = 0$ , and so, the terms corresponding to these coefficients disappear from the above equation (e.g. see Berthelot and Ling [1999]). Consequently, according to the Kirchhoff-Love hypotheses and neglecting transverse shear and rotary inertia, the 4<sup>th</sup> order problem governing the transverse displacement  $w(x, y, t)$  of an undamped thin composite plate will be obtained by Eq.(2.3.1) as follows (e.g., see Lesueur and Nicolas [1989], Jones [1999], Berthelot and Ling [1999]):

$$D_{11} \frac{\partial^4 w}{\partial x^4} + 2(D_{12} + 2D_{66}) \frac{\partial^4 w}{\partial x^2 \partial y^2} + D_{22} \frac{\partial^4 w}{\partial y^4} + M \frac{\partial^2 w}{\partial t^2} = q(t, x, y) \quad (2.3.2)$$

The well-known particular case of this 4<sup>th</sup> order problem and 6<sup>th</sup> order problem when  $D_t = D_{11} = D_{22} = D_{12} + 2D_{66} = D$ , and  $g = 0$  presents the governing equation of motion of thin isotropic plates under Kirchhoff-Love hypotheses as follows (e.g., see Lesueur and Nicolas [1989], Jones [1999]):

$$D \nabla^4 w(x, y, t) + M \frac{\partial^2 w(x, y, t)}{\partial t^2} = q(t, x, y) \quad (2.3.3)$$

In the current study, this particular case has also been used for validating the efficiency of the proposed methodology. In next Chapters, this equation will be used to model the behavior of isotropic panels for further validations of the simulations and modeling.

Moreover, in the case of free vibration when  $q(t, x, y) = 0$ , considering the wave  $e^{i(\omega t - k_x x - k_y y)}$  propagating within the plate, the fourth order problem introduced by Eq.(2.3.2) leads to the 4<sup>th</sup> order dispersion relation as follows:

$$D_{11} k_x^4 + 2(D_{12} + 2D_{66}) k_x^2 k_y^2 + D_{22} k_y^4 - M \omega^2 = 0 \quad (2.3.4)$$

where  $k_x$  and  $k_y$  are the wave numbers in the  $x$  and  $y$  directions, respectively.

### 2.3.1 Modal decomposition

By a modal decomposition and taking into account an ad hoc damping loss factor  $\eta$  for dissipation, the response  $H$  to a harmonic point force such  $q(t) = e^{i\omega t}$  at point  $(x_0, y_0)$ , will be as follows (e.g., see Lafont et al. [2014]):

$$H(x, y; x_0, y_0; \omega) = \sum_{n \geq 0} H_n(\omega) \psi_n(x_0, y_0) \psi_n(x, y) \quad (2.3.5)$$

where  $\psi_n$  denotes the modal function of mode  $n$ , the frequency response coefficient  $\{H_n(\omega)\}$  is obtained as  $H_n(\omega) = M^{-1}(\omega_n^2 - \omega^2 + i\eta\omega_n\omega)^{-1}$ , and  $\omega_n$  is the angular natural frequency belonging to the modal function  $\psi_n$ .

Based on the above modal decomposition for the harmonic response (i.e. Eq.2.3.5), the transverse displacement  $w(x, y, t)$  can be modeled if the modes  $\psi_n$  can be correctly calculated. Thus, according to Eq.(2.3.5), the function  $\tilde{w}(x, y; \omega)$  as the Fourier transform function of  $w(x, y, t)$  is obtained by

$$\tilde{w}(x, y; \omega) = \sum_{n \geq 0} \tilde{q}(\omega) H_n(\omega) \psi_n(x_0, y_0) \psi_n(x, y) \quad (2.3.6)$$

where  $\tilde{q}(\omega)$  is the Fourier transform of the external force  $q(t)$ . In certain particular cases like simply supported boundary condition, we can have an analytical expression for the modal functions (e.g., see Lafont et al. [2014], Le Bot [2015]). Furthermore, in Chapter 5 regarding the updating of models and parameters, we will also see how the modal functions can be initially predicted in terms of hierarchical trigonometric functions while considering specified boundary conditions, and how real laboratory measurements can assist us to have a reliable estimation of these critical functions and update them.

## 2.4 Radiation and Rayleigh integration

The sound pressure level (SPL) of sounds radiated from the vibrating composite panel, can be acquired for vibroacoustic assessments. Hence, for simulating the SPL at an arbitrary distance from the vibrating plate in a free field, the well-known Rayleigh integration with time dependence  $e^{i\omega t}$  can be applied to the modeled full-vibration field as follows (e.g., see Fahy [2000]):

$$p(x, y, z; \omega) = i\omega\rho_0 \iint_S v(x', y') \frac{e^{ikR}}{2\pi R} dS' \quad (2.4.1)$$



where the panel is supposed to be embedded in a rigid baffle, the acoustic pressure is assumed to be radiated from the panel in fluid half-space  $z > 0$ ,  $p(x, y, z; \omega)$  is the pressure field at the location  $(x, y, z)$ ,  $\omega$  is the angular frequency,  $\rho_0$  is the air density,  $v(x', y')$  is the vibration velocity at the point  $(x', y')$  located in the plate area  $S$ ,  $dS' = dx'dy'$  is the differential element of the plate surface,  $k = \frac{\omega}{c_0}$  is the wave number,  $c_0$  is the sound speed in the air, and  $R = \sqrt{(x - x')^2 + (y - y')^2 + z^2}$ . The geometric configuration employed in Rayleigh integration is depicted in Figure 2.2. The modal decomposition described before can be employed for modeling the velocity  $v = \omega w$ , and the displacement field  $w$  over the panel.

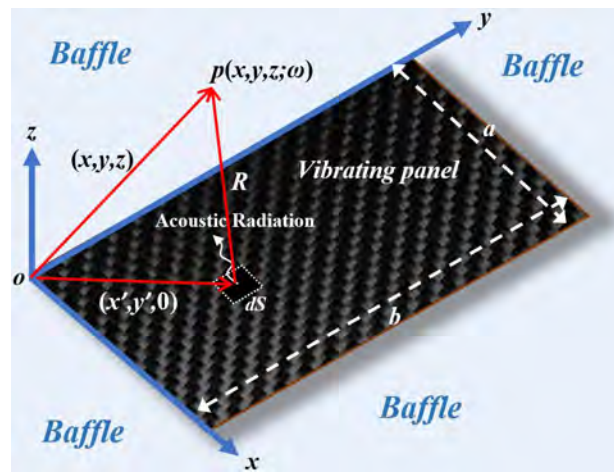


Figure 2.2: The geometrical configuration corresponding to the Rayleigh integration and radiation of the vibrating composite panel embedded in a baffle

## 2.5 Discussion

In this chapter, we presented an analytical investigation of the vibration characteristics of composite panels. To accomplish this objective, the chapter was dedicated a comprehensive discussion of the partial differential equations, specifically the 6th and 4th order problems governing the vibrational behavior exhibited by diverse composite panels. The 4th and 6th order problem formulations rely on specific assumptions, namely the Kirchhoff-Love and Mead assumptions, respectively. The Kirchhoff-Love assumptions, which exclude considerations of transverse shear and rotary inertia, establish the validity of the 4th order problem for thin composite panels. On the other hand, the Mead assumptions extend the applicability of the 6th order problem to composite panels by accounting for the shear effect in the flexural motions of these panels. In the current thesis, these problems will form the bases on

which simulations and mathematical modeling in the current thesis are constructed. In the following two chapters, the 4th and 6th-order problems will be employed for simulating and modeling the vibroacoustic behavior of certain panels including some isotropic and composite panels. Then the models and simulations will undergo examination through measurements conducted in real laboratory experiments. To achieve this, the different types of panels were tested under two distinct laboratory conditions: the first one with diffuse acoustic field excitation and the other one with mechanical excitation. Additionally, within this current thesis, the 4th and 6th-order problems will serve as the foundation for developing a hybrid updating method useful for precise vibroacoustic modeling of composite panels. Furthermore, the results obtained from all the simulations and models will undergo perceptual validation and assessment in specific psychoacoustic tests. These problems will also be applied in the design and psychoacoustic optimization of a particular type of composite panels. The technical scenario of the current thesis has been summarized in Figure 2.3. Accordingly, the following two chapters will discuss the modeling of vibroacoustic behaviors of composite panels subjected to acoustic and mechanical excitations.

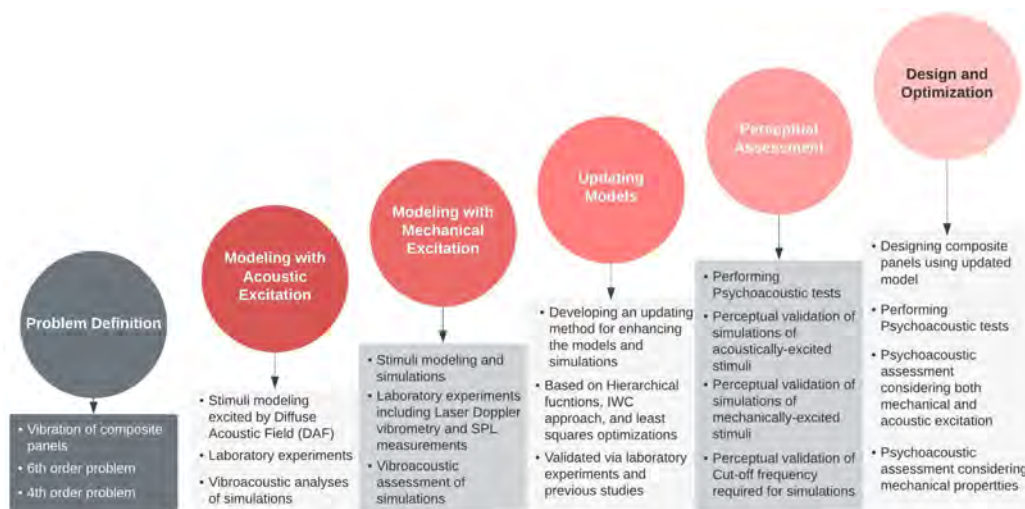


Figure 2.3: Thesis scenario: From concepts of the 6th and 4th order problems, through modeling stimuli with acoustic and mechanical excitations, updating strategies, perceptual assessment, to composite panel designs and optimizations



## Chapter 3

# Modeling with diffuse acoustic excitation

In this chapter, the mathematical/numerical and experimental steps required by the vibro-acoustic modeling of composite and isotropic plates excited by a diffuse acoustic field (DAF) are discussed. Herein, the analytical modeling was performed by 4th and 6th order problems adapted for the composite and isotropic plates, and moreover, the numerical modeling was carried out via the Finite Element Method (FEM). The experimental observations were also performed by means of an acoustic test cabin used for ideally generating a diffuse acoustic field. The various types of analytical and numerical simulations including synthesized sounds required by future psychoacoustic analyses, as well as experimental observations including recorded sounds were investigated and compared.

Herein, the proposed strategy starts with the mathematical analyses associated with the excitation of panels and then it is essential to adopt an appropriate analytical model for predicting the vibration as the next step. Another step consists in computing the pressure field, caused by the sound radiated by the vibrating plate. For this purpose, the chapter presents certain numerical simulations and some computational prerequisites and then it provides us with experimental results and their comparisons with the mathematical modeling and simulations. Finally, the study ends with synthesizing sounds, which will be used by psychoacoustic assessments required for designing composite panels. Fig.3.1 summarizes the strategy used in this chapter. Also, it is noteworthy that some parts of this chapter have been incorporated within the work referenced as AllahTavakoli et al. [2023b].



Figure 3.1: an overview of the strategy used in this chapter, required for vibro/psychoacoustically assessing and designing composite panels

### 3.1 Methodology

In the numerical and experiments study of this chapter, certain panels including some isotropic steel and aluminium panels and an aluminium composite panels are investigated. Hence, first, assume a vibrating isotropic thin flat plate, which has a  $a \times b$  rectangular shape. Then suppose a case that the plate can be excited by a harmonic point force such  $e^{i\omega t}$  at point  $(x_0, y_0)$ . In such case, according to the Kirchhoff-Love hypothesis and neglecting transverse shear and rotary inertia, as discussed by Chapter 2, the 4<sup>th</sup> order will be satisfied for the panel, and so, the response of the vibrating panel to a harmonic point force can be obtained via the modal decomposition (see Section 2.3.1).

Furthermore, in both the numerical and experimental of this chapter, the panels have been analyzed with a simply-supported boundary condition. Thus, when the mode index is represented as a double subscript, denoted as  $(n_1, n_2)$ , the expressions for the undamped natural frequencies under this simply supported boundary condition can be described as follows (e.g. see Guyader [2013]):

$$\omega_n = \sqrt{D/m} \left( \left( \frac{n_1\pi}{a} \right)^2 + \left( \frac{n_2\pi}{b} \right)^2 \right) \quad (3.1.1)$$

where the mode shapes are  $\psi_n(x, y) = (2/\sqrt{ab}) \sin(n_1\pi x/a) \sin(n_2\pi y/b)$  and  $(x, y) \in [0, a] \times [0, b]$ . Now, if the plate is embedded in a rigid baffle, the acoustic pressure radiated from the plate in fluid half-space  $z$  can be evaluated by the Rayleigh integration discussed before (see Section 2.4). Hence, according to the Rayleigh integration and the relation between the velocity and displacement (i.e.  $v = i\omega w$ ), we have

$$p(x, y, z; \omega) = \text{Ray}(w) = -\omega^2 \rho_0 \iint_S w(x', y') \frac{e^{ikR}}{2\pi R} dx' dy' \quad (3.1.2)$$

where  $\text{Ray}$  is the Rayleigh integral operator, which converts the flexural displacement  $w$  to the pressure field  $p$ . According to the above equation as well as the Rayleigh integration and modal decomposition, the acoustic pressure at point  $(x, y, z)$ , caused

by the response  $H$  to the harmonic point force such  $e^{i\omega t}$  at point  $(x_0, y_0)$ , can be obtained as follows:

$$p(x, y, z; \omega) = \sum_{n \geq 0} H_n(\omega) \psi_n(x_0, y_0) \text{Ray}(\psi_n) \quad (3.1.3)$$

On the other hand, as discussed in Chapter 2 regarding composite panels, when the shear effects are not negligible, the flexural vibrating motion is expected to satisfy the 6<sup>th</sup> order problem rather than the 4<sup>th</sup> order problem. Hence, according to Eq.(2.2.4), the natural frequencies corresponding to the flexural vibration of the composite plate could be obtained by the sixth-order dispersion relation (i.e. Eq.(2.2.5)), and so, we have

$$\omega_n = \sqrt{\frac{D_t k_n^4}{m} \left( 1 + \frac{\acute{g}Y}{k_n^2 + \acute{g}} \right)} \quad (3.1.4)$$

where  $k_n$  is the wave number corresponding to the mode index  $n$ , and considering the mode shapes  $\{(2/\sqrt{ab}) \sin(n_1\pi x/a) \sin(n_2\pi y/b)\}$ , we have  $k_n = \sqrt{(n_1\pi/a)^2 + (n_2\pi/b)^2}$ . By comparison of the above equations, we can clearly see that the 6<sup>th</sup> order problem is the generalization of the 4<sup>th</sup> order problem, and the solutions of these problems become equal when the shear effects of the composite plate are neglected (compare the solution of Eq.3.1.4 with Eq.3.1.1 when  $\acute{g} = 0$ ). So, based on Eq.3.1.4, the frequency response associated with the 6<sup>th</sup> order problem can similarly be achieved by the modal decomposition.

### 3.1.1 Diffuse acoustic excitation

Now, consider a diffuse acoustic field (DAF)  $p_e$  as a random pressure field excitation on the plate (see Fig.3.2). Ideally, a diffuse field is expected to be homogeneous and isotropic (e.g. see Misol et al. [2014]). So, if we assume that the excitation is stationary with respect to time, the power spectral density of the DAF as the external excitation can be expressed as follows Narayanan and Shanbhag [1981]:

$$S_{p_e}(x_0, y_0; x'_0, y'_0; \omega) = S_{p_e}(\omega) C(x_0, y_0; x'_0, y'_0; \omega) \quad (3.1.5)$$

where  $C(x_0, y_0; x'_0, y'_0; \omega)$  is in the form of a correlation function between two arbitrary points  $(x_0, y_0)$  and  $(x'_0, y'_0)$  where the DAF can be exerted on the plate, and this function can be regarded as the spectrum of the correlation coefficient. If the external excitation is assumed to be an ideal white noise, the function  $S_{p_e}$  will be constant. Herein, the quantity  $S_{p_e}$  has been observed by the Beta cabin, which was employed to produce and monitor an ideal diffuse acoustic field (DAF) in the labo-

ratory experiments. In addition, herein, the theoretical formulation of the spectrum of the correlation function  $C(x_0, y_0; x'_0, y'_0; \omega)$  has been considered as follows Misol et al. [2014], Marchetto et al. [2017]:

$$C(x_0, y_0; x'_0, y'_0; \omega) = \frac{\sin(k_0 r)}{k_0 r} \quad (3.1.6)$$

where  $r = \sqrt{(x_0 - x'_0)^2 + (y_0 - y'_0)^2}$ ,  $k_0 = \omega/c_0$  is the acoustic wave number, and  $c_0$  is the sound speed in air.

So, considering Equations 3.1.3 and 3.1.5, the spectrum (i.e. auto-spectral density (ASD)) of the sound pressure  $p$  at the location  $(x, y, z)$  will be obtained as follows (c.f. Narayanan and Shanbhag [1981]):

$$S_p(x, y, z; \omega) = \sum_{n \geq 0} \sum_{\hat{n} \geq 0} \text{Ray}(\psi_n) \overline{\text{Ray}(\psi_{\hat{n}})} H_n(\omega) \overline{H_{\hat{n}}(\omega)} S_{p_e}(\omega) I_{n\hat{n}}(\omega) \quad (3.1.7)$$

where

$$I_{n\hat{n}}(\omega) = \sum_{(x_0, y_0) \in S} \sum_{(x'_0, y'_0) \in S} \psi_n(x_0, y_0) \overline{\psi_{\hat{n}}(x'_0, y'_0)} C(x_0, y_0; x'_0, y'_0; \omega) \quad (3.1.8)$$

, and  $S = [0, a] \times [0, b] \subset \mathbb{R}^2$  is the plate surface area,  $\sum_{(x_0, y_0) \in S}$  is the discrete form of the 2D integration over the plate, and  $\bar{\circ}$  is the complex conjugate of  $\circ$ .

Accordingly, based on the methodology described in this Section, we could per-

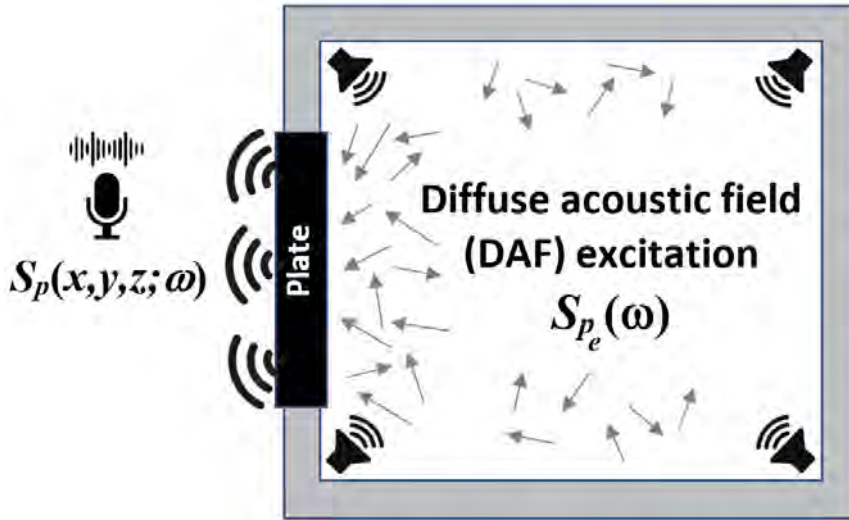


Figure 3.2: The DAF as a random pressure field excitation: the objective is to model the spectrum of the pressure level at an arbitrary receiver point, caused by the excited vibrating plate

form certain numerical and laboratory experiments. In the next Section, some of

numerical simulations executed before laboratory experiments have been explained in details.

## 3.2 Numerical simulations

Before carrying out any laboratory experiments, it was necessary to perform certain numerical simulations in order to numerically assure ourselves of the analytical modeling and simulations, and also in order to fulfill some numerical prerequisite of the problem. Herein, a finite elements method (FEM) was employed as the numerical tool for re-validating the procedures of the proposed strategy and the numerical prerequisite were attained via certain numerical comparisons. The finite element method was performed by means of ANSYS/APDEL and applied to a  $40\text{cm} \times 60\text{cm}$  aluminium plate with a thickness of  $4\text{mm}$ . It was supposed that the mass density, young modulus, Poisson ratio, and loss damping factor of the plate are equal to  $2500\text{kg/m}^3$ ,  $70\text{GPa}$ ,  $0.22$ , and  $0.001$ , respectively.

Additionally, the finite element of FEM was defined such that it has four nodes, is suitable for analyzing thin to moderately-thick shell structures, is well-suited for linear and large rotation, and has six degrees of freedom (three translations and three rotations) at each node. In this numerical simulation, the boundary condition was considered to be simply supported at all the edges of the plate and a mechanical nodal excitation with a white noise spectrum was assumed for the modeling (the nodal excitation was exert on a node with the location  $x = 0.12\text{m}$ ,  $y = 0.40\text{m}$  where  $x \in [0, a]$ ,  $y \in [0, b]$ , and  $a = 40\text{m}$ , and  $b = 0.60\text{m}$ ).

Moreover, the element mesh size was considered  $8.6\text{mm}$  that is half of the expected value of the minimum wave number. Accordingly, the numerical simulation could be performed under the aforementioned condition, and as an example Fig.3.3 illustrates the vibration field at the middle point of the plate, approximated via the FEM, as well as its comparison with the analytical modeling achieved via solving the 4<sup>th</sup> order problem (i.e via applying Eq.3.1.1 to the modal decomposition relation). In this figure, we can see that the numerical result coincides with the analytical prediction of the problem (see Fig.3.3). This step of the numerical simulations as well as its corresponding comparisons with the analytical models is essential in the strategy in order to double-check the procedures and to avoid any mistakes in the implementation of the proposed approach.

Furthermore, in order to have accurate approximation of the Rayleigh integration and consequently have an accurate prediction of the pressure field at an arbitrary receiver point, we needed to do other numerical analyses. After modeling the vibration field over the plate, the discretization and computation of the Rayleigh integral



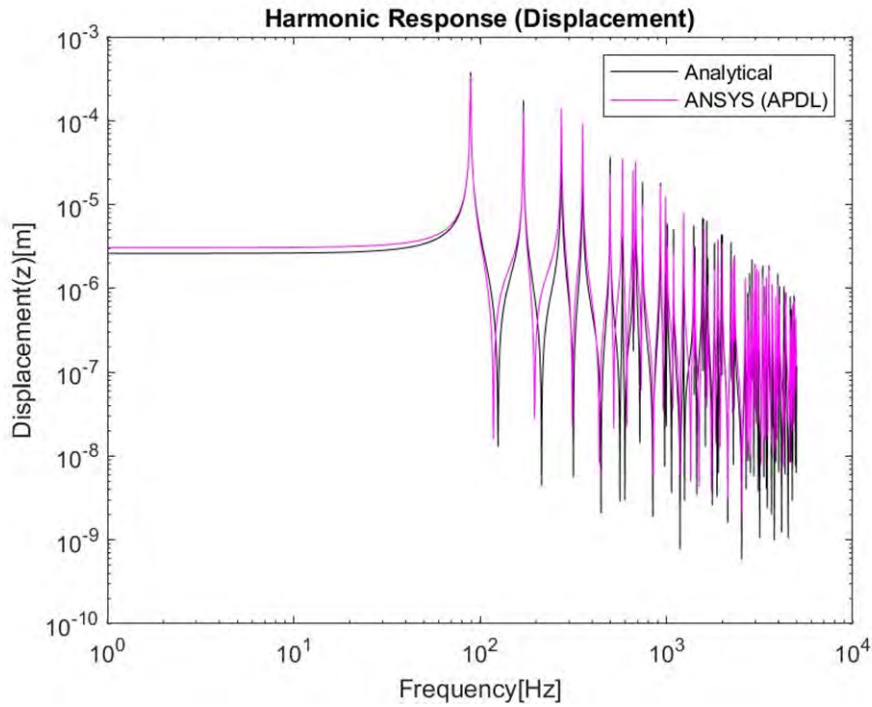


Figure 3.3: a comparison between the FEM and analytical approach for  $f \in [0, 10\text{kHZ}]$

is a tricky part and regarding the frequency range and the desired accuracy, at first we need to have a proper understanding of the optimum value of the mesh size and the appropriate method for the discrete 2D integration. Although it is usually recommended to consider six to ten nodes per the minimum wavelength to have an accurate estimation of mode shapes (e.g. see Marburg [2008]), high numbers of nodes and consequently small mesh sizes can lead to increasing the amount of computation and its processing time. In order to avoid it and find an optimum value of the mesh size, in this step, we assumed the solution obtained by the mesh size equal to  $\lambda_{Min}/6$  as the most accurate value of the solution and then we compared other solutions with this solution as a reference ( $p_{Ref}$ ).

On the other hand, as mentioned above, it was required to adopt a proper approach for discretizing and approximating the Rayleigh integration. For this purpose, at the same time, we examined three different numerical integration approaches: 1) Discretization & simple summation, 2) Trapezoidal approach, and 3) Quadrature Method Shampine [2008]. Fig.3.4 sums up these results, which illustrates how both the trapezoidal and Quadrature methods can start to have an acceptable accuracy from mesh sizes less than  $\lambda_{Min}/2$ . Accordingly, in the current study for continuing other numerical computations the mesh size was assumed equal to  $\lambda_{Min}/2 = 8.6\text{mm}$  and the trapezoidal approach has been used for approximating the Rayleigh inte-

gration.

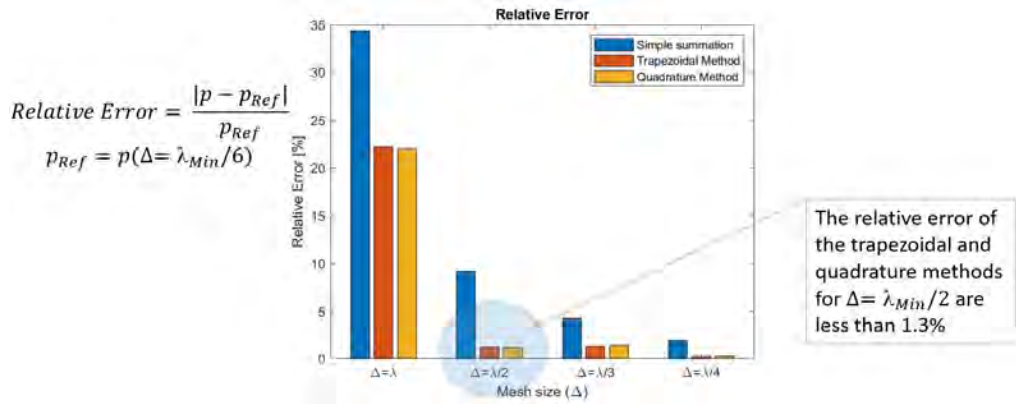


Figure 3.4: the relative error associated with the integration approaches and different values of the mesh size

### 3.3 Laboratory experiments

Herein, we had certain objectives for performing the laboratory experiments. Our objectives were 1) to experimentally check the mathematical and numerical modeling and simulations, 2) to experimentally investigate the possibility of DAF excitation in the mathematical modeling of the vibration and pressure field, required for the proposed vibro/psychoacoustical assessments, 3) to record the sound radiated by the plate with the purpose of a perceptual validation of the obtained synthesized sounds for such an excitation, and 4) to investigate various configurations of the problems and their limitations. For this purpose, we used an acoustic test cabin, (a Mecanum Inc. product, called Beta cabin, see Inc.). This Beta cabin is usually used for a quick and accurate estimation of sound absorption and transmission loss on medium-sized samples, and it is based on the concept of diffuse acoustic field. So, by means of this instrument, herein we could produce a diffuse field inside of the cabin, and utilize it as a diffuse acoustic excitation for testing some sample plates, and then we could measure the pressure field at different distances from the vibrating plates by means of a microphone system. Fig.3.5 illustrates both the instruments employed in the laboratory experiments and the experimental setup within the laboratory. Also, the geometric and mechanical parameters of the tested plates, used by these laboratory experiments, have been considered as Table3.1.

After acquiring the sound pressure level (SPL) at different distances from the vibrating plates, the precise observations of the DAF spectrum  $S_{pe}(\omega)$  inside the Beta

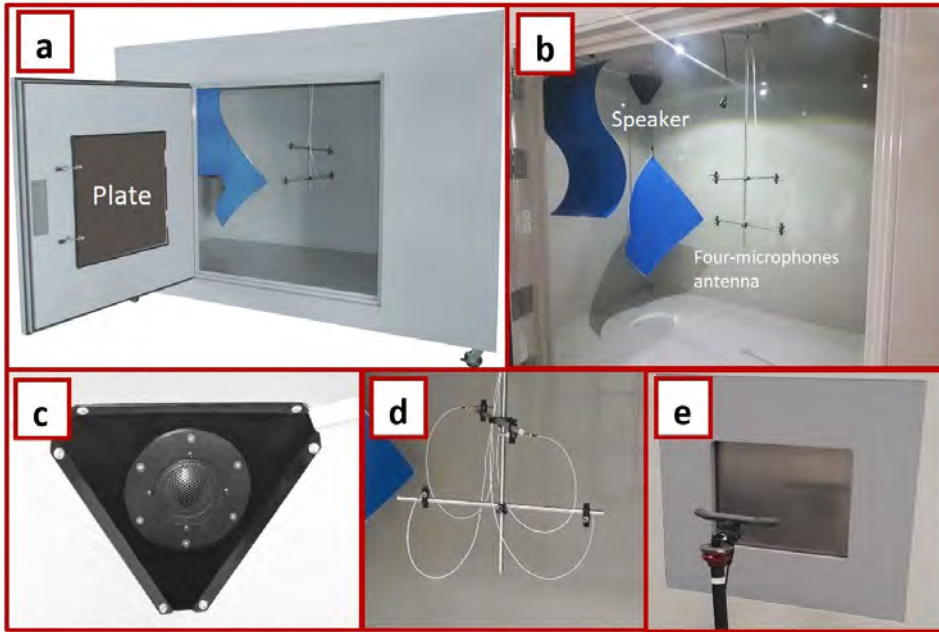


Figure 3.5: a) Beta Cabin with the plate under study, b) inside Beta Cabin with microphones, c) four uncorrelated speakers required for generating an ideal DAF, d) a 4-microphones antenna for acquiring the DAF spectrum, e) the microphone system to record the sound radiated by the plate

Table 3.1: the geometric and mechanical characteristics of the tested plates

No	Material	a × b [cm]	h [mm]	Mechanical properties
1	Steel	61 × 61	2	$E = 210GPa, \nu = 0.29, \eta = 0.005, \rho = 7.8g/cm^3$
2	Aluminium	61 × 61	5	$E = 70GPa, \nu = 0.33, \eta = 0.02, \rho = 2.5g/cm^3$
3	Steel	33.9 × 29.2	2	$E = 210GPa, \nu = 0.29, \eta = 0.005, \rho = 7.8g/cm^3$
4	Aluminium	33.9 × 29.2	5	$E = 70GPa, \nu = 0.33, \eta = 0.02, \rho = 2.5g/cm^3$
5	Aluminium composite	33.9 × 29.2	2	$D_t = 40GPam^3, \nu = 0.3, \rho = 2.2g/cm^3, \eta = 0.01, \beta = 0, G = 1MPa, h_1, h_2 = 0.9mm, 0.2mm$

cabin, which were measured during each experiment, enabled us to straightforwardly perform the proposed method described in Section 3.1.1. Fig.3.6 illustrates the main shape of the measured DAF spectrum  $S_{p_e}(\omega)$ . Accordingly, Eq.(3.1.7) and the measured DAF spectrum  $S_{p_e}(\omega)$  could provide us with the modeled spectrum of pressure field, and consequently we could carry out comparisons between the modeled spectrum of pressure field and the SPL measured by the microphone system. Figures3.7 to 3.11 present the corresponding comparisons for the laboratory experiments of the sample plates, performed at the distance 50cm from the plates. In these figures, the spectra of the simulated and experimental results have been illustrated. The figures demonstrate the alignment between the simulated results, derived from the

proposed approach outlined in Section 3.1, and the experimental data. The agreement between them is quite strong. However, certain pronounced resonances present in simulations, which are absent in the experimental results. This discrepancy may arise due to the untuned values of the loss damping factors. Tuning and updating mechanical parameters, such as the loss damping factor, requires additional measurements, such as laser vibratory measurements, as elaborated in Chapter 5. In the proposed approach, the 4<sup>th</sup> and 6<sup>th</sup> order problems are employed for the modeling and simulations associated with the isotropic and composite plates, respectively.

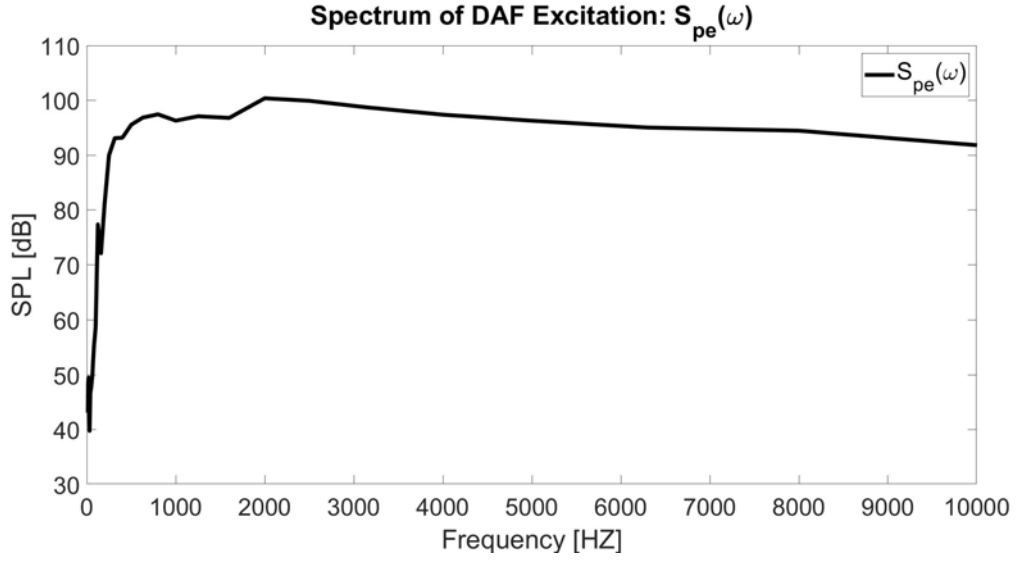


Figure 3.6: the spectrum  $S_{pe}(\omega)$  of the DAF excitation, measured during the experiments

### 3.4 Discussion and concluding remarks

In this chapter, the main target was to provide theoretical and practical steps for vibroacoustic modeling of panels excited by a DAF, which we ultimately needed for vibro/psychoacoustically assessing and designing composite panels. Based on such a target, first we presented a theoretical strategy for analytical modelings of the problems, where the 4<sup>th</sup> and 6<sup>th</sup> order problems were the bases of vibroacoustic modelings of isotropic and composite plates, respectively. Then we could complete the theoretical strategy by means of certain numerical and experimental experiments to practically examined our main ideas. First, certain numerical validations and prerequisites were fulfilled and then the laboratory experiments were performed to examine the proposed analytical procedures.

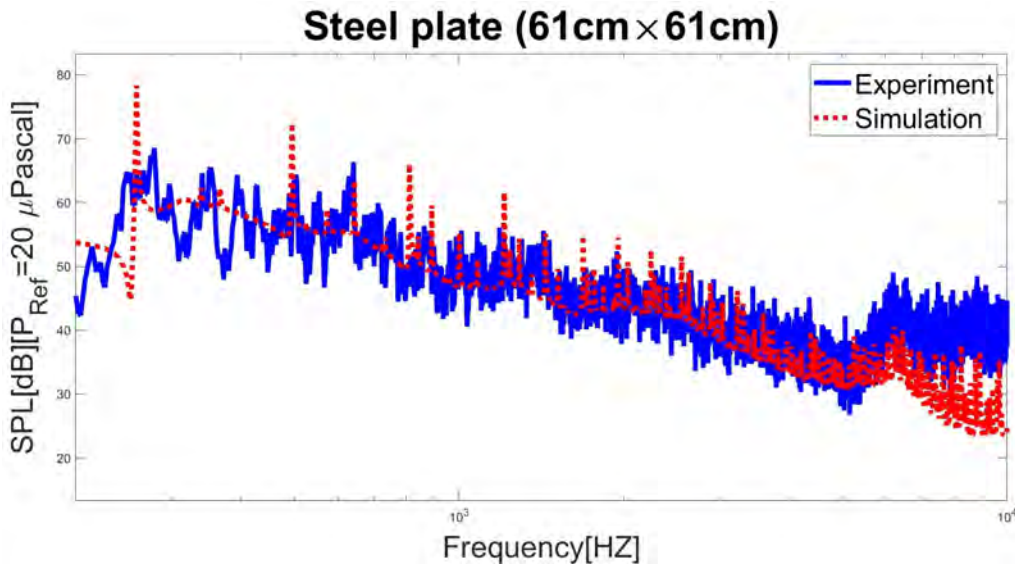


Figure 3.7: the measured and modeled SPL spectra radiated by the vibrating  $61\text{cm} \times 61\text{cm}$  steel plate excited by the DAF

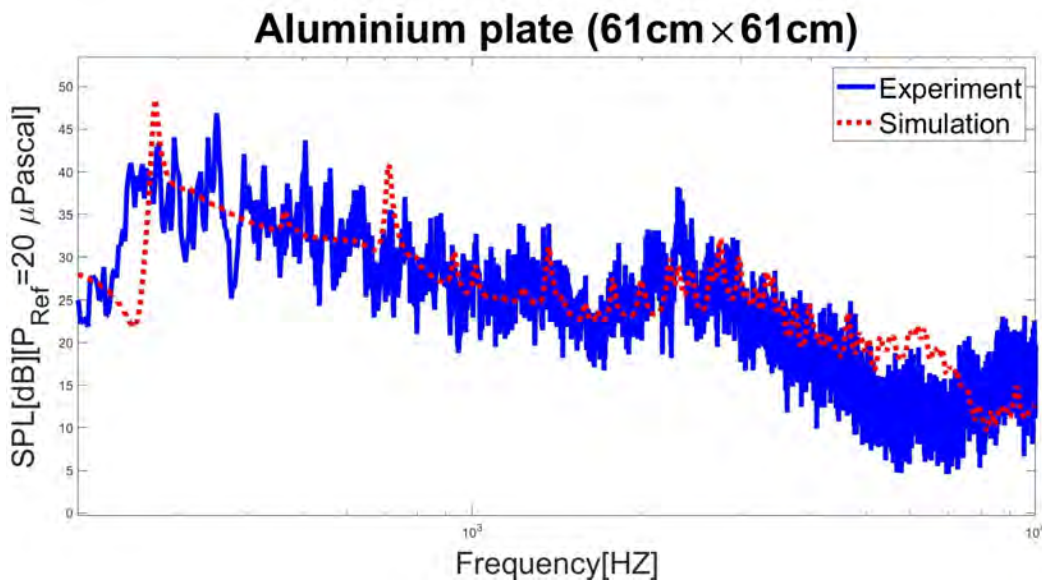


Figure 3.8: the measured and modeled SPL spectra radiated by the vibrating  $61\text{cm} \times 61\text{cm}$  aluminium plate excited by the DAF

Meanwhile, a clear understating of DAF, which herein plays a key role of the random pressure field excitation, was another important issue. We required to theoretically investigate the DAF excitation and precisely model it via stochastic analyses. On the other hand, it was also essential to ideally generate such DAF excitation field in practice. Hence, in the laboratory experiments, we utilized an acoustic test cabin

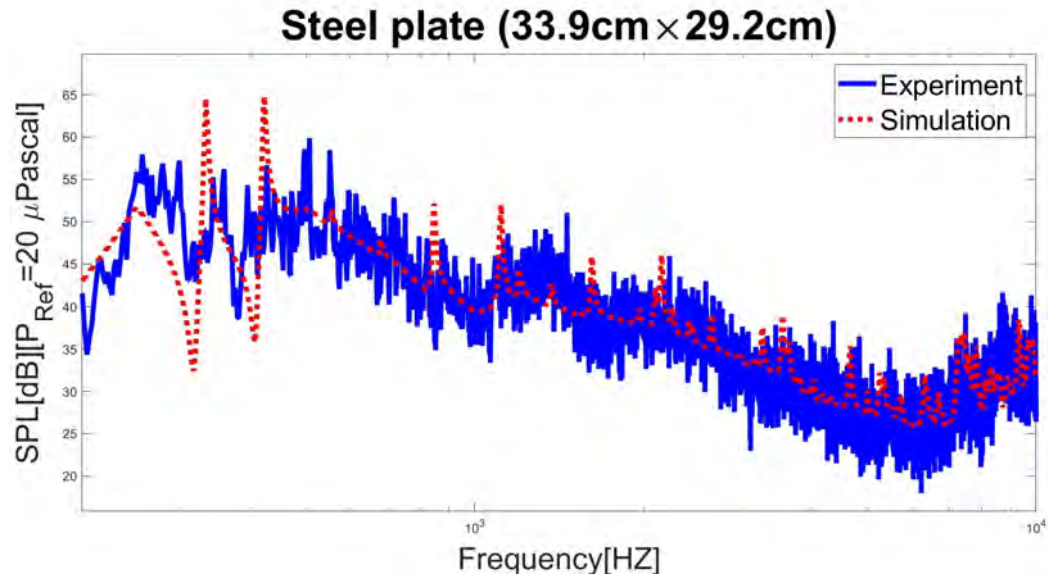


Figure 3.9: the measured and modeled SPL spectra radiated by the vibrating  $33,9\text{cm} \times 29,2\text{cm}$  steel plate excited by the DAF

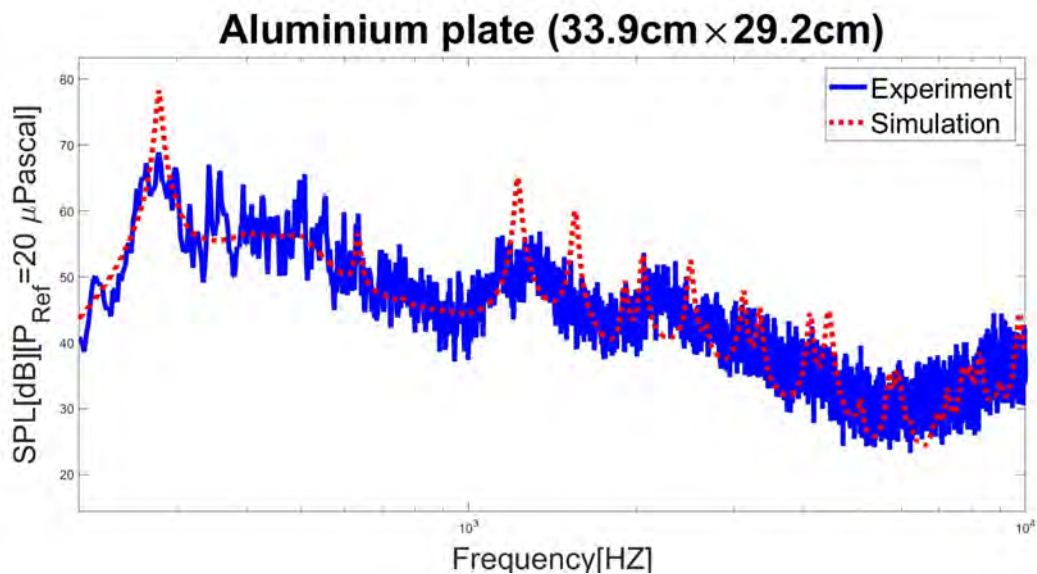


Figure 3.10: the measured and modeled SPL spectra radiated by the vibrating  $33,9\text{cm} \times 29,2\text{cm}$  aluminium plate excited by the DAF

for ideally generating the DAF excitation and exerting it to different sample plates. The experiments were performed for 4 isotropic sample plates with different sizes as well as a composite one, and finally, the acquired experimental results were compared with the mathematical modeling and simulations. The comparisons were able to experimentally approve the main ideas of the study, and the experimental results

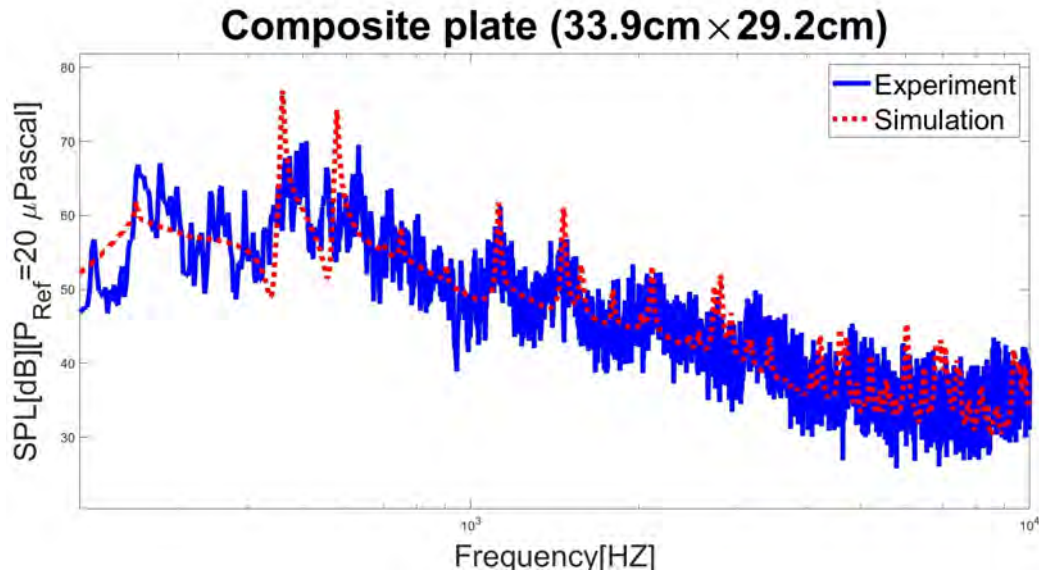


Figure 3.11: the measured and modeled SPL spectra radiated by the vibrating  $33,9\text{cm} \times 29.2\text{cm}$  composite plate excited by the DAF

associated with the isotropic plates and the composite one could approve the abilities of the  $4^{\text{th}}$  and  $6^{\text{th}}$  order problems in the proposed approach.

Accordingly, based on the agreements accomplished by by the various numerical and laboratory experiments with the mathematical modelings, the proposed strategy was made ready to be used for precisely synthesizing sounds required by corresponding psychoacoustic tests and analyses, and consequently, for completing the proposed auditory evaluation step required for vibro/psychoacoustically investigating composite panels. Now, continuing the strategy outlined in this chapter, the upcoming chapter will further explore vibration modeling for composite panels, this time focusing on mechanical excitation.

# Chapter 4

## Modeling with mechanical excitation

In this chapter, we have undertaken a comprehensive exploration of vibroacoustic modeling for composite panels subjected to mechanical excitation. This investigation encompasses both theoretical insights and practical experimentation. To accomplish this, we conducted a range of laboratory experiments, incorporating laser Doppler vibrometry and sound pressure level measurements. These measurements were executed on two types of panels: thick composite (sandwich with a Nomex honeycomb core) and thin composite (CFRP laminate) panels. Additionally, we included two isotropic plates made of steel and aluminum in our experiments to enhance the validation process. The outcomes of these experiments will serve as a critical foundation for our upcoming phases of the thesis aiming at developing precise vibroacoustic models that address psychoacoustic concerns and undergo thorough perceptual validation.

### 4.1 Mechanical excitation

In continuation of the study carried out in the previous chapter, the current study aims to explore the vibroacoustic modeling of composite panels when subjected to mechanical excitation. The fundamental principles governing the vibroacoustic modeling of composite panels under a point-wise mechanical load were discussed in Chapters 2 and 3, which originated from the 4th and 6th order problem formulations and modal decomposition. Hence, let's reconsider a scenario where we have a rectangular composite panel with dimensions  $a \times b$ . Additionally, let's imagine a situation in which this panel can be excited by a point-wise mechanical load,



denoted as  $\tilde{q}(\omega)e^{i\omega t}$ , applied at a point  $(x_0, y_0)$ , as depicted in Fig.4.1. In such a scenario, by considering the boundary conditions, we can derive expressions for the modal shapes associated with the vibrating plate. Subsequently, modal decomposition allows us to express the flexural vibration field over the vibrating panel, as illustrated in Equation (2.3.6). Accordingly, the functions  $\tilde{v}(x, y; \omega)$  and  $\tilde{w}(x, y; \omega)$  as the Fourier transform function of the vibration velocity  $v$  and displacement  $w$  at the point  $(x, y, t)$ , caused by the point-wise excitation are obtained by

$$\begin{cases} \tilde{v}(x, y; \omega) = \sum_{n \geq 0} \omega \tilde{q}(\omega) H_n(\omega) \psi_n(x_0, y_0) \psi_n(x, y) \\ \tilde{w}(x, y; \omega) = \sum_{n \geq 0} \tilde{q}(\omega) H_n(\omega) \psi_n(x_0, y_0) \psi_n(x, y) \end{cases} \quad (4.1.1)$$

The above expression of the velocity  $v$  can be used by the Rayleigh integration for predicting the sound pressure level (see Eq.(2.4.1)). Furthermore, the modal shapes can be predicted numerically using methods such as Finite Element Analysis (FEM) or analytically formulated using specific analytical functions like hierarchical functions, as elaborated in Chapter 5. In the laboratory experiments conducted in the current chapter, we examine specimens of vibrating panels subjected to clamped boundary conditions. These modal shapes are analytically formulated using hierarchical functions, as detailed in Chapter 5. So, following this, we can express the pressure level of the sound radiated by the vibrating panel when excited by point-wise mechanical loads. This can be achieved by utilizing the modeled vibration velocity of the panel (i.e. Eq.(4.1.1)) and employing the Rayleigh integration method, similar to Equation (3.1.3) discussed in Chapter 3, as follows:

$$p(x, y, z; \omega) = \sum_{n \geq 0} \tilde{q}(\omega) H_n(\omega) \psi_n(x_0, y_0) Ray(\psi_n) \quad (4.1.2)$$

where  $Ray$  is the Rayleigh operator as defined by Eq.(3.1.2). In the following section, we present a detailed account of the actual laboratory experiments necessary for examining the modeling of mechanically excited panels.

## 4.2 Laboratory experiments

We chose four plates including a thick sandwich composite plate (with a Nomex honeycomb core), and a Carbon-Fiber-Reinforced Polymer (CFRP) laminate composite plate as well as two isotropic plates (aluminium and steel ones). Nomex honeycomb cores have been widely used in composite sandwich panels. Nomex (DuPont de Nemours, Inc.) honeycomb cores can be an appropriate choice for manufacturing thick sandwich panels concerning their environmental resistance, flammability prop-

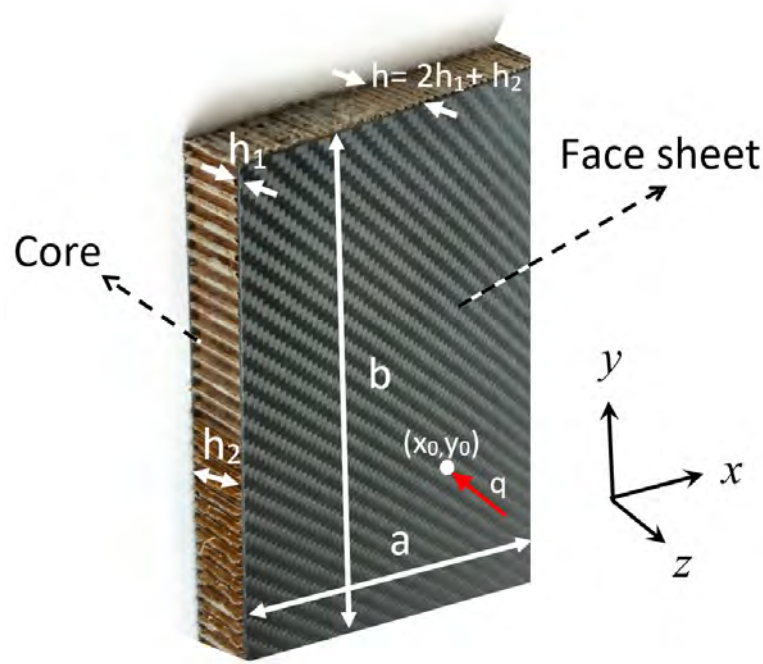


Figure 4.1: The geometrical configuration associated with an example of a thick composite sandwich panel with a Nomex honeycomb core covered by CFRP face sheets subjected to point-force mechanical excitation  $q = \tilde{q}(\omega)e^{i\omega t}$

erties, dielectric properties, and galvanic compatibility with face sheets (Roy et al. [2014]). On the other hand, Carbon fiber reinforced plastics (CFRP) laminate is a type of composite panel, which is made of extremely strong and light fiber-reinforced plastics that contain carbon fibers, have found extensive usage as structural components in various types of advanced structures (cf. Qi et al. [2019]). In addition to the two composite plates, we also examined two isotropic ones (aluminium and steel). The usage of the isotropic plates had the advantage that the modeling and simulation could additionally be tested and validated for the special case of the 4<sup>th</sup> order equation (see Eq.(2.3.3)) that is applicable for isotropic plates, too.

In this study, the above experimental plates sometimes referred to as specimens, are examined in controlled laboratory conditions in a semi-anechoic chamber whose dimensions were  $3.4m(W) \times 5m(L) \times 1.9m(H)$ . The semi-anechoic chamber possessed a measuring window (with dimensions  $60cm \times 40cm$ ), which could be used for vibroacoustic measurements of vibrating plates (the semi-anechoic room was coupled to another untreated room) (see Figure 4.3).

### 4.2.1 Experimental set-up

The experimental set-up of the current study has been summed up by Figure 4.2, and some views of the laboratory configuration have been shown by Figure 4.3. For performing vibration measurements, a scanning laser vibrometer system (PSV-300-F/S High Frequency Scanning Vibrometer System), manufactured by Polytec Co., has been used. The scanning laser vibrometer system was used to measure the full-vibration field associated with the flexural displacement of the vibrating plates from the inside of the semi-anechoic chamber when the plates were been shaken from the other side of the measuring window (see Figure 4.3). The specimens were installed in the  $40\text{cm} \times 60\text{cm}$  measuring window in such a way that the boundary condition of the vibrating plates was similar to a clamped boundary condition. For this purpose, in the experiments of each specimen, all the screws of the measuring window frame were installed with a torque of  $30\text{Nm}$  (see Figure 4.3 (b)). Also, a shaker was used for a point-wise excitation of the plates from the back while it was attached to a piezoelectric sensor as the force transducer with sensitivity  $105.5\text{mV/N}$  for measuring and sending the force signal to the spectrum analyzer (see Figure 4.3 (c)). In addition to the laser measurements, the sound radiated from the vibrating plates in the semi-anechoic chamber was recorded at a distance of  $50\text{cm}$  from the middle of the vibrating plates. Herein, the sounds were recorded with an omnidirectional microphone, manufactured by Brüel & Kjær Co., with a sensitivity equal to  $27.3\text{mV/Pa}$ . After calibration, the sound pressure level (SPL) was calculated. Figure 4.3 (e) illustrates the microphone facing the vibrating plate and recording the sounds. Also, the scanning laser system was equipped with a spectrum analyzer acquiring the signals sent from the laser vibrometer as well as other sensors including the piezoelectric sensor and the microphone. The spectrum analyzer enabled a white noise signal to be generated and sent to a signal generator for producing the voltage required by the shaker. Then, the laser vibrometer, microphone, and piezoelectric sensor of the force transducer simultaneously sent their signal to the spectrum analyzer that gathered the spectra of all the data in a unique database including the spectra belonging to all the sensors.

### 4.2.2 Characteristics of specimens

The four specimens had the dimensions  $42\text{cm} \times 62\text{cm}$  that could be clamped and installed in the measuring window. One of the specimens was a thick sandwich plate with a Nomex honeycomb core covered by two face sheets, and its total thickness was equal to  $13.9\text{mm}$ . The two face sheets of this composite structure are made

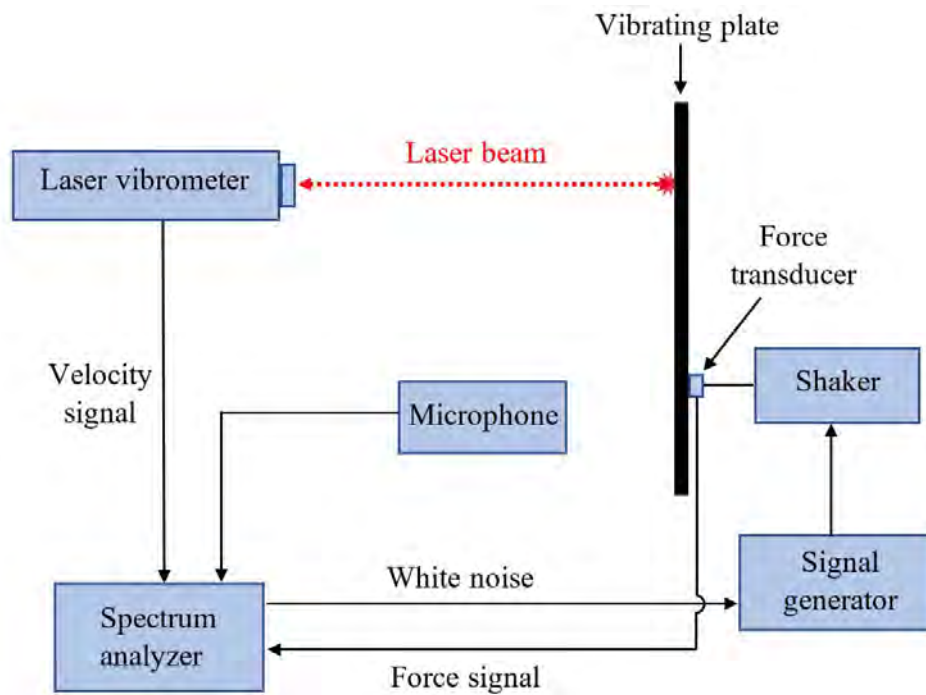


Figure 4.2: The schematic diagram of the experimental set-up

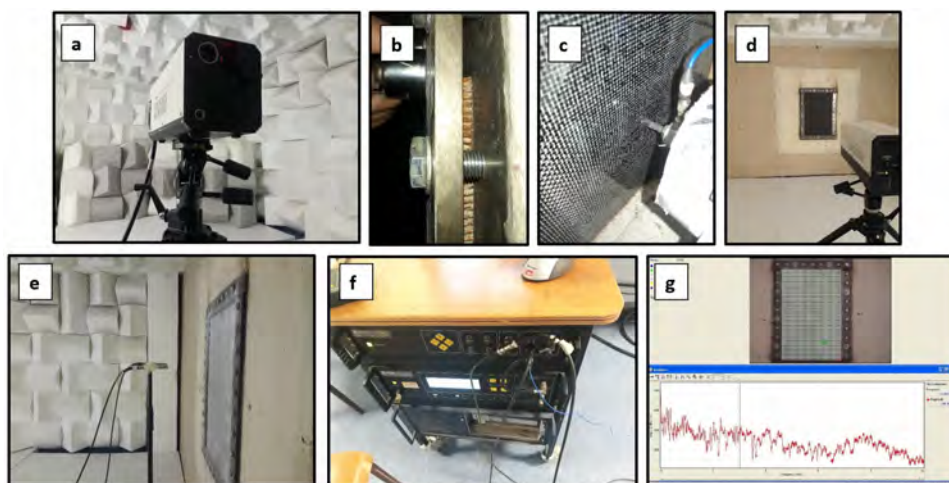


Figure 4.3: Some views of the configuration associated with the laboratory experiments: a) the PSV-300-F/S Scanning Vibrometer head, b) the clamped boundary condition performed with a torque equal to 30Nm for screws of the window frame, c) the shaker attached to the plate and connected to a piezoelectric sensor sending the force signal, d) the measuring window, and the floor covered by soundproofing forms e) the microphone recording the sound, f) the spectrum analyzer, g) the spectrum analyzer software

of two CFRP plates, seemingly woven, surrounding the Nomex honeycomb core, where the thickness of each face sheet and core is 0.2mm and 13.5mm, respectively.

According to the literature, we could have an initial prediction on some characteristics of the core. According to the mechanical characterization study of Nomex honeycomb core done by Roy et al. [2014] and Zhou et al. [2021], the equivalent shear modulus of the core was initially taken as 50Mpa. Also, each face sheet was initially assumed to be equivalent to a laminate composed of CFRP plys with a layout [0/90]. According to the studies of Shahdin et al. [2011], Qi et al. [2019], Zhou et al. [2021], the mechanical properties of the CFRP plys with epoxy matrix after curing were considered as what presented in Table 4.1. The other specimen was a composite laminate plate made of 25 CFRP plys with a symmetric layout as [(+45/-45/0/+90/0/+45/-45/0/+90/0/+45/-45)2 0]S. For this laminate plate, herein sometimes called a thin composite plate, the mechanical characteristics of each ply after curing were also assumed to be equal to what is presented in Table 4.1. The aforementioned values of the mechanical properties for each component of the two composite panels enabled the study to have an initial evaluation of the effective mechanical properties of the composite panels. Accordingly, a prediction on the equivalent values of the bending stiffness coefficients could be obtained by calculating the ABD stiffness matrix in classical laminate theory (CLT) where the bending stiffness could be initially estimated as follows:

$$D_{ij} = \frac{1}{3} \sum_k \bar{Q}_{ij}^k (z_k^3 - z_{k-1}^3) \quad (4.2.1)$$

where  $[\bar{Q}_{ij}^k]$  is the transformed reduced stiffness matrix,  $z_k$  is the represents the vertical position in the  $k^{th}$  layer of the composite plate from the mid-plane measured in meters, and  $i, j = 1, 2, 6$  (e.g., see Kaw [2005], Daniel et al. [2006]). In addition, we had a 3mm thick aluminum plate, as well as a 0.85mm thick steel plate. At the initial step, the Young modulus and Poisson ratio of the aluminium specimen were presumed to be equal to 70GPa and 0.33, and also, for the steel specimen to be equal to 210GPa and 0.28, respectively. Furthermore, the precise values of the mass density associated with specimens could be obtained via measuring the dimensions and the weights of the specimens. Thus, the measured values of the mass densities corresponding to the composite thick sandwich, thin composite laminate, and the aluminium and steel plates have been obtained equal to 138, 1506, 2648, and 7769  $kg/m^3$ , respectively.

Accordingly, we could reach initial approximations of the flexural bending stiffness coefficients associated with the plates. According to Table 4.1, the shear modulus of the composite sandwich was assumed to be equal to 50MPa, and its total flexural stiffness coefficient  $D_t$  required by the 6<sup>th</sup> order problem was obtained equal to 935Nm. Similarly, according to the initial information on the mechanical parameters,

Table 4.1: The initial information on the mechanical parameters. The mechanical properties of each CFRP ply with epoxy matrix after curing are based on the assessments of Shahdin et al. [2011], Qi et al. [2019], Zhou et al. [2021], and those of the Nomex core are based on the studies of Adams and Maheri [1993], Roy et al. [2014], Zhou et al. [2021]. The mass densities were measured in the laboratory experiments

	$E_1$	$E_2$	$G_{12}$	$\nu$	$h$ [mm]	$\rho$ [kg/m <sup>3</sup> ]
CFRP ply	140 GPa	7 GPa	3 GPa	0.3	0.14-0.2	1506
Nomex core	100 MPa	100 MPa	50 MPa	0.25	13	80
Aluminium	70 GPa	70 GPa	30 GPa	0.33	3	2648
Steel	210 GPa	210 GPa	80 GPa	0.29	0.85	7769

the flexural bending stiffness corresponding to the aluminium and steel plates were equal to 176Nm, and 12Nm, respectively. Besides, according to Eq.(4.2.1) as well as the information of Table 4.1, the orthotropic bending coefficients of the thin composite laminate plate were equal to  $D_{11} = 237\text{Nm}$ ,  $D_{22} = 163\text{Nm}$ ,  $D_{12} = 72\text{Nm}$ , and  $D_{66} = 75\text{Nm}$ . In this work, at the initial stage, we used these initial values of the bending stiffness for providing an initial prediction on the vibroacoustic behaviors of the specimens when they are mechanically excited with a white-noise point-wise force.

### 4.2.3 Measurements

The full-field vibration measurements for all the specimens were performed via the PSV-300-F/S laser doppler vibrometer (LDV) while the shaker was exerting a point-wise excitation with a white-noise behavior to the specimens. The analyzer of the PSV-300-F/S system provided the shaker with the white noise signal, and the LDV enabled non-contact vibration measurements of the specimens' surfaces to be undertaken. The LDV directed laser beams at the surface of interest, and the vibration amplitude and frequency were extracted from the Doppler shift of the reflected laser beam frequency due to the motion of the vibrating plates. Originally, the output of an LDV is a continuous signal presenting the velocity field of the vibrating plates, which could be converted to the full-field vibration field. Also, herein, we performed the laser scanning on 1855 nodes for both the sandwich and laminates plates, and on 2109 and 2035 nodes for the aluminum and steel plates, respectively. It means that the average spatial resolution of the laser scanning was between 0.87cm to 0.94cm. The measurement acquired for the frequency range [3.125Hz, 10kHz] with the frequency resolution equal to 3.125Hz. Since one of the main goals of these

experiments was the use of the measurements in psychoacoustic experiments, herein the maximum frequency range of the LDV system (i.e. [3.125Hz, 10kHz]) has been selected to perform measurements.

Furthermore, in Chapter 5, we will explore another primary usage of the laser vibratory measurements in current research, which involves updating models and parameters. This task necessitates experimental information on natural frequencies and their corresponding modes, obtained from 3D full-field vibratory measurements. For extracting the natural frequencies and their corresponding mode shapes from the full-field vibration field, we adopted a technique for the identification of frequency response function (FRF), based on the concept of the Single-input multiple-output (SIMO) systems. For this purpose, first, a number of the laser observation nodes for each plate were selected, where the velocity was measured for the desired frequency range [3.125Hz, 10kHz]. Then considering the observed force signal as a single-input (SI) and considering the measured velocity as the Multiple-outputs, we could form a SIMO system, and hence, its natural frequencies could be extracted from the system by the Least-Squares Complex Exponential Method. The least-squares complex exponential method estimates the FRF corresponding to each Single-input multiple-output (SIMO) system and fits to the response a set of complex damped sinusoids using Prony's method (see Heylen et al. [1997]; He and Fu [2001]; Brandt [2011], Ozdemir and Gumussoy [2017]). In Chapter 5, the measured values of the model shapes were used in the updating procedures.

Furthermore, in the laboratory experiments, an essential measurement for assessing the modeling and simulations was the Sound Pressure Level (SPL). The SPL was obtained using omni-directional microphones, which were closely monitored by the LDV system. The microphone had been previously calibrated at a frequency of 1kHz, with a sound level of 94dB. Consequently, based on the modeling of the flexural displacement  $w$  and the SPL emitted by the vibrating panels under mechanical excitation (as discussed in Section 5.1), we can draw comparisons between the laboratory measurements and the simulations. The figures 4.4 to 4.7 provide some representations of these comparisons between the simulations and measurements. The detailed comparisons and analyses of the measurements and simulations are discussed in depth in Chapter 5 regarding the updating procedures.

### 4.3 Discussion

In this chapter, we have explored the vibroacoustic modeling applied to composite panels under mechanical excitation. This exploration encompasses a combination of theoretical insights and practical experimentation. To achieve this, we conducted a

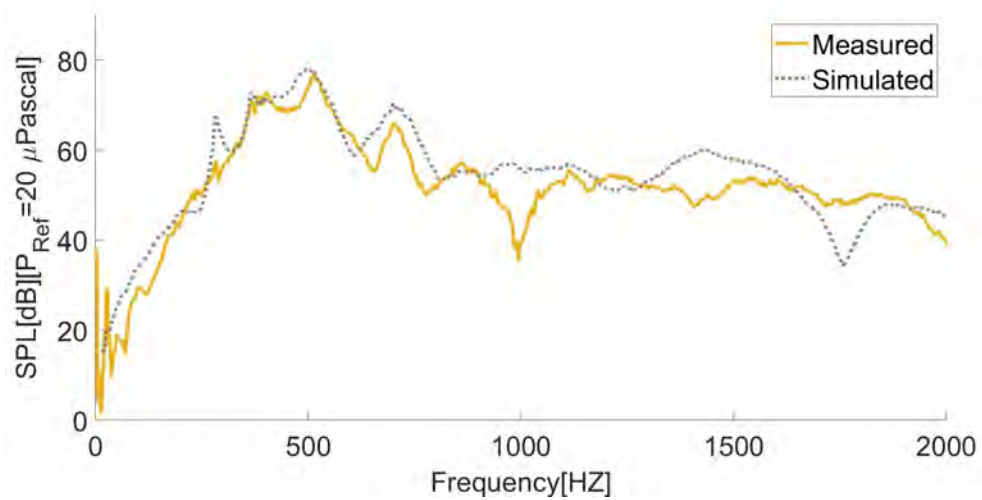


Figure 4.4: The measured and simulated SPLs at 50cm distance for the sandwich plate

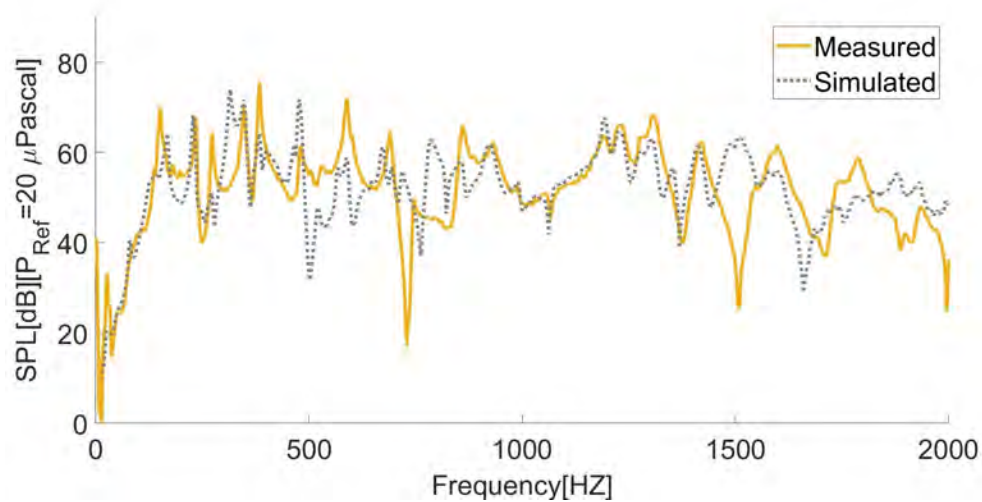


Figure 4.5: The measured and simulated SPLs at 50cm distance for the composite laminate plate

series of laboratory experiments, utilizing techniques such as laser Doppler vibrometry and sound pressure level measurements. These measurements were carried out on different composite and isotropic panels including a thick composite panel with a Nomex honeycomb core, and a thin CFRP laminate composite panel as well as two isotropic plates composed of steel and aluminum for enhancing the validation process. The outcomes derived from these experiments will lay the essential foundation for the upcoming phases of the thesis, which are dedicated to improving vibroacoustic models, with a specific focus on addressing psychoacoustic aspects and subjecting them to rigorous perceptual validation. Hence, to ensure the highest level of accu-



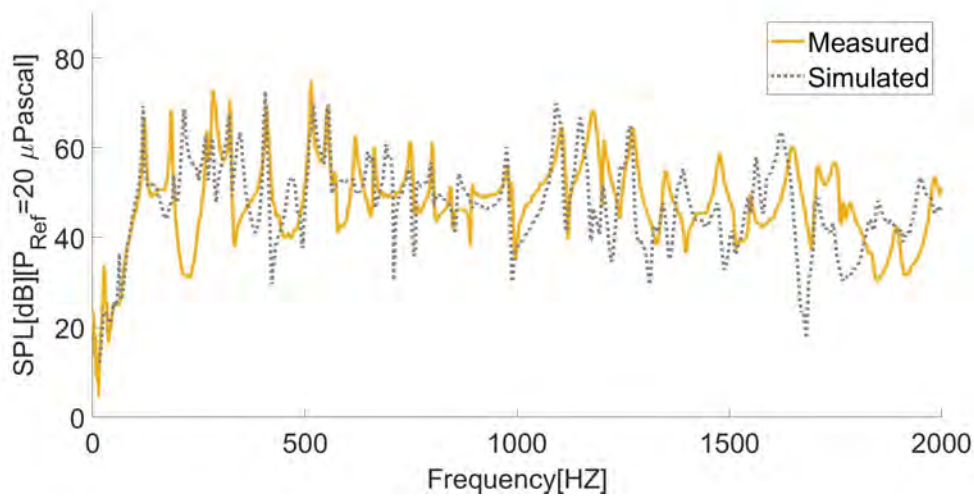


Figure 4.6: The measured and simulated SPLs at 50cm distance for the aluminium plate

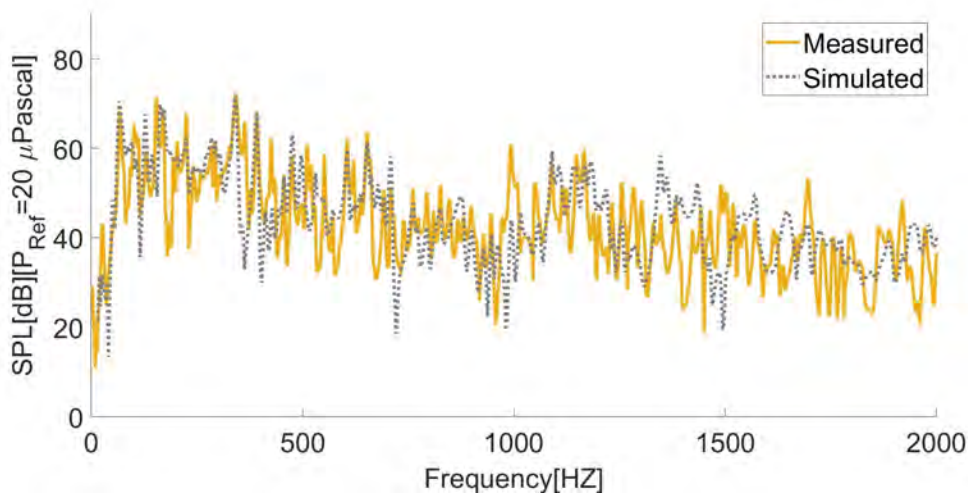


Figure 4.7: The measured and simulated SPLs at 50cm distance for the steel plate

racy in our simulations and achieve a strong agreement between the simulations and these laboratory measurements, it is crucial that we update and enhance the existing models for vibrating panels, which can minimize the uncertainty of simulations to the greatest extent possible. Therefore, the next chapter will be dedicated to the critical process of updating models and parameters. Additionally, a more comprehensive analysis and discussion of the results will be provided in the following chapter.

# Chapter 5

## Updating models and parameters

For accurate vibroacoustic modeling of panels, updating models and parameters is an essential stage. In this chapter, we aim to theoretically and experimentally review this stage. For this purpose, a hybrid updating method is proposed, incorporating hierarchical functions, inhomogeneous wave correlation approach, and least squares optimizations. Then various laboratory measurements presented in the previous chapter, including Laser Doppler Vibrometry measurements as well as sound pressure levels, are analyzed. The analyses of the experiments indicate the ability of the hybrid approach to adjust parameters and precisely model vibroacoustic behaviors of the panels. In the next stages of the thesis, the proposed hybrid method will play an important role in enhancing the precision of vibroacoustic modeling, and subsequently, it will enable us to accurately synthesize sounds necessary for conducting psychoacoustic tests and perceptual assessment. It is worth mentioning that certain sections of this chapter, as well as the previous one, have been incorporated into the article authored by AllahTavakoli et al. [2023a].

### 5.1 Introduction

The optimal design of composite structures is a burning issue (e.g., see Jones [2018]), and having a precise prediction about their vibroacoustic behavior is an essential stage for design optimization. The uncertainty remaining in numerical models and their parameters is the major barrier to precisely modeling the structure dynamics (e.g., see Friswell and Mottershead [1995]). Hence, model and parameter updating will be essential to reduce such uncertainty remaining in the models, and their parameters (Friswell and Mottershead [1995]). The purpose of parameter updating is to present physical meaning to a deficient model from real experiments where the

model suffers from a lack of precise knowledge about mechanical parameters, boundary conditions, and component connections (Mottershead and Friswell [1993]). Although in recent decades, many studies can be found in this regard, this issue is still of great interest to many researchers for either updating or identifying parameters in different case studies (e.g., see Girardi et al. [2021], Standoli et al. [2021], Chengwei et al. [2022]).

In the research conducted in the nineties, one can come across useful studies for reviewing advanced methods of updating (e.g., see Friswell [1990], Mottershead and Friswell [1993] and Humbert [1999]). These studies were then followed by studies on parameter identification, model updating, damage identification, and health monitoring in the context of different mechanical behaviors at the beginning of the 21st century (Farrar et al. [2001], Sinha et al. [2002], Carden and Fanning [2004], Živanović et al. [2005], Kerschen et al. [2006]). Afterward, other studies like Chen et al. [2006] performed analyses for investigating model and data uncertainties in structural dynamics with a case study of composite sandwich panels. Chen et al. [2006] dealt with the experimental identification, model updating, and validation of a non-parametric probabilistic method.

Meanwhile, parameter identification was another important issue in the parameter updating associated with composite sandwich panels. For instance, for the parameter identification, following Berthaut et al. [2005] which set the bases of inhomogeneous wave correlation method (IWC), Ichchou et al. [2008] proposed an approach and applied it to one and two-dimensional sandwich structures with honeycomb cores. Their approach is founded on the k-space characteristics of measured or simulated data and it starts from the spatially distributed fields of a vibrating structure for identifying the complete dispersion curve. The method of Ichchou et al. [2008] uses a harmonic field as the primary input, and then the correlation between this harmonic field and an inhomogeneous wave is calculated, leading to a wavenumber-dependent objective function, called Inhomogeneous Wave Correlation (IWC). Also, the approach includes an inverse technique for the optimization of the correlation index. Ichchou et al. [2008] successfully compared the technique with another wavenumber identification tool proposed by McDaniel et al. [2000] and McDaniel and Shepard Jr [2000]. Finally, in this research, parameter identification was attained via a least square algorithm, where a sandwich honeycomb was examined via the proposed method, and the results were successfully validated by an analytical model of Nilsson and Nilsson [2002]. Afterward, the IWC approach was also followed by other researchers in their parameter identification studies like Chronopoulos et al. [2013], Cherif et al. [2015], and Van Belle et al. [2017].

Besides, nowadays by virtue of high-tech laser vibrometers and digital cameras, we

are able to carry out the parameter identification and updating via using full-field vibration data. The increasing usage of these technologies in modal analysis has made full-field measurement of vibration mode shapes available (Mottershead et al. [2011]). Wang et al. [2011] presented a study on model updating from full-field vibration measurement using digital image correlation. This study shows how such a comparison of structural responses between predictions and full-field vibration measurements is an essential step in model updating.

In recent years, we can also come across other different studies for updating, optimizing, and identifying mechanical parameters of composite panels. For instance, Esfandiari [2014] proposed a model updating algorithm for estimating structural parameters at the element level using frequency domain representation of the strain data. Also, Tsai et al. [2015] propounded the optimization approach that could optimize material properties of a composite panel for a sound transmission problem. Wang et al. [2017] proposed a model updating method based on acceleration frequency response function (FRF), and applied a Kriging model to structural acceleration FRF-based model updating. Also, Cuadrado et al. [2019] provided an approach for the model updating of uncertain parameters of carbon/epoxy composite plates from experimental modal data.

Furthermore, along with the above-mentioned studies, another type of updating method has emerged in recent years, which attempts to employ artificial intelligence and machine learning techniques for updating parameters and models. For example, Hwang and He [2006] proposed an adaptive real-parameter simulated annealing genetic algorithm incorporated with natural frequency error function to estimate elastic properties of composite materials. Also, De Albuquerque et al. [2010] assessed delamination damages on composite plates using an Artificial Neural Network for the radiographic image analysis. Katunin and Przystała [2014] performed a damage assessment on composite plates using fractional wavelet transform of modal shapes with an optimized selection of spatial wavelets. Petrone and Meruane [2017] used an inverse modeling method based on a parallel genetic algorithm for updating mechanical properties throughout a composite panel in order to get a good numerical-experimental correlation. Tam et al. [2019] proposed an identification approach for isotropic and composite panels, known as, the two-stage meta-heuristic hybrid GA-ACO-PSO optimization method that uses the natural frequency error function, and FRF error function in its first and second stages, respectively. Also, Khatir et al. [2021] proposed another two-stage approach to study damage detection, localization, and quantification in Functionally Graded Material (FGM) plate structures.

The integration of various methods to suggest a hybrid approach comes with certain limitations such as challenges related to compatibility between the methods,

heightened complexity for users, and the requirement for meticulous assessments. However, these limitations can be largely addressed through the implementation of a specific structure, clear formulations and procedures, and detailed experimental evaluations. The main advantage of a hybrid method is the utilization of the proven capabilities of previously established methods and its progressive implementation, allowing for the controlled evaluation and enhancement of the updated parameters and model at each stage.

In this chapter, continuing the above-mentioned studies, the proposed hybrid approach is founded on concepts of Hierarchical functions, IWC approach, and least squares optimizations, and finally, its abilities are successfully examined in laboratory experiments. Such validated abilities of the proposed method for calculations up to high frequencies, normally not considered in classical simulations, will also be capable of presenting accurate modeling from a perceptual point of view in future psychoacoustic studies, which is one of the future goals of this research, too.

Herein, the originality of the proposed hybrid approach owes much to the analytical formulations of the problems, using the capabilities of the IWC technique during updating procedures, and completing the procedures with the total least square optimization, while the ground-truth laboratory measurements accompany and control the procedures in all the steps. The Hierarchical functions have facilitated the advantage of the hybrid method in analyzing the problem analytically and preparing it for optimizations. Additionally, the IWC approach has empowered the parameter identification and control of initial values for the mechanical parameters of the composite panels. Lastly, the utilization of the least squares methods has enhanced the optimization capabilities of the hybrid approach.

## 5.2 Hybrid Updating Method

Herein, the methodology starts with the hierarchical functions required for modeling high-order bending modes and consequently modeling the flexural vibration. The variational formulation is analyzed via the hierarchical functions, and then the IWC technique is presented for performing an initial tuning to mechanical parameters used in the formulation. Afterward, the procedure of model updating is explained, and at last, the methodology ends with the least square optimization and updated values of the parameters. The structure and main stages of the proposed hybrid updating method are illustrated by Figure 5.1.

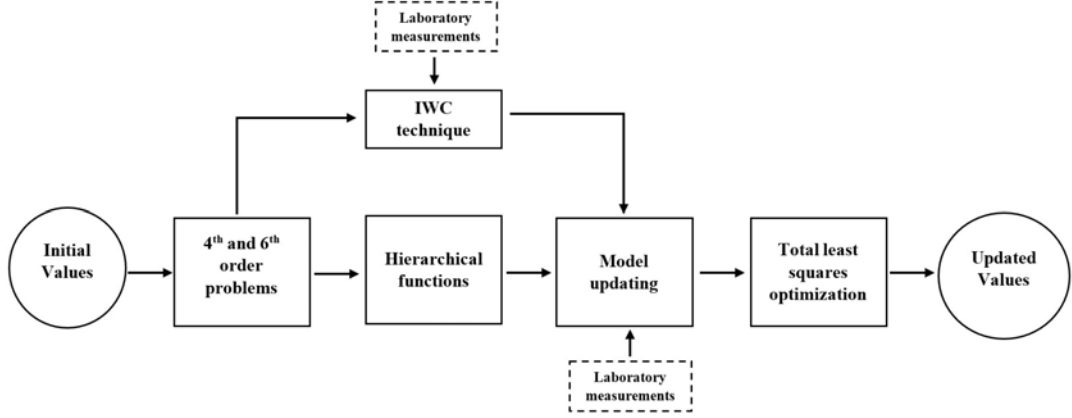


Figure 5.1: The schematic diagram illustrating the hybrid updating method

### 5.2.1 Hierarchical functions and formulations

Hierarchical functions are employed to model flexural motion of the plate structure where these functions are constructed by a type of trigonometric functions. The hierarchical functions can provide us with a better convergence rate when predicting high-order natural flexural modes of rectangular vibrating plates with any boundary conditions (Beslin and Nicolas [1997]). Hence, according to the Rayleigh–Ritz method, the Fourier transform of the flexural displacement  $\tilde{w}(x, y; \omega)$  can be approximated by the following relation (Beslin and Nicolas [1997], Jaouen et al. [2005]):

$$\tilde{w}(x, y; \omega) = \sum_n \tilde{w}_n(\omega) \phi_n(x, y) \quad (5.2.1)$$

where  $\{\tilde{w}_n\}$  are complex coefficients, and the hierarchical functions  $\{\phi_n\}$  are defined as follows:

$$\phi_n(x, y) = \alpha_l(\xi) \alpha_k(\eta) \quad (5.2.2)$$

where  $n = n(l, k)$ , and  $\xi = 2x/a - 1$  and  $\eta = 2y/b - 1$  are dimensionless space variables, and the functions  $\{\alpha_l\}$  are of the following form (Beslin and Nicolas [1997], Jaouen et al. [2005]):

$$\alpha_l(\xi) = \sin(a_l \xi + b_l) \sin(c_l \xi + d_l) \quad (5.2.3)$$

where the coefficients  $\{a_l, b_l, c_l, d_l\}$  are defined in Table 5.1, and meanwhile, the order  $l$  enables us to consider various Boundary Conditions (B.Cs) for the vibrating plate as follows:

Table 5.1: The coefficients  $\{a_l, b_l, c_l, d_l\}$  required for defining the hierarchical functions

	$a_l$	$b_l$	$c_l$	$d_l$
$l = 1$	$\pi/4$	$3\pi/4$	$\pi/4$	$3\pi/4$
$l = 2$	$\pi/4$	$3\pi/4$	$-\pi/2$	$-3\pi/2$
$l = 3$	$\pi/4$	$-3\pi/4$	$\pi/4$	$-3\pi/4$
$l = 4$	$\pi/4$	$-3\pi/4$	$\pi/2$	$-3\pi/2$
$l \geq 5$	$(l-4)\pi/2$	$(l-4)\pi/2$	$\pi/2$	$\pi/2$

- Free B.C:  $l \geq 1$
- Simply Supported B.C:  $l = 2, 4$  and  $l \geq 5$
- Clamped B.C:  $l \geq 5$

Since the laboratory experiments were performed for vibrating plates under boundary conditions near the clamped boundary condition, from here on the clamped boundary condition is considered. However, according to the above-mentioned theories, the concepts of the methodology will remain the same for other types of conditions. Besides, in practice, the choice of a large value for parameter  $n$  in the Rayleigh–Ritz approximation (i.e. Eq.5.2.1) enables us to estimate a greater number of modes in the problem. On the other hand, to achieve convergence of the approximation and obtain an appropriate solution, the maximum number of modes should be appropriately selected for the modal decomposition (i.e. Eq.(2.3.5) in Chapter 2)). It is possible to demonstrate that the maximum number of modes  $N$  is a function of the desired maximum frequency when the problem is treated as a two-dimensional system (e.g., see chapter 6.3 in Le Bot [2015]). Now, according to the Rayleigh–Ritz approximation based on the hierarchical functions, we can reach variational formulations for both the 4<sup>th</sup> and 6<sup>th</sup> order problems.

### For 4<sup>th</sup> order problem

So, if the hierarchical function  $\phi_m$  with the order  $m$  plays the role of a test function in the variational formulation for the 4<sup>th</sup> order problem (see Eq.(2.3.2)), we will have

the following equation for the case of free vibration (i.e. when  $q = 0$ ):

$$\begin{aligned} D_{11} \int_0^b \int_0^a \frac{\partial^4 \tilde{w}}{\partial x^4} \phi_m dx dy + 2(D_{12} + 2D_{66}) \int_0^b \int_0^a \frac{\partial^4 \tilde{w}}{\partial x^2 \partial y^2} \phi_m dx dy + \\ D_{22} \int_0^b \int_0^a \frac{\partial^4 \tilde{w}}{\partial y^4} \phi_m dx dy - M\omega^2 \int_0^b \int_0^a \tilde{w} \phi_m dx dy = 0 \end{aligned} \quad (5.2.4)$$

and subsequently, according to the Rayleigh–Ritz approximation (i.e. Eq.(5.2.1)), we will also have

$$\begin{aligned} D_{11} \sum_n \tilde{w}_n \int_0^b \int_0^a \frac{\partial^4 \phi_n}{\partial x^4} \phi_m dx dy + 2(D_{12} + 2D_{66}) \sum_n \tilde{w}_n \int_0^b \int_0^a \frac{\partial^4 \phi_n}{\partial x^2 \partial y^2} \phi_m dx dy + \\ D_{22} \sum_n \tilde{w}_n \int_0^b \int_0^a \frac{\partial^4 \phi_n}{\partial y^4} \phi_m dx dy - M\omega^2 \sum_n \tilde{w}_n \int_0^b \int_0^a \phi_n \phi_m dx dy = 0 \end{aligned} \quad (5.2.5)$$

Thus, according to the integration by parts and the characteristics of the hierarchical functions defined for the clamped boundary condition (i.e. when  $n, m \geq 5$ ), we have

$$\begin{aligned} D_{11} \sum_n \tilde{w}_n \int_0^b \int_0^a \frac{\partial^2 \phi_n}{\partial x^2} \frac{\partial^2 \phi_m}{\partial x^2} dx dy + 2(D_{12} + 2D_{66}) \sum_n \tilde{w}_n \int_0^b \int_0^a \frac{\partial^2 \phi_n}{\partial x \partial y} \frac{\partial^2 \phi_m}{\partial x \partial y} dx dy + \\ D_{22} \sum_n \tilde{w}_n \int_0^b \int_0^a \frac{\partial^2 \phi_n}{\partial y^2} \frac{\partial^2 \phi_m}{\partial y^2} dx dy - M\omega^2 \sum_n \tilde{w}_n \int_0^b \int_0^a \phi_n \phi_m dx dy = 0 \end{aligned} \quad (5.2.6)$$

Accordingly, the above equation changes into  $\mathbf{K}\tilde{\mathbf{w}} - \omega^2\mathbf{M}\tilde{\mathbf{w}} = \mathbf{0}$  where  $\tilde{\mathbf{w}} = [\tilde{w}_n]$ , and the stiffness matrix  $\mathbf{K} = [K_{mn}]$  and mass matrix  $\mathbf{M} = [M_{mn}]$  belonging to the 4<sup>th</sup> order problem are defined as follows:

$$\mathbf{K} = [K_{mn}] = \left[ \int_0^b \int_0^a \left( D_{11} \frac{\partial^2 \phi_n}{\partial x^2} \frac{\partial^2 \phi_m}{\partial x^2} + 2(D_{12} + 2D_{66}) \frac{\partial^2 \phi_n}{\partial x \partial y} \frac{\partial^2 \phi_m}{\partial x \partial y} + D_{22} \frac{\partial^2 \phi_n}{\partial y^2} \frac{\partial^2 \phi_m}{\partial y^2} \right) dx dy \right] \quad (5.2.7)$$

$$\mathbf{M} = [M_{mn}] = \left[ M \int_0^b \int_0^a \phi_n \phi_m dx dy \right] \quad (5.2.8)$$

### For 6<sup>th</sup> order problem

Similarly, based on the 6<sup>th</sup> order problem introduced in Chapter 2, we can also obtain the following formulation for the case of free vibration in the 6<sup>th</sup> order problem (i.e.



when  $q = 0$ ):

$$\begin{aligned} D_t \int_0^b \int_0^a \nabla^6 \tilde{w} \phi_m dx dy - D_t \dot{g}(1+Y) \int_0^b \int_0^a \nabla^4 \tilde{w} \phi_m dx dy \\ - M\omega^2 \int_0^b \int_0^a (\nabla^2 \tilde{w} - \dot{g}\tilde{w}) \phi_m dx dy = 0 \end{aligned} \quad (5.2.9)$$

So, subsequently, the Rayleigh–Ritz approximation (i.e. Eq.(5.2.1)) implies that

$$\begin{aligned} D_t \sum_n \tilde{w}_n \int_0^b \int_0^a \nabla^6 \phi_n \phi_m dx dy - D_t \dot{g}(1+Y) \sum_n \tilde{w}_n \int_0^b \int_0^a \nabla^4 \phi_n \phi_m dx dy \\ - M\omega^2 \sum_n \tilde{w}_n \int_0^b \int_0^a (\nabla^2 \phi_n - \dot{g}\phi_n) \phi_m dx dy = 0 \end{aligned} \quad (5.2.10)$$

Therefore, using the integration by parts, and considering the characteristics of the hierarchical functions defined for the clamped boundary condition (i.e. the hierarchical functions with the orders  $n, m \geq 5$ ), we will obtain

$$\begin{aligned} D_t \sum_n \tilde{w}_n \int_0^b \int_0^a \nabla^3 \phi_n \cdot \nabla^3 \phi_m dx dy + D_t \dot{g}(1+Y) \sum_n \tilde{w}_n \int_0^b \int_0^a \nabla^2 \phi_n \nabla^2 \phi_m dx dy \\ - M\omega^2 \sum_n \tilde{w}_n \int_0^b \int_0^a (\nabla \phi_n \cdot \nabla \phi_m + \dot{g}\phi_n \phi_m) dx dy = 0 \end{aligned} \quad (5.2.11)$$

where the dot  $\cdot$  is the sign of the inter product,  $\nabla^3(\bullet) = \nabla(\nabla^2(\bullet))$ , and  $\nabla(\bullet) = (\frac{\partial(\bullet)}{\partial x}, \frac{\partial(\bullet)}{\partial y})$  is the gradient operator. Consequently, the above relation is also formed into  $\mathbf{K}\tilde{\mathbf{w}} - \omega^2\mathbf{M}\tilde{\mathbf{w}} = \mathbf{0}$ , and the stiffness matrix  $\mathbf{K} = [K_{mn}]$  and mass matrix  $\mathbf{M} = [M_{mn}]$  corresponding to the 6<sup>th</sup> order problem are obtained as follows:

$$\mathbf{K} = [K_{mn}] = \left[ \int_0^b \int_0^a D_t (\nabla^3 \phi_n \cdot \nabla^3 \phi_m + \dot{g}(1+Y) \nabla^2 \phi_n \nabla^2 \phi_m) dx dy \right] \quad (5.2.12)$$

$$\mathbf{M} = [M_{mn}] = \left[ M \int_0^b \int_0^a (\nabla \phi_n \cdot \nabla \phi_m + \dot{g}\phi_n \phi_m) dx dy \right] \quad (5.2.13)$$

The above formulation for the 6<sup>th</sup> order problem indicates that the stiffness and mass matrices are formed by (semi-) inner products of Sobolev spaces (cf. Adams and Fournier [2003]).

### 5.2.2 Inhomogeneous wave correlation technique

First, we need to have a certain initial knowledge about the mechanical parameters including Young modulus, Poisson ratio, shear modulus, and bending rigidity coefficients for constructing the governing equations. Although one can usually obtain such initial knowledge of the parameters from previous studies, and any initial information about the parameters is enough to theoretically perform the updating procedure, and we do not expect much from their precision, in practice these initial values should be both reliable and acceptable. For this purpose, we can utilize methods of property identification for identifying effective structural properties. Hence, as introduced in Section 5.1, according to the abilities of the inhomogeneous wave correlation method (IWC) technique (Berthaut et al. [2005], Ichchou et al. [2008]), this approach can be helpful in this step, and hence, herein, we used IWC technique for initially tuning the mechanical parameters of composite panels before performing the model updating and associated optimizations.

The IWC approach starts with an acquired full field of the vibrating panel, for constructing the  $k$ -space. This technique uses the acquired full field of vibration like  $w$  as the primary input, which can be acquired in a controlled laboratory condition via Laser precise Doppler Vibrometers (LDVs) or precise digital cameras. Then the correlation between the full field and an inhomogeneous wave  $o_{k,\gamma,\theta}$  is calculated. This correlation leads us to a wavenumber-dependent objective function, the so-called Inhomogeneous Wave Correlation (IWC) as follows (Berthaut et al. [2005], Ichchou et al. [2008]):

$$\text{IWC}(k, \gamma, \theta) = \frac{\left| \int_0^b \int_0^a w \bar{o}_{k,\gamma,\theta} dx dy \right|}{\sqrt{\int_0^b \int_0^a |w|^2 dx dy \int_0^b \int_0^a |\bar{o}_{k,\gamma,\theta}|^2 dx dy}} \quad (5.2.14)$$

where  $o_{k,\gamma,\theta} = e^{-ik(\theta)(1+i\gamma(\theta))(x \cos(\theta)+y \sin(\theta))}$ ,  $k(\theta)$  is the wave number in the direction  $\theta$ , and  $\gamma(\theta)$  is the wave attenuation defined by Lyon et al. [1995]. So, the maximization of the above IWC objective function implies the identification of the complex wave number  $k$  for the given direction  $\theta$  in the  $k$ -space. Then, based on the identified wave number in various directions of the  $k$ -space as well as considering the dispersion relations (see Chapter 2), we can perform identification of mechanical properties of the composite panel too, see (Ichchou et al. [2008]). In the current study, this approach has been used for initially predicting the mechanical effective properties of panels before going through the model updating and associated optimization.

### 5.2.3 Model updating

Experimental knowledge about the full vibration field of the vibrating panel is required for adjusting the models and their associated parameters. Nowadays, such experimental data about the full vibration field can be acquired via advanced scanning laser vibrometers or high-speed cameras (Stanbridge et al. [2004], Mottershead et al. [2011], Wang et al. [2011]). In this step, we apply the mode shapes, extracted from the full-field vibration data, acquired from laboratory experiments, to the models of the 4<sup>th</sup> and 6<sup>th</sup> order problems (in the next Section the procedure required for extracting the modes from the experimental data has been discussed).

So, first assume that the columns of the matrix  $\Psi_M = [\psi_l^M] = [\psi_l^M(x_k, y_k)]$  contains the measured values of the mode shapes acquired in laboratory experiments (where  $\psi_l^M$  is the  $l^{\text{th}}$  column of the matrix  $\Psi_M$ , which contains the measured values of the  $l^{\text{th}}$  modal function  $\psi_n$ , and  $\psi_l^M(x_k, y_k)$  is the measured value of the  $l^{\text{th}}$  mode at the node  $k$  with coordinates  $(x_k, y_k)$ ). The measured values of the mode shapes should be projected to the hierarchical base functions. For this purpose, the measured values of the  $l^{\text{th}}$  mode shape at the node  $k$  can be approximated by the Rayleigh–Ritz method and hierarchical function as follows (see Eq.(5.2.1)):

$$\psi_l^M(x_k, y_k) = \sum_n \Psi_{nl}^M(\omega) \phi_n(x_k, y_k) \quad (5.2.15)$$

The above relation constitutes a system of linear equation, where on the left-hand side we have the measured values of the mode shapes  $[\psi_l^M(x_k, y_k)]$ , and on the right-hand side we have the known coefficients  $[\phi_n(x_k, y_k)]$  (the known values of  $n^{\text{th}}$  hierarchical functions at the node  $k$ ).

So, by means of solving the above linear system, we can reach another form of the measured mode matrix  $\Psi_M = [\Psi_{nl}^M]$  that is actually the projection of the measured modes onto the hierarchical functions. Furthermore, before using this matrix it is recommended to normalize its columns in the following way:  $\Psi_l := \Psi_l (\Psi_l^T \mathbf{M} \Psi_l)^{-\frac{1}{2}}$  where  $\Psi_l$  is the  $l^{\text{th}}$  column of the matrix  $\Psi_M$  before normalization, i.e.  $\Psi_l$  is the measured  $l^{\text{th}}$  mode shape and formed by the hierarchical functions before normalization. For more information on this type of normalization (e.g., see Baruch [1978]). Now, the measured values of the mode shapes are ready to be used by the model updating.

Thus, for the 4<sup>th</sup> and 6<sup>th</sup> order problems (see Subsections 5.2.1 and 5.2.1) if we suppose that the stiffness matrix  $\mathbf{K}$  is more affected by the uncertainties than the mass matrix  $\mathbf{M}$ , we can consider the mass matrix  $\mathbf{M}$  as the reference matrix. So, by means of the following least squares optimization, Baruch method, we can find

the correction to the stiffness matrix  $\delta\mathbf{K}$  as well as the optimized matrix of mode shapes  $\hat{\Psi}$  as follows (see Baruch [1978], Humbert [1999]):

$$\left\{ \begin{array}{l} \left\| \mathbf{M}^{-\frac{1}{2}} \delta\mathbf{K} \mathbf{M}^{-\frac{1}{2}} \right\|_F^2 \rightarrow Min \\ \hat{\mathbf{K}} \hat{\Psi} = \mathbf{M} \hat{\Psi} \Omega_M^2 \\ \hat{\mathbf{K}} = \hat{\mathbf{K}}^T \end{array} \right. , \quad \left\{ \begin{array}{l} \left\| \mathbf{M}^{\frac{1}{2}} \delta\Psi \right\|_F^2 \rightarrow Min \\ \hat{\Psi}^T \mathbf{M} \hat{\Psi} = \mathbf{I} \end{array} \right. \quad (5.2.16)$$

where  $\delta\mathbf{K} = \hat{\mathbf{K}} - \mathbf{K}$ , and  $\delta\Psi = \hat{\Psi} - \Psi_M$  is the correction to the mode shapes, also,  $\|\bullet\|_F$  is the Frobenius norm, and  $\Omega_M$  is a diagonal matrix whose diagonal elements consists of measured values of angular natural frequencies corresponding to the measured modes. Baruch [1978] showed that the solution to the above optimization will be as follows:

$$\begin{aligned} \delta\mathbf{K} &= -\mathbf{K} \hat{\Psi} \hat{\Psi}^T \mathbf{M} - \mathbf{M} \hat{\Psi} \hat{\Psi}^T \mathbf{K} + \mathbf{M} \hat{\Psi} \hat{\Psi}^T \mathbf{K} \hat{\Psi} \hat{\Psi}^T \mathbf{M} + \mathbf{M} \hat{\Psi} \Omega_M^2 \hat{\Psi}^T \mathbf{M} \\ \hat{\Psi} &= \Psi_M (\Psi_M^T \mathbf{M} \Psi_M)^{-\frac{1}{2}} \end{aligned} \quad (5.2.17)$$

Herein, the above solution enables us to update the associated stiffness matrices obtained by Eqs.(5.2.7) and (5.2.12), and consequently, it will enable us to update the corresponding parameters of the 4<sup>th</sup> and 6<sup>th</sup> order problems as discussed in the following subsection.

### 5.2.4 Total least squares optimization

Accordingly, suppose that the vector  $\mathbf{p} = [p_i]$  consists of the parameters to be updated. We know that the stiffness matrix is a function of the parameters (i.e.  $\mathbf{K} = \mathbf{K}(\mathbf{p})$  and  $K_{nm} = K_{nm}([p_i])$ ). Hence, we have

$$\delta K_{nm} = \sum_i \frac{\partial K_{nm}}{\partial p_i} \delta p_i \quad (5.2.18)$$

So, considering the correction to the stiffness matrix  $\delta\mathbf{K} = [\delta K_{nm}]$  obtained via Eq.(5.2.17) and laboratory experiments, the above equation for all the elements of the matrix  $\delta\mathbf{K} = [\delta K_{nm}]$  constitutes a system of linear equations like  $\mathbf{b} = \mathbf{A} \mathbf{x}$  where  $\mathbf{x}$  as the unknown vector consists of the corrections to the parameters ( $\mathbf{x} = \delta\mathbf{p} = [p_i]$ ), the vector  $\mathbf{b} = [\delta K_{nm}]$  as the known data consists of the elements of  $\delta\mathbf{K}$  obtained via Eq.(5.2.17), and the matrix  $\mathbf{A} = [\frac{\partial K_{nm}}{\partial p_i}]$  is formed by the derivatives of the elements of the stiffness matrix as discussed in the following.

**For 4<sup>th</sup> order problem**

For the 4<sup>th</sup> order problem, we have three independent parameters, which can be estimated via the above-mentioned linear problem. According to Eq.(5.2.7) formulating the stiffness matrix of the 4<sup>th</sup> order problem via the hierarchical functions, the three independent parameters are  $p_1 = D_{11}$ ,  $p_2 = D_{12} + 2D_{66}$ , and  $p_3 = D_{22}$ , and we have (see Eq.(5.2.7))

$$\frac{\partial K_{mn}}{\partial p_1} = \frac{\partial K_{mn}}{\partial D_{11}} = \int_0^b \int_0^a \frac{\partial^2 \phi_n}{\partial x^2} \frac{\partial^2 \phi_m}{\partial x^2} dx dy \quad (5.2.19)$$

$$\frac{\partial K_{mn}}{\partial p_2} = 2 \int_0^b \int_0^a \frac{\partial^2 \phi_n}{\partial x \partial y} \frac{\partial^2 \phi_m}{\partial x \partial y} dx dy \quad (5.2.20)$$

$$\frac{\partial K_{mn}}{\partial p_3} = \frac{\partial K_{mn}}{\partial D_{22}} = \int_0^b \int_0^a \frac{\partial^2 \phi_n}{\partial y^2} \frac{\partial^2 \phi_m}{\partial y^2} dx dy \quad (5.2.21)$$

**For 6<sup>th</sup> order problem**

Also, for the 6<sup>th</sup> order problem, we have two parameters whose corrections can also be estimated by Eq.(5.2.18). Thus, according to Eq.(5.2.12) formulating the stiffness matrix of the 6<sup>th</sup> order problem via the hierarchical functions, the two parameters are  $p_1 = D_t$ , and  $p_2 = D_t g'$ , related to the total flexural rigidity and the shear parameter of the core, and hence, we have (see Eq.(5.2.12))

$$\frac{\partial K_{mn}}{\partial p_1} = \int_0^b \int_0^a \nabla^3 \phi_n \cdot \nabla^3 \phi_m dx dy \quad (5.2.22)$$

$$\frac{\partial K_{mn}}{\partial p_2} = (1 + Y) \int_0^b \int_0^a \nabla^2 \phi_n \nabla^2 \phi_m dx dy \quad (5.2.23)$$

**Updating parameters**

Accordingly, now we can solve Eq.(5.2.18) for finding the corrections to the parameters and consequently updating the parameters. Herein, we employed the total least squares method (TLS) for adjusting and solving Eq.(5.2.18). The total least squares method is a natural generalization of the least squares method, recommended for solving a system of linear equations when all the given data including both the model  $\mathbf{A}$  and  $\mathbf{b}$  suffer from uncertainties, and it has a wide range of applications in system theory, signal processing, and computer algebra (Markovsky and Van Huffel

[2007]). In order to estimate the residual parameters  $[\delta p_i]$  and subsequently update the parameters  $[p_i]$ , according to the total least squares method, the solution to the equation Eq.(5.2.18) formed into  $\mathbf{b} = \mathbf{A}\mathbf{x}$  will be as follows (see Markovsky and Van Huffel [2007]):

$$\delta \hat{\mathbf{p}} = \hat{\mathbf{x}} = (\mathbf{A}^T \mathbf{A} - \sigma_{n+1}^2 \mathbf{I})^{-1} \mathbf{A}^T \mathbf{b} \quad (5.2.24)$$

where the elements of  $\mathbf{A} = [\frac{\partial K_{nm}}{\partial p_i}]$  are obtained by Eqs.(5.2.19) to (5.2.22),  $\sigma_{n+1}$  is the smallest singular value of the matrix  $[\mathbf{A} \ \mathbf{b}]$ , and  $\mathbf{I}$  is the identity matrix. So, at last the updated parameters  $\hat{\mathbf{p}}$  will be obtained by adding the estimated corrections  $\delta \hat{\mathbf{p}}$  to the initial parameters  $\mathbf{p}$  (i.e.  $\hat{\mathbf{p}} = \mathbf{p} + \delta \hat{\mathbf{p}}$ ).

### 5.3 Updating procedures

First, parameter identification was performed for the problems formulated by the hierarchical functions. Although prior knowledge of the properties of the specimens' components (cf. Table 1 and Chapter 4) can be helpful to have a prediction on the mechanical parameters of the specimens, in practice such prior information may be far from the reality and may mislead the problems about the true solutions. As described in Section 5.2.2, the identification of the properties was performed by the IWC technique. For this purpose, considering the full-field vibration measurements for each specimen, the wave numbers corresponding to 20 frequencies and in 180 directions could be extracted from the measurements by means of the maximization of the IWC function (see Eq.(5.2.14)). Herein, for the frequencies, the center frequencies of one-third octave bands from 125Hz to 10kHz were used, and the 180 directions were equal to 1 degree to 180 degrees. On the other hand, the dispersion equations enable mathematical relationships between the frequencies, their corresponding wave numbers, and the mechanical properties (see Chapter 2). So, these mathematical relationships could provide us with a system of equations finding the mechanical properties of the specimens (see Ichchou et al. [2008]). Table 5.2 summarizes the properties obtained by the IWC technique.

In the next step, the mechanical parameters identified by the IWC technique were used in the model updating procedures. Herein, the 6<sup>th</sup> order problem was used for the formulation and modeling associated with the thick composite sandwich plate; the 4<sup>th</sup> order problem with its general form was used for the modeling of the thin composite laminate specimen, and also, the particular case of the 4<sup>th</sup> order problem adapted for thin isotropic plates (i.e. Eq.(2.3.3)) was also utilized for the formulation and modeling corresponding to the aluminium and steel plates. Therefore, applying the identified parameters to the analytical formulations of the stiffness

Table 5.2: The mechanical properties of the composite sandwich, laminate, aluminium, and steel plates, identified by the IWC technique

Sandwich	Laminate	Aluminium	Steel
$D_t = 1093\text{Nm}$	$D_{11} = 259\text{Nm}, D_{22} = 136\text{Nm}$	$E = 76\text{GPa}$	$E = 213\text{GPa}$
$G_c = 68\text{MPa}$	$D_{12} + 2D_{66} = 189\text{Nm}$		

and mass matrices introduced by the hierarchical functions (i.e. Equations (5.2.7), (5.2.8), (5.2.12), and (5.2.13) ), we could analytically calculate these matrices, and then apply them to the model updating solution (i.e. Eq.(5.2.17)). The model updating solution requires the measured mode shapes, which we could extract from the full-field laser measurement. The updated modal shapes are one of the main outputs of the model-updating procedures (see Eq.(5.2.17)), and since they are essentially needed for the modal decomposition and for finding the final solution to the problem, we need to have an idea on their quality. Modal Assurance Criterion (MAC) is a type of correlation criterion, which makes it possible to measure the quality of calculated mode shapes, and also enables to match two families of modes. For instance, for the calculated and measured modes, the cross MAC is defined and calculated as follows (e.g., see Humbert [1999]):

$$MAC(\psi_l^M, \psi_l) = \frac{|\psi_l^M \cdot \psi_l|}{\sqrt{\psi_l^M \cdot \psi_l^M} \sqrt{\psi_l \cdot \psi_l}} \quad (5.3.1)$$

where  $\cdot$  denotes the inner product, and the vectors  $\psi_l^M$  and  $\psi_l$  are the  $l^{th}$  measured and calculated modes, respectively. The MAC values are between 0 and 1, and a value close to 1 indicates a good correlation between the calculated and measured modal shapes. In Figures 5.2 to 5.5, the MAC values have been illustrated for cases performed before and after the updating procedures. As seen in these figures, after applying the updating procedures to the modal shapes, we can see that the values of the cross MAC have been enhanced for all the calculated modes associated with all the plates. The figures demonstrate that the updating procedures for the problems associated with the 4 specimens could enhance the MAC matrices by decreasing the elements other than the diagonal and increasing the diagonal elements of the MAC matrices and pushing them toward 1 (for example, compare Figures 5.2 (a) and (b)). It means that the updated mode shapes are closer to the real measured values by comparison with the old ones obtained before the updating while they also satisfy the 4<sup>th</sup> or 6<sup>th</sup> order problems. In fact, at the first step, the hierarchical functions could provide reliable modelings of the problems, and they were so help-

ful in presenting the approach with the required formulations, but in practice, such modelings are not enough for precise vibroacoustic predictions, and the updating procedures based on real data are required, which can enhance the modeling and its corresponding parameters, and move the models towards the reality. Herein, the MAC shows such achievement in bringing modeling to reality.

Consequently, based on Eq.(5.2.24), the updating approach will present the required corrections to the parameters identified by the IWC approach, and find the final updated parameters for each specimen. Table 5.3 has summarized the corrected values of the mechanical parameters.

In the above-mentioned procedures for identifying the parameters, we did not

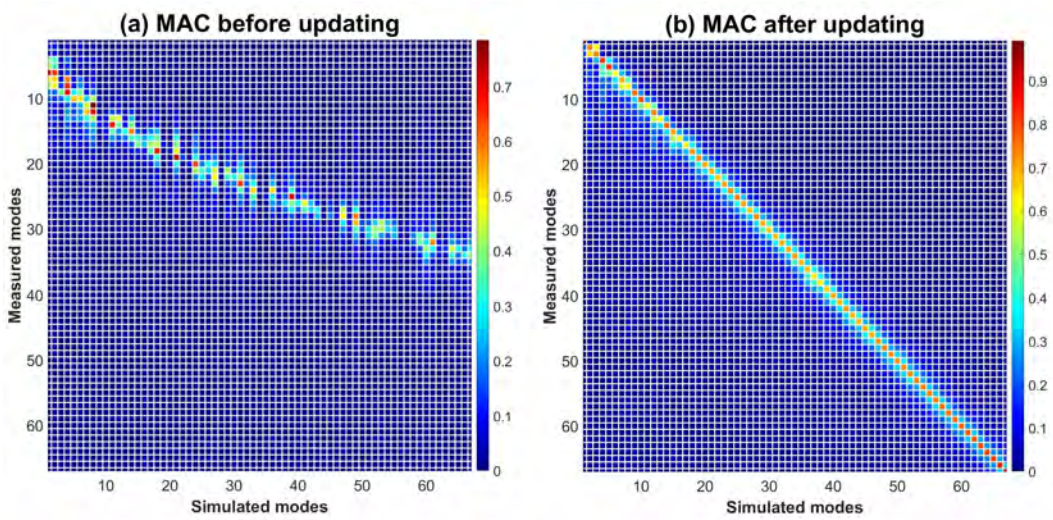


Figure 5.2: The MAC corresponding to the composite sandwich specimen: a) a view of the elements of the MAC matrix before the updating, and b) after the updating

use the initial information (Table 4.1) on the mechanical parameters. As mentioned before, we used this initial knowledge only for obtaining a prediction of the vibroacoustic behaviors of the specimens, and now these values can be helpful to have an independent assessment of the updated parameters. The presented approach only depends on the IWC approach for identifying the parameters before the model updating procedures. Comparing Table 5.3 and Table 4.1, we can realize that although the updated values and the initial values have been obtained independently, they are close to each other. For instance, the estimated total bending stiffness of the composite sandwich plate  $D_t = 1034\text{Nm}$  (see Table 5.3) implies that the Young modulus of the face sheet to be equal to  $153\text{GPa}$ . This value is in good agreement with the assessments of Qi et al. [2019] if the mechanical properties of the face sheet are approximated by a CFRP laminate with layout  $[0/90]$ . Qi et al. [2019] proposed a method for predicting the mechanical properties of CFRP based on cross-scale simu-



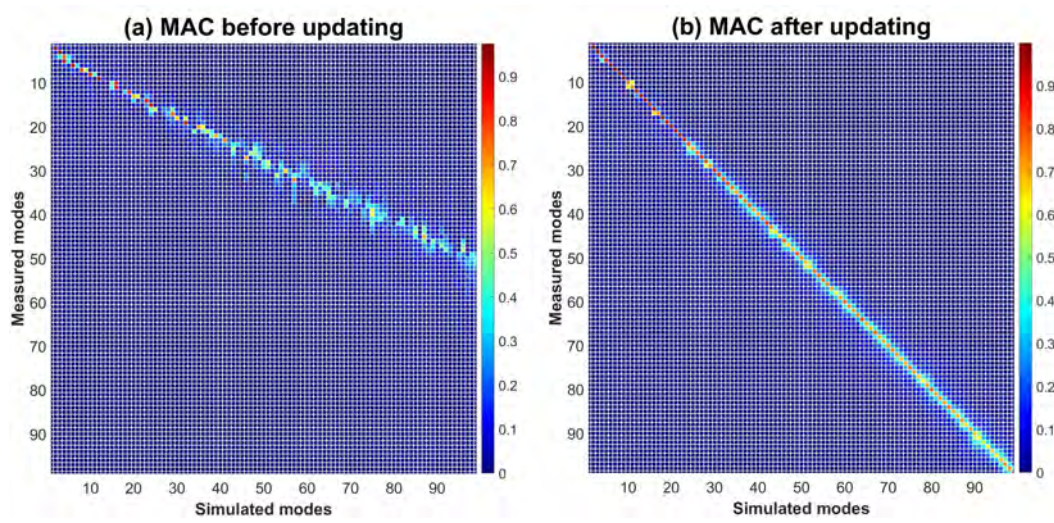


Figure 5.3: The MAC corresponding to the composite laminate specimen: a) a view of the elements of the MAC matrix before the updating, and b) after the updating

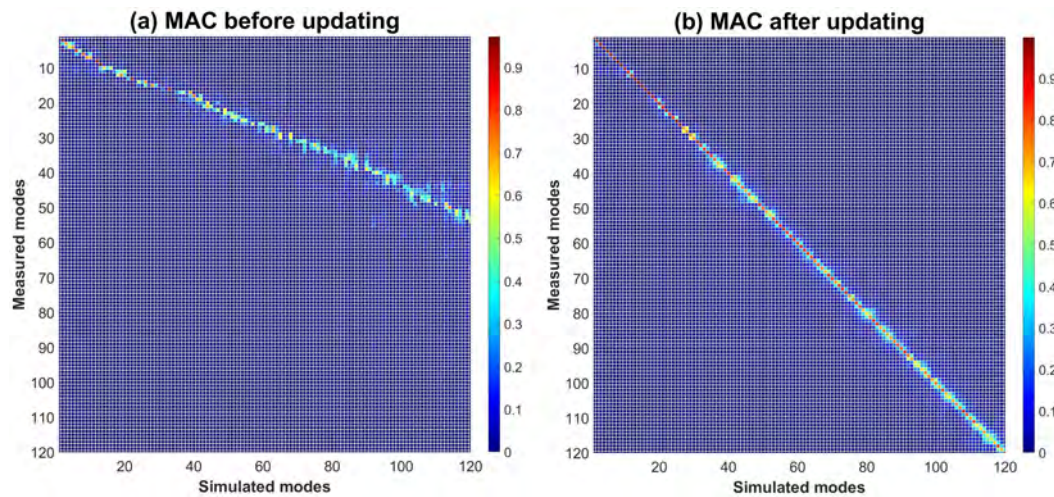


Figure 5.4: The MAC corresponding to the aluminium specimen: a) a view of the elements of the MAC matrix before the updating, and b) after the updating

lation. In this study, a series of experiments were performed in order to show that the results of the prediction approach and the experiments are in good agreement. The preliminary information on mechanical properties of the CFRP ply, summarized in Table 4.1, is based on this research. Moreover, considering this research, the values of the mechanical properties of the CFRP could present a prediction on the flexural bending stiffness coefficients of the laminate plate, too. For this purpose, considering the layout  $[(+45/-45/0/+90/0/+45/-45/0/+90/0/+45/-45)_2 0]_S$  for the composite laminate plate, and based on Eq.(4.2.1) and Table 4.1, the flexural bending stiff-

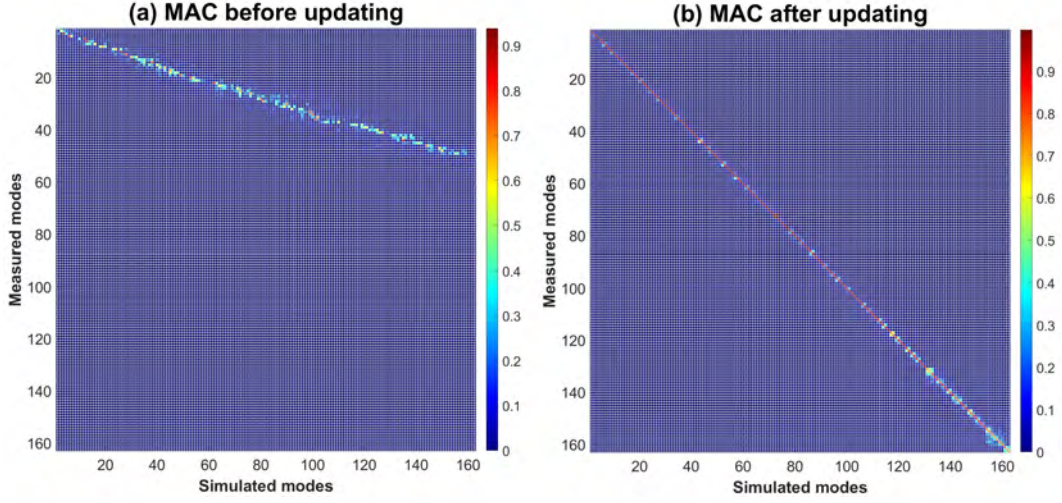


Figure 5.5: The MAC corresponding to the steel specimen: a) a view of the elements of the MAC matrix before the updating, and b) after the updating

Table 5.3: The updated mechanical properties of the composite sandwich, laminate, aluminium, and steel plates

Sandwich	Laminate	Aluminium	Steel
$D_t = 1034\text{Nm}$	$D_{11} = 274\text{Nm}, D_{22} = 126\text{Nm}$	$E = 74\text{GPa}$	$E = 202\text{GPa}$
$G_c = 71\text{MPa}$	$D_{12} + 2D_{66} = 182\text{Nm}$		

ness coefficients of the laminate were obtained as  $D_{11} = 237\text{Nm}$ ,  $D_{22} = 163\text{Nm}$ ,  $D_{12} = 72\text{Nm}$ , and  $D_{66} = 75\text{Nm}$ , which are in a good agreement with both the IWC results (cf. Table 5.2), and the updated parameters (Table 5.3). Furthermore, the Nomex core shear modulus, which is identified by the IWC approach and updated by the updating approach, is not far from the assessments of the studies carried out by Adams and Maheri [1993] and Zhou et al. [2021]. Table 4.1 includes an approximate prediction on the mechanical properties of Nomex honeycomb, based on the studies of Adams and Maheri [1993], and Zhou et al. [2021].

### 5.3.1 Vibroacoustic comparisons

For the vibroacoustic assessment of the proposed approach, we made two types of comparisons using vibration measurements (acquired by the LDV instrument), and SPL recorded by the microphone. Figure 5.6 illustrates a comparison between the average of the measured vibration field and the simulated one for the frequency interval [0Hz,3kHz]. In this figure, it is clearly seen that the updating procedures could

significantly enhance the simulations performed based on the sixth-order problem. In this figure, the agreement of the average value of the simulated vibration after updating with the actual value taken with the laser system is clearly evident. On the other hand, the disparity between the simulated values prior to the updating and the measured values may primarily be attributed to uncertainties in the initial values of mechanical parameters and the unknown intricacy of the boundary conditions, necessitating the usage of the updating method.

Moreover, according to these results, it is understood that the Root Mean Square (RMS) of the errors associated with the simulations in the two states after and before the updating for the composite panel was  $4.32 \times 10^{-7}\text{m}$  and  $2.44 \times 10^{-8}\text{m}$ , respectively, and this means that the updating method has the ability to improve the simulation by around 17.7 times from this point of view (herein, the simulation error is obtained from the difference between the simulation values and the values taken with the LDV system).

In addition, the same comparison between the sound pressure levels of the sounds radiated from the vibrating plate has been carried out. The SPL at a distance of 50cm from the middle point of the vibrating plates, has also been acquired for the additional assessment of the updating approach. The measured sound pressure spectrum was compared with the simulated ones. For simulating the SPL at an arbitrary distance from the vibrating plate in the semi-anechoic chamber, we used the modeled full-vibration field and the Rayleigh integration.

Also, the modal decomposition described in Chapter 2 is employed for modeling the velocity  $v = \omega w$ , and the displacement field  $w$  over the plate. For this purpose, the updated modes were used, and the frequency response could be obtained by the natural frequencies estimated by the Least-Squares Complex Exponential Method, introduced in Section 4.2.3. Besides, this method had the ability to present us with an average prediction on the loss damping factor  $\eta$  of the specimens. The least-squares complex exponential method can be utilized to analyze the frequency response function (FRF) of vibration obtained from the laser measurements. In fact, the least-squares complex exponential method applies the Prony's method to the FRF, which allows to fit a collection of complex damped exponential functions to the FRF, using a least squares optimization. The complex exponential functions represent the modes present in the FRF, and meanwhile, the poles of these complex damped exponential functions correspond to the complex frequencies at which the FRF exhibited decay and oscillation. By estimating the damping ratios using the complex frequencies, namely the poles, the loss damping factors can be determined too (see chapter 9.5 in He and Fu [2001]). Accordingly, the average loss damping factor for the composite sandwich, laminate, aluminium, and steel plates were equal

to 0.0916, 0.0451, 0.0158, and 0.0087, respectively. The range of these average values is consistent with prior research that has explored nearly related case studies regarding the loss damping factor (e.g., see Ghinet and Atalla [2011], Li and Narita [2013], Cherif et al. [2015], Sarlin et al. [2012]).

In addition, the measurements allowed for the calculation of modal density and modal overlap factor (MOF). Modal density was determined by counting the natural frequencies that were detected by the Least-Squares Complex Exponential Method. The MOF could also be calculated by incorporating the loss damping factor ( $\eta$ ) and the modal density ( $d$ ) for a given frequency ( $f$ ), resulting in the equation  $\text{MOF} = d\eta f$ . The findings revealed that the average modal densities for the composite sandwich, laminate, aluminium, and steel plates were 0.007, 0.01, 0.012, and 0.016, respectively. Correspondingly, the average MOF values were 3.07, 2.23, 0.95, and 0.71, respectively. As the investigation encompassed a wide frequency range, including high frequencies, it was anticipated the average MOF values would be high. Comparing these values with the average loss damping factor, it becomes evident that the modal overlap factor in the experiments was primarily influenced by the loss damping factor, rather than the modal density. Hence, amongst the specimens, the composite sandwich exhibited the highest MOF due to its superior loss damping factor (e.g., see Ege et al. [2009], Denis et al. [2014] for more information on MOF and its interpretation).

Consequently, Figure 5.7 shows the measured SPL spectrum and ones simulated before and after the updating for the composite sandwich plate. In Figure 5.7, especially in the zoom window for the frequency range of 0 to 2000 Hz, it is evident that the updated simulation is more consistent with the actual measurement acquired by the microphone. In other words, these SPL results also indicate the ability of the updating approach in improving the calculation associated with the 6<sup>th</sup> order problem of the sandwich panel.

Also, for the composite laminate specimen, similar vibroacoustic comparisons between the measurements and the simulated ones could be performed. Figures 5.8, and 5.9 show the comparisons corresponding to the average vibration field and the sound pressure level corresponding to the composite laminate panel, respectively. According to these figures, we can see the improvements in the simulations for both the vibration and the SPL after applying the updating procedures to the calculations. So, the vibration observations taken with the LDV system show how the RMS value of the simulation error in the state of applying the updating method compared to the state before applying the updating method has decreased from a value of  $3.37 \times 10^{-7}$  m to a value of  $1.16 \times 10^{-7}$  m, which shows that the modeling and simulation of vibration field for the laminate panel have improved by about 2.93

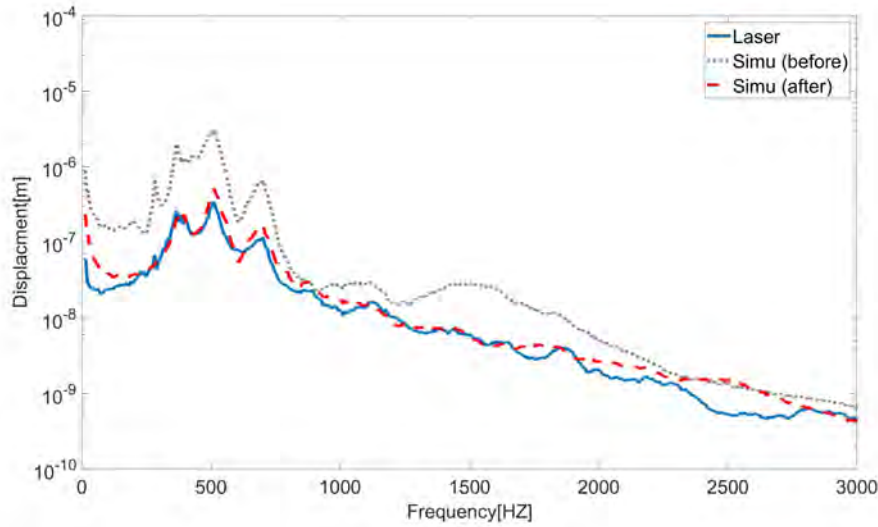


Figure 5.6: The average of the vibration field for the composite sandwich plate, measured by the LDV system (Laser), compared with the simulations done before and after the updating (Simu (before and after))

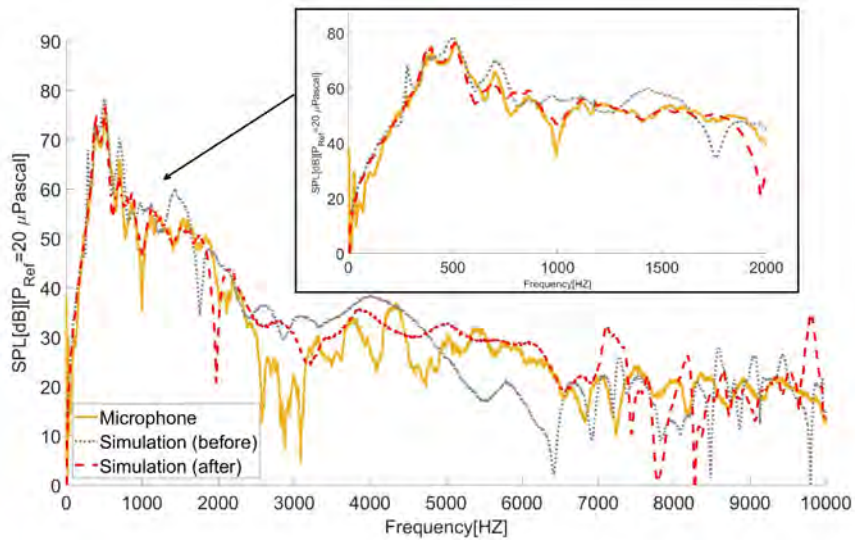


Figure 5.7: The SPL comparison corresponding to the composite sandwich plate, between the simulations (before and after updating) and microphone measurement; the small zoom window shows such SPL comparison for low frequencies

times from the point of view of the RMS errors.

Furthermore, for the other specimens, aluminium, and steel plates, we also carried out similar comparisons between the measurements and the simulated ones. As discussed before, the measurements associated with the aluminium and steel plates

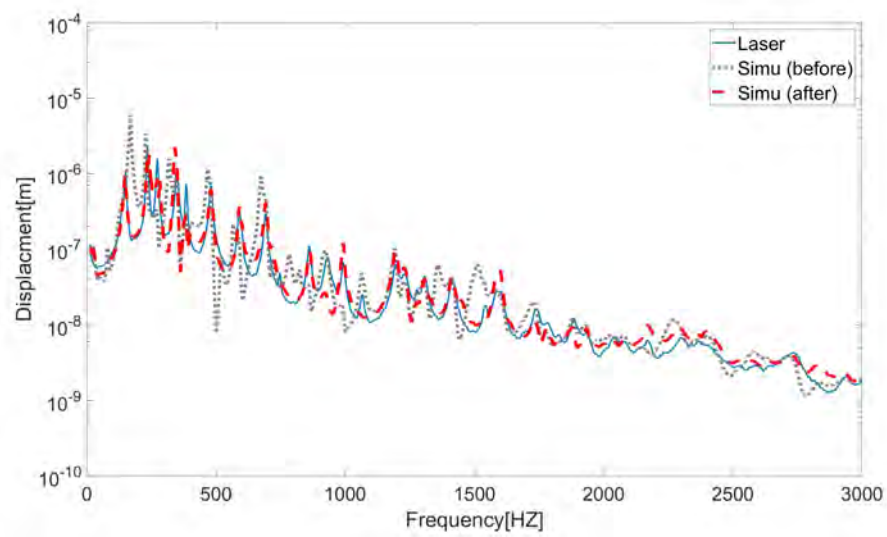


Figure 5.8: The average of the vibration field for the composite laminate plate, measured by the LDV system (Laser), compared with the simulations done before and after the updating (Simu (before and after))

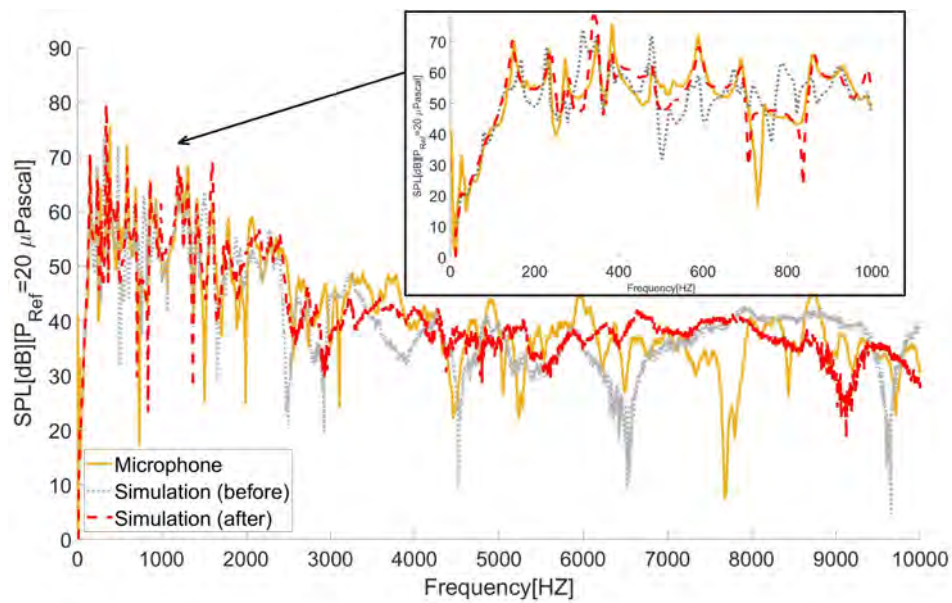


Figure 5.9: The SPL comparison corresponding to the composite laminate plate, between the simulations (before and after updating) and microphone measurement; the small zoom window shows such SPL comparison for low frequencies

have been performed as extra validations for the updating procedures associated with the 4<sup>th</sup> order problem. Figures 5.10, and 5.11 have summarized the comparisons corresponding to the average vibration field over the aluminium, and steel

plates, respectively, and also, Figures 5.12, and 5.13 illustrate the comparison of the SPL spectra for the frequency interval  $[0, 1000]$ Hz before and after the updating procedures. According to these figures, similar to the results of the composite panels (sandwich and laminate ones), we can see the enhancement in the simulations for both the vibration and the sound pressure levels. Based on the results obtained with the LDV (laser) system, the RMS of the simulation error in two states, before and after the updating, was obtained for the aluminum plate, respectively,  $5.30 \times 10^{-7}$ m and  $1.19 \times 10^{-7}$ m, and similarly, for the steel plate, the values of  $1.45 \times 10^{-6}$ m and  $4.47 \times 10^{-7}$ m were obtained, respectively. Therefore, this means that from the RMS point of view, the updating method has been able to enhance the modeling and simulation corresponding to the aluminum and steel plates by 4.46 and 3.25 times, respectively, which are actually the improvement to the model of the 4<sup>th</sup> order problem.

Moreover, Appendix B also contains additional results that demonstrate the effectiveness of the updating procedures in improving the simulations of the sound pressure level.

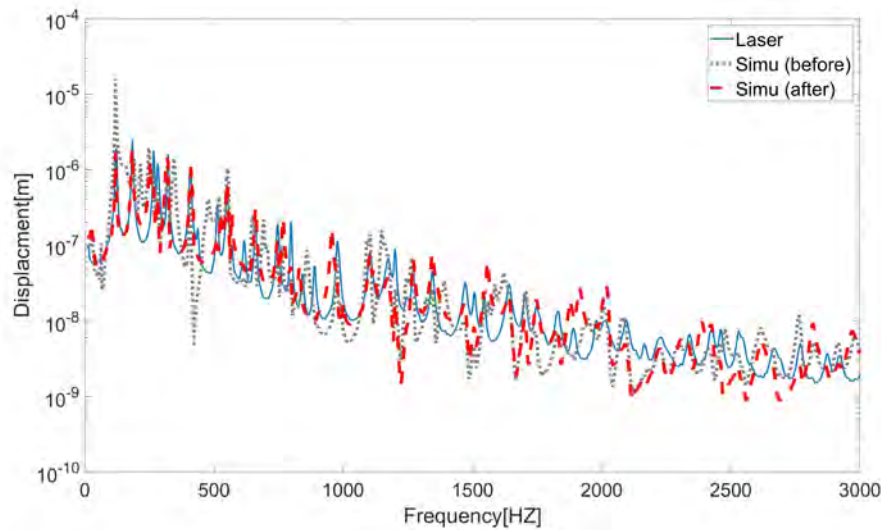


Figure 5.10: The average of the vibration field for the aluminium plate, measured by the LDV system (Laser), compared with the simulations done before and after the updating (Simu (before and after))

### 5.3.2 Discussion of results

The results were also consistent with previous research in which almost similar case studies were conducted. For example, in the numerical calculations, in order to

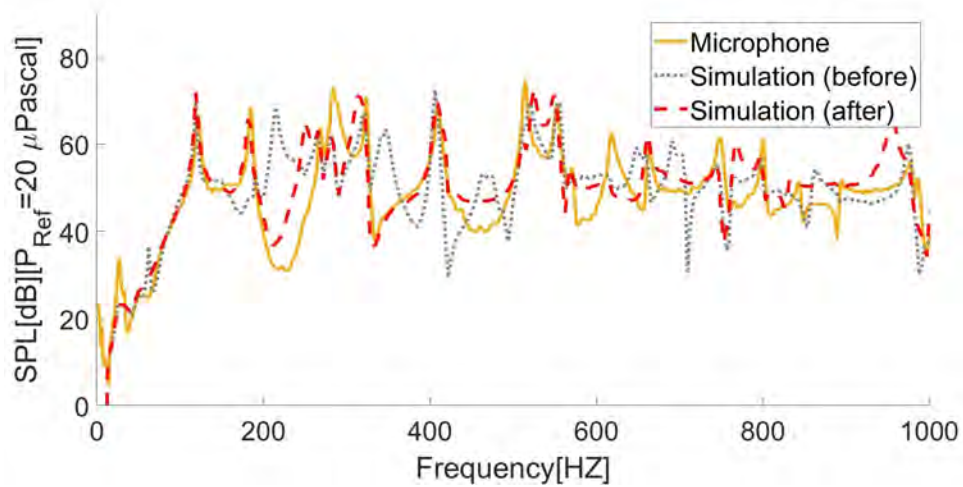


Figure 5.11: The SPL comparison corresponding to the aluminium plate, between the simulations (before and after updating) and microphone measurement

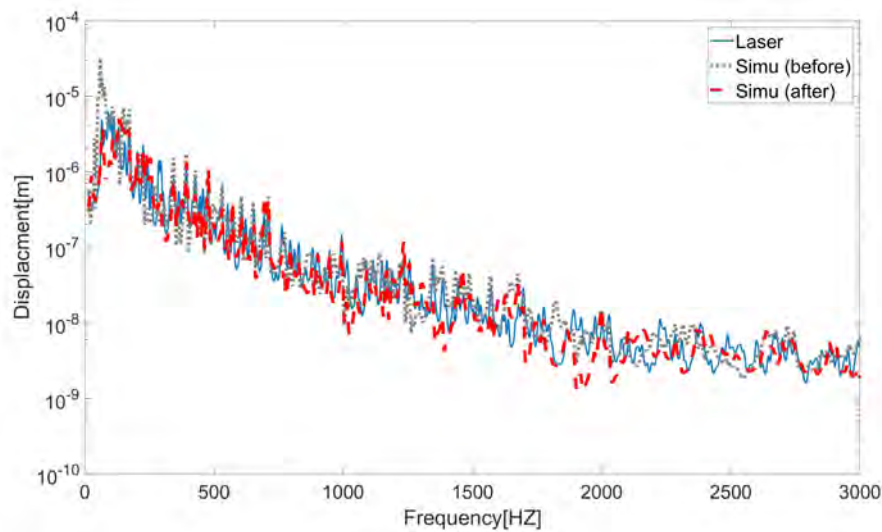


Figure 5.12: The average of the vibration field for the steel plate, measured by the LDV system (Laser), compared with the simulations done before and after the updating (Simu (before and after))

preliminarily have the mechanical properties of the composite sandwich and laminate specimens, the characteristics of the CFRP ply with epoxy matrix as well as the Nomex core were extracted from some previous studies such as Shahdin et al. [2011], Qi et al. [2019], Zhou et al. [2021], Adams and Maheri [1993], Zhou et al. [2021] (see Chapter 4). Then, at each stage, the calculated parameters were compared with these preliminary values. Of course, the final updated parameters, while



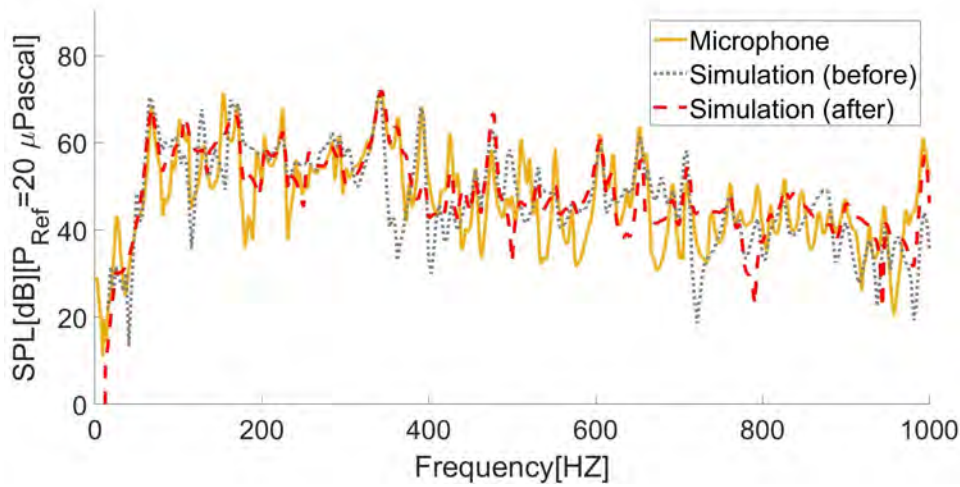


Figure 5.13: The SPL comparison corresponding to the steel plate, between the simulations (before and after updating) and microphone measurement

being close to such preliminary values, have also enhanced the vibroacoustic simulations. According to these results, the shear modulus of the Nomex core of the composite sandwich panel as one of the updated parameters was obtained at the IWC and final steps of the proposed hybrid approach, equal to 68MPa and 71MPa, respectively, which are close to the preliminary value obtained from the literature. Similarly, according to the previous studies on the mechanical properties of the CFRP ply with epoxy matrix, at first, the bending stiffness coefficients corresponding to the composite laminate and sandwich panel, could also be initially assessed via the classical laminate theory. Then the bending stiffness coefficients, obtained at the IWC and final steps, were able to show their good agreement with such preliminary assessment (cf. Table 1 in Chapter 4 and Tables 5.2 and 5.3).

## 5.4 Discussion and concluding remarks

In this Chapter, the study aimed to develop a hybrid updating approach adapted for the 4<sup>th</sup> and 6<sup>th</sup> order problems, required for the vibroacoustic modeling of composite panels. This approach is based on the hierarchical functions for analytically formulating the problems, IWC technique for the initial identification of parameters, and least squares optimizations including Baruch and total least squares method for updating models and parameters. The approach utilizes the IWC method, employing the 4<sup>th</sup> and 6<sup>th</sup> order dispersion relations for parameter identification. It follows the

model updating process via the Baruch method, which is fed with the parameters identified by the IWC. The hierarchical functions provide the models with analytical formulations facilitating the Baruch method, and the solutions provided by the Baruch method are used for finalizing the parameter updating process via the total least squares method. In fact, in the proposed hybrid approach, the methods are employed step by step, utilizing their respective capabilities in each stage to complement one another.

Herein, the main idea of the research was examined by laboratory experiments, including laser doppler vibrometry (LDV) measurements and sound recording for measuring spectra of sound pressure levels (SPL). The measurements were performed for some panels, including a composite sandwich panel, and a composite laminate one, as well as two isotropic plates for additional assessments. The efficiency of the method was attained through the progressive implementation of the proven capabilities of the aforementioned methods, where the progressive implementation facilitated the controlled evaluation of parameters, and avoided any time-consuming trial and error procedures. It was examined by different vibroacoustic comparisons between the measurements and the simulations enjoying updated parameters. The LDV measurements indicated the ability of the approach in enhancing the simulations for modeling the vibration field. Furthermore, the comparison associated with the measured SPL spectra could experimentally validate the accuracy of the simulated vibration. Such ability of the updating method in the precise modeling of the SPL can also be beneficial for the vibroacoustic modeling required in future perceptual assessment, which is one of the future goals of this research, too.

Moreover, the improvement of the Modal Assurance Criterion (MAC) can also be mentioned as one of the numerical achievements. The proposed method could significantly enhance the cross MAC between the calculated and measured modes.

Accordingly, the study successfully attained a high level of agreement among all the collected data, which encompassed laboratory vibroacoustic measurements, mathematical simulations enhanced through updating procedures, and preliminary information on mechanical parameters. This consistency serves as evidence of the capabilities of the proposed hybrid approach for model and parameter updating, particularly in addressing 4th and 6th order problems, with a specific focus on thin and thick composite panels. These findings hold significant promise for conducting accurate simulations essential to the integrated vibroacoustic and psychoacoustic design of composite panels in other phases of the thesis. The next chapter is devoted to the perceptual assessment of the simulations and the models employed.



# Chapter 6

## Perceptual assessment

### 6.1 Introduction

In this chapter, the focus has been seeking to assess the synthesized sounds and the accurate model of the vibrating panels from a perceptual point of view. A series of psychoacoustic laboratory experiments were conducted on various panels made from different materials (including a composite Nomex-core sandwich, a CFRP laminate, and an aluminium composite plate as well as steel and aluminium isotropic plates for additional validations). The psychoacoustic test including three sessions was performed for 40 participants from 18 to 61 years old. The corresponding analyses were carried out to validate the models from a perceptual perspective. The modeling and simulations were confirmed by psychoacoustic analyses, highlighting the potential usefulness of considering both vibroacoustic and psychoacoustic perspectives for designing composite panels.

Psychoacoustic tests are counted as a crucial tools used in research associated with the field of auditory perception to know how humans perceive and process sounds. One common research target in the psychoacoustic tests is to find the dissimilarities (or similarities) between paired sounds, which can present us with insights into auditory discrimination and perception. Although psychoacoustic investigations on composite panels have often been overlooked in recent studies, certain research on psychoacoustic assessments of other mechanical structures like isotropic panels can be found in the literature, see Chapter 1. Continuing the previous studies, in the current chapter we aimed at presenting auditory evaluation of the simulations stemming from the vibroacoustic modeling of composite panels for design optimization purposes. Herein, the research considers perceptual assessment in addition to the conventional vibroacoustic assessments. This viewpoint on the problem can assist

us in having an accurate understanding of composite panels from a psychoacoustic point of view and human acoustic comfort.

## 6.2 Psychoacoustic test

### 6.2.1 Participants

In the psychoacoustic test, 40 participants, comprising 23 females and 17 males aged between 18 to 61, took part in the auditory evaluation. The participants' age had an average of 28.9 years and a standard deviation of 12.8 years. The participants were students and staff of ENTPE. Also, all the participants were paid for participating in the psychoacoustic experiments. They all declared normal hearing abilities, and signed a written consent before the experiment.

### 6.2.2 Apparatus

The audio signals were played back using Sennheiser HD600 open-back headphones and a high-quality LynxTWO sound card. The test took place in a quiet room, located in the experimental villa at ENTPE's campus, with a background noise level of 24 dB(A), where participants engaged with a computer interface. The computer interface was developed in the MATLAB environment and used for stimulus presentation and response entry. This interface provides guidance to participants throughout the test and allows for the recording of responses. Before the test, a Cortex Manikin MK2 was utilized for recording the sounds and checking the sound pressure levels of the stimuli expected to be heard by participants (cf. Table 6.1). The resulting audio files were post-processed using dBsonic software. Figure 6.1 shows the Cortex Manikin MK2.

### 6.2.3 Stimuli

Considering laboratory measurements carried out in the previous chapters, herein, psychoacoustic test was conducted across three sessions. Session 1 focused on evaluating sounds from plates excited with a mechanical load, while Session 2 considered sounds from plates excited with diffuse acoustic field (DAF) (hereafter simply called acoustic excitation). Finally, Session 3 aimed to look at the optimal value of the maximum frequency in modeling from the perceptual point of view. In the first



Figure 6.1: The Cortex Manikin MK2 used before the psychoacoustic test. Before conducting the test, it was necessary to measure the sound pressure level, expected to be heard by participants, by means of the Cortex Manikin MK2

session, 8 stimuli were considered, obtained both from recordings and simulations for steel, aluminum, composite laminate, and composite sandwich plates under the mechanical excitation (see the SPL spectra corresponding to these stimuli in Figures 5.7 to 5.13 in Chapter 5). In Session 2, 6 stimuli were considered, obtained from recordings and simulations for the aluminum, steel, and composite aluminum plates under acoustic excitation (see the SPL spectra corresponding to these stimuli in Figures 3.9 to 3.11 in Chapter 3).

Additionally, Session 3 was designed with 7 stimuli for finding the optimal value for the maximum frequency. Based on the simulation of the composite sandwich panel excited by the mechanical excitation (see Figure 5.7 in Chapter 5), the set of seven stimuli was generated using cutoff frequencies at 2 kHz, 3 kHz, 4 kHz, 5 kHz, 6 kHz, and 7 kHz. This selection aimed to assess the most suitable maximum frequency from a perceptual point of view. Knowledge of this maximum frequency was essential for the accurate execution of the simulations. The duration of each stimulus in all the sessions was 3 seconds, and after adjusting the stimulus sound pressure level for the listening test, the average sound pressure level ranged between 57.8 and 60.3 dB(A).

In all the computations for synthesizing the sounds, the frequency step has been set at 3.125Hz for Session 1 (mechanical excitation), 1Hz for Session 2 (acoustic excitation), and 3.125Hz for Session 3 (cutoff frequency). For Sessions 1 and 3, the chosen frequency step matches the resolution of the laser measurements performed by the

Table 6.1: The stimuli used in the psychoacoustic test, including the simulated sounds and ones recorded during the vibroacoustic laboratory experiments

<i>Session</i>	<i>Sound No.</i>	<i>Material</i>	<i>Excitation</i>	<i>Status</i>	<i>SPL [dB(A)]</i>
<b>Session 1</b>	<b>1</b>	Steel	Mechanical	Recorded	59.7
	<b>2</b>	Aluminium	Mechanical	Recorded	59
	<b>3</b>	Composite Laminate	Mechanical	Recorded	58.3
	<b>4</b>	Composite Sandwich	Mechanical	Recorded	59.5
	<b>5</b>	Steel	Mechanical	Simulated	60.3
	<b>6</b>	Aluminium	Mechanical	Simulated	58.8
	<b>7</b>	Composite Laminate	Mechanical	Simulated	58.9
	<b>8</b>	Composite Sandwich	Mechanical	Simulated	59.4
<b>Session 2</b>	<b>1</b>	Steel	Acoustic	Recorded	58.8
	<b>2</b>	Aluminium	Acoustic	Recorded	59.4
	<b>3</b>	Composite Aluminium	Acoustic	Recorded	57.8
	<b>4</b>	Steel	Acoustic	Simulated	58.3
	<b>5</b>	Aluminium	Acoustic	Simulated	59.1
	<b>6</b>	Composite Aluminium	Acoustic	Simulated	59.1
<b>Session 3</b>	<b>1</b>	Composite Sandwich	Mechanical	Simulated	59.4
	<b>2</b>	Composite Sandwich	Mechanical	Simulated	59.8
	<b>3</b>	Composite Sandwich	Mechanical	Simulated	59.4
	<b>4</b>	Composite Sandwich	Mechanical	Simulated	59.7
	<b>5</b>	Composite Sandwich	Mechanical	Simulated	58.4
	<b>6</b>	Composite Sandwich	Mechanical	Simulated	58.3
	<b>7</b>	Composite Sandwich	Mechanical	Simulated	59.3

LDV system, as detailed in Section 4.2.3. In the case of Session 2, a 1Hz-frequency step was selected to provide sufficient resolution for computing the Sound Pressure Level (SPL) while minimizing computation time. Moreover, the maximum frequency considered in all computations was 10kHz, except for certain stimuli in Session 3, where we examined various values of cutoff frequency and aimed to perceptually determine the optimal maximum frequency value for the simulations. The upper limit of 10 KHz was fixed by observing the energy decrease at high frequencies from the sound pressure level spectra of the different recordings.

## 6.2.4 Method

The listening test procedure used here was based on a paired-comparison method, designed by Faure [2003], Trollé [2009], and it has been followed with certain modifications. In numerous studies focused on the sound quality of industrial products, a perceptual space is established through dissimilarity comparison between on pairs of stimuli. It is highly discriminating, but a drawback of this approach is its potential for significant time consumption when dealing with a large number of stimuli, e.g., see Chevret and Parizet [2007], Parizet and Koehl [2012], Michaud et al.

[2013]. Several studies have explored alternative methods for assessing dissimilarity (or similarity) between stimuli, especially in cases where a larger number of stimuli are present in each session (e.g. see Chevret and Parizet [2007], Parizet and Koehl [2012], Michaud et al. [2013]). In contrast to these studies, the current research involves a smaller number of stimuli (c.f. Michaud et al. [2013] and Table 6.1). Furthermore, although studies on alternative methods often emphasize the primary limitation of the paired comparison method, namely its relatively slow test execution, they commonly validate their findings by comparing themselves with outcomes obtained from the paired comparison method due to its high discriminative capability (e.g. see Chevret and Parizet [2007], Michaud et al. [2013]).

Hence, as shown in Table 6.1, the number of stimuli per session was not big. Therefore, the paired comparison technique enabled us to capture all conceivable dissimilarity judgments among the stimuli without imposing excessive fatigue on the participants. Throughout the experiment, including the instruction, training, and all dissimilarity judgments across the three test sessions, the average time spent per participant was 45 minutes. The training part preceding each session was organized based on three distinct stimuli chosen from all the stimuli available at each session. These stimuli were selected by the author and the thesis supervisors. Furthermore, the sequence in which pairs of sounds are presented, as well as the arrangement of sounds within each pair, are randomized for each participant, ensuring that the order of presentation does not introduce bias. Moreover, the sessions were presented to the participants in a random order to avoid any methodological bias when investigating the effects of excitation type and maximum frequency. Accordingly, the method allowed for the listening test, and its detailed methodology is summarized as follows:

- Prior to sessions, detailed instruction was presented on the screen (see Figure 6.2)
- A training part familiarized participants with the sounds being tested before each session, to help them learn the test steps, understand the interface and response scale dynamics
- The full test for each session began after the completion of its training part; during each training, participants were exposed to a varied sample of paired stimuli specific to the session
- Each stimulus was played for 3 seconds, with a pause of 0.5 seconds between the paired stimuli



- The participants listened to pairs of sounds and were asked to judge the difference between sounds of each pair; participants could re-listen to the sounds of each pair as many times as they needed
- The participants were presented with the question, "How do you judge the sounds?" and asked to rate and provide dissimilarity judgments using a continuous numerical scale that ranges from 0 to 10. Verbal descriptors, such as "Very similar" for 0 and "Very different" for 10, are associated with the endpoints of the scale, see Figure 6.3
- The interface collected the participant's dissimilarity judgments on the stimuli
- A separate folder was created for each participant and all the data during the experiment, including all the dissimilarity matrices and the required variables, are stored in the corresponding folder

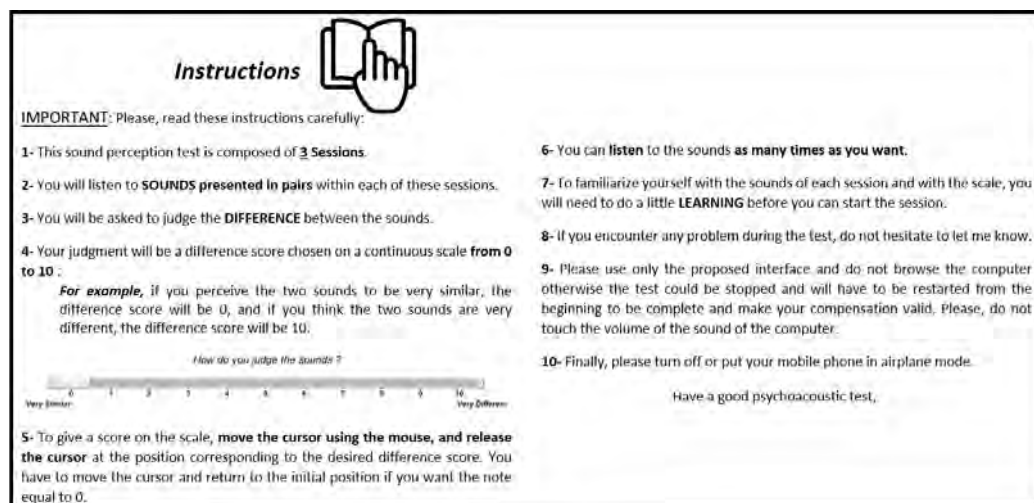


Figure 6.2: The first screen of the interface prompts participants to read the instruction for the test. Although the interface was designed in a way that is user-friendly and easy to understand for all the participants, before each test it was necessary to give the participants general tips about the test

### 6.2.5 Preparing sound files

The signals were previously encoded in WAV format with a 16-bit resolution using Matlab. The amplitude values were coded in the range of  $[-1, +1]$  using 16-bit coding, which provided a total of  $2^{16}$  possible amplitude values. To maintain the relative level differences between the signals while optimizing the coding, the pressure

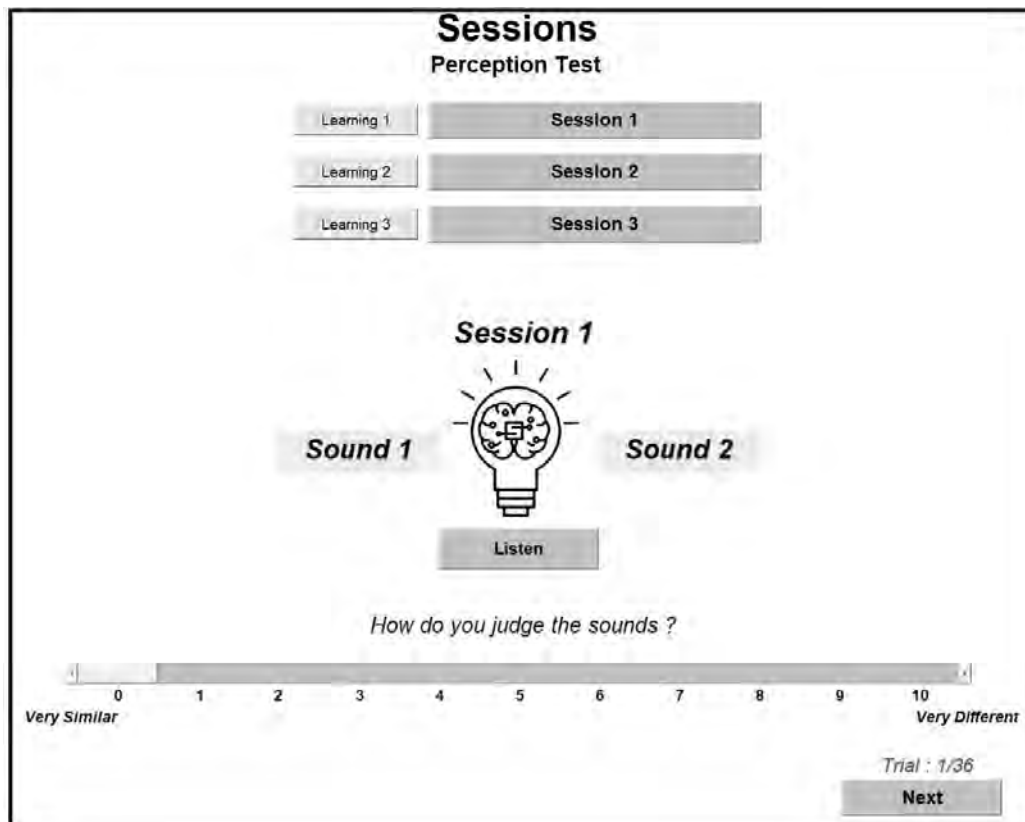


Figure 6.3: An screenshot of the interface presenting a listening panel for the three sessions accompanied by their learning (training) parts, which allowed participants to listen the paired sounds (paired stimuli) as many times as they want, and compare the sounds based on their dissimilarities

values of each signal were divided by the maximum value detected across all the corrected signals immediately before encoding. Also, to create sound stimuli for auditory assessment, recorded or simulated sound sequences were converted into short stereophonic samples lasting three seconds for the left and right channels. To avoid clicks caused by non-zero pressure values during playback, each sample was subject to a fade-in and a fade-out of 0.1s at the beginning and end, respectively. The fade-in and fade-out were used to ensure that stimuli are presented to the participants in a consistent and controlled way and that each participant hears the entire stimulus.

## 6.3 Results

### 6.3.1 Classification of participants

Clustering and dendrograms are helpful tools to identify outliers in the dataset acquired via the participants. Outliers are data points that differ significantly from the rest of the dataset and can affect the results of the analysis (e.g. see Hodge and Austin [2004]). Outliers can be identified as points that do not belong to any of the clusters or belong to small, isolated clusters, which can be located at the bottom of the dendrogram and have a long branch length or high dissimilarity score compared to other points.

The main objective of clustering is to detect the presence of participants who display abnormality in their listening and judging abilities throughout the entire test. Herein, to conduct the clustering analysis of the participants, we utilized the Ascending Hierarchical Classification (AHC) method. AHC enabled us to create a hierarchical indexed tree, i.e. the dendrogram. The dendrogram represents a nested classification system that becomes more heterogeneous as the size of the classes increases Gordon [1999]. The detailed stages of the participant clustering have been designed by Faure [2003] and Trollé [2009], and in the following, a summary of the steps taken in this study has been described.

In brief, in order to perform the AHC method resulting in the dendrogram and clustering, the dissimilarities between the participants were required to be estimated. To calculate the dissimilarities between participants, their responses to different pairs of stimuli were analyzed. To accomplish this, the measure  $d(i, j)$  was used to quantify the dissimilarity between two participants  $i$  and  $j$  as follows Trollé [2009]:

$$d(i, j) = 1 - r(i, j) \quad (6.3.1)$$

where  $r(i, j)$  is the linear Bravais-Pearson correlation coefficient between the dissimilarity scores noted by the two participants  $i$  and  $j$ . The dissimilarity index  $d(i, j)$  was calculated for all pairs of participants  $(k, l)$  and then respectively reported in a symmetric matrix  $D$ .

Initially, the number of classes is equal to the number of participants, which are the terminal elements of the dendrogram. The terminal elements refer to the individual participants or data points that are being clustered. These are the lowest-level elements in the hierarchy of the clustering, and they are represented as the leaves or endpoints of the branches on the dendrogram. Through an algorithmic process, the classification identifies the two participants with the closest dissimilarity measure

and merges them into a new class. This results in two branches starting from the two terminal elements and converging into a knot on the dendrogram. The dissimilarities between the newly formed class and the remaining participants are updated using an aggregation criterion. The process is repeated until all the participants are aggregated into a single class, which produces a matrix of dissimilarities between participants called ultrametric distances. These distances represent the levels of aggregation of the different classes and are plotted along the ordinate on the dendrogram (e.g. see Gordon [1999]).

Moreover, herein, a series of aggregation methods including Single linkage, Complete linkage, Average linkage, Weighted linkage, Centroid linkage, Median linkage, and Ward linkage, used in clustering or data analysis, has been examined. The Single linkage method, referred to as the nearest neighbor method, uses the smallest distance between objects in the two clusters. The Complete linkage criterion, known as the farthest neighbor approach, utilizes the largest distance between objects in the two clusters. The Average linkage method calculates the average distance between all pairs of objects in any two clusters. The Centroid linkage method employs the Euclidean distance between the centroids of the two clusters while the Median linkage method uses the Euclidean distance between the weighted centroids of the two clusters. The Weighted average linkage recursively defines the distance between two clusters by averaging the distance between one cluster and a second cluster's components (i.e. the Weighted average method uses a recursive definition for the distance between two clusters, for example, if cluster 1 was produced by merging two clusters  $m$  and  $n$ , the distance between 1 and another cluster like 2 is defined as the average of the distance between the clusters  $m$  and 2 and the distance between the clusters  $n$  and 2). The Ward's linkage criterion is defined as the incremental sum of squares, that is, the increase in the total within-cluster sum of squares as a result of joining two clusters (e.g. see Ferreira and Hitchcock [2009]).

In addition, the analysis considers a final criterion that measures the degree of adequacy between the calculated ultrametric distances and original dissimilarities between the participants. The level of adequacy is quantified using two coefficients, the cophenetic correlation coefficient and the Goodman-Kruskal coefficient, both of which measure how well the calculated ultrametric distances match the original dissimilarities, e.g. see Sokal and Rohlf [1962], Farris [1969], Goodman et al. [1979]. As seen from Table 6.2, for the three sessions of the test, the average linkage method among all the aggregation methods has the highest values of the cophenetic and Goodman-Kruskal correlation coefficients. Therefore, herein it was recommended to use the average linkage method for the classification process.

So, based on the average linkage method the aggregation was performed and the

dendrogram associated with the clustering was achieved from data of each session. The dendrogram offers numerous partitioning options that range from the finest score, consisting of as many classes as participants, to the most coarse score, which comprises a single class containing all the participants. To determine the optimal number of classes  $m$ , a quality index is calculated for each partition with a varying number of classes. The quality index is defined as follows (e.g. see Nakache and Confais [2004], Trollé [2009]):

$$Q(m) = \frac{1}{P} \sum_{k=1}^m n_k s_k \quad (6.3.2)$$

where  $Q(m)$  represents the quality index of a partition with  $m$  classes, with a value between 0 and 1.  $P$  represents the total number of participants,  $n_k$  represents the number of participants in class  $C_k$ , and  $s_k$  represents the average silhouette value in class  $C_k$ . The silhouette value  $s_k$  for a participant  $k$  provides insight into the quality of its classification. In fact, the silhouette value of a participant is a measure of how well it is classified relative to the other participants in its class and to the participants in the closest neighboring class. Hence, it is a numerical indicator of the quality of a participant's classification, which is calculated by dividing the average distance between participant  $k$  and all other participants in the same class by the average distance between participant  $k$  and the participants in the closest class. Hence, the optimal number of classes is the one that displays a first peak on the quality index curve with respect to the minimum number of classes  $m$ .

Consequently, outliers participants can be identified by the dendograms. Hence, as it is clear from the dendograms of all sessions (see Figures 6.4, 6.6, and 6.8), one of the participants (participant number 40) is separate from all other participants in all the clustering dendograms and is placed in a separate cluster. This shows that the responses of this participant to the stimuli are significantly different from those of other participants. Moreover, as can be seen from the figures related to the Silhouette values (see Figures 6.5, 6.7, and 6.9), the high Silhouette values for the number of classes 2 shows the high quality of classification with this number of classes in all the sessions. In these figures, each column corresponds to a specific number of classes, and distinct colors within each column represent individual classes. The length of each segment indicates the weighted Silhouette values associated with its respective class. For example, as illustrated in Figures 6.5, 6.7, and 6.9, when the number of classes is set to 2, two distinct colors are used to represent these two classes. Notably, the class represented by the color blue exhibits the highest weighted Silhouette value among all the classes. Accordingly, one participant (the participant with number 40) was designed as an outlier participant and removed from the relevant analyses.

Table 6.2: The series of aggregation methods, and the quantified level of adequacy, used for the three Sessions, corresponding to the stimuli produced with a mechanical excitation in Session 1, with an acoustic excitation in Session 2, and with different cutoff frequency values in Session 3

Methods	Session 1 (Mechanical)		Session 2 (Acoustic)		Session 3 (cutoff Freq)	
	Cophenetic	Goodman-Kruskal	Cophenetic	Goodman-Kruskal	Cophenetic	Goodman-Kruskal
Single	0.46	0.30	0.72	0.60	0.65	0.49
Complete	0.59	0.57	0.56	0.50	0.56	0.53
<b>Average</b>	<b>0.69</b>	<b>0.66</b>	<b>0.79</b>	<b>0.75</b>	<b>0.70</b>	<b>0.63</b>
Weighted	0.58	0.53	0.55	0.54	0.51	0.48
Centroid	0.65	0.62	0.79	0.73	0.71	0.62
Median	0.59	0.49	0.52	0.50	0.55	0.58
Ward	0.57	0.58	0.59	0.55	0.49	0.48

Furthermore, we repeated the aggregation and classification of the participants using the Centroid linkage method as well. This was because the results obtained from this aggregation method were somewhat comparable to those of the average method, particularly for Session 3 (see Table 6.2). Similarly, the classification results obtained through the Centroid linkage method confirmed the findings from the average linkage method, and it also identified the 40th participant as an outlier amongst the others.

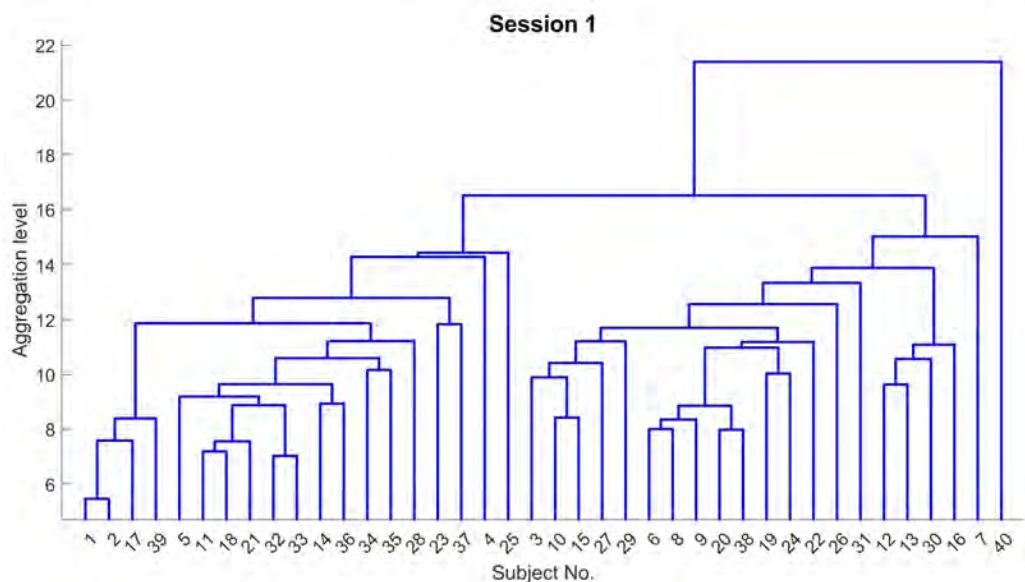


Figure 6.4: The Dendrogram associated with the classification of participants and outlier detection in Session 1 associated with the stimuli produced by the mechanical excitation

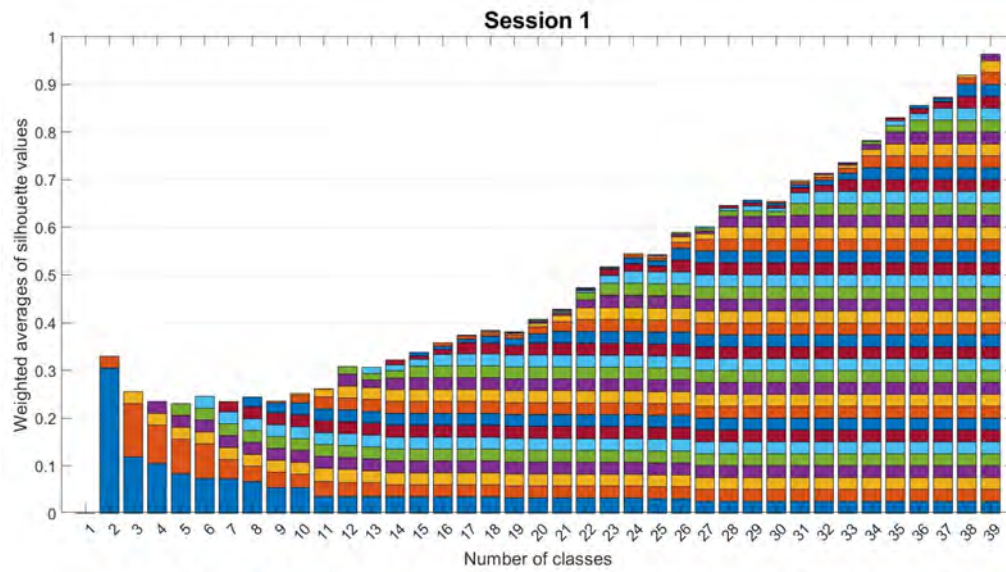


Figure 6.5: Weighted Silhouette values corresponding to the different classes of the participants in Session 1 associated with the stimuli produced by the mechanical excitation

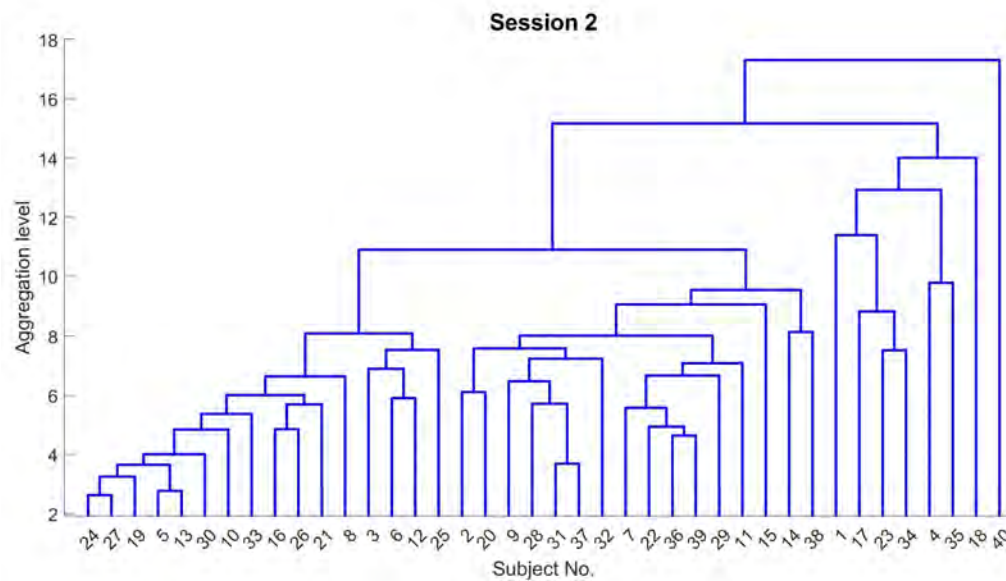


Figure 6.6: The Dendrogram associated with the classification of participants and outlier detection in Session 2 associated with the stimuli produced by the acoustic excitation

### 6.3.2 Multidimensional scaling technique

Following the completion of the clustering analysis of the participants and identification of any outliers within the participants, we proceeded with the analysis of dissimilarity judgments. To establish the perceptual space of dissimilarity and ac-

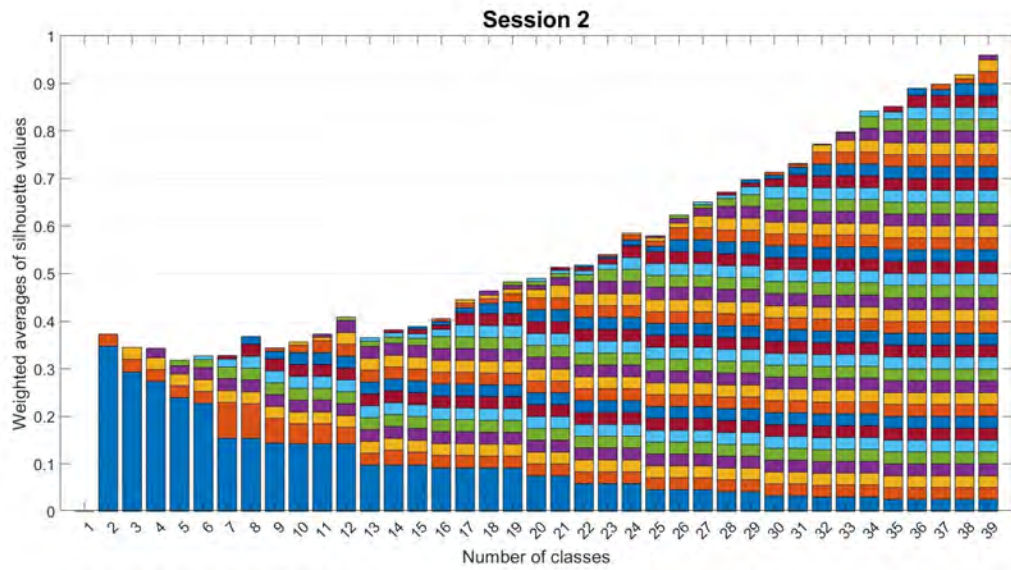


Figure 6.7: Weighted Silhouette values corresponding to the different classes of the participants in Session 2 associated with the stimuli produced by the acoustic excitation

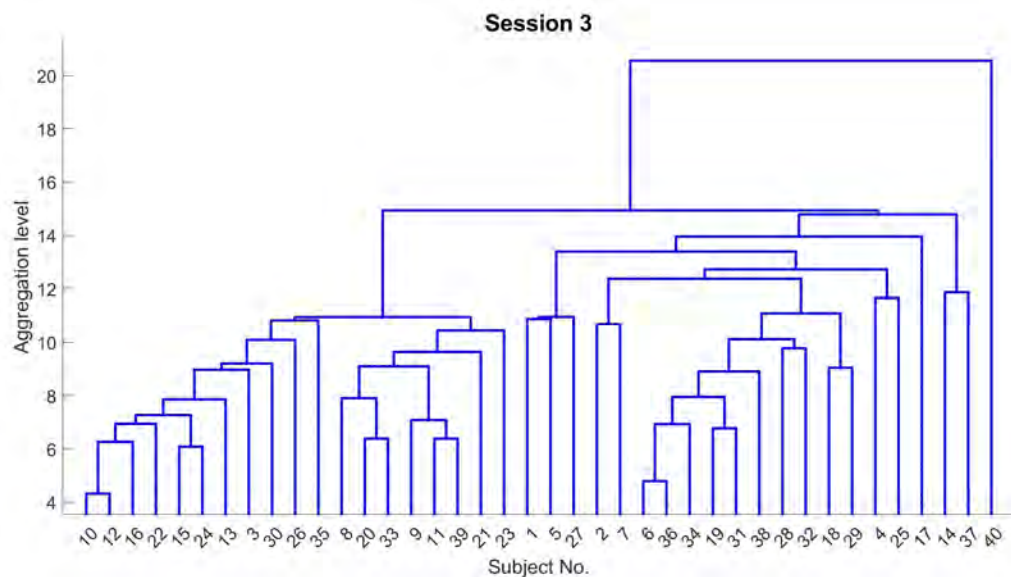


Figure 6.8: The Dendrogram associated with the classification of participants and outlier detection in Session 3 associated with the simulated stimuli filtered with different values of the cutoff frequency

count for the perceived distances between stimuli, we utilized the multidimensional scaling technique. Multidimensional scaling (MDS) is a statistical technique used to visualize the similarity or dissimilarity among a set of objects or items (e.g. see Carroll and Arabie [1998]). It attempts to find a low-dimensional representation of the



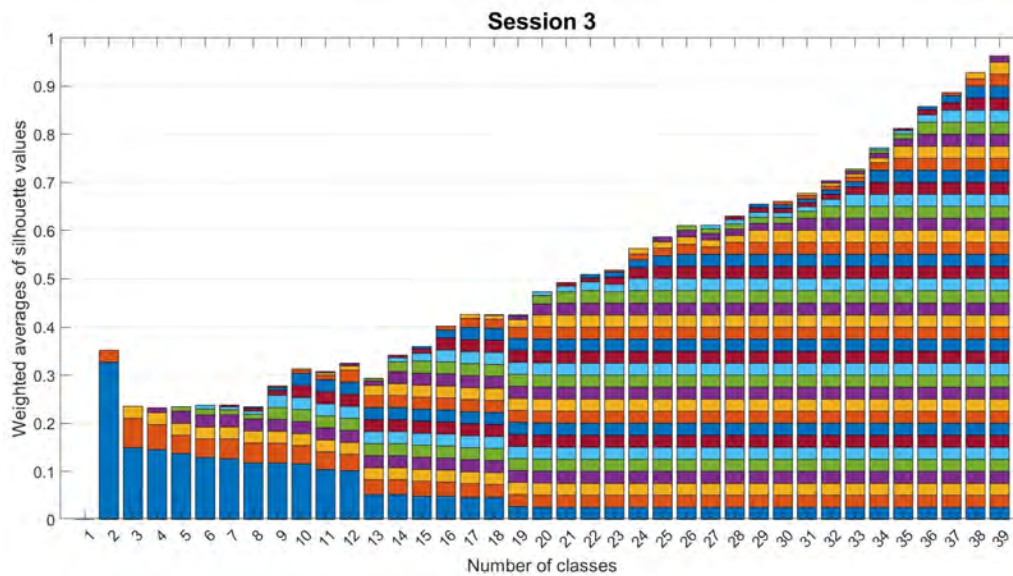


Figure 6.9: Weighted Silhouette values corresponding to the different classes of the participants in Session 3 associated with the simulated stimuli filtered with different values of the cutoff frequency

objects (i.e. stimuli) in a high-dimensional space based on their pairwise similarity or dissimilarity that can be obtained by human-based experiments. MDS algorithms can be used for exploratory data analysis, to visualize the structure of data, and identify clusters or patterns of stimuli. It can also be used as a confirmatory tool, to test hypotheses about the structure of the data or to compare the similarity structures of different datasets associated with the stimuli, and so, can provide us with valuable insights into the underlying patterns and relationships among a set of stimuli. Hence, an MDS algorithm takes a distance matrix containing the distances between every pair of stimuli in a set (which, herein, was obtained via the psychoacoustic test), along with a user-defined number of dimensions,  $N$ . The algorithm then positions each stimulus in  $N$ -dimensional space, creating a lower-dimensional representation of the perceptual space (e.g. see Carroll and Arabie [1998], Eom [2009], Borg et al. [2012]).

### Individual Differences Scaling (INDSCAL)

INDSCAL, standing for Individual Differences Scaling, is an MDS algorithm used in various fields like psychometrics, psychophysics, and psycho-mathematics to quantitatively analyze the relationships between multiple variables, specifically those that involve ratings or judgments made by individuals and participants (see Carroll and

Chang [1970], Carroll [1972], Carroll and Arabie [1998], Borg and Groenen [2005]). The primary goal of INDSCAL is to identify the underlying dimensions or coordinates of the stimuli in the perceptual space that explain the patterns of correlations or similarities between the ratings made by different individuals. These dimensions or coordinates can be interpreted as the psychological or cognitive processes that influence the ratings (for example, in the current study, the perceptual dimensions and coordinates are related to auditory attributes that influenced the ratings made by the participants). INDSCAL can be applied to different types of data, such as dissimilarity (or similarity) judgments between different stimuli. This method assumes that the dissimilarity distance between stimuli  $j$  and  $k$  for participant  $i$ ,  $d_{jk}^i$ , is related to the dimensions of the perceptual space by the following equation Carroll and Arabie [1998] :

$$d_{jk}^i = \left[ \sum_{n=1}^N w_n^i (x_{jn} - x_{kn})^2 \right]^{\frac{1}{2}} \quad (6.3.3)$$

The above equation represents a weighted version of the Euclidean distance formula, where  $N$  represents the dimensionality of the stimulus space.  $x_{jn}$  denotes the coordinate of stimulus  $j$  on the  $n^{\text{th}}$  dimension of the perceptual space, and  $w_n^i$  represents the weight assigned to the  $n^{\text{th}}$  dimension for the  $i^{\text{th}}$  participant, indicating its perceptual importance. The input data required for INDSCAL is a matrix of dissimilarity data, represented by  $\mathbf{D}^i = [d_{ij}^i]$ , which denotes the dissimilarity of stimuli  $j$  and  $k$  for participant  $i$ . The output of INDSCAL is comprised of two matrices:  $\mathbf{X} = [x_{jn}]$ , an  $S \times N$  matrix of stimulus coordinates, and  $\mathbf{W} = [w_n^i]$ , an  $P \times N$  matrix of participant weights, where  $S$  and  $P$  are the numbers of stimuli and participants, respectively Carroll and Arabie [1998].

In this study, we utilized the INDSCAL algorithm to analyze dissimilarity data collected during the three sessions of the psychoacoustic test, with the aim of constructing a perceptual space. The INDSCAL analyses were conducted in MATLAB programming environment, and thanks to Prof. Etienne Parizet at the LVA of INSA Lyon for sharing his algorithm as an example to be considered. Furthermore, determining the ideal number of dimensions for the perceptual space is a crucial concern. This decision significantly impacts both the complexity of the problem and the robustness of stimulus coordinates within the perceptual space.

### Number of perceptual dimensions

The optimal number of dimensions must be determined to prevent certain problems like overfitting and the instability of estimated coordinates in the perceptual space. On the other hand, the chosen number of dimensions should support effective re-

construction of dissimilarity matrix measurements. In light of such considerations, we have conducted calculations for varying numbers of perceptual space dimensions, aiming to minimize both the number of the dimensions and the distance between the measured and calculated dissimilarities. To achieve this goal, we employed the L-Curve method, which aids us in striking a balance between two objectives: namely, 1) minimizing the distance between the measured and calculated dissimilarities for increasing the accuracy, and 2) minimizing the number of perceptual dimensions to prevent the overfilling and complexity of the model. This is accomplished by visualizing how these objectives trade off against each other. Such visualization of the distance between the measured and calculated dissimilarities against the number of dimensions is usually referred to as a 'Scree plot' or 'Stress curve', and can be used to find the dimensionality (see, for example Borg and Groenen [2005]). The predominant pattern observed in scree plots indicates a decreasing trend in stress as the number of dimensions increases, forming L-curve or elbow shapes (e.g. see Borg and Groenen [2005]; Jaworska and Chupetlovska-Anastasova [2009]; Hout et al. [2013]). Except for some variations in the scree plots illustrated in Figures 6.11 and 6.12, which may be attributed to a small number of stimuli regarding the different types of stimuli, we also observed such predominant L-curve pattern in most of the scree plots investigated in the current research (c.f Figure 6.10 in this chapter and Figures 7.7 and 7.8 in Chapter 7).

Meanwhile, the L-curve method was initially developed for the purpose of selecting the regularization parameter in ill-posed problems (e.g. see Hansen [1999]) and it has application in multi-objective optimization when two objectives want to be optimized (e.g. see Ponsi et al. [2021]). Herein, this method has been used for selecting the number of dimensions by identifying the point of maximum curvature, called corner or elbow, in the scree plot. Herein, for managing the analyses regarding the L-Curve method and finding the corner representing the optimum parameter, we utilized a MATLAB regularization tools developed by Hansen [2023] (refer to Hansen [2007]).

Figure 6.10 to 6.12 illustrate the L-Curve results, where starting from a dimensionality of 2 and beyond (it is worth mentioning that in the L-Curve results of the present study, we have determined the difference between the measured and calculated dissimilarity matrices using the 2-norm). These results demonstrate the significance of a balanced approach to dimensionality selection in the perceptual space. Herein, according to these figures, we can see that by keeping the number of dimensions at 2 or 3 as the corners of the L-Curve, we can effectively manage both concerns regarding the number of dimensions, and the need for accurate modeling and calculations of the dissimilarity matrix. Herein, for all the three sessions, we opted to choose 2

dimensions instead of 3. This decision was driven by the fact that when working with 2 dimensions, we observed more stable solutions, compared to 3 dimensions. Conversely, when we used 3 dimensions, we encountered an instability in the form of larger error ellipsoids of the coordinates. It is important to note that as we involve a larger number of perceptual dimensions, the number of unknowns also increases for finding the coordinates of the stimuli in the perceptual space. This increase in unknowns further contributes to the instability in the computational process of reaching the perceptual dimensions. Such instability phenomena for constructing the perceptual space have been observed and reported in other case studies, such as Trollé [2009].

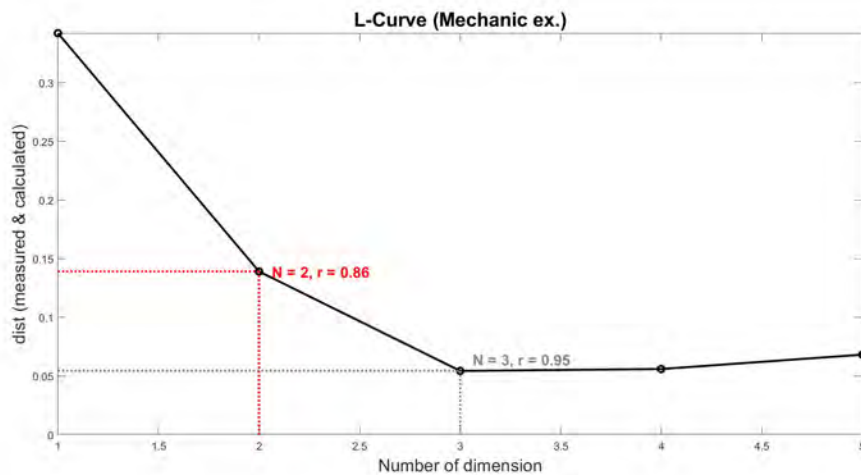


Figure 6.10: The L-curve (i.e. scree plot) between the distance between the calculated and measured dissimilarity matrices with respect to the number of dimensions in the perceptual space for Session 1 ( $r$  indicates the correlation between the measured and calculated dissimilarities)

### 6.3.3 Perceptual space and model validation

Therefore, we have chosen a two-dimensional perceptual space for conducting psychoacoustic assessments on the stimuli. As a result, we can have the 2D coordinates of the stimuli within this perceptual space. Furthermore, by using the bootstrap method (Weinberg et al. [1984]), a 95% confidence ellipse has been calculated for each stimulus in the perceptual space, as carried out by Trollé [2009]. As can be seen from the results of sessions 1 and 2 (see Figures 6.13 and 6.14), the positions of the simulated stimuli are close to the recorded stimuli in the perceptual space. If the positions of the simulated stimuli are located within the 95% confidence intervals of the recorded stimuli and vice versa, it shows, from a perceptual point of view, the

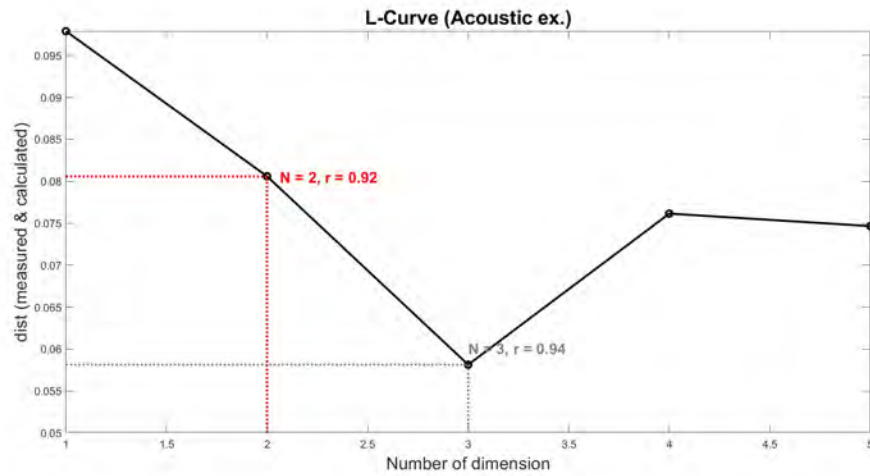


Figure 6.11: The L-curve (i.e. scree plot) between the distance between the calculated and measured dissimilarity matrices with respect to the number of dimensions in the perceptual space for Session 2 ( $r$  indicates the correlation between the measured and calculated dissimilarities)

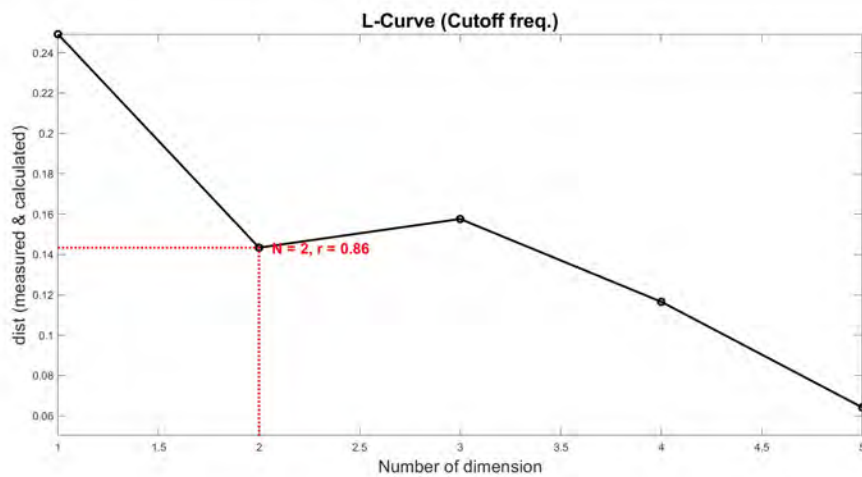


Figure 6.12: The L-curve (i.e. scree plot) between the distance between the calculated and measured dissimilarity matrices with respect to the number of dimensions in the perceptual space for Session 3 ( $r$  indicates the correlation between the measured and calculated dissimilarities)

closeness of the mathematical modeling to the real measurements with 95% certainty.

### Mechanical excitation

Figure 6.13 displaying the perceptual space for the first session with the mechanically excited panels, clearly demonstrates the close similarity between the simulated

stimulus for the composite sandwich panel and the measured stimulus recorded by microphone. It is quite clear that the positions of the simulated and recorded stimuli are within 95% confidence intervals of each other. The simulation was carried out using the modeling approach based on the 6<sup>th</sup> problem, as discussed in Chapters 4 and 5. Thus the agreement between the simulated and recorded stimuli in the perceptual space provides further evidence of the effectiveness of the modeling for the composite sandwich panel. In addition, Figure 6.13 demonstrates that such agreement between the simulated and recorded stimuli is also obtained for the composite laminate and steel panels. The results of Session 1 indicate that the participants may have had some difficulties in recognizing and differentiating the stimuli of the laminate and aluminum panels during the psychoacoustic test. As a result, these stimuli were perceived as very close to each other in the perceptual space. From a theoretical point of view, this proximity can be attributed to the similarity in some mechanical parameters of these samples, as discussed in Chapters 4 and 5. For example, the stiffness-to-mass ratio for the composite laminate and aluminum plates is around 38 and 24  $Nm^3/kg$ , respectively, which is relatively close compared to the stiffness-to-mass ratios for the composite sandwich and steel plates, which are around 480 and 2  $Nm^3/kg$ , respectively. This proximity in the stiffness-to-mass ratio for the laminate and aluminum panels results in the closeness of their natural frequencies, leading to similar responses to the excitation. However, the simulated and recorded stimuli of the laminate panel still conform each other via their confidence ellipse. Even, as seen in the results, the simulated and recorded stimuli of the aluminium panel are also close enough to each other, considering the confidence ellipse associated with the simulated stimulus (see Figure 6.13).

Furthermore, based on our personal observations during the stimuli listening, we noticed distinct patterns in the session with the mechanical excitation, investigating the perceptual dimensions. In this session, when moving from the lowest point to the highest point on Dimension 1, there is a noticeable transition from loud to soft sounds. This transition is especially evident when listening to stimuli involving aluminum and composite plates. In contrast, Dimension 2 seemed to represent a shift from treble to bass sounds, which was particularly noticeable when comparing stimuli from aluminum and steel plates.

### **Acoustic excitation**

The results of Session 2 demonstrate that the perceptual agreement between simulated stimuli and recorded ones was also noticeable for the acoustically excited

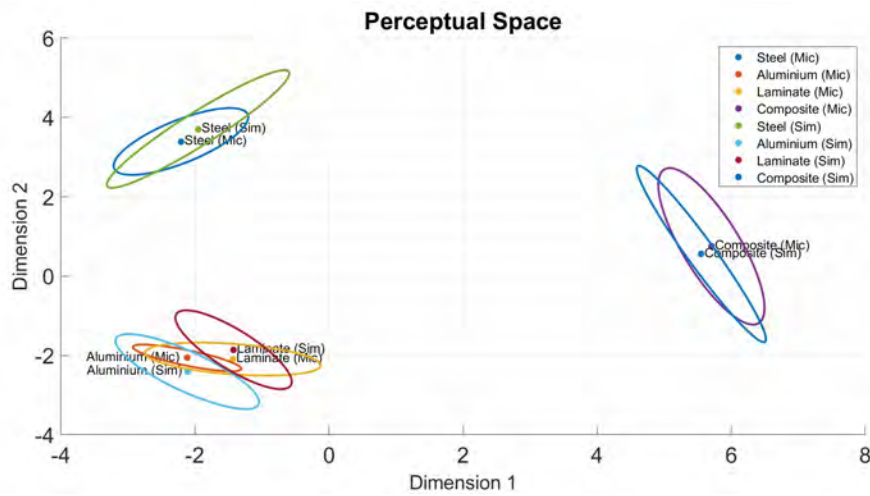


Figure 6.13: The perceptual space of the stimuli of Session 1, associated with the simulations and recordings of sounds radiated from the mechanically excited panels, including the positions of the stimuli and the ellipses representing the 95% confidence intervals for stimuli coordinates

panels. Figure 6.14 illustrates that for both the composite and steel panels, the simulated stimuli and the laboratory-recorded ones are closely positioned within the 95% confidence ellipses. However, for the aluminum panel, the simulated and recorded stimuli are far apart, indicating that the modeling for this panel is not accurate enough from a perceptual perspective. This phenomenon can be attributed to the high thickness of the aluminum panel because for the isotropic panels, including the steel and aluminum ones, the 4th-order problem was utilized to model the solution based on Kirchhoff–Love hypotheses, which assume that the panel must be thin enough to be modeled by the 4th-order problem. Therefore, the high thickness of the aluminum panel increases the uncertainty in the 4th-order problem, leading to uncertainties in the results of the perceptual space, as depicted in Figure 6.14. It is worth mentioning that the thickness of the steel and aluminum panels used in this study is 2 mm and 5 mm, respectively; additionally, to model the composite panel, the 6th-order problem was used instead of the 4th-order problem.

Also, in this session similar to the session with the mechanical excitation, we examined the patterns of the stimuli based on our personal observations during the stimuli listening. Hence, we found that Dimension 2 was primarily associated with a transition from bass to treble sounds. The lowest and highest points on this dimension represented this contrast. However, this transition was not as clear-cut as in the mechanical session. As illustrated in the figure of the perceptual space (i.e. Figure 6.14), there were large error ellipsoids for stimuli in this session compared with the mechanical session (see Figure 6.13), indicating that participants found it challenging to differentiate the stimuli.

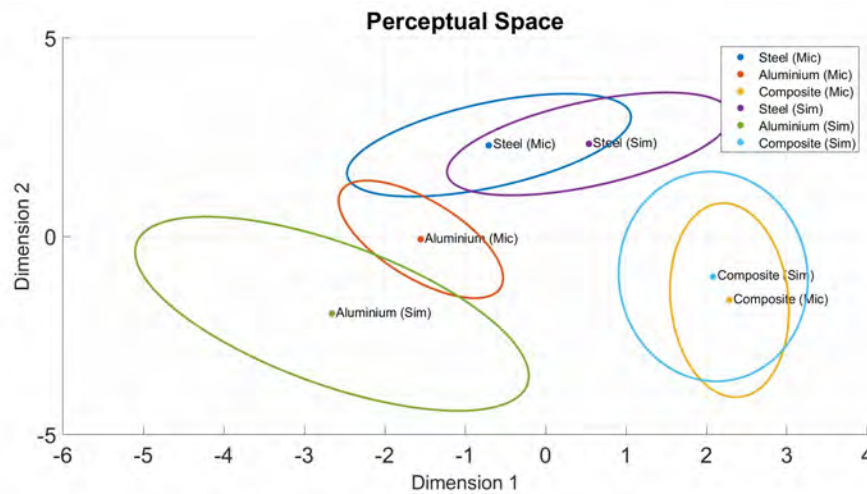


Figure 6.14: The perceptual space of the stimuli of Session 2, associated with the simulations and recordings of sounds radiated from the acoustically excited panels, including the positions of the stimuli and the ellipses representing the 95% confidence intervals for stimuli coordinates

### Cutoff frequency

Based on Figure 6.15, it is evident that the maximum frequency (cutoff frequency) plays a crucial role in terms of perception. As the maximum frequency increases, the simulated stimulus gradually approaches the original simulated stimulus (labeled "Composite (Sim)") (see Figure 6.15 from right to left), reaching the cutoff frequency equal to 7kHz. The original simulated stimulus was obtained by the maximum frequency equal to 10kHz, which had a high degree of similarity with the real recorded stimuli (labeled "Composite (Mic)") (see Figure 6.13).

So, as depicted in Figure 6.15, the simulated stimulus generated with a maximum frequency of 7kHz and the original simulated stimulus (labeled "Composite (Sim)" in Figure 6.15) are located within each other's confidence ellipses, indicating that they are highly similar with 95% confidence. Therefore, based on this result, a maximum frequency of 7 kHz was selected for the subsequent simulations and modeling discussed in the next Chapter.

Additionally, it is worth mentioning that, in the third session, although the L-Curve technique suggested the dimensionality equal to 2 for the perceptual space, a 1D perceptual space may also be anticipated since only a single parameter (i.e., the cutoff frequency) was applied to the stimuli. Hence, we also explored a dimensionality equal to 1 for the perceptual space of this session. In this instance, the dimension of the 1D perceptual space exhibited a similar pattern for the distribution of stimuli



in the perceptual space. The dimension in the 1D perceptual space and the 1st dimension in the 2D perceptual space showed a slight difference and a high statistical correlation equal to ( $r = 0.99, p < 0.001$ ).

In this session, akin to the two preceding sessions, we also endeavored to discern patterns in the stimuli through our personal observations while listening to them. Dimension 1 appeared to be linked with the progression from treble sounds to bass sounds. For example, when comparing the stimulus with a cutoff frequency of 7 kHz to that with a cutoff frequency of 2 kHz on Dimension 1, we could perceive a transition from treble to bass sounds, which aligns with our expectations.

It is worth mentioning that this section exclusively focused on perceptually assessing distinctions between recordings and simulations, validating the models and simulations from an auditory perceptual standpoint. Correlation analysis was considered irrelevant due to the limited amount of data. However, in the subsequent Chapter, dedicated to the structure design optimization from a perceptual point of view, a larger number of stimuli and data will be considered in order to allow the final objective of this thesis work to be achieved with the interpretation of the results from an auditory perceptual perspective.

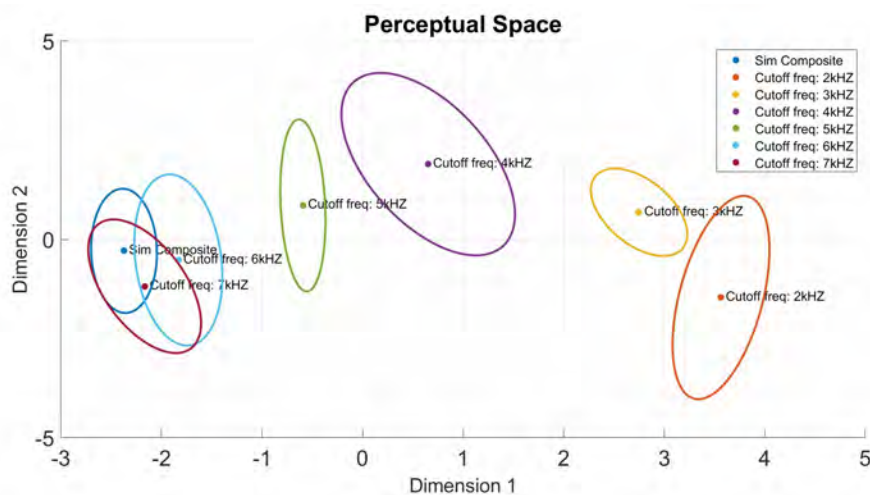


Figure 6.15: The perceptual space of the stimuli of Session 3, associated with the simulations with different cutoff frequencies, including the positions of the stimuli and the ellipses representing the 95% confidence intervals for the stimuli coordinates

## 6.4 Summary and discussion

This chapter provided us with psychoacoustic processes required for obtaining an accurate modeling of vibrating panels from a perceptual point of view. The psychoa-

coustic test was performed for 40 participants with an age range of 18 to 61. The modeling and simulations were confirmed by psychoacoustic analyses, highlighting the potential usefulness of considering both vibroacoustic and psychoacoustic perspectives for designing composite panels. The psychoacoustic test was conducted across three sessions, with each session having a specific target. Based on the laboratory vibroacoustic experiments conducted before (see Chapters 3, 4, and 5), the pairwise comparison approach was used for dissimilarity evaluation of the acquired and simulated stimuli. A MATLAB-based interface was developed for this purpose and used for performing the dissimilarity evaluation of paired stimuli. After the test, the clustering and dendrograms were used to identify outliers in the data acquired via the participants. Afterwards, the multidimensional scaling approach, INDSCAL, was used to establish the perceptual space of the dissimilarity and account for the perceived distances between the stimuli. The results indicated that the simulated stimuli were close to the recorded stimuli in the perceptual space, and these results were confirmed by the statistical tests and the confidence intervals achieved by the bootstrap analyses.

Finally, the topics addressed in this chapter involve the validation of the mathematical models and simulations discussed in the previous chapters, from the auditory perceptual point of view. These validated models will ultimately be used in the next chapter for the design of composite panels.



# Chapter 7

## Design and optimization

In continuation of Chapter 6, this chapter places its emphasis on the design and optimization of vibrating composite panels from a perceptual perspective. Initially, specific composite panels were designed, building upon the model that was adjusted and updated in Chapter 5. Subsequently, a series of psychoacoustic laboratory experiments were conducted on these designs, each possessing distinct mechanical properties. These psychoacoustic tests involved 40 participants aged between 19 and 63 years. Finally, using the outcomes of the psychoacoustic tests, corresponding analyses were undertaken to assess and optimize the designs.

### 7.1 Composite panel design

According to the theories and experiments outlined in Chapter 5, we have developed an updated model for composite sandwich panels featuring CRFP<sup>1</sup> face sheets and a Nomex hexagonal honeycomb core. Building upon the updated model, we can now extend our modeling and simulation efforts to explore various designs with specific mechanical and geometrical characteristics from a perceptual point of view. Table 7.1 summarizes the geometrical and mechanical parameters of the sandwich composite panel tested in the laboratory experiments, in relation to the associated updating procedures. In this table, the parameters  $h_f$ ,  $h_c$ ,  $D_t$ ,  $E_f$ ,  $G$  and  $\eta$  represent, respectively, the thickness of the face sheets, thickness of the core, total bending stiffness, Young modulus of face sheets, the shear modulus of the core, and loss damping factor. The loss damping factor  $\eta$  was estimated by the Least-Squares Complex Exponential Method and the laser measurements (see Sections 4.2.3 and 5.3.1), and the mechanical parameters  $D_t$ ,  $E_f$  and  $G$  were updated following the

---

<sup>1</sup>Carbon-Fiber-Reinforced Polymer

Table 7.1: The geometrical and mechanical parameters associated with the composite sandwich panel tested in the laboratory experiments in Chapter 5 ( $a$  and  $b$ : dimensions of panel,  $h_f$ : thickness of face sheets,  $h_c$ : thickness of core,  $D_t$ : total bending stiffness,  $E_f$ : Young modulus of face sheets,  $G$ : shear modulus of core, and  $\eta$ : loss damping factor)

	<i>Geometrical parameters</i>				<i>Mechanical parameters</i>			
Parameters	$a$ [cm]	$b$ [cm]	$h_f$ [mm]	$h_c$ [mm]	$D_t$ [Nm]	$E_f$ [GPa]	$G$ [MPa]	$\eta$
Values	40	60	0.2	13.5	1034	50.12	71.17	0.0916

procedures outlined in Chapter 5. Additionally, Figure 7.1 schematically presents an overview of the composite panel geometric characteristics, including those of its core. Furthermore, considering that the core is composed of a hexagonal honeycomb

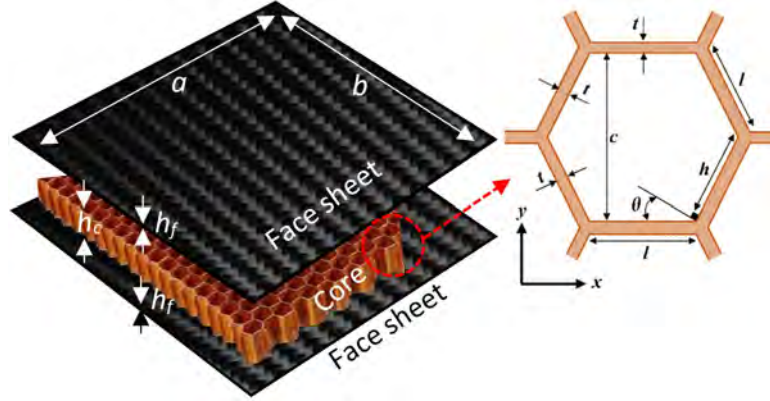


Figure 7.1: The designed composite sandwich panel with a hexagonal honeycomb core

cells, the following equation establishes a relationship between the effective shear modulus of the core  $G$  and the parameters of the honeycomb unit cells (e.g. see chapter 4.5 in Gibson and Ashby [1997]):

$$\frac{h/l + \sin\theta}{(1 + 2h/l) \cos\theta} \frac{t}{l} \leq \frac{G_{xz}}{G_s} \leq \frac{1}{2} \frac{h/l + 2\sin^2\theta}{(h/l + \sin\theta) \cos\theta} \frac{t}{l} \quad (7.1.1)$$

$$\frac{G_{yz}}{G_s} = \frac{\cos\theta}{(h/l + \sin\theta)} \frac{t}{l} \quad (7.1.2)$$

where  $h$  is the vertical member length,  $l$  is the angled member length,  $t$  is the wall thickness, and  $\theta$  is the cell angle (see Figure 7.1). Moreover,  $G_s$  represents the shear modulus of the material employed within the cell wall. In the case of a regular hexagonal honeycomb core, we have  $h = l$  and  $\theta = 30^\circ$ ; these conditions imply that the core exhibits an isotropic behaviour within the  $xy$ -plane (i.e.  $G = G_{xz} = G_{yz}$ ).

Table 7.2: The parameters of the unit cell associated with the hexagonal honeycomb core of the sandwich panel ( $c$ : cell size,  $l$ : angled member length,  $h$ : vertical member length,  $t$ : wall thickness,  $\theta$ : cell angle,  $G_s$ : shear modulus of material,  $E_s$ : Young modulus of material, and  $\rho_s$ : mass density of material)

	<i>Cell parameters</i>							
Parameters	$c$ [mm]	$l$ [mm]	$h$ [mm]	$t$ [mm]	$\theta$ [deg]	$G_s$ [GPa]	$E_s$ [GPa]	$\rho_s$ [kg/m <sup>3</sup> ]
Values	3	1.73	1.73	0.1	60	2.03	5.27	1370

Thus, when examining a regular hexagonal honeycomb core, Eqs. (7.1.1) and (7.1.2) will be reduced to the following equation (e.g. see Kelsey et al. [1958], Gibson and Ashby [1997])

$$G = \frac{G_s t}{\sqrt{3} l} = \frac{G_s t}{c} \quad (7.1.3)$$

Furthermore, other physical characteristics of the hexagonal honeycomb core like its in-plane Young modulus  $E_c$  and mass density  $\rho_c$  can be obtained from the characteristics of its unit cell as follows (e.g. see Gibson and Ashby [1997]):

$$E_c = 2.3 \left(\frac{t}{l}\right)^3 E_s, \quad \rho_c = \frac{2}{\sqrt{3}} \frac{t}{l} \rho_s \quad (7.1.4)$$

As a result, given that the composite sandwich panel employed in our laboratory experiments featured a regular hexagonal honeycomb core composed of Nomex aramid fiber paper, the above relations allowed us to make predictions regarding the mechanical characteristics of the unit cell material. Table 7.2 provides a summary of the geometrical and mechanical properties associated with the unit cell of the sandwich panel core. In this table, we present the measured values of the cell wall thickness  $t$  and cell size  $c$  obtained using a caliper during the laboratory experiments of the mechanical excitation. The member length  $l$  is calculated as  $l = c/\sqrt{3}$ . The shear modulus  $G_s$ , corresponding to the Nomex paper serving as the material for the unit cell, is determined using Eq.(7.1.3) along with the updated value of the core shear modulus  $G$ . Additionally, we have determined the Young modulus of the Nomex paper, denoted as  $E_s$  (cf. Table7.2), considering the Nomex paper as an isotropic material. This relationship is expressed as  $E_s = 2(1 + 2\nu)G_s$ , where  $\nu = 0.3$ . This estimated Young modulus  $E_s$ , obtained from the aforementioned equations and the updated value of the core shear modulus, is in a good agreement with the range of the Young modulus values obtained in similar studies, such as Roy et al. [2014].

Besides, Eq.(7.1.3) can prove valuable for designing composite sandwich panels with different values of the core shear modulus. For instance, by adjusting the mechanical properties of the core material,  $G_s$  and  $E_s$ , or modifying the dimensions of

the unit cells,  $t$  and  $l$ , we can design cores with different shear modulus values. In the preparation of the designs and their corresponding stimuli, as described in the following parts, we have varied the core shear modulus from 20MPa to 80MPa. This implies that the relative parameter  $t/l$  has ranged from 0.0171 to 0.0684, assuming the same material as used in the composite panel tested in the experiments and employed for the updated model. This range of variation for the relative parameter  $t/l$  (or  $t/h$ ) has also been explored in other studies like Zergoune et al. [2017] that conducted certain numerical simulations to assess the geometrical configuration and parameters of the core in a composite sandwich panel. In this research, the authors investigated the relative parameters  $t/l$  and  $t/h$  within the range of 0.011 to 0.044. They focused on a sandwich panel with Nomex aramid core, which exhibited mechanical properties similar to those utilized in our current study. Zergoune et al. [2017] demonstrated that the relative factors  $t/l$  and  $t/h$  exert significant influences on vibroacoustic characteristics, including the transition frequency and sound transmission loss (STL). They observed that, particularly at mid-frequencies, an increase in the relative factors  $t/l$  and  $t/h$  led to an increase in the transition frequency and an enhancement in the STL curves. Furthermore, based on certain numerical simulations examining the impact of cell angles  $\theta$  on STL, they demonstrated that the cell angle does not significantly affect STL, and the best performance for the equivalent bending stiffness were achieved when  $\theta$  was approximately equal to  $28^\circ$ , which is close to that of a regular hexagonal honeycomb. Additionally, their research underscored the importance of sandwich core thickness  $h_c$  on the transition frequency and STL (for additional information refer to Zergoune et al. [2017]).

Similarly, for the other parameters, we obtained a logical range of variations from previous similar studies. To achieve this, we considered the values of the parameters obtained from, or used in, the updating procedures as the reference values (i.e., the parameter values mentioned in Table 7.1). Then, for each design, we varied each parameter around its respective reference value. In Chapter 5, we demonstrated how the updated parameter values were aligned with the measurements and results of previous studies. Consequently, we organized the parameters for 10 composite panel designs as described in Table 7.3. The range of parameter variation was derived from recent studies with case studies on composite panels and beams that are approximately similar, such as the works by Ghinet and Atalla [2011], Li and Narita [2013], Montalvão et al. [2013], Cherif et al. [2015], Sarlin et al. [2012], Zergoune et al. [2017], Qi et al. [2019], Zhou et al. [2021], Collins et al. [2022]. In Table 7.3, the variation of each parameter is independent of the other parameters, except for the equivalent parameters including the total bending stiffness  $D_t$ , the equivalent Young modulus  $E_{equi}$ , and the total surface mass density  $M$ , which were derived from the

Table 7.3: The geometrical, mechanical, and equivalent parameters associated with the composite sandwich panels designed for psychoacoustic tests ( $h_f$ : face sheet thickness,  $h_c$ : core thickness,  $E_f$ : Young modulus of face sheet,  $G$ : shear modulus of core,  $\eta$ : loss damping factor,  $D_t$ : total bending stiffness,  $E_{equi}$ : equivalent Young modulus,  $M$ : surface mass density, and  $D_t/M$ : stiffness-to-mass ratio)

	<i>Geometrical parameters</i>		<i>Mechanical parameters</i>			<i>Equivalent parameters</i>			
	$h_f$ [mm]	$h_c$ [mm]	$E_f$ [GPa]	$G$ [MPa]	$\eta$	$D_t$ [Nm]	$E_{equi}$ [GPa]	$M$ [kg/m <sup>2</sup> y]	$D_t/M$ [Nm <sup>3</sup> /kg]
<b>Design 1</b>	0.2	13.5	30	71.17	0.0916	655	2.66	1.92	341
<b>Design 2</b>	0.2	13.5	70	71.17	0.0916	1480	6.02	1.92	771
<b>Design 3</b>	0.2	13.5	50.12	20	0.0916	1068	4.34	1.92	557
<b>Design 4</b>	0.2	13.5	50.12	80	0.0916	1100	4.47	1.92	573
<b>Design 5</b>	0.2	13.5	50.12	71.17	0.02	1093	4.44	1.92	570
<b>Design 6</b>	0.2	13.5	50.12	71.17	0.06	1093	4.44	1.92	570
<b>Design 7</b>	1.1	13.5	50.12	71.17	0.0916	6650	18.77	5	1330
<b>Design 8</b>	2	13.5	50.12	71.17	0.0916	13640	27.79	8.08	1687
<b>Design 9</b>	0.2	6	50.12	71.17	0.0916	220	9.15	1.23	178
<b>Design 10</b>	0.2	18	50.12	71.17	0.0916	1951	3.42	2.33	837

other parameters. The bending stiffness could be obtained by using the laminate theory and calculating the stiffness matrix (refer to (4.2.1)), and consequently, the equivalent Young modulus can be derived from  $D_t = E_{equi}H^3/12/(1 - \nu^2)$  when we have  $H = 2h_f + hc$  as the total thickness of the sandwich panel and  $\nu$  as the Poisson ratio. Additionally, the surface mass density of the composite panel could be determined using the mass density of the face sheets ( $\rho_f$ ) and the core mass density ( $\rho_c$ ) through the equation:  $M = 2\rho_f h_f + \rho_c h_c$ .

### 7.1.1 Vibroacoustic modeling

For the vibroacoustic modeling of the aforementioned designs associated with the composite sandwich panels, the updated model of the 6<sup>th</sup> order problem was used to determine the updated mode shapes by referencing Eq.(5.2.17). Considering the mode shapes, we could subsequently calculate the natural frequency of each mode for various designs of the vibrating panel, using their respective properties (see Table 7.3). This calculation involves utilizing the wave number associated with each mode and the 6th order dispersion relation, as explained in Eq.(2.2.5). Then, by applying the modal decomposition discussed in Chapter 2, we could analyze the flexural vibration field of the vibrating panel with its new designs. Subsequently, in a manner similar to the previous simulations described in Chapter 4, we could model the sound pressure field at an arbitrary distance from the vibrating panel using the Rayleigh integration (see Chapter 2). In this context, just as in the previous simulations, we modeled the sound pressure level at a distance of 50 cm from each panel design. Table 7.4 presents the sound pressure levels in dB(A) for the synthesised sounds associated with various designs for two types of excitation, namely, mechanical and



Table 7.4: The sound pressure levels of the stimuli, associated with the different designs of the composite panel, excited by the mechanical and acoustic excitations, [unit: dB(A)]

↓ Excitation   Design →	Design 1	Design 2	Design 3	Design 4	Design 5	Design 6	Design 7	Design 8	Design 9	Design 10
<b>Mechanical</b>	56.3	55.3	55.7	55.8	56.3	55.7	55.6	55.4	56	56.4
<b>Acoustic</b>	53.4	52.8	51.9	52.8	53	52	52.1	52.3	53.8	52.4

acoustic excitations. The conditions of the excitations were similar to those in the real laboratory experiments presented in Chapters 3 and 4. As was done with the previous tests discussed in Chapter 6, in this case, these stimuli were also adjusted by the Cortex Manikin MK2 to ensure the comfort of the participants.

## 7.2 Psychoacoustic tests

Herein, to conduct the psychoacoustic test aimed at evaluating the composite sandwich panel designs, we adhered to similar protocols and procedures employed in Chapter 6 for perceptual validation and psychoacoustic assessments of simulations. Additionally, the current tests incorporates preference score measurements.

### 7.2.1 Participants

A total of 40 participants, consisting of 22 females and 18 males, spanning an age range from 19 to 63 years, actively participated in the auditory evaluation. The average age of the participants was 35.8 years, with a standard deviation of 15.3 years. These individuals were from the students and staff of the ENTPE. All participants were engaged in every test session. Moreover, all participants received compensation for their involvement in the psychoacoustic experiments. Prior to the commencement of the experiment, each participant confirmed their normal hearing abilities and provided written consent for their participation.

### 7.2.2 Test conditions

The apparatus used was identical to the one employed in the previous psychoacoustic tests for the perceptual assessments in Chapter 6. In a controlled experiment at ENTPE's campus, audio signals were played through Sennheiser HD600 headphones and a high-quality LynxTWO sound card in a quiet room with a background noise level of 24 dB(A). Participants interacted with a MATLAB-based computer interface that guided them through the test and recorded their responses. Before the test,

sound pressure levels of stimuli were adjusted using a Cortex Manikin MK2, placed at the participants' position. The audio files were later processed using dBsonic software.

### 7.2.3 Stimuli

For the 10 composite sandwich panel designs, we carried out psychoacoustic tests in two distinct sessions, each with a specific excitation. For Session 1, our focus was to assess the preference and psychoacoustic qualities of these designs when subjected to mechanical excitation. Session 2 involved assessing the designs, subjected to an acoustic field excitation. The duration of each stimulus corresponding to each design in the two sessions was 3 seconds, and after adjusting the stimuli for the comfort of the participants in the listening tests, the average sound pressure level ranged between 51.9 and 56.3 dB(A) (see Table 7.4). Hereafter, Sessions 1 and 2 shall be referred to as the "mechanical session" and the "acoustic session," respectively.

Furthermore, the same sound file preparation was used as in Section 6.2.5, encoding signals in 16-bit WAV format with amplitude values ranging from -1 to +1. For this purpose, the pressure values were normalized, created three-second stereophonic samples with 0.1s fade-in and fade-out to ensure consistent presentation to participants.

### 7.2.4 Method

To conduct psychoacoustic tests for evaluating the designs, we followed the paired-comparison method outlined in Chapter 6. In the current listening tests, we integrated preference judgments into the methodology. So, the method allowed us to capture both dissimilarity and preference judgments among the stimuli without overly fatiguing the participants. Throughout the experiment, including instructions, training, and all dissimilarity and preference assessments conducted in two test sessions, the average time spent per participant ranged from 40 to 45 minutes, approximately 20 to 23 minutes for each session. Also, similar to the tests conducted in Chapter 6, the presentation order of the pairs of sounds and the arrangement of sounds within each pair were randomized for each participant, mitigating the risk of introducing any presentation-related bias. Furthermore, we presented the sessions to participants in a random order. In each session, participants first received detailed on-screen instructions (in either French or in English, depending on their language abilities), as illustrated by the English version in Figure 7.2. They also had a training part to familiarize themselves with the test sounds and interface. Each

session involved listening to pairs of sounds, and giving dissimilarity and preference ratings. The stimuli were played for 3 seconds each, with a brief 0.5 seconds pause in between. Participants rated the dissimilarity between sounds on a numerical continuous scale from 0 to 10, with verbal descriptors at the endpoints from very similar to very different. The measure of preference was a dichotomous choice. The interface collected their judgments and stored all data in individual participant folders.

## 7.3 Results

In this section, we investigate the process of the measurements acquired in the two sessions of the psychoacoustic test and provide a comprehensive discussion of their corresponding analyses. We begin by addressing the crucial step of outlier detection and classification necessary for data preprocessing. Subsequently, we evaluated the designs from psychoacoustic point of view.

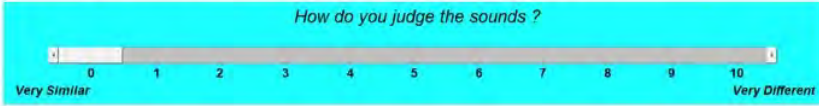
### 7.3.1 Classification and outliers detection

Similar to the classification performed in Chapter 6, herein, the Ascending Hierarchical Classification (AHC) was employed to perform clustering analysis on the participants. The detailed stages of participant clustering were discussed in Chapter 6. In Table 7.5, it is evident that across the two test sessions, the average linkage method among all aggregation methods consistently exhibited the highest values for both cophenetic and Goodman-Kruskal correlation coefficients (e.g. see Sokal and Rohlf [1962], Farris [1969], Goodman et al. [1979]). Using the average linkage method, aggregation was executed, leading to the development of dendrograms for each session. To ascertain the optimal number of classes, a quality index was computed for various partition configurations (see Eq.(6.3.2)). As demonstrated in the dendrogram for the mechanical session (refer to Figures 7.3), participants 12 and 31 consistently stand apart from the remaining participants, forming a distinct cluster for the mechanical session. Similarly, in the dendrogram for the acoustic session (refer to Figures 7.5), participant 12 also emerges as a standalone outlier, positioned within a separate cluster for the acoustic session. These findings indicate that the responses of these particular participants to the stimuli significantly deviate from those of the others. Furthermore, as evident from the Silhouette values, high Silhouette values for a two-class configuration indicate a high-quality classification for both sessions when we consider the number of classes to be 2 (see Figures 7.4 and 7.6). Consequently, participants 12 and 31 were identified as outliers for the mechanical

## Instructions

**IMPORTANT:** Please, read these instructions carefully:

- 1- This sound perception test is composed of **2 Sessions**.
- 2- You will listen to **SOUNDS presented in pairs** within each of these sessions.
- 3- You will be asked to judge the **DIFFERENCE** and **PREFERENCE** between the sounds.
- 4- Your judgment of the **difference** will be a difference score chosen on a continuous scale **from 0 to 10**:  
*For example*, if you perceive the two sounds to be very similar, the difference score will be 0, and if you think the two sounds are very different, the difference score will be 10.



How do you judge the sounds ?

- 5- To give a score on the scale, **move the cursor using the mouse, and release the cursor** at the position corresponding to the desired difference score. You have to move the cursor and return to the initial position if you want the note equal to 0.
- 6- For the judgement of the **preference**, you should answer the following question:
 

which sound do you prefer ?

**Sound 1**       **Sound 2**

**And select one of the two sounds.**

- 7- You can **listen** to the sounds **as many times as you want**.
- 8- To familiarize yourself with the sounds of each session and with the scale, you will need to do a little **TRAINING** before you can start the session.
- 9- If you encounter any problem during the test, do not hesitate to let me know.
- 10- Please use only the proposed interface and do not browse the computer otherwise the test could be stopped and will have to be restarted from the beginning to be complete and make your compensation valid. Please, do not touch the volume of the sound of the computer.
- 11- Finally, please turn off or put your mobile phone in airplane mode.

Have a good psychoacoustic test,

Figure 7.2: The English version of the initial interface: participants are guided with an instruction before the test

session, and participant 12 as an outlier for the acoustic session. Therefore, the participants 12 and 31, and the participant 12 were excluded from the analyses corresponding to the sessions of mechanical and acoustic excitations, respectively. It is

Table 7.5: The series of aggregation methods and the quantified level of adequacy: : cophenetic and Goodman-Kruskal (e.g. see Sokal and Rohlf [1962], Farris [1969], Goodman et al. [1979]), used for the two Sessions

Methods	<i>Mechanical Session</i>		<i>Acoustic Session</i>	
	Cophenetic	Goodman-Kruskal	Cophenetic	Goodman-Kruskal
Single	0.62	0.42	0.64	0.45
Complete	0.5	0.50	0.46	0.47
<b>Average</b>	<b>0.76</b>	<b>0.68</b>	<b>0.80</b>	<b>0.68</b>
Weighted	0.65	0.65	0.66	0.64
Centroid	0.74	0.63	0.78	0.61
Median	0.60	0.57	0.61	0.54
Ward	0.50	0.51	0.52	0.54

worth mentioning that in the above classification procedures, the dissimilarity data were utilized for the outlier detection. The same procedures were also conducted using the preference data, to reveal consistent outliers in each session. Likewise, the AHC analysis applied to the preference data revealed participants 12 and 31 as outliers in the mechanical session, and participant 12 as an outlier in the acoustic session.

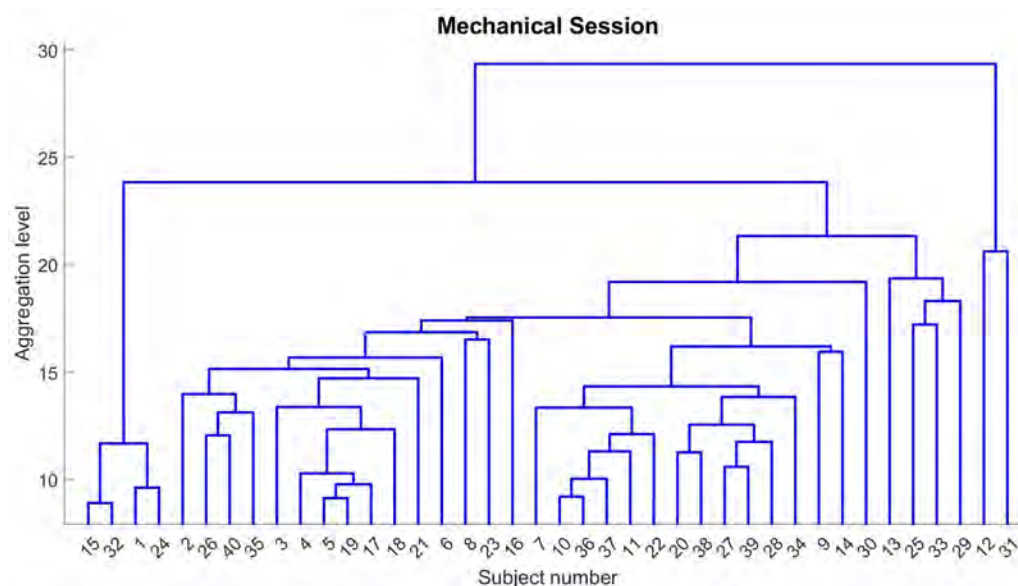


Figure 7.3: The Dendrogram associated with the classification of participants and outlier detection in the mechanical session

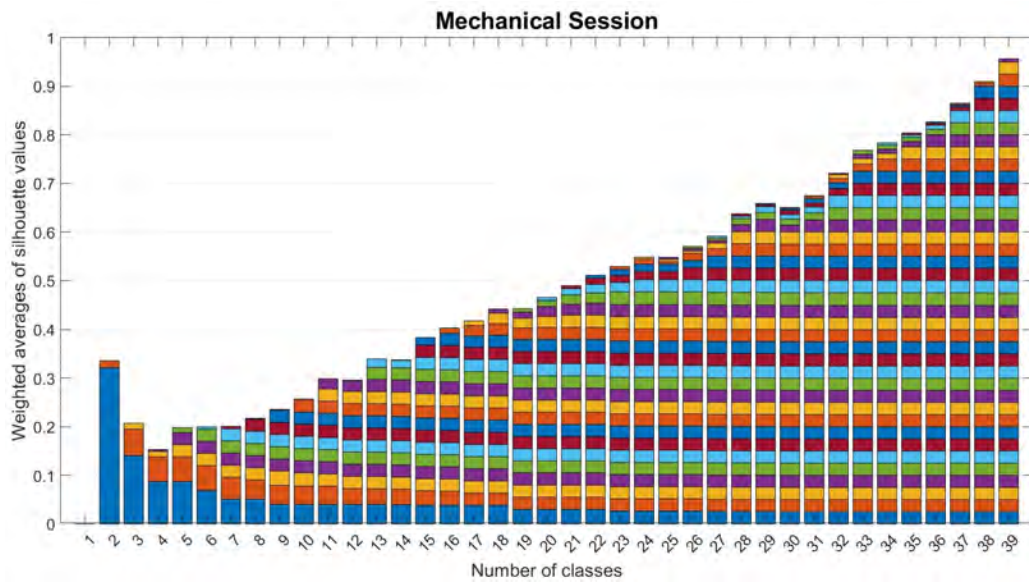


Figure 7.4: Weighted Silhouette values corresponding to the different classes of the participants in the mechanical session

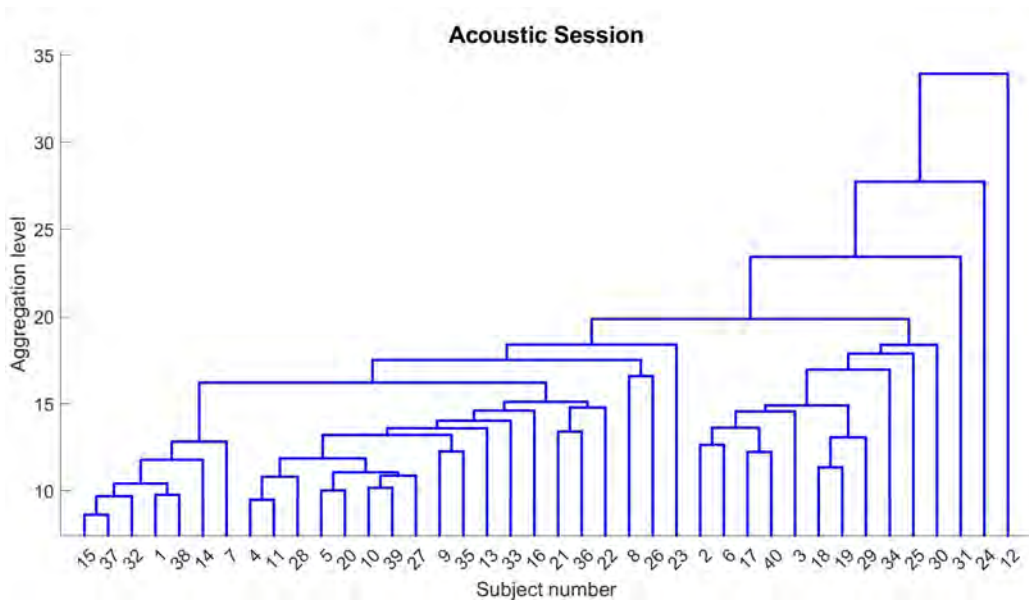


Figure 7.5: The Dendrogram associated with the classification of participants and outlier detection in the acoustic session

### 7.3.2 Perceptual space

Similar to the analyses conducted in Chapter 6, for constructing the perceptual space enclosing the stimuli, we have utilized the INDSCAL algorithm to analyze

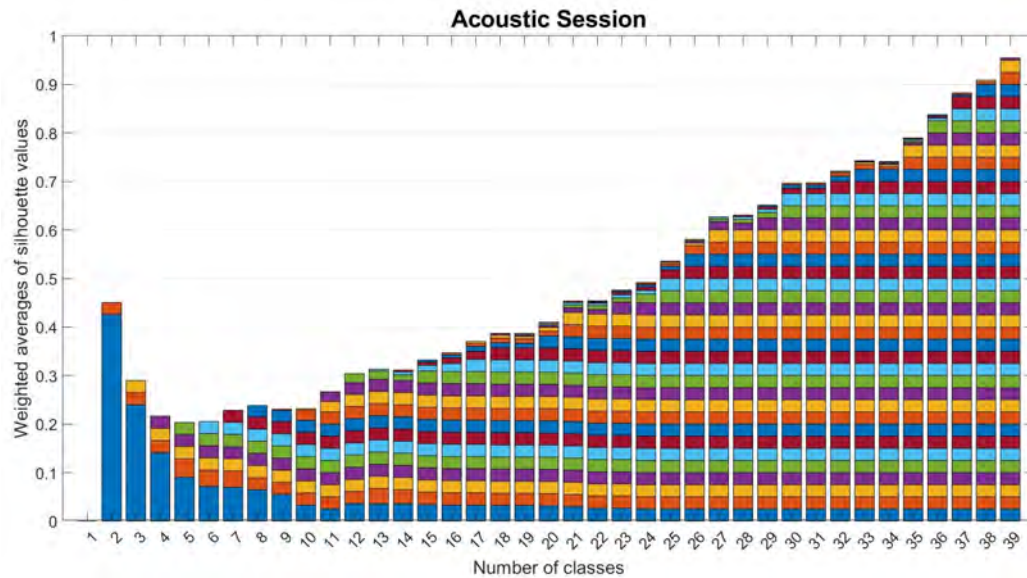


Figure 7.6: Weighted Silhouette values corresponding to the different classes of the participants in the acoustic session

the dissimilarity data collected during the two sessions of the psychoacoustic test (see Carroll and Chang [1970], Carroll [1972], Carroll and Arabie [1998], Borg and Groenen [2005]). Additionally, similar to the previous analyses, we employed the L-curve method to determine the optimal number of the perceptual dimensions from the scree plots. The L-curve method indicates the number of dimensions that strike a balance between effective reconstruction (i.e. accurate calculation of dissimilarity) and complexity in the problem-solving process (i.e. number of dimensions) (e.g., see Hansen [1999]). In light of these considerations, we conducted computations for various numbers of dimensions within the perceptual space. According to the L-curve results (see Figures 7.7 and 7.8), we maintained the number of dimensions at 2.

Accordingly, utilizing the INDSCAL method and considering two dimensions for the perceptual space, we were able to construct a perceptual space that encompasses the stimuli in both sessions. Figures 7.9 and 7.10 illustrate the coordinates of the stimuli in the perceptual spaces corresponding to the mechanical and acoustic sessions. In addition, the confidence interval for each stimulus, represented as a 2D error ellipse in the perceptual space (see Trollé [2009]), has been determined using the bootstrap technique at a 95% confidence level (see Weinberg et al. [1984]), similar to the findings discussed in Chapter 6.

Furthermore, at a glance, one can find a similarity between the two distributions of stimulus coordinates in the two perceptual spaces associated with the two sessions.

The arrangement of the stimuli within perceptual spaces begins on the left side with Design 9 having the lowest value for dimension 1. Following Design 9, both Design 1 and Design 3 also exhibit the lowest dimension 1 values, while dimension 2 is increasing for them. Designs 4 and 6 reach their peak values for dimension 2, while Designs 2, 5, and 10 see dimension 2 values decreasing. Finally, in Designs 7 and 8, dimension 1 reaches its maximum values. This behavioral pattern holds true for the stimuli of the designs across both mechanical and acoustic sessions within the perceptual spaces.

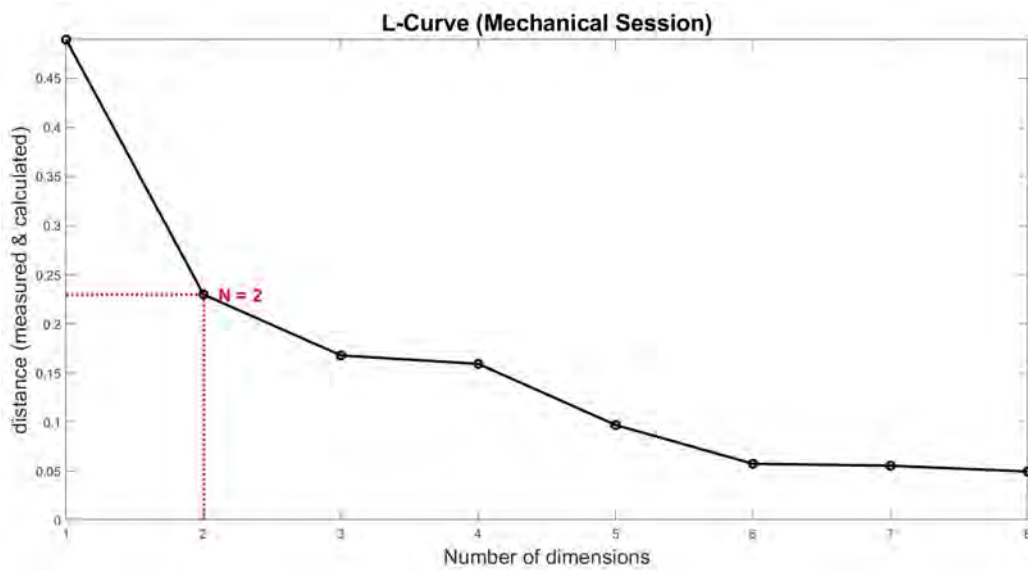


Figure 7.7: The L-curve (i.e. scree plot) between the error of the calculation (the 2-norm distance between the measured and calculated dissimilarity), and the number of perceptual dimensions corresponding to the mechanical session

### 7.3.3 Preference score

Preference judgments have been converted into preference rates in accordance with Case 5 of the Law of Comparative Judgments presented by Thurstone [1927] that proposed five specific instances of the law of comparative judgment, or measurement model. A crucial instance within the model is Case 5. In this particular model case, the greatest simplification is made by assuming that the discriminial dispersions of stimuli are all uniform and uncorrelated, and then the preference score as the distinction between stimuli can be directly inferred from the proportion matrix (e.g. see Bramley [2007] and Trollé [2009]).

Also, to accommodate the interaction between the dissimilarity test and the preference test when dealing with "very similar" responses, we have made adjustments



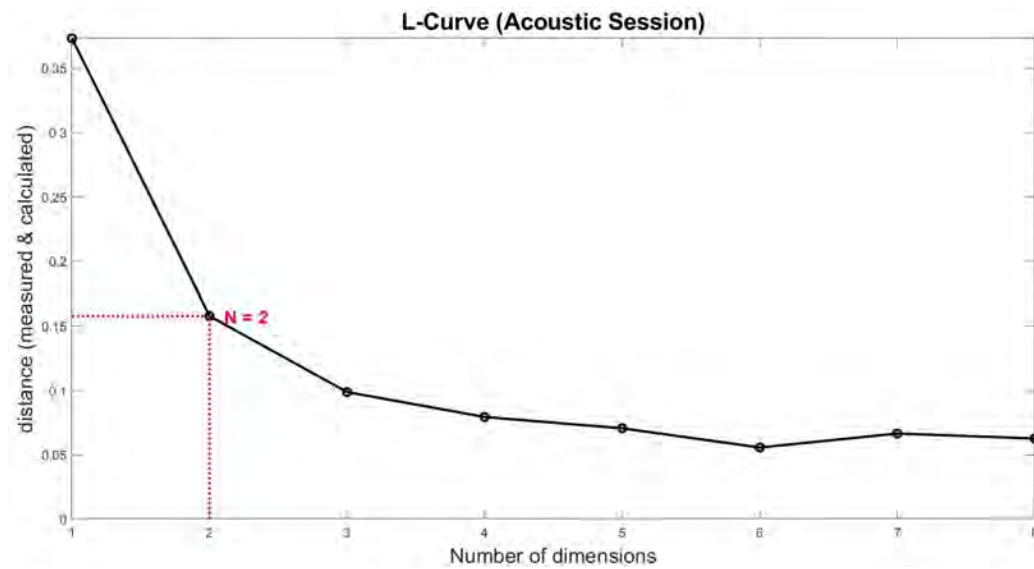


Figure 7.8: The L-curve (i.e. scree plot) between the error of the calculation (the 2-norm distance between the measured and calculated dissimilarity), and the number of perceptual dimensions corresponding to the acoustic session

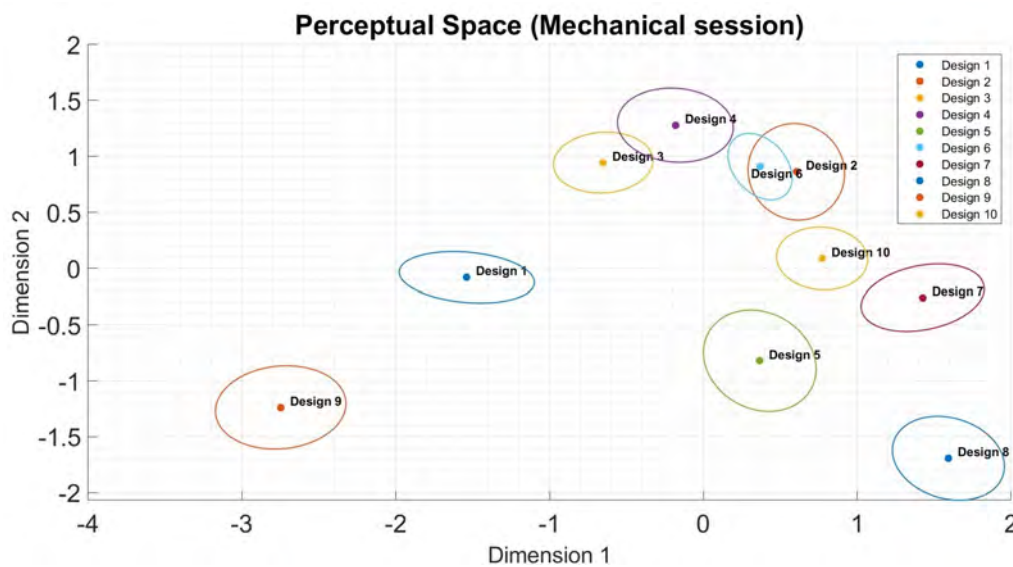


Figure 7.9: The perceptual space and the coordinates of the stimuli, corresponding to the mechanical session

to the proportion matrix. This adjusted proportion matrix is sometimes denoted as the updated proportion matrix (e.g. see Faure and Marquis-Favre [2005], Trollé [2009]). So, the updated proportion matrix is defined for  $n$  stimuli using the following

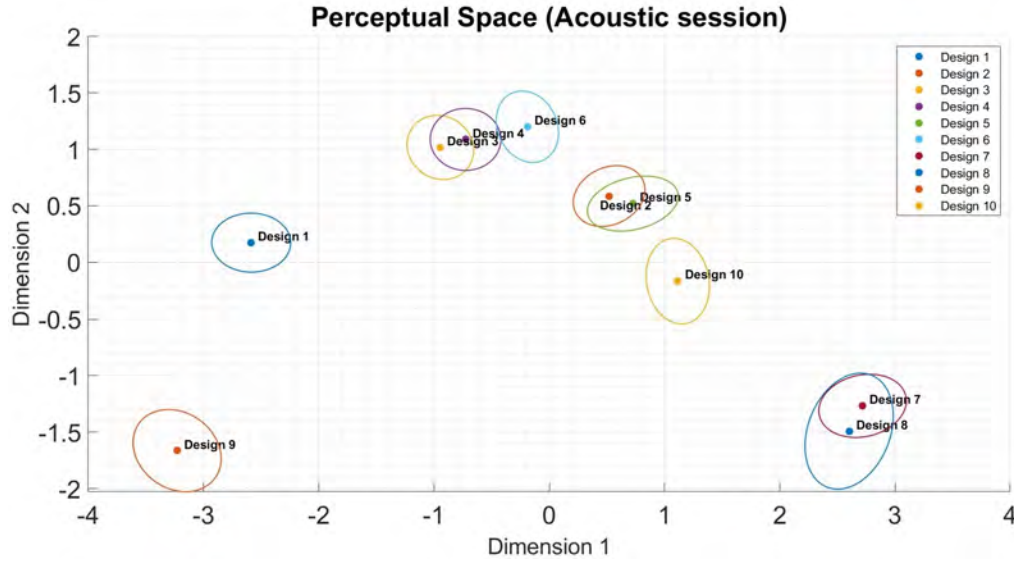


Figure 7.10: The perceptual space and the coordinates of the stimuli, corresponding to the acoustic session

equations:

$$\mathbf{P} = \begin{bmatrix} p_{11} & p_{12} & \cdots & p_{1j} & \cdots & p_{1n} \\ p_{21} & p_{22} & \cdots & p_{2j} & \cdots & p_{2n} \\ \vdots & \vdots & \ddots & \vdots & \ddots & \vdots \\ p_{i1} & p_{i2} & \cdots & p_{ij} & \cdots & p_{in} \\ \vdots & \vdots & \ddots & \vdots & \ddots & \vdots \\ p_{n1} & p_{n2} & \cdots & p_{nj} & \cdots & p_{nn} \end{bmatrix}, \quad \begin{aligned} p_{ij} &= \frac{N_{ij} + \frac{N_{D_{ij}}}{2}}{N_s} \\ p_{ji} &= \frac{N_{ji} + \frac{N_{D_{ij}}}{2}}{N_s} = 1 - p_{ij} \end{aligned} \quad (7.3.1)$$

where  $N_{ij}$  represents the frequency with which the  $i^{th}$  sound is favored over the  $j^{th}$  sound,  $N_{D_{ij}}$  signifies the count of instances in which responses indicated a high degree of similarity between the  $i^{th}$  and  $j^{th}$  sounds, characterizing them as 'very similar.'  $N_s$  stands for the total number of subjects in the study. The formula presented above combines dissimilarity and preference judgments, and this combination between dissimilarity and preference assessments results in a reduction in test duration and listener weariness.

Also, the 95% confidence intervals on preference scores are calculated using the bootstrap technique (e.g. see Weinberg et al. [1984]). Through bootstrap sampling, we obtained participant samples, computed proportion matrices, and derived preference scores. Finally, we estimated standard deviation and confidence intervals for the preference scores. Figures 7.11 and 7.12 depict the mean preference scores for both the mechanical and acoustic sessions, along with their respective 95% confi-

dence intervals related to the stimuli. Analyzing these visuals, it becomes evident that among all the designs, Design 2 stands out with the highest preference score in the mechanical session, while Designs 7 and 8 excel in the acoustic session.

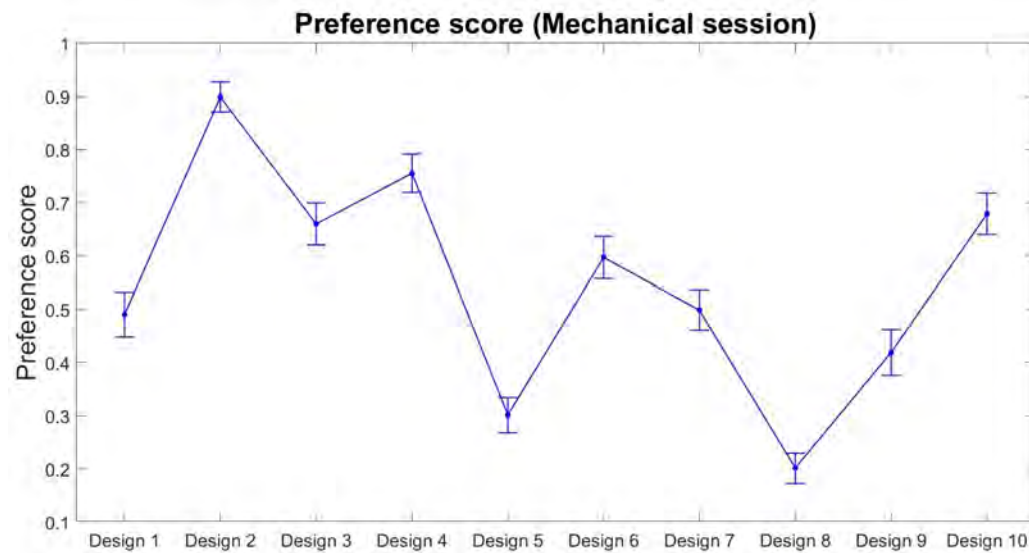


Figure 7.11: The preference scores corresponding to the different designs in the mechanical session

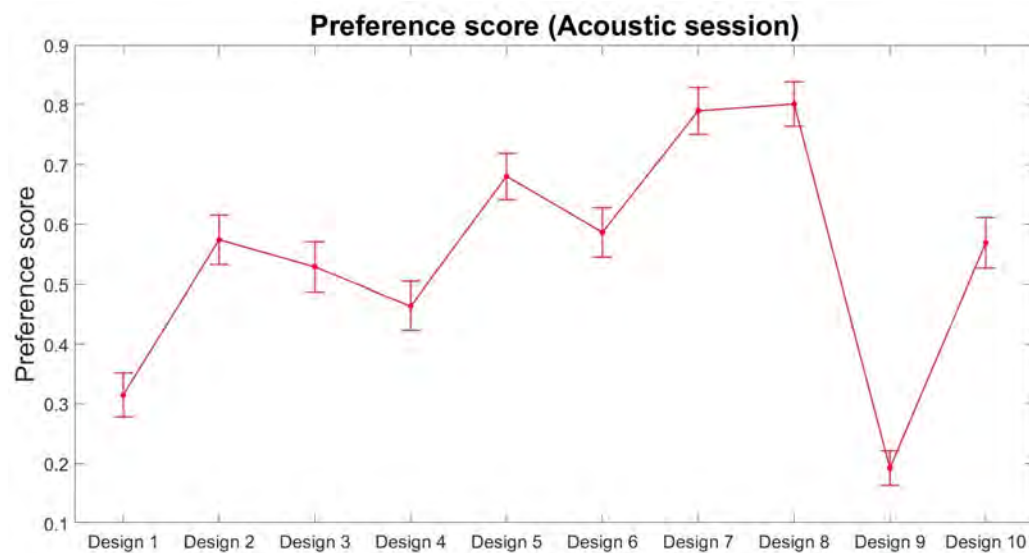


Figure 7.12: The preference scores corresponding to the different designs in the acoustic session

### 7.3.4 Correlation of preference with perceptual dimensions

Analyzing data from each test session, we observed a correlation between the preference score and one of the dimensions within the perceptual space. The statistical analysis revealed a significant correlation between preference and the 2nd dimension for the mechanical session, where the correlation between the preference and the 2nd dimension was found to be ( $r = 0.88, p = 0.001$ ) (see Figure C.5). On the other hand, for the acoustic session, the statistical analysis revealed a significant correlation between preference and the 1st perceptual dimension, where this correlation was ( $r = 0.97, p < 0.001$ ) (see Figure C.9).

Furthermore, Figures 7.9 to 7.12 illustrate a clear correlation between preference and the aforementioned perceptual dimensions. When we compare the perceptual space of the mechanical session with the preference scores, it becomes evident that the preference increases from the bottom to the top of the perceptual space (specifically, on Dimension 2) (see Figures 7.9 and 7.11, and for instance, follow Design 8 to Designs 2 and 4). On the other hand, for the acoustic session, we observe how the preference increases from the left side to the right side of the perceptual space (specifically, on Dimension 1) (see Figures 7.10 and 7.12, and for instance, follow Design 9 to Designs 8).

### 7.3.5 Impression of stimuli ranked in perceptual space

Based on our personal impressions while listening to the stimuli, we observed certain patterns in both the mechanical and acoustic sessions. In the mechanical session, Dimension 1 appeared to be associated with the progression from bass sounds to treble sounds, with the lowest and highest stimulus positions indicating the extremes of this transition. This shift is clearly illustrated, for example, when we compare the personal impressions of designs 9 and 8, where these designs have almost similar values of Dimension 2, but they differ significantly in Dimension 1, and highlighting the transition from bass to treble. On the other hand, in Dimension 2, there is a slight shift from loud to soft sounds, which becomes apparent, for instance, when comparing some designs like 2 and 5.

Moving on to the acoustic session, we found that Dimension 1 was primarily linked to a shift from loud to soft sounds, with the lowest and highest stimulus positions representing the contrast between these two audio characteristics. Still from listening, it became evident that Dimension 2 reflects a transition from bass to treble sounds.

### 7.3.6 Psychoacoustic analysis

In order to interpret the dimensions of perceptual space as well as the preference scores from the psychoacoustic point of view, these features were initially investigated through a listening study. The objective was to evaluate which auditory attributes could potentially explain each perceptual dimension and the preference score. Subsequently, a correlation analysis was performed between them and indices representing auditory attributes. For this purpose, the dBsonic sound analysis software has been used for calculating the psychoacoustic indices of the stimuli for each session. So, the psychoacoustic indices including loudness [sone], sharpness [acum], roughness [asper], tonality [Hz], and fluctuation [vacil] associated with the stimuli of each session were estimated and then the correlation of the indices with the dimensions of the perceptual space and preference score were investigated.

Zwicker's loudness calculation is based on ISO532B (Zwicker et al. [1991]) and DIN 45631 in dBsonic software (dBsonic Manual [2005]), leading to same loudness results, for example, for non-stationary environmental noises, as the Zwicker's loudness calculation from the software Artemis (Head Acoustics) based on the last version of the standards, ISO532-1 (2017) (cf. Legros [2020]). Also, the tonality was derived by the standard DIN 45681-2002 (e.g. see DIN45681:2005-03 [2005-03] and DIN45681:2006-08 [2006-08]), and the sharpness, roughness, and fluctuation were calculated based on the models developed by Aures [1985a,b]. Moreover, the spectral center of gravity (SCG), defined as the spectral centroid (SC) of the signal, has been calculated in Hz using MATLAB (e.g. see Trollé [2009], Engel et al. [2021]). The SC is used to describe the perceived brightness of timbre. A higher SC suggests more energy in higher frequencies, making a sound appear sharper, while a lower SC indicates more energy in lower frequencies.

Thus, we proceeded to investigate potential linear regression relationships between the psychoacoustic indices, perceptual space dimensions, and preference scores associated with the stimuli in the two test sessions, in order to find a model for the preference of the designs based on the psychoacoustic indices. Based on the available data, the regression analyses revealed a strong correlation between some indices and the perceptual dimensions and preference in the sessions with the both mechanical and acoustic excitations.

In the perceptual space of the mechanical session, Dimension 1 exhibited noteworthy correlations with the Sharpness and SC, as indicated by the statistical parameters ( $r = 0.71, p = 0.023$ ) and ( $r = 0.78, p = 0.008$ ), respectively (see Figures C.1 and C.2). Also, the statistical results demonstrated that the preference for the stimuli in the mechanical session exhibited a significant correlation with the loudness, with

statistical parameters ( $r = -0.83, p = 0.003$ ) (see FigureC.6). Although a notable correlation was observed between preference and the second perceptual dimension (as shown in subsection 7.3.4), Dimension 2 did not demonstrate a significant correlation with loudness in the mechanical session (its statistical parameters for testing the correlation were ( $r = -0.59, p = 0.07$ )) (see FigureC.4). The correlation coefficient sign and the difficulty to reach significance for this correlation coefficient were in line with our impression of a slight shift from loud to soft when listening to stimuli along this dimension. This result was linked to the weak variation in dB(A) between stimuli (cf. Table 7.4) resulting from the variation of the mechanical parameters of the sandwich panel (cf Table 7.3). It has to be mentioned that Dimension 2 could not pass the statistical tests regarding the correlation with other psychoacoustic and acoustic indices, too.

Regarding the acoustic session, notably, Dimension 1 showed a significant correlation with the loudness, with the statistical parameters ( $r = -0.95, p < 0.001$ ) (see Figure C.8). Moreover, Dimension 2 in the acoustic session displayed a significant correlation with Sharpness, supported by the parameters ( $r = 0.81, p = 0.005$ ) (see Figure C.10). On the other hand, the statistical results demonstrated that the preference score in the acoustic session exhibited a significant correlation with the loudness, with statistical parameters ( $r = -0.95, p = 0.001$ ) (see FigureC.11). As mentioned in Section 7.3.4, in the acoustic session, the preference exhibited a significant correlation with the 1st dimension of the perceptual space, too.

Furthermore, we conducted an examination of the relationship between preference and the SPL[dB(A)]. In the mechanical session, this correlation did not yield statistically significant results, as indicated by the parameters ( $r = -0.19, p = 0.588$ ). Conversely, during the acoustic session, unlike the mechanical session, we observed a statistically significant correlation between preference and SPL [dB(A)], supported by the parameters ( $r = -0.72, p = 0.018$ ). However, it's important to note that this correlation was weaker than the significant correlation between preference and loudness.

In any case, as a result, the above-mentioned statistical examination of the correlation between preference and loudness suggests the possibility of constructing a linear model for predicting the preference. Interestingly, our findings indicated that the coefficients of this model appear to be statistically consistent across the two independent sessions involving the mechanical and acoustic excitations. Such a linear model can take the form of the following equation:

$$P(s) = \alpha N(s) + \alpha_0 \quad (7.3.2)$$

Table 7.6: The statistical results associated with the regression model  $P(s) = \alpha N(s) + \alpha_0$  between the preference and loudness for the mechanical session

$R^2$ (adjusted)	<i>p-value</i>			<i>Estimated coefficients</i>		<i>Standard deviations</i>	
	Overall	$\alpha_0$	$\alpha$	$\alpha_0$	$\alpha$	$\alpha_0$	$\alpha$
0.66	0.003	$p < 0.001$	0.003	<b>2.329</b>	<b>-0.343</b>	0.420	0.081

Table 7.7: The statistical results associated with the regression model  $P(s) = \alpha N(s) + \alpha_0$  between the preference and loudness for the acoustic session

$R^2$ (adjusted)	<i>p-value</i>			<i>Estimated coefficients</i>		<i>Standard deviations</i>	
	overall	$\alpha_0$	$\alpha$	$\alpha_0$	$\alpha$	$\alpha_0$	$\alpha$
0.89	$p < 0.001$	$p < 0.001$	$p < 0.001$	<b>1.763</b>	<b>-0.228</b>	0.140	0.026

Here,  $N(s)$  represents the loudness in sones according to Zwicker's calculation method ISO532B, and  $P$  stands for the preference score corresponding to the stimulus  $s$ . Tables 7.6 and 7.7 display the coefficients derived for the aforementioned model, corresponding to both the mechanical and acoustic sessions. These coefficients were estimated using psychoacoustic data (i.e. the preference scores and loudness of the stimuli) associated with these two independent sessions with mechanical and acoustic excitations. Tables 7.6 and 7.7 indicate that the coefficients of the model in both sessions are statistically significant. The adjustment quality of these two preference models is displayed in Figures 7.13 and 7.14 for the two sessions. To compare the two models, we cross-predicted preference scores between acoustic and mechanical sessions. Figures 7.15 and 7.16 are displaying the prediction quality of the two preference models. It led to a good prediction quality when applying mechanical preference model on the acoustic session. Such a good prediction quality was not obtained when applying the acoustic preference model on the mechanical session. Thus it is proposed to consider only the mechanical preference model to be used for the two types of excitation.

### 7.3.7 Mechanical parameters

When examining the statistical correlation of the physical parameters of the designs, including the mechanical, geometrical, and equivalent parameters (see Table 7.3), with the dimensions of the perceptual space as well as preference scores, the problem becomes increasingly intricate. The complexity arises from the definitions and relationship of the parameters of the designs. Some of these parameters are functions of others, and notably, there are non-linear relationships among some of these parameters. Consequently, the task of establishing a linear regression model between certain physical parameters of the designs and the perceptual dimensions

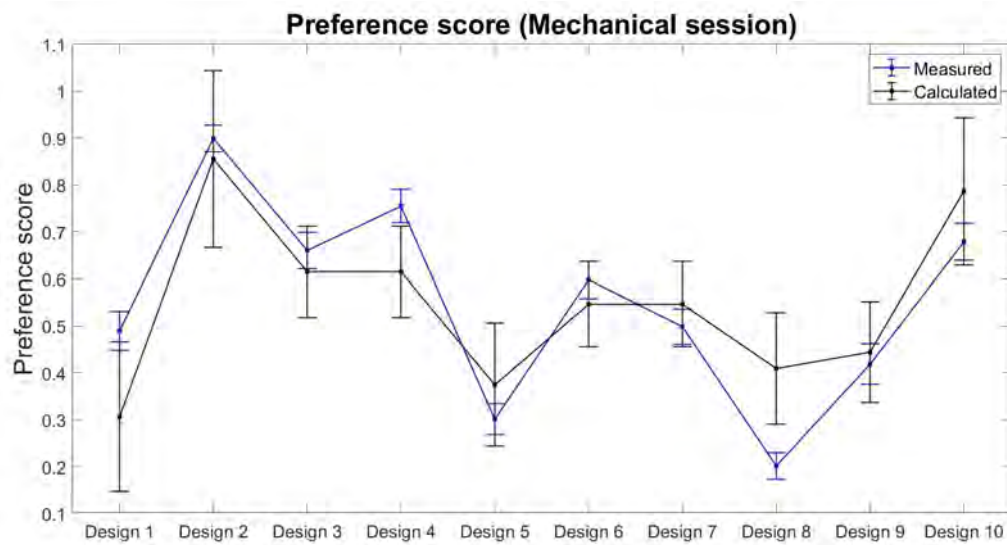


Figure 7.13: Adjustment quality for the mechanical preference model: the comparison of the measured and calculated preference scores corresponding to the mechanical session, along with their respective 95% confidence intervals

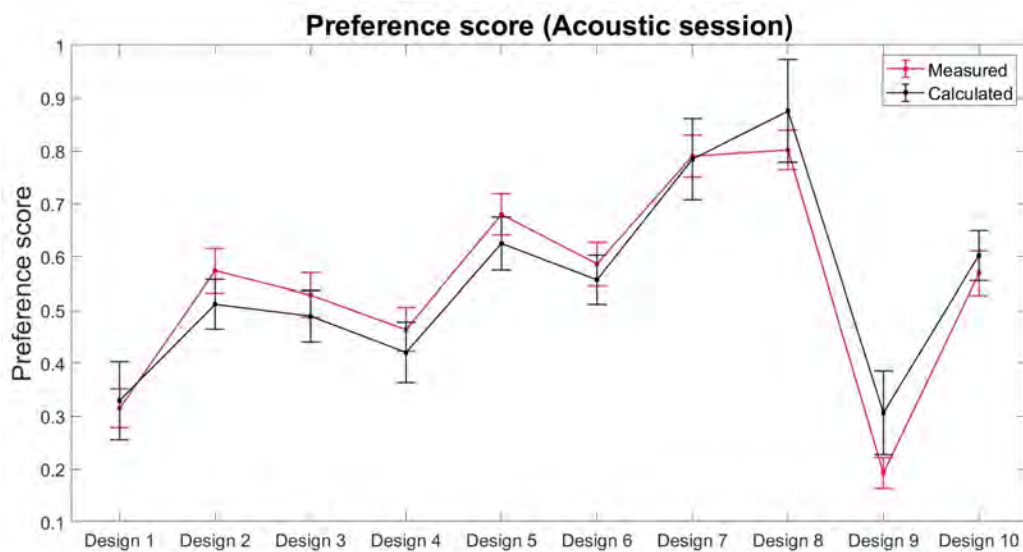


Figure 7.14: Adjustment quality for the acoustic preference model: the comparison of the measured and calculated preference scores corresponding to the acoustic session, along with their respective 95% confidence intervals

and preference scores becomes notably challenging, particularly when dealing with a wide range of variations of the parameters.

Herein, the statistical analyses indicated that the stiffness-to-mass ratio correlates with dimension 1 in both sessions with mechanical and acoustic excitations (see Fig-



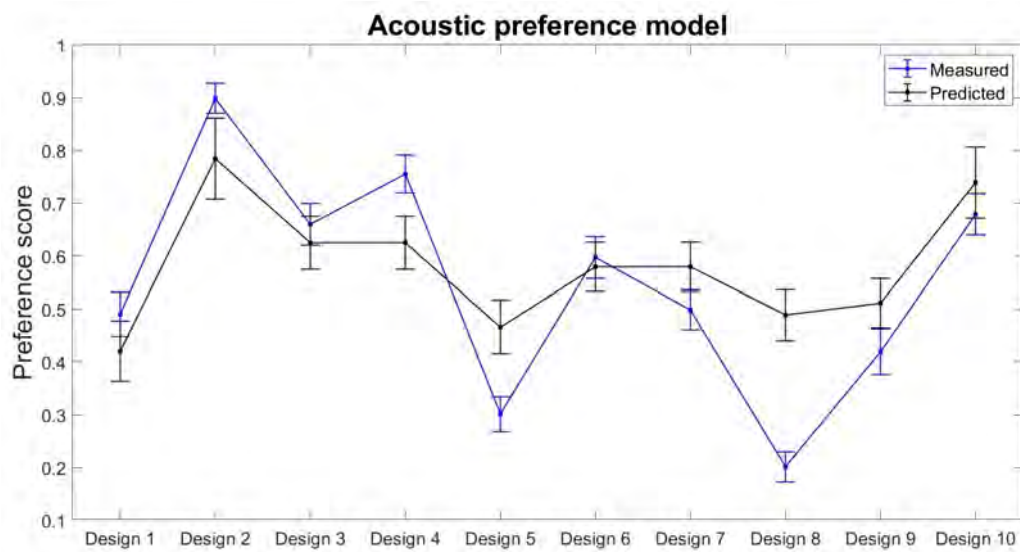


Figure 7.15: Prediction quality of the acoustic preference model: the comparison of the measured preference scores of the mechanical session with the one predicted by the acoustic preference model, along with their respective 95% confidence intervals

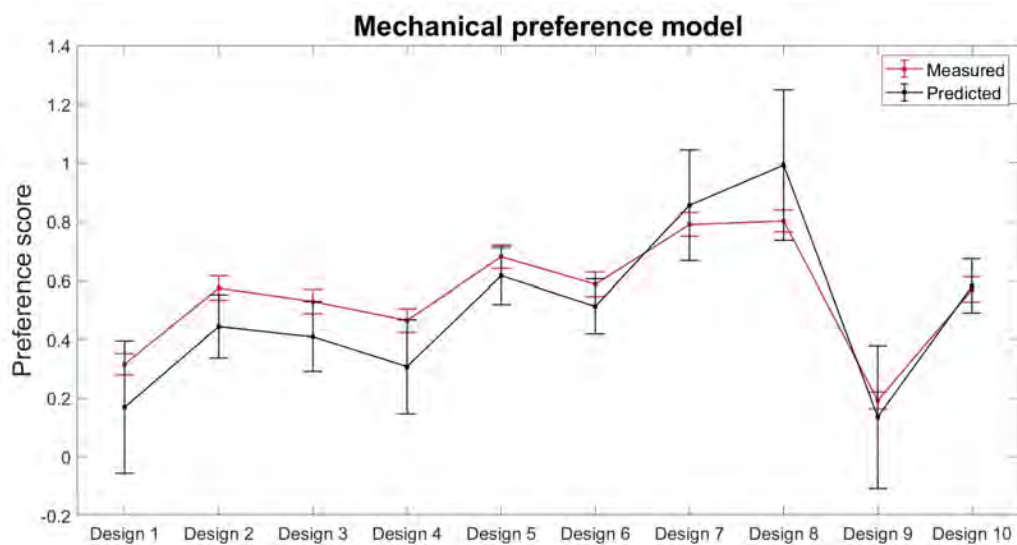


Figure 7.16: Prediction quality of the mechanical preference model: the comparison of the measured preference scores of the acoustic session with the one predicted by the mechanical preference model, along with their respective 95% confidence intervals

ures C.3 and C.7). On the other hand, in the mechanical session, dimension 1 is also statistically associated with the sharpness (see Figure C.1), while in the acoustic session, it is connected with the loudness (see Figure C.8). The stiffness-to-mass ratio is the ratio of the bending stiffness and surface mass density of the panel that di-

rectly influence both the amplitude and natural frequency of the frequency response (refer to Eqs.2.3.5 and 2.3.6). From the theoretical point of view, this parameter is capable of impacting the amplitudes at natural frequencies and consequently quantities related to the amplitude and energy of the signal such as sound pressure level and loudness. Moreover, since the stiffness-to-mass ratio is considered as a crucial parameter in determining the values of the natural frequencies of a vibrating panel (e.g. see Eqs.3.1.1 and 3.1.4), its variation leads to a shift of natural frequencies (as illustrated in Figure C.13 in Appendix C), and then leads to variations of indices, such as spectral centroid (SC) and sharpness, which account for the distribution of the energy according to the frequencies. Herein, upon analyzing the both sessions, it interestingly becomes evident that in the mechanical excitation session, the Dimension 1, which is connected to the stiffness-to-mass ratio, is also linked it to sharpness and spectral centroid (see Figures C.1 and C.2). And similarly, in the acoustic excitation session, the Dimension 1, which is connected to the stiffness-to-mass ratio, is also linked to loudness and sound pressure level (SPL). Such results are explained by the fact that considering the acoustic excitation applied to all points of the surface of the vibrating panel, the stiffness-to-mass ratio variations impact amplitudes at more natural frequencies, compared to the mechanical excitation. Hence, it could predominantly influence the loudness and sound pressure level.

Figures C.13 and C.14 in Appendix C illustrate a SPL comparison among designs with varying stiffness-to-mass ratios for the sessions with mechanical and acoustic excitations, respectively. The designs have been chosen in a manner that aligns their changes in the perceptual space as closely as possible with dimension 1. These figures demonstrate how, changes in the stiffness-to-mass ratio for the mechanical session can influence and shift resonance frequencies, and also, in the acoustic session, they showcase how such variations can impact the amplitude of the sound pressure level.

Now, at this step, the primary objective is to identify critical physical parameters that may potentially influence both preference and perceptual dimensions. Discovering these influential parameters, which can impact preferences, proves valuable in fine-tuning mechanical parameters during the design phase of composite structures in future studies. Additionally, given the observed correlation between perceptual dimensions and preferences, understanding such relationships between the physical parameters and perceptual dimensions may also prove beneficial in the design phase of composite structures. Therefore, in the initial step, we examined the correlation and linear regression between each individual parameter of the designs (see Table 7.3), the perceptual dimensions, and the preference scores corresponding to both sessions. Moreover, we also had certain experimental limitations in varying specific parameters. For instance, when the number of variations for each parameter

was increased, we had to correspondingly increase the number of stimuli, potentially leading to a longer duration for the psychoacoustic test. As a result, we had only a limited number of variations for some parameters (see Table 7.3). Therefore, considering such limitation, the primary objective of the statistical analysis in this phase was to identify the most influential parameters that could impact the auditory perception and preference. Meanwhile, the parameters that exhibited the most variation are the bending stiffness, equivalent Young modulus, mass density, and stiffness-to-mass ratio (see Table 7.3). This variation proved advantageous for these parameters, attaining more robust results in the statistical analysis, compared to other parameters. Remarkably, the statistical analysis revealed that the stiffness-to-mass ratio (denoted as  $D_t/M$ ) exhibited the strongest correlation among all the physical parameters with the perceptual dimensions. Specifically, the 1st dimension in both the mechanical and acoustic sessions, along with the preference score in the acoustic session, displayed the highest correlations with the stiffness-to-mass ratio when compared to other physical parameters. The corresponding correlations, denoted as  $r$ , of  $D_t/M$  with the 1st dimension in both the mechanical and acoustic sessions, as well as with the preference score in the acoustic session, were found to be ( $r = 0.85, p = 0.002$ ), ( $r = 0.90, p < 0.001$ ), and ( $r = 0.85, p = 0.002$ ), respectively (also, see Figures C.3), C.7, and C.12. These correlation values emphasize the statistical significance of the relationships between the perceptual space and the preference score with the stiffness-to-mass ratio. However, in the mechanical session, the preference did not exhibit any significant statistical linear relationships with any of the physical parameters.

As a result, we started an investigation into the regression-based statistical analyses between several physical parameters and preference scores, in order to find a model for calculating the preference scores by means of the mechanical parameters. In this regard, we specifically selected parameters that maintained statistical and physical independence from one another. We subjected 175 unique combinations of the parameters of the designs to the regression modeling. These combinations include single, double and triple combinations of mechanical parameters. Among these combinations, we were able to identify a suitable linear regression model for the acoustic session. However, no reasonable or acceptable linear regression model could be found for the mechanical session when considering the linear relationship between mechanical parameters and preference. Consequently, the presence of nonlinear terms in this model was suspected. Hence, for the mechanical session, we also explored various nonlinear regression models, including terms with a power of 2. Ultimately, from the array of tested regression models for the both sessions, we selected the one with the highest adjusted coefficient of determination,  $R^2$ , while tak-

ing into account the independency and physical meaningfulness between the chosen parameters. Tables 7.8 and 7.9 provide a comprehensive overview of the statistical parameters associated with the regression models, which was developed to model the preference scores in the two sessions with respect to the mechanical parameters. In fact, in two sessions with inherently different excitations, it can not be expected to achieve identical models of mechanical parameters with the same coefficients. It is important to note that the coefficients of these models also depend on other factors like characteristics of mechanical and acoustic excitations. However, from these two models, we can reach the critical mechanical parameters that determine the preference scores. Notably, the regression analyses in the both sessions showed that the preference scores depend on the same mechanical parameters: stiffness-to-mass ratio  $D_t/M$  and loss damping factors  $\eta$  (c.f. Tables 7.8 and 7.9). In these tables, the p-values associated with the regression analyses and the estimated coefficients, considering a 95% confidence level, are acceptable and statistically significant.

Furthermore, to independently evaluate the correlation between preferences and these crucial parameters (the stiffness-to-mass ratio  $D_t/M$  and loss damping factors  $\eta$ ), and to ensure that the preferences are dependent on these parameters, we conducted partial correlation analyses. In this context, we examined the partial correlation between these parameters and preferences. For the session with mechanical excitation, first we calculated the partial correlation between the loss damping factor  $\eta$  and the preference score, while controlling for the effects of  $D_t/M$  and the nonlinear term  $(D_t/M)^2$ . The estimated partial correlation of  $\eta$  with the preference and the corresponding p-value were ( $r = 0.86, p = 0.006$ ). Similarly, we performed a partial correlation between the stiffness-to-mass ratio  $D_t/M$  and the preference score, while controlling for the effects of  $\eta$  and the nonlinear term  $(D_t/M)^2$ , yielding the result ( $r = 0.89, p = 0.002$ ). Likewise, for the session with acoustic excitation, we conducted the partial correlation analyses to obtain the partial correlations of  $D_t/M$  and  $\eta$  with preferences. This was done while controlling for the effect of one parameter on the correlation of the other. The partial correlations of  $\eta$  and  $D_t/M$  were obtained equal ( $r = -0.80, p = 0.009$ ) and ( $r = 0.95, p < 0.001$ ), respectively. As can be seen, in all these results, the partial correlations are significant. Notably, the partial correlation between the stiffness-to-mass ratio  $D_t/M$  and preference for the acoustic session showed an increase compared to the value of the ordinary correlation mentioned before.

Remarkably, in both of the aforementioned regression models of the two sessions, the stiffness-to-mass ratio and the loss damping factor  $\eta$  emerges as crucial factors in determining the preference. For instance, when we compared the preference plot corresponding to the acoustic session with the properties of the designs (c.f. Table

Table 7.8: The regression model for preference  $P$  in the mechanical session in relation to the mechanical parameters  $\eta$ , and  $D_t/M$ , where  $r$  is the correlation between the modeled and measured preference, and the model is defined as

$$P = \alpha_0 + \alpha_1\eta + \alpha_2D_t/M + \alpha_3(D_t/M)^2$$

	<i>p-value</i>					<i>Estimated coefficients</i>				<i>Standard deviations</i>				
$R^2$ (adjusted)	overall	$\alpha_0$	$\alpha_1$	$\alpha_2$	$\alpha_3$	$\alpha_0$	$\alpha_1$	$\alpha_2$	$\alpha_3$	$\alpha_0$	$\alpha_1$	$\alpha_2$	$\alpha_3$	$r$
0.86	$p < 0.001$	0.02	$p < 0.001$	$p < 0.001$	$p < 0.001$	<b>-0.304</b>	<b>5.290</b>	<b>0.001</b>	<b>-8.312E-07</b>	0.102	0.009	2.569E-04	1.310E-07	0.94

Table 7.9: The regression model for preference  $P$  in the acoustic session in relation to the mechanical parameters  $\eta$ , and  $D_t/M$ , where  $r$  is the correlation between the modeled and measured preference, the regression model is defined as

$$P = \alpha_0 + \alpha_1\eta + \alpha_2D_t/M$$

	<i>p-value</i>				<i>Estimated coefficients</i>			<i>Standard deviations</i>			
$R^2$ (adjusted)	Overall	$\alpha_0$	$\alpha_1$	$\alpha_2$	$\alpha_0$	$\alpha_1$	$\alpha_2$	$\alpha_0$	$\alpha_1$	$\alpha_2$	$r$
0.87	$p < 0.001$	$p < 0.001$	0.01	$p < 0.001$	<b>0.538</b>	<b>-3.443</b>	<b>3.93E-04</b>	0.084	9.75E-01	5.10E-05	0.95

7.3 and Figure 7.12), it becomes evident that there is a strong correlation between preference and the stiffness-to-mass ratio (expressed as  $D_t/M$ ). Designs with a high stiffness-to-mass ratio, such as Designs 7 and 8, consistently achieve high preference scores, whereas designs with low preference scores, such as Design 9 and 1, consistently exhibit the lowest preference scores among all the designs (c.f Table 7.3 and Figure 7.12). In Tables 7.8 and 7.9, the parameter  $r$  represents the correlation between the preference scores calculated via the regression models and the measured preference scores, demonstrating a strong correlation between the calculated and measured ones. Additionally, when concluding the analysis of the mechanical parameters, it is essential to note that, from a statistical perspective, achieving an accurate and correct estimation of the parameters in the aforementioned models necessitates more measurements gathered from a broader range of designs and a greater variety of parameter variations.

### 7.3.8 Optimal designs

For completing the analyses, a question emerges regarding the optimal designs among those analyzed. In this scenario, guided by the results from the analysis of the preference scores, we will delve into a multi-objective optimization problem where the concept of the Pareto Front can offer a set of optimal solutions. In the context of multi-objective optimization, the Pareto Front defines the collection of optimal solutions where no alternative solution surpasses them in all objectives simultaneously. It comprises the non-dominated solutions, often referred to as Pareto-optimal solutions, which encompass all conceivable optimal choices for the multi-objective optimization problem. The Pareto Front is formally defined as follows (e.g. see

Branke [2008], Deb [2011]):

$$\text{PF} = \{x \in X \mid \nexists \hat{x} \in X \text{ where } x \prec \hat{x}\} \quad (7.3.3)$$

where PF represents the Pareto Front,  $X$  denotes the set of candidate solutions (like the 10 designs in the current study), and  $x$  and  $\hat{x}$  represent individual solutions in the set  $X$ .  $\nexists$  signifies the "there does not exist" condition, and  $\prec$  represents dominance,  $\hat{x} \prec x$  indicating that  $x$  dominates  $\hat{x}$  (i.e.,  $x$  is at least as good as  $\hat{x}$  in all objectives and strictly better in at least one). From a perceptual standpoint, when considering the preference scores in both mechanical and acoustic sessions, we engage in a two-objective optimization. Figure 7.17 displays the 10 designs tested in the psychoacoustic assessment, revealing the Pareto Front comprising Designs 2, 6, 7, and 8 as the optimal non-dominated solutions. These designs consistently outperform others in terms of preference scores in both sessions. For instance, Design 2 outperforms Designs 1, 3, 4, 9, and 10 in both mechanical and acoustic sessions. When comparing Design 2 and Design 7, neither can dominate the other, as each excels in one of the preference score categories, but Design 7 exhibits superior preference scores in both mechanical and acoustic sessions when compared to Designs 1, 5, and 9. This suggests that Design 7 has outperformed these designs.

Upon closer examination of the Pareto Front, featuring designs 2, 6, 7, and 8, we can identify most optimal solutions amongst these designs again. For instance, analyzing the 95% confidence intervals represented as ellipses in two-dimensional space, we observed that in the acoustic session, there is no significant difference between the preference scores of designs 2 and 6. However, when considering the mechanical session, design 2 proves to be superior to design 6. Similarly, comparing design 7 to design 8 and factoring in confidence intervals, we find no significant differences in the acoustic session, but in the mechanical session, design 7 outperforms design 8, making it the more optimal choice. Hence, the Pareto Front could actually identify designs 2 and 7 as the optimal choices out of the 10 designs under study.

Indeed, these two designs represent the best options from a psychoacoustic perspective, although with different mechanical parameters. Now, to determine the most suitable choice for our specific application, we must emphasize the mechanical properties of these optimal solutions. Referring to Table 7.3, Design 7 exhibits a superior stiffness-to-mass ratio (for instance, in certain applications such as aircraft or robotic structure design, this ratio holds critical significance when selecting materials for structural components (e.g. see Shearer and Cesnik [2007], Kim et al. [2016], Warwick et al. [2019], Pires et al. [2022])). However, Design 2 is lighter than Design 7 (see Table 7.3). Furthermore, it is worth noting that what makes these Pareto solutions, namely Designs 2 and 7, particularly noteworthy is how they vary

depending on the characteristics of the face sheets during the design phase. Design 2 aimed to assess the influence of Young's modulus of the face sheets  $E_f$ , while design 7 aimed to evaluate the effect of face sheet thickness  $h_f$ . These Pareto results underscore the substantial impact of face sheet characteristics in composite sandwich panel design (c.f. Table 7.3 and Figure 7.17).

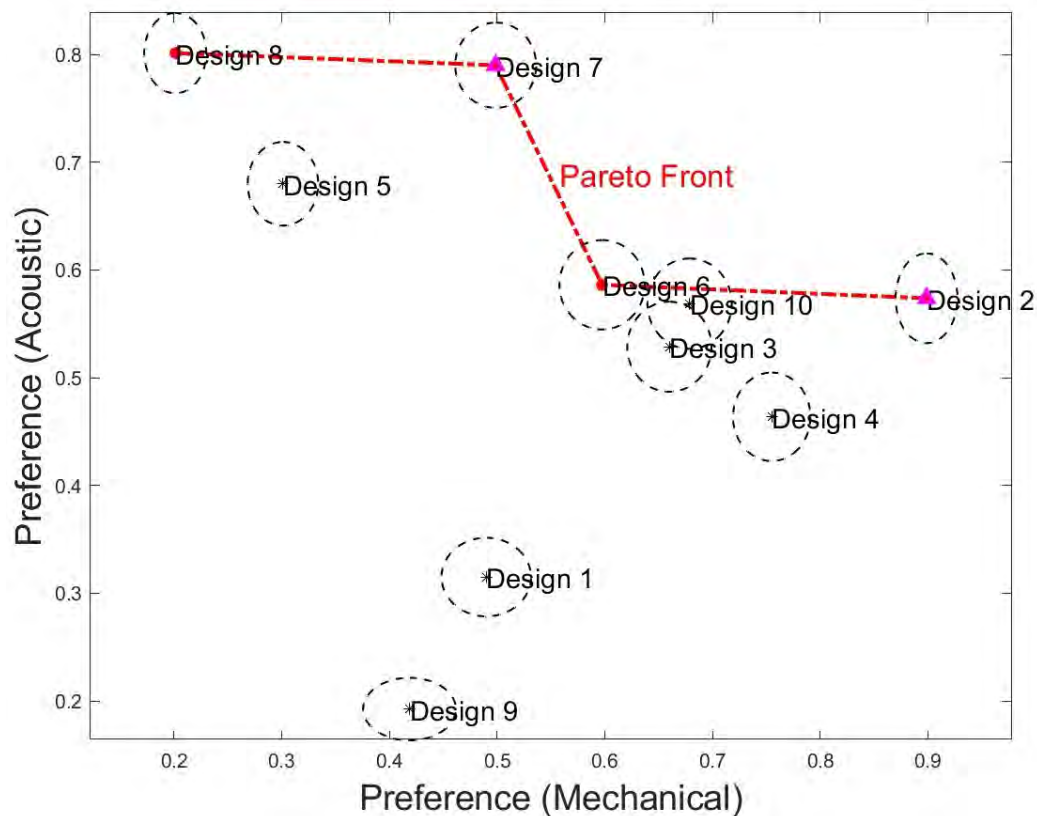


Figure 7.17: The Pareto Front: the graph displays the Pareto optimal solutions (the solutions located on the red dash-dot line) in a 2D space of solutions, illustrating the preference scores for both mechanical and acoustic sessions, displaying the preference scores of the 10 designs accompanied by their respective 95% confidence intervals

## 7.4 Summary and discussion

This chapter primarily focuses on the design and optimization of vibrating composite panels from a perceptual standpoint. We developed 10 composite panel designs, building upon the model refined and updated in Chapter 5. We carefully examined the geometrical and mechanical parameters of the composite vibrating panels, including the core shear modulus, drawing from insights gained from similar previous studies. These parameters were tried to be meticulously arranged and planned for

the psychoacoustic testing.

The stimuli corresponding to each design were simulated using the updated model and the Rayleigh integration method. Two separate sessions of psychoacoustic experiments were conducted: one based on mechanical excitation and the other based on acoustic excitation. After obtaining the psychoacoustic measurements, we pre-processed the data using AHC (Ascending Hierarchical Clustering) to detect and remove outliers.

Subsequently, we applied the INDSCAL method, the Multidimensional Scaling technique, to construct the perceptual space associated with the two sessions. Before constructing these perceptual spaces, we utilized the L-curve method to determine the optimal number of dimensions required. Once the perceptual spaces were created, we computed preference scores for each session and analyzed their correlation with the dimensions of the perceptual space.

Before investigating the psychoacoustic analyses, we discussed the perceptual impressions and feelings elicited by the stimuli. The psychoacoustic analyses were then conducted based on the psychoacoustic indices obtained from dBsonic software. These analyses shed light on how psychoacoustic indices relate to perceptual dimensions and their impact on preference scores.

Notably, all the psychoacoustic results highlighted that loudness had the most significant effect on preference in both sessions even when weak differences are observed in dB(A). To address this, we developed a linear model for predicting preference based on loudness. Additionally, we explored the correlations between mechanical parameters and the perceptual space as well as the preference score. Our findings revealed that the stiffness-to-mass ratio and the loss damping factor were the most influential physical parameters among all the parameters considered. Furthermore, we introduced two regression models that relate the preference observed in the two sessions to various mechanical parameters. Finally, among all the designs, an attempt was made to identify the optimal designs using the Pareto method of multi-objective optimization. The selected designs as the optimal Pareto solutions revealed that the Young modulus and the thickness of the face sheet are the most influential parameters for designing the optimum designs, where these two parameters,  $E_f$  and  $h_f$ , are the determining factors for the stiffness-to-mass ratio  $D_t/M$  that also served as a determining factor for the preference score. It is worth mentioning that such relationship between the mechanical properties and the auditory attributes has been investigated in other studies, such as Faure and Marquis-Favre [2005], Miloudi et al. [2010]. The research of Faure and Marquis-Favre [2005] revealed a significant correlation between the mechanical properties of an isotropic plate, specifically its thickness, Young's modulus, and damping factor, and the preference score. Further-



more, Miloudi et al. [2010] conducted an evaluation of the impact of various physical parameters on the perception of sound generated by various impacted plates. This evaluation was carried out through a combination of design of experiments methodology and preference testing. The model and statistical tools employed in Miloudi et al. [2010] enabled the assessment of the influence of predominant factors, including thickness, damping, material composition, and boundary conditions, on both radiated noise and the associated perception of sounds.

Furthermore, herein, from both theoretical and perceptual points of view, we could observe how the critical parameter, stiffness-to-mass ratio  $D_t/M$ , is capable of influencing certain psychoacoustic indices: loudness, sharpness, and SC. Such effects of mechanical parameters on various psychoacoustic indices have also been investigated in other studies (e.g. see Atamer and Altinsoy [2021]).

# Chapter 8

## General conclusion

After conducting a comprehensive analysis of flexural vibration models for composite panels, examining the vibroacoustic behavior of composite panels under both acoustic and mechanical excitations, as well as investigating the updating procedures required for enhancing the models, and consequently conducting psychoacoustic assessments of the simulations and designs, this part aims to summarize the key accomplishments of the thesis.

### 8.1 Mathematical model analysis

In this thesis, first we have conducted a thorough analytical examination of the vibroacoustic characteristics exhibited by composite panels. The research delve into the intricacies of the models and partial differential equations governing these vibrational behaviors, with particular focus on both 4th and 6th order problem formulations. To achieve this objective, we discussed in-depth the 6th and 4th order problems that govern the vibrational behavior of various composite panels (see Chapter 2). These problem formulations rely on specific assumptions, namely the Kirchhoff-Love assumptions for the 4th order problem and the Mead assumptions for the 6th order problem. The Kirchhoff-Love assumptions, which neglect transverse shear and rotary inertia effects, validate the applicability of the 4th order problem to thin composite panels. Conversely, the Mead assumptions extend the relevance of the 6th order problem to sandwich composite panels by accounting for shear effects in the flexural motions of these panels. Throughout this thesis, these problem formulations have served as the cornerstone upon which our simulations and mathematical models have been constructed. We have studied both the 4th and 6th order problems to simulate and model the vibroacoustic behavior of various panels, encompassing

isotropic, composite laminate, and composite sandwich panels. Subsequently, we subjected these models and simulations to careful examination through real laboratory experiments. To accomplish this, we tested different panel types under two distinct laboratory conditions: one involving diffuse acoustic field excitation and the other involving mechanical excitation. Furthermore, within the framework of this thesis, the 4th and 6th-order problems have provided the foundational principles for the development of a hybrid updating method. This method has proven invaluable for precise vibroacoustic modeling of composite panels. As part of our research, we planned to subject the results obtained from our simulations and models to perceptual validation and assessment in specialized psychoacoustic tests. In addition to their role in theoretical analysis, these problem formulations have been instrumental in guiding the design and psychoacoustic optimization of a specific type of composite panels.

## 8.2 Vibroacoustic modeling

In the context of the thesis, a primary objective was to establish a comprehensive framework for modeling the vibrational and acoustic behavior of panels excited by acoustic and mechanical loads. This framework was essential for synthesizing sounds radiated from the vibrating panels, which in turn was required by the psychoacoustic tests. For this purpose, regarding the acoustic excitation, the methodology began with the formulation of a theoretical strategy and the application of stochastic analyses to address the modeling of the panels excited by a Diffuse Acoustic Field (DAF). As mentioned before, specifically, we focused on the 4th and 6th order problems as the foundational elements of our vibroacoustic models. Subsequently, we obtained a stochastic model for the spectrum of the sound pressure level produced by the vibrating panels. Afterwards, the methodology was examined by certain numerical simulations and laboratory experiments. We endeavored to ideally generate a DAF excitation field in a controlled condition during the laboratory experiments. For this purpose, an acoustic test cabin was utilized, which allowed the experiments to generate and apply a DAF excitation to various sample plates. The laboratory experiments involved four isotropic sample panels of different sizes and one composite panel. Subsequently, we compared the experimental results with our mathematical models and simulations. These comparisons served to empirically validate the stochastic analyses employed in the vibroacoustic modeling of panels excited by DAF. Furthermore, the experimental results obtained from both the isotropic and composite panels affirmed the effectiveness of our 4th and 6th order problem-based approach. As a result, the proposed methodology also showed its ability in accu-

rately synthesizing the sounds required for psychoacoustic tests and analyses of the panels excited by a diffuse acoustic field (see Chapter 3).

Similarly, regarding the mechanical excitation, we conducted an extensive investigation into vibroacoustic modeling for composite panels excited by a point-wise mechanical load, which involved a combination of theoretical analysis and practical experimentation. To achieve this, a series of laboratory experiments were carried out within an anechoic chamber (see Chapter 4). These experiments incorporated laser Doppler vibrometry and sound pressure level measurements and were performed on various panel types, including a thick composite panel consisting of a Nomex honeycomb core and CFRP facesheets, a thin composite panel made of CFRP laminate, as well as two isotropic plates composed of steel and aluminum. These additional isotropic plates were included to provide further validation for the vibroacoustic models. The results obtained from these experiments validated the models used for vibroacoustic modeling of the composite panels, and they also enabled us to update the models via the proposed updating method. These updated models are essential for achieving the level of modeling accuracy required to address psychoacoustic concerns and undergo rigorous perceptual validation.

### 8.3 Hybrid updating method

In this thesis, a novel hybrid updating approach adapted for vibroacoustic modeling of composite panels was developed and proposed. This approach was developed to enhance models obtained by the 4th and 6th order problems. It relied on the hierarchical functions for analytical problem formulation, the IWC<sup>1</sup> technique for initial parameter estimation, and utilized least squares optimization methods. The hybrid approach employed the aforementioned techniques and methods sequentially, employing their unique strengths at each stage to complement one another effectively. Hence, the method's efficiency was achieved through the systematic implementation of the established capabilities of these methods, facilitating the controlled evaluation of parameters while eliminating time-consuming trial and error procedures.

The proposed hybrid approach was examined through the laboratory experiments conducted under the mechanical excitation conditions, including the LDV and SPL measurements. So, the laboratory experiments indicated that the results of the updating procedures achieved a remarkable level of consistency among all collected data, encompassing laboratory vibroacoustic measurements, mathematically enhanced simulations via updating procedures, and preliminary mechanical parameter infor-

---

<sup>1</sup>Inhomogeneous Wave Correlation

mation obtained from previous similar studies. This consistency provided strong evidence of the capabilities of the proposed hybrid approach for model and parameter updating, particularly in addressing the fourth and sixth order problems, with a specific focus on thin and thick composite panels. Accordingly, these findings of the updating approach enabled us to conduct precise simulations based on the updated models that are essential for the integrated design of composite panels, encompassing both vibroacoustic and psychoacoustic aspects, as used in other parts of the thesis (for additional information refer to Chapter 5).

## 8.4 Psychoacoustic assessment

At the final stage of this thesis, both the models and the synthesized sounds played a crucial role in assessing the composite panel designs from a perceptual perspective. Consequently, it became necessary to subject the models and synthesized sounds to an auditory assessment. As a result, this thesis not only presented the psychoacoustic processes essential for validating the models but also aimed at achieving a precise modeling of vibrating panels from a perceptual standpoint.

Within the scope of this thesis, a psychoacoustic experiment was conducted in the three sessions to assess the models used in vibroacoustic modeling of composite panels. The modeling and simulations were subsequently confirmed through psychoacoustic analyses, underscoring the potential benefits of considering both vibroacoustic and psychoacoustic perspectives in composite panel design. To this end, a psychoacoustic test was conducted across the three distinct sessions, each with a specific focus. One session aimed to psychoacoustically evaluate simulations performed with mechanical excitation, another session focused on psychoacoustic assessments of simulations using acoustic excitation, and the final session was dedicated to psychoacoustically determining the optimal value of the maximum frequency (i.e., the cut-off frequency) in the simulations (see Chapter 6).

Additionally, building upon the preceding laboratory vibroacoustic experiments, we employed a pairwise comparison approach to evaluate dissimilarities between the recorded and simulated stimuli. Following the psychoacoustic tests for the three sessions, we employed clustering and dendrogram analysis to identify outliers within the participant data. Subsequently, the multidimensional scaling approach, specifically INDSCAL, was employed to establish the perceptual space, accounting for perceived distances between the stimuli. The results indicated that the simulated stimuli closely resembled the recorded stimuli within the perceptual space. These findings were further validated through statistical tests and confidence intervals obtained from bootstrap analyses, affirming the credibility of the models from a per-

ceptual perspective.

## 8.5 Composite panel design

The final mission of the thesis was primarily dedicated to the design and optimization of vibrating composite panels, with a particular focus on their perceptual aspects. For this purpose, we produced certain composite panel designs, building upon the updated models we had developed earlier. Following this, a series of psychoacoustic laboratory experiments were carried out on these designs, each possessing distinct mechanical and geometrical properties. The meticulous examination encompassed both the geometrical and mechanical parameters of the composite vibrating panels, including the core shear modulus. These parameters were thoughtfully organized and planned in preparation for the psychoacoustic testing phase, drawing upon insights obtained from similar prior studies. Of particular note, all psychoacoustic results underscored that loudness held the most significant effect on the preference in both testing sessions. Thus, we constructed a linear model for predicting preference based on loudness. Interestingly, both independent sessions yielded similar regression models for predicting preference associated with each design, based on the loudness of the radiated sound. Furthermore, we delved into the correlations between mechanical parameters and the perceptual space, as well as the preference scores. The findings in the both sessions illuminated that the stiffness-to-mass ratio and the loss damping factor stood out as the most influential physical parameters among all those considered. Additionally, we introduced two regression models that establish a connection between the preference observed in the two sessions and various mechanical parameters. Ultimately, when taking into account the preferences expressed in both sessions for both types of excitation, and considering the stiffness-to-mass ratio, the optimal design can be identified among all the proposed designs (see Chapter 7).

## 8.6 Perspectives

Now, we can conclude the thesis by exploring various perspectives for future studies. Concerning vibroacoustic experiments, we can conduct additional laboratory experiments using different configurations, materials, and dimensions of composite panels under varying boundary conditions and excitations. By increasing the number of these laboratory experiments, along with obtaining further validations, we can enhance the updated models with more measurements. For instance, in future

studies, when considering a composite sandwich panel with CFRP face sheets or a CFRP laminate, different layouts for constructing the composite panel layers can be examined. So, for the joint psychoacoustic and vibroacoustic design of the composite panel, different laminate layouts and their effects on perceptual dimensions, psychoacoustic indicators, and ultimately, preference scores, can be investigated. Additionally, concerning laboratory experiments, we can examine other types of sandwich panels like those with CFRP face sheets and honeycomb aluminum cores, which have numerous applications in aerospace studies. Then these panels can be thoroughly studied in psychoacoustic assessments.

Also, in future psychoacoustic studies, the mechanical and geometrical parameters can be tested and investigated with greater variations. In this case, it will be necessary to utilize alternative techniques for assessing dissimilarity and preference to avoid extending the test duration. Techniques like Free Sorting and SPPR methods can prove to be helpful in such situations.

As another significant aspect to consider for future studies, we can propose the utilization of Artificial Intelligence and Deep Learning methods for psychoacoustic analyses of the designs. Given that psychoacoustic analyses are based on human decisions and judgments, we can explore the possibility of modeling these human behaviors using machine learning and deep learning techniques. However, it's important to note that this area is still in its early stages of research, and conducting detailed feasibility studies is necessary to provide accurate and comprehensive information.

# Bibliography

- RD Adams and MR Maheri. The dynamic shear properties of structural honeycomb materials. *Composites science and technology*, 47(1):15–23, 1993. (document), 4.1, 5.3, 5.3.2
- Robert A Adams and John JF Fournier. *Sobolev spaces*. Elsevier, 2003. 5.2.1
- Airbus©. Airbus A350 family - passenger aircraft, 2012. URL <https://www.airbus.com/aircraft/passenger-aircraft/a350xwb-family/a350-900.html>. (document), 1.1
- Yahya AllahTavakoli, Mohamed N Ichchou, Catherine Marquis-Favre, and Nacer Hamzaoui. On a hybrid updating method for modeling vibroacoustic behaviors of composite panels. *Journal of Sound and Vibration*, 565:117902, 2023a. 2.3, 5
- Yahya AllahTavakoli, Catherine Marquis-Favre, Mohamed Ichchou, and Nacer Hamzaoui. On the vibro-acoustic modeling of panels excited by diffuse acoustic field (daf). In *INTER-NOISE and NOISE-CON Congress and Conference Proceedings*, volume 265, pages 4354–4365. Institute of Noise Control Engineering, 2023b. 2.3, 3
- Magnus Alvelid. Sixth order differential equation for sandwich beam deflection including transverse shear. *Composite Structures*, 102:29–37, 2013. 2.2
- MP Arunkumar, Jeyaraj Pitchaimani, KV Gangadharan, and MC Lenin Babu. Influence of nature of core on vibro acoustic behavior of sandwich aerospace structures. *Aerospace Science and Technology*, 56:155–167, 2016. 1.2.1
- Serkan Atamer and M Ercan Altinsoy. Sound quality of dishwashers: Annoyance perception. *Applied Acoustics*, 180:108099, 2021. 7.4
- Wilhelm Aures. Berechnungsverfahren für den sensorischen wohlklang beliebiger schallsignale. *Acta Acustica united with Acustica*, 59(2):130–141, 1985a. 7.3.6



- Wilhelm Aures. Ein berechnungsverfahren der rauhigkeit. *Acta Acustica united with Acustica*, 58(5):268–281, 1985b. 7.3.6
- Ever J Barbero. *Introduction to composite materials design*. CRC press, 2010. 2.1
- Menahem Baruch. Optimization procedure to correct stiffness and flexibility matrices using vibration tests. *AIAA journal*, 16(11):1208–1210, 1978. 5.2.3, 5.2.3
- Alain Berry, Olivier Robin, Francesco Franco, Sergio De Rosa, and Giuseppe Petrone. Similitude laws for the sound radiation of flat orthotropic flexural panels. *Journal of Sound and Vibration*, 489:115636, 2020. 2.3
- J Berthaut, MN Ichchou, and L Jezequel. K-space identification of apparent structural behaviour. *Journal of Sound and Vibration*, 280(3-5):1125–1131, 2005. 5.1, 5.2.2
- Jean-Marie Berthelot and Frederick F Ling. *Composite materials: mechanical behavior and structural analysis*, volume 435. Springer, 1999. 2.1, 2.3, 2.3
- O Beslin and J Nicolas. A hierarchical functions set for predicting very high order plate bending modes with any boundary conditions. *Journal of sound and vibration*, 202(5):633–655, 1997. 5.2.1, 5.2.1
- Ingwer Borg and Patrick JF Groenen. *Modern multidimensional scaling: Theory and applications*. Springer Science & Business Media, 2005. 6.3.2, 6.3.2, 7.3.2
- Ingwer Borg, Patrick JF Groenen, and Patrick Mair. *Applied multidimensional scaling*. Springer Science & Business Media, 2012. 6.3.2
- Abdelmadjid Boudjemai, R Amri, Abdeldjelil Mankour, H Salem, MH Bouanane, and Djilali Boutchicha. Modal analysis and testing of hexagonal honeycomb plates used for satellite structural design. *Materials & Design*, 35:266–275, 2012. 2.1
- Tom Bramley. Paired comparison methods. *Techniques for monitoring the comparability of examination standards*, 246:294, 2007. 7.3.3
- Anders Brandt. *Noise and vibration analysis: signal analysis and experimental procedures*. John Wiley & Sons, 2011. 4.2.3
- Jürgen Branke. *Multiobjective optimization: Interactive and evolutionary approaches*, volume 5252. Springer Science & Business Media, 2008. 7.3.8

- Georges Canévet, Dominique Habault, Sabine Meunier, and Florence Demirdjian. Auditory perception of sounds radiated by a fluid-loaded vibrating plate excited by a transient point force. *Acta Acustica united with Acustica*, 90(1):181–193, 2004. 1.2.2
- E Peter Carden and Paul Fanning. Vibration based condition monitoring: a review. *Structural health monitoring*, 3(4):355–377, 2004. 5.1
- J Douglas Carroll. Individual differences and multidimensional scaling. *Multidimensional scaling: Theory and applications in the behavioral sciences*, 1:105–155, 1972. 6.3.2, 7.3.2
- J Douglas Carroll and Phipps Arabie. Multidimensional scaling. *Measurement, judgment and decision making*, pages 179–250, 1998. 6.3.2, 6.3.2, 7.3.2
- J Douglas Carroll and Jih-Jie Chang. Analysis of individual differences in multidimensional scaling via an n-way generalization of “eckart-young” decomposition. *Psychometrika*, 35(3):283–319, 1970. 6.3.2, 7.3.2
- C Chen, Denis Duhamel, and Christian Soize. Probabilistic approach for model and data uncertainties and its experimental identification in structural dynamics: Case of composite sandwich panels. *Journal of Sound and vibration*, 294(1-2): 64–81, 2006. 5.1
- FEI Chengwei, LIU Haotian, Rhea Patricia Liem, CHOY Yatsze, and HAN Lei. Hierarchical model updating strategy of complex assembled structures with uncorrelated dynamic modes. *Chinese Journal of Aeronautics*, 35(3):281–296, 2022. 5.1
- Raef Cherif, Jean-Daniel Chazot, and Nouredine Atalla. Damping loss factor estimation of two-dimensional orthotropic structures from a displacement field measurement. *Journal of sound and vibration*, 356:61–71, 2015. 5.1, 5.3.1, 7.1
- Patrick Chevret and Etienne Parizet. An efficient alternative to the paired comparison method for the subjective evaluation of a large set of sounds. In *Proceedings of the 19th International Congress on Acoustics (ICA 2007), Madrid*, pages 1–5, 2007. 6.2.4
- D Chronopoulos, B Troclet, O Bareille, and M Ichchou. Modeling the response of composite panels by a dynamic stiffness approach. *Composite Structures*, 96: 111–120, 2013. 5.1

- Craig Collier, Phil Yarrington, Mark Pickenheim, Brett Bednarczyk, and Jim Jeans. Analysis methods used on the nasa composite crew module (ccm). In *49th AIAA/ASME/ASCE/AHS/ASC Conference, 16th AIAA/ASME/AHS Conference, 10th AIAA Conference, 9th AIAA Gossamer Spacecraft Forum, 4th AIAA Conference*, page 2251, 2008. (document), 1.1, 1.2
- Maurice N. Collins, Mario Culebras, and Guang Ren. Chapter 8 - the use of lignin as a precursor for carbon fiber-reinforced composites. In Debora Puglia, Carlo Santulli, and Fabrizio Sarasini, editors, *Micro and Nanolignin in Aqueous Dispersions and Polymers*, pages 237–250. Elsevier, 2022. ISBN 978-0-12-823702-1. doi: <https://doi.org/10.1016/B978-0-12-823702-1.00011-6>. URL <https://www.sciencedirect.com/science/article/pii/B9780128237021000116>. 7.1
- M Cuadrado, JA Artero-Guerrero, J Pernas-Sánchez, and D Varas. Model updating of uncertain parameters of carbon/epoxy composite plates from experimental modal data. *Journal of Sound and Vibration*, 455:380–401, 2019. 5.1
- Isaac M Daniel, Ori Ishai, Issac M Daniel, and Ishai Daniel. *Engineering mechanics of composite materials*, volume 1994. Oxford university press New York, 2006. 1.1, 4.2.2
- dBsonic Manual. dbsonic sound analysis software. *Software manual*, 2005. URL <https://www.dbkes.com.tr/brosur/dbsonic.pdf>. 7.3.6
- Victor Hugo C De Albuquerque, João Manuel RS Tavares, and Luís MP Durão. Evaluation of delamination damage on composite plates using an artificial neural network for the radiographic image analysis. *Journal of Composite Materials*, 44(9):1139–1159, 2010. 5.1
- Kalyanmoy Deb. Multi-objective optimisation using evolutionary algorithms: an introduction. In *Multi-objective evolutionary optimisation for product design and manufacturing*, pages 3–34. Springer, 2011. 7.3.8
- Florence Demirdjian, Dominique Habault, Sabine Meunier, and Georges Canévet. Can we hear the complexity of vibrating plates. In *Proceedings of the CFADAGA conference*, 2004. 1.2.2
- Florence Demirdjian, Sabine Meunier, Dominique Habault, and Georges Canévet. A comparative study of recorded and computed sounds radiated by vibrating plates. In *Proc. of Forum Acusticum*, 2005. 1.2.2

- Vivien Denis, Adrien Pelat, François Gautier, and Benjamin Elie. Modal overlap factor of a beam with an acoustic black hole termination. *Journal of Sound and Vibration*, 333(12):2475–2488, 2014. 5.3.1
- Raffaella Di Sante. Fibre optic sensors for structural health monitoring of aircraft composite structures: Recent advances and applications. *Sensors*, 15(8):18666–18713, 2015. (document), 1.1
- DIN45681:2005-03. Akustik - bestimmung der tonhaltigkeit von geräuschen und ermittlung eines tonzuschlages für die beurteilung von geräuschimmissionen. 2005-03. URL <https://dx.doi.org/10.31030/9601912>. 7.3.6
- DIN45681:2006-08. Akustik - bestimmung der tonhaltigkeit von geräuschen und ermittlung eines tonzuschlages für die beurteilung von geräuschimmissionen, berichtigungen zu din 45681:2005-03, mit ed. 2006-08. URL <https://dx.doi.org/10.31030/9759735>. 7.3.6
- Ke Wei Ding, Gang Wang, and Wan Yun Yin. Application of composite sandwich panels in construction engineering. *Applied Mechanics and Materials*, 291:1172–1176, 2013. A
- Christophe Droz, Zakaria Zergoune, Régis Boukadia, Olivier Bareille, and MN Ichchou. Vibro-acoustic optimisation of sandwich panels using the wave/finite element method. *Composite Structures*, 156:108–114, 2016. 1.2.1
- Christophe Droz, Olivier Bareille, and Mohamed N Ichchou. A new procedure for the determination of structural characteristics of sandwich plates in medium frequencies. *Composites Part B: Engineering*, 112:103–111, 2017. 2.2
- Tim Duerinck, Geerten Verberkmoes, Claudia Fritz, Marc Leman, Luc Nijs, Mathias Kersemans, and Wim Van Paepegem. Listener evaluations of violins made from composites. *The Journal of the Acoustical Society of America*, 147(4):2647–2655, 2020. 1.2.2
- Fabian Duvigneau, Steffen Liefold, M Höchstetter, JL Verhey, and U Gabbert. Engine sound weighting using a psychoacoustic criterion based on auralized numerical simulations. In *10th European Congress and Exposition on Noise Control Engineering-EuroNoise, Maastricht, ISSN*, pages 2226–5147, 2015. (document), 1.2.2, 1.7
- Kerem Ege, Xavier Boutillon, and Bertrand David. High-resolution modal analysis. *Journal of Sound and Vibration*, 325(4-5):852–869, 2009. 5.3.1

- Margret Sibylle Engel, André Fiebig, Carmella Pfaffenbach, and Janina Fels. A review of the use of psychoacoustic indicators on soundscape studies. *Current Pollution Reports*, pages 1–20, 2021. 7.3.6
- Sean Eom. Multidimensional scaling. In *Author Cocitation Analysis: Quantitative Methods for Mapping the Intellectual Structure of an Academic Discipline*, pages 225–254. IGI Global, 2009. 6.3.2
- F Errico, Mohamed Ichchou, S De Rosa, F Franco, and O Bareille. Investigations about periodic design for broadband increased sound transmission loss of sandwich panels using 3d-printed models. *Mechanical Systems and Signal Processing*, 136:106432, 2020. 1.2.1
- A Esfandiari. Structural model updating using incomplete transfer function of strain data. *Journal of Sound and Vibration*, 333(16):3657–3670, 2014. 5.1
- Frank J Fahy. *Foundations of engineering acoustics*. Elsevier, 2000. 2.4
- J Fan and J Njuguna. An introduction to lightweight composite materials and their use in transport structures. In *Lightweight Composite Structures in Transport*, pages 3–34. Elsevier, 2016. 1.1, A
- Charles R Farrar, Scott W Doebling, and David A Nix. Vibration-based structural damage identification. *Philosophical Transactions of the Royal Society of London. Series A: Mathematical, Physical and Engineering Sciences*, 359(1778):131–149, 2001. 5.1
- James S Farris. On the cophenetic correlation coefficient. *Systematic Zoology*, 18(3):279–285, 1969. (document), 6.3.1, 7.3.1, 7.5
- Julien Faure. *Influence des paramètres structuraux d’une plaque rayonnante sur la perception sonore*. PhD thesis, Lyon, INSA, 2003. 6.2.4, 6.3.1
- Julien Faure and Catherine Marquis-Favre. Perceptual assessment of the influence of structural parameters for a radiating plate. *Acta Acustica united with Acustica*, 91(1):77–90, 2005. 1.2.2, 7.3.3, 7.4
- Laura Ferreira and David B Hitchcock. A comparison of hierarchical methods for clustering functional data. *Communications in Statistics-Simulation and Computation*, 38(9):1925–1949, 2009. 6.3.1
- Michael Friswell and John E Mottershead. *Finite element model updating in structural dynamics*, volume 38. Springer Science & Business Media, 1995. 5.1

- Michael I Friswell. *Updating finite element models using measured vibration data*. PhD thesis, Aston University, 1990. 5.1
- Claudia Fritz, Joseph Curtin, Jacques Poitevineau, and Fan-Chia Tao. Listener evaluations of new and old italian violins. *Proceedings of the National Academy of Sciences*, 114(21):5395–5400, 2017. 1.2.2
- Sebastian Ghinet and Nouredine Atalla. Modeling thick composite laminate and sandwich structures with linear viscoelastic damping. *Computers & Structures*, 89(15-16):1547–1561, 2011. 5.3.1, 7.1
- Lorna J. Gibson and Michael F. Ashby. *Cellular Solids: Structure and Properties*. Cambridge Solid State Science Series. Cambridge University Press, 2 edition, 1997. doi: 10.1017/CBO9781139878326. 7.1, 7.1, 7.1
- Ronald F Gibson. *Principles of composite material mechanics*. CRC press, 2007. 2.1
- Maria Girardi, Cristina Padovani, Daniele Pellegrini, and Leonardo Robol. A finite element model updating method based on global optimization. *Mechanical Systems and Signal Processing*, 152:107372, 2021. 5.1
- Victor Giurgiutiu. In *Structural health monitoring of aerospace composites*, pages 1–23. Academic Press, Oxford, 2015. ISBN 978-0-12-409605-9. doi: <https://doi.org/10.1016/B978-0-12-409605-9.00001-5>. URL <https://www.sciencedirect.com/science/article/pii/B9780124096059000015>. 1.1
- Leo A Goodman, William H Kruskal, Leo A Goodman, and William H Kruskal. *Measures of association for cross classifications*. Springer, 1979. (document), 6.3.1, 7.3.1, 7.5
- Allan David Gordon. *Classification*. CRC Press, 1999. 6.3.1, 6.3.1
- Nassardin Guenfoud, Christophe Droz, Mohamed N Ichchou, Olivier Bareille, Elke Deckers, and Wim Desmet. On the multi-scale vibroacoustic behavior of multi-layer rectangular core topology systems. *Mechanical Systems and Signal Processing*, 143:106629, 2020. 1.2.1
- Laurent Guillaumie. Vibroacoustic flexural properties of symmetric honeycomb sandwich panels with composite faces. *Journal of Sound and Vibration*, 343:71–103, 2015. 2.3
- Jean-Louis Guyader. *Vibration in continuous media*. John Wiley & Sons, 2013. 3.1

- Per Christian Hansen. The l-curve and its use in the numerical treatment of inverse problems. 1999. Computational Inverse Problems in Electrocardiology Conference. 6.3.2, 7.3.2
- Per Christian Hansen. Regularization tools version 4.0 for matlab 7.3. *Numerical algorithms*, 46:189–194, 2007. 6.3.2
- Per Christian Hansen. regtools: Regularization tools:. 2023. URL <https://www.mathworks.com/matlabcentral/fileexchange/52-regtools>. 6.3.2
- Jimin He and Zhi-Fang Fu. 9 - modal analysis methods – time domain. In Jimin He and Zhi-Fang Fu, editors, *Modal Analysis*, pages 180–197. Butterworth-Heinemann, Oxford, 2001. ISBN 978-0-7506-5079-3. doi: <https://doi.org/10.1016/B978-075065079-3/50009-7>. URL <https://www.sciencedirect.com/science/article/pii/B9780750650793500097>. 4.2.3, 5.3.1
- Hexcel©. Hexcel ready to fly on the a350 xwb. *Reinforced Plastics*, 57(3):25–26, 2013. ISSN 0034-3617. doi: [https://doi.org/10.1016/S0034-3617\(13\)70089-4](https://doi.org/10.1016/S0034-3617(13)70089-4). URL <https://www.sciencedirect.com/science/article/pii/S0034361713700894>. (document), A.1
- Ward Heylen, Stefan Lammens, Paul Sas, et al. *Modal analysis theory and testing*, volume 200. Katholieke Universiteit Leuven Leuven, Belgium, 1997. 4.2.3
- Jens Hjortkjær and Stephen McAdams. Spectral and temporal cues for perception of material and action categories in impacted sound sources. *The Journal of the Acoustical Society of America*, 140(1):409–420, 2016. 1.2.2
- Victoria Hodge and Jim Austin. A survey of outlier detection methodologies. *Artificial intelligence review*, 22:85–126, 2004. 6.3.1
- Michael C Hout, Megan H Papesh, and Stephen D Goldinger. Multidimensional scaling. *Wiley Interdisciplinary Reviews: Cognitive Science*, 4(1):93–103, 2013. 6.3.2
- Louis Humbert. *Recalage des modèles éléments finis à partir de mesures vibratoires*. PhD thesis, Ecully, Ecole centrale de Lyon, 1999. 5.1, 5.2.3, 5.3
- Shun-Fa Hwang and Rong-Song He. A hybrid real-parameter genetic algorithm for function optimization. *Advanced Engineering Informatics*, 20(1):7–21, 2006. 5.1
- MN Ichchou, O Bareille, and J Berthaut. Identification of effective sandwich structural properties via an inverse wave approach. *Engineering Structures*, 30(10):2591–2604, 2008. 5.1, 5.2.2, 5.2.2, 5.3

- Mecanum Inc. Mecanum's acoustic test cabin. URL <https://www.mecanum.com/cabine-test-acoustique?lang=en>. 3.3
- Doug L James, Jernej Barbič, and Dinesh K Pai. Precomputed acoustic transfer: output-sensitive, accurate sound generation for geometrically complex vibration sources. *ACM Transactions on Graphics (TOG)*, 25(3):987–995, 2006. 1.2.2
- L Jaouen, B Brouard, N Atalla, and C Langlois. A simplified numerical model for a plate backed by a thin foam layer in the low frequency range. *Journal of Sound and Vibration*, 280(3-5):681–698, 2005. 5.2.1, 5.2.1
- Natalia Jaworska and Angelina Chupetlovska-Anastasova. A review of multidimensional scaling (mds) and its utility in various psychological domains. *Tutorials in quantitative methods for psychology*, 5(1):1–10, 2009. 6.3.2
- Robert M. Jones. *Mechanics of Composite Materials (2nd edition)*. CRC press, 1999. 2.3, 2.3
- Robert M Jones. *Mechanics of composite materials*. CRC press, 2018. 5.1
- Andrzej Katunin and Piotr Przystalka. Damage assessment in composite plates using fractional wavelet transform of modal shapes with optimized selection of spatial wavelets. *Engineering Applications of Artificial Intelligence*, 30:73–85, 2014. 5.1
- Autar K Kaw. *Mechanics of composite materials*. CRC press, 2005. 1.1, 2.1, 4.2.2
- S Kelsey, RA Gellatly, and BW Clark. The shear modulus of foil honeycomb cores: A theoretical and experimental investigation on cores used in sandwich construction. *Aircraft Engineering and Aerospace Technology*, 30(10):294–302, 1958. 7.1
- Gaetan Kerschen, Keith Worden, Alexander F Vakakis, and Jean-Claude Golinval. Past, present and future of nonlinear system identification in structural dynamics. *Mechanical systems and signal processing*, 20(3):505–592, 2006. 5.1
- Samir Khatir, Samir Tiachacht, Cuong Le Thanh, Emad Ghandourah, Seyedali Mirjalili, and Magd Abdel Wahab. An improved artificial neural network using arithmetic optimization algorithm for damage assessment in fgm composite plates. *Composite Structures*, 273:114287, 2021. 5.1
- Byung Jun Kim, Dae Kyu Yun, Sang Hun Lee, and Gang-Won Jang. Topology optimization of industrial robots for system-level stiffness maximization by using part-level metamodels. *Structural and multidisciplinary optimization*, 54:1061–1071, 2016. 7.3.8



- Michael T Kirsch. Composite crew module: Primary structure. Technical report, 2011. (document), 1.1, 1.2
- Mendel Kleiner, Bengt-Inge Dalenbäck, and Peter Svensson. Auralization-an overview. *Journal of the Audio Engineering Society*, 41(11):861–875, 1993. 1.2.2
- William L. Ko. Heat shielding characteristics and thermostructural performance of a superalloy honeycomb sandwich thermal protection system (TPS). 2004. A
- William L. Ko, Van T. Tran, and Jeff Bowles. Lunar Return Reentry Thermal Analysis of a Generic Crew Exploration Vehicle Wall Structures. 2007. (document), 1.1, A, A.2
- Kyohei Kohsaka, Kuniharu Ushijima, and Wesley J Cantwell. Study on vibration characteristics of sandwich beam with bcc lattice core. *Materials Science and Engineering: B*, 264:114986, 2021. 2.2
- Anna G Koniuszewska and Jacek W Kaczmar. Application of polymer based composite materials in transportation. *Progress in Rubber Plastics and Recycling Technology*, 32(1):1–24, 2016. 1.1
- Thibault Lafont, Nicolas Totaro, and Alain Le Bot. Review of statistical energy analysis hypotheses in vibroacoustics. *Proceedings of the Royal Society A: Mathematical, Physical and Engineering Sciences*, 470(2162):20130515, 2014. 2.3.1, 2.3.1
- Alain Le Bot. *Foundation of statistical energy analysis in vibroacoustics*. OUP Oxford, 2015. 2.3.1, 5.2.1
- Quentin Legros. *Caractérisation physique et perceptive des bruits de passage de TGV pour une amélioration des modèles de gêne*. Master thesis report. ENTPE, 2020. 7.3.6
- Claude Lesueur and Jean Nicolas. Rayonnement acoustique des structures (acoustic radiation of structures), 1989. 2.3, 2.3
- Jinqiang Li and Yoshihiro Narita. Analysis and optimal design for the damping property of laminated viscoelastic plates under general edge conditions. *Composites Part B: Engineering*, 45(1):972–980, 2013. 5.3.1, 7.1
- Richard H Lyon, Richard G DeJong, and Manfred Heckl. Theory and application of statistical energy analysis, 1995. 5.2.2

- Steffen Marburg. Discretization requirements: How many elements per wavelength are necessary? In *Computational Acoustics of Noise Propagation in Fluids-Finite and Boundary Element Methods*, pages 309–332. Springer, 2008. 3.2
- Christophe Marchetto, Laurent Maxit, Olivier Robin, and Alain Berry. Vibroacoustic response of panels under diffuse acoustic field excitation from sensitivity functions and reciprocity principles. *The Journal of the Acoustical Society of America*, 141(6):4508–4521, 2017. 3.1.1
- Ivan Markovsky and Sabine Van Huffel. Overview of total least-squares methods. *Signal processing*, 87(10):2283–2302, 2007. 5.2.4
- Stephen McAdams, Vincent Roussarie, Antoine Chaigne, and Bruno L Giordano. The psychomechanics of simulated sound sources: Material properties of impacted thin plates. *The Journal of the Acoustical Society of America*, 128(3):1401–1413, 2010. 1.2.2
- J Gregory McDaniel and W Steve Shepard Jr. Estimation of structural wave numbers from spatially sparse response measurements. *The Journal of the Acoustical Society of America*, 108(4):1674–1682, 2000. 5.1
- J Gregory McDaniel, Pierre Dupont, and Liming Salvino. A wave approach to estimating frequency-dependent damping under transient loading. *Journal of sound and vibration*, 231(2):433–449, 2000. 5.1
- Denys John Mead. *The effect of certain damping treatments on the response of idealized aeroplane structures excited by noise*. Air Force Materials Laboratory, Research and Technology Division, Air Force . . . , 1965. 2.2
- DJ Mead. The damping properties of elastically supported sandwich plates. *Journal of Sound and Vibration*, 24(3):275–295, 1972. 2.2
- DJ Mead and S Markus. The forced vibration of a three-layer, damped sandwich beam with arbitrary boundary conditions. *Journal of sound and vibration*, 10(2):163–175, 1969. 1.2.1, 2.2, 2.2
- Han Meng, Marie-Annick Galland, Mohamed Ichchou, Olivier Bareille, FX Xin, and TJ Lu. Small perforations in corrugated sandwich panel significantly enhance low frequency sound absorption and transmission loss. *Composite Structures*, 182:1–11, 2017. (document), 1.2.1, 1.3
- S Meunier, D Habault, and G Canévet. Auditory evaluation of sound signals radiated by a vibrating surface. *Journal of sound and Vibration*, 247(5):897–915, 2001. 1.2.2

- Pierre-Yohan Michaud, Sabine Meunier, Philippe Herzog, Mathieu Lavandier, and Gérard Drouet d'Aubigny. Perceptual evaluation of dissimilarity between auditory stimuli: an alternative to the paired comparison. *Acta Acustica united with Acustica*, 99(5):806–815, 2013. 6.2.4
- Abdelhamid Miloudi, Hamzaoui Nacer, and Guyader Jean Louis. Subjective evaluations of sound radiated by impacted plates, using the design of experiments method. *Applied acoustics*, 71(6):531–538, 2010. 7.4
- Malte Misol, Christian Bloch, Hans Peter Monner, and Michael Sinapius. Performance of active feedforward control systems in non-ideal, synthesized diffuse sound fields. *The Journal of the Acoustical Society of America*, 135(4):1887–1897, 2014. 3.1.1, 3.1.1
- Diogo Montalvão, RALD Cláudio, António MR Ribeiro, and J Duarte-Silva. Experimental measurement of the complex young's modulus on a cfrp laminate considering the constant hysteretic damping model. *Composite Structures*, 97:91–98, 2013. 7.1
- John E Mottershead and MI Friswell. Model updating in structural dynamics: a survey. *Journal of sound and vibration*, 167(2):347–375, 1993. 5.1
- John E Mottershead, Michael Link, and Michael I Friswell. The sensitivity method in finite element model updating: A tutorial. *Mechanical systems and signal processing*, 25(7):2275–2296, 2011. 5.1, 5.2.3
- Maria Mrazova. Advanced composite materials of the future in aerospace industry. *Incas bulletin*, 5(3):139, 2013. 1.1, A
- Jean-Pierre Nakache and Josiane Confais. *Approche pragmatique de la classification: arbres hiérarchiques, partitionnements*. Editions Technip, 2004. 6.3.1
- S Narayanan and RL Shanbhag. Sound transmission through elastically supported sandwich panels into a rectangular enclosure. *Journal of Sound and Vibration*, 77(2):251–270, 1981. 1.2.1, 2.2, 2.2, 3.1.1, 3.1.1
- S Narayanan and RL Shanbhag. Sound transmission through a damped sandwich panel. *Journal of Sound and Vibration*, 80(3):315–327, 1982. 1.2.1, 2.2, 2.2, 2.2
- E Nilsson and AC Nilsson. Prediction and measurement of some dynamic properties of sandwich structures with honeycomb and foam cores. *Journal of sound and vibration*, 251(3):409–430, 2002. 1.2.1, 5.1

- Georgios Ntourmas, Florian Glock, Sebastian Deinert, Fernass Daoud, Gerd Schuhmacher, Dimitrios Chronopoulos, Ender Özcan, and Jelena Ninić. Stacking sequence optimisation of an aircraft wing skin. *Structural and Multidisciplinary Optimization*, 66(2):31, 2023. 1.2.1
- James F O'Brien, Perry R Cook, and Georg Essl. Synthesizing sounds from physically based motion. In *Proceedings of the 28th annual conference on Computer graphics and interactive techniques*, pages 529–536, 2001. 1.2.2
- James F O'Brien, Chen Shen, and Christine M Gatchalian. Synthesizing sounds from rigid-body simulations. In *Proceedings of the 2002 ACM SIGGRAPH/Eurographics symposium on Computer animation*, pages 175–181, 2002. (document), 1.2.2, 1.2.2, 1.6
- Ahmet Arda Ozdemir and Suat Gumussoy. Transfer function estimation in system identification toolbox via vector fitting. *IFAC-PapersOnLine*, 50(1):6232–6237, 2017. 4.2.3
- Giulia Palomba, Gabriella Epasto, and Vincenzo Crupi. Lightweight sandwich structures for marine applications: a review. *Mechanics of Advanced Materials and Structures*, 29(26):4839–4864, 2022. A
- Etienne Parizet and Vincent Koehl. Application of free sorting tasks to sound quality experiments. *Applied Acoustics*, 73(1):61–65, 2012. 6.2.4
- Giuseppe Petrone and Viviana Meruane. Mechanical properties updating of a non-uniform natural fibre composite panel by means of a parallel genetic algorithm. *Composites Part A: Applied Science and Manufacturing*, 94:226–233, 2017. 5.1
- Felipe Alves Pires, Martin Wandel, Christian Thomas, Elke Deckers, Wim Desmet, and Claus Claeys. Improving the sound transmission loss of an aircraft ceiling panel by locally resonant metamaterials. Technical report, SAE Technical Paper, 2022. 7.3.8
- Federico Ponsi, Elisa Bassoli, and Loris Vincenzi. A multi-objective optimization approach for fe model updating based on a selection criterion of the preferred pareto-optimal solution. In *Structures*, volume 33, pages 916–934. Elsevier, 2021. 6.3.2
- Giorgio Pulvirenti, Nicolas Totaro, and Etienne Parizet. A perceptual evaluation of numerical errors in acoustic fem simulation for sound quality applications. *Applied Acoustics*, 207:109295, 2023. 1.2.2

- Zhenchao Qi, Yong Liu, and Wenliang Chen. An approach to predict the mechanical properties of cfrp based on cross-scale simulation. *Composite Structures*, 210:339–347, 2019. (document), 4.2, 4.2.2, 4.1, 5.3, 5.3.2, 7.1
- K Renji, PS Nair, and S Narayanan. Modal density of composite honeycomb sandwich panels. *Journal of Sound and Vibration*, 195(5):687–699, 1996. 1.2.1
- MG Roest. *Design of a composite guitar*. Master thesis report, Delft University of Technology (TU Delft), 2016. 1.2.2
- Rene Roy, Sung-Jun Park, Jin-Hwe Kweon, and Jin-Ho Choi. Characterization of nomex honeycomb core constituent material mechanical properties. *Composite Structures*, 117:255–266, 2014. (document), 4.2, 4.2.2, 4.1, 7.1
- S. Sajan and D. Philip Selvaraj. A review on polymer matrix composite materials and their applications. *Materials Today: Proceedings*, 47:5493–5498, 2021. ISSN 2214-7853. doi: <https://doi.org/10.1016/j.matpr.2021.08.034>. URL <https://www.sciencedirect.com/science/article/pii/S2214785321054614>. International Conference on Sustainable materials, Manufacturing and Renewable Technologies 2021. 1.1
- Essi Sarlin, Yi Liu, Minnamari Vippola, Markus Zogg, Paolo Ermanni, Jyrki Vuorinen, and T Lepistö. Vibration damping properties of steel/rubber/composite hybrid structures. *Composite Structures*, 94(11):3327–3335, 2012. 5.3.1, 7.1
- Amir Shahdin, Joseph Morlier, Laurent Mezeix, Christophe Bouvet, and Yves Gourinat. Evaluation of the impact resistance of various composite sandwich beams by vibration tests. *Shock and Vibration*, 18(6):789–805, 2011. (document), 4.2.2, 4.1, 5.3.2
- Lawrence F Shampine. Vectorized adaptive quadrature in matlab. *Journal of Computational and Applied Mathematics*, 211(2):131–140, 2008. 3.2
- Christopher M Shearer and Carlos ES Cesnik. Nonlinear flight dynamics of very flexible aircraft. *Journal of Aircraft*, 44(5):1528–1545, 2007. 7.3.8
- RP Shimpi and HG Patel. A two variable refined plate theory for orthotropic plate analysis. *International Journal of Solids and Structures*, 43(22-23):6783–6799, 2006. 2.3
- Jyoti K Sinha, MI Friswell, and S Edwards. Simplified models for the location of cracks in beam structures using measured vibration data. *Journal of Sound and vibration*, 251(1):13–38, 2002. 5.1

- Robert R Sokal and F James Rohlf. The comparison of dendrograms by objective methods. *Taxon*, pages 33–40, 1962. (document), 6.3.1, 7.3.1, 7.5
- Anthony B Stanbridge, Milena Martarelli, and David J Ewins. Measuring area vibration mode shapes with a continuous-scan ldv. *Measurement*, 35(2):181–189, 2004. 5.2.3
- G Standoli, E Giordano, G Milani, and F Clementi. Model updating of historical belfries based on oma identification techniques. *International Journal of Architectural Heritage*, 15(1):132–156, 2021. 5.1
- Jun Hui Tam, Zhi Chao Ong, and Kye Wenn Ho. Composite material identification using a two-stage meta-heuristic hybrid approach incorporated with a two-level frf selection scheme. *Journal of Sound and Vibration*, 456:407–430, 2019. 5.1
- Meenu Teotia and RK Soni. Applications of finite element modelling in failure analysis of laminated glass composites: A review. *Engineering Failure Analysis*, 94:412–437, 2018. 2.1, 2.3
- Louis L Thurstone. A law of comparative judgment. *Psychological review*, 34(4): 273, 1927. 7.3.3
- A Trollé, C Marquis-Favre, and J Faure. An analysis of the effects of structural parameter variations on the auditory perception of environmental noises transmitted through a simulated window. *Applied Acoustics*, 69(12):1212–1223, 2008. 1.2.2
- Arnaud Trollé. *Evaluation auditive de sons rayonnés par une plaque vibrante à l'intérieur d'une cavité amortie: ajustement des efforts de calcul vibro-acoustique*. PhD thesis, INSA de Lyon, 2009. (document), 1.2.2, 1.5, 6.2.4, 6.3.1, 6.3.1, 6.3.2, 6.3.3, 7.3.2, 7.3.3, 7.3.6
- Arnaud Trolle, Catherine Marquis-Favre, and Nacer Hamzaoui. Auditory evaluation of sounds radiated from a vibrating plate inside a damped cavity: adjustment of the frequency resolution of vibro-acoustical computing. *Acta Acustica united with Acustica*, 98(3):441–450, 2012. (document), 1.2.2, 1.5
- Yu-Ting Tsai, SJ Pawar, and Jin H Huang. Optimizing material properties of composite plates for sound transmission problem. *Journal of Sound and Vibration*, 335:174–186, 2015. 5.1
- Lucas Van Belle, Claus Claeys, Elke Deckers, and Wim Desmet. On the impact of damping on the dispersion curves of a locally resonant metamaterial: Modelling and experimental validation. *Journal of Sound and Vibration*, 409:1–23, 2017. 5.1

- JT Wang, CJ Wang, and JP Zhao. Frequency response function-based model updating using kriging model. *Mechanical Systems and Signal Processing*, 87:218–228, 2017. 5.1
- Weizhuo Wang, John E Mottershead, Alexander Ihle, Thorsten Siebert, and Hans Reinhard Schubach. Finite element model updating from full-field vibration measurement using digital image correlation. *Journal of Sound and Vibration*, 330(8):1599–1620, 2011. 5.1, 5.2.3
- Braden T Warwick, Chris K Mechefske, and Il Yong Kim. Topology optimization of a pre-stiffened aircraft bulkhead. *Structural and Multidisciplinary Optimization*, 60:1667–1685, 2019. 7.3.8
- Sharon L Weinberg, J Douglas Carroll, and Harvey S Cohen. Confidence regions for indscal using the jackknife and bootstrap techniques. *Psychometrika*, 49:475–491, 1984. 6.3.3, 7.3.2, 7.3.3
- Z Zergoune, MN Ichchou, O Bareille, B Harras, R Benamar, and B Troclet. Assessments of shear core effects on sound transmission loss through sandwich panels using a two-scale approach. *Computers & Structures*, 182:227–237, 2017. (document), 1.2.1, 1.4, 7.1
- Jie Zhang, Dan Yao, Ruiqian Wang, and Xinbiao Xiao. Vibro-acoustic modelling of high-speed train composite floor and contribution analysis of its constituent materials. *Composite Structures*, 256:113049, 2021. (document), A, A.3
- Yong Zhou, Anna Liu, Yongzheng Xu, Yunli Guo, Xiaosu Yi, and Yuxi Jia. Frequency-dependent orthotropic damping properties of nomex honeycomb composites. *Thin-Walled Structures*, 160:107372, 2021. (document), 4.2.2, 4.1, 5.3, 5.3.2, 7.1
- Stana Živanović, ALEKSANDAR Pavic, and Paul Reynolds. Vibration serviceability of footbridges under human-induced excitation: a literature review. *Journal of sound and vibration*, 279(1-2):1–74, 2005. 5.1
- Eberhard Zwicker, Hugo Fastl, Ulrich Widmann, Kenji Kurakata, Sonoko Kuwano, and Seiichiro Namba. Program for calculating loudness according to din 45631 (iso 532b). *Journal of the Acoustical Society of Japan (E)*, 12(1):39–42, 1991. 7.3.6

# Appendix A

## Diverse applications of composite structures

In aerospace studies, the A350XWB stands as an exceptional example of utilizing composite materials, which incorporates 53% composites, 19% AL/AL-Li, 14% Titanium, and 6% steel of the weight. Its rear fuselage section, stabilizers, and fin/rudder assembly are made of carbon fiber structures (see Figure A.1). Additionally, its fuselage panels, frames, window frames, clips, and door are constructed using carbon fiber reinforced polymers (CFRP), with the door frame structure featuring a combination of CFRP and titanium. By incorporating these composite materials into the A350XWB, Airbus has extended the service intervals of the aircraft from 6 to 12 years, significantly reducing maintenance costs for customers and enhancing the aircraft's environmental friendliness Mrazova [2013].

Today, advanced composites have played a pivotal role in various space programs, including the development of launch vehicles, the space shuttle, satellites, space telescopes, and the International Space Station. Notably, these composites possess exceptional qualities, surpassing the structural materials utilized during the Apollo missions Ko et al. [2007] (see Figure A.2). The significant applications of composite material in space studies can be found in research of crew exploration vehicles (CEVs), and since the Apollo missions, various advanced materials like adapted honeycomb sandwich panels have been developed for this purpose, e.g. see Ko [2004], Ko et al. [2007].

Furthermore, considering the importance of weight reduction in modern transportation technologies like high-speed trains, it becomes evident that it is an efficient strategy for reducing costs and minimizing air pollution, regardless of the energy source used, be it oil (petrol, diesel, etc.), biofuels, electric power, or fuel



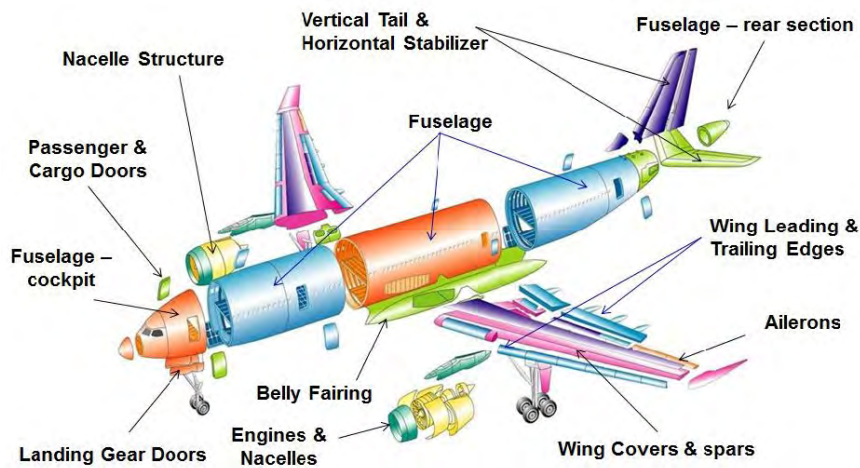


Figure A.1: Many components of the A350 XWB, such as fuselage panels, wing, stabilizers and fin/rudder assembly, incorporate composite materials Hexcel© [2013]

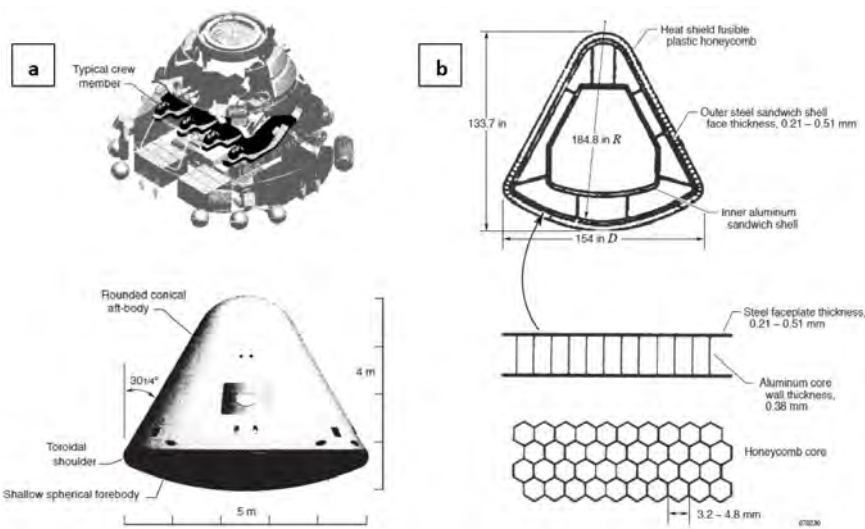


Figure A.2: a) Geometry of a candidate CEV of the Apollo capsule, and b) its double-walled composite sandwich construction Ko et al. [2007]

cells. Furthermore, the utilization of the latest generation of composite materials holds tremendous promise in achieving this objective Fan and Njuguna [2016]. Meanwhile, with the increasing speed of vehicles like high-speed trains and the operation of more complex lines, the challenges posed by vehicle noises, particularly interior noises, have escalated. The prominent noise sources in this domain include wheel/rail noises and vibration, aerodynamic noises, and noises caused by vibration in structural connections. The primary paths for noise transmission are airborne sound and structure-borne sound, for instance, originating from the floor. To miti-

gate interior noise in vehicles, it is crucial to control the noise sources and optimize the transfer paths. For instance, Figure A.3 depicts a structural model of a composite floor in a high-speed train. Zhang et al. [2021] have used this structural model for investigating the vibroacoustic modeling of the composite floor in high-speed trains, as well as conducted an analysis of the contributions made by its constituent materials for controlling the noise and vibration.

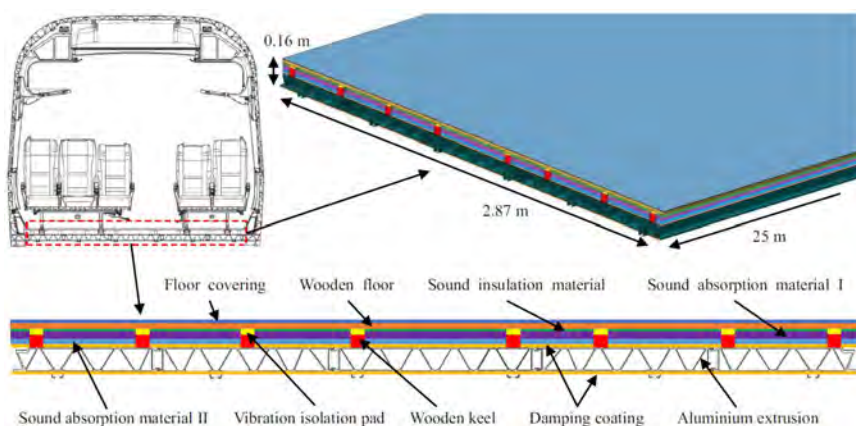


Figure A.3: The structural model of composite floor in high-speed train with different components and different uses Zhang et al. [2021]

Another application of composite materials belongs to the modern stage of civil industries. In the realm of civil engineering, composite sandwich panels have emerged as a novel constructional material, finding widespread application Ding et al. [2013]. The utilization of composite materials in building construction has become increasingly prevalent, driven by the growing demand for lightweight, durable, and cost-effective solutions. These materials are now being employed in the construction of stairs, landings, balusters, banisters, as well as in the creation of facades with intricate and aesthetically pleasing designs, addressing architectural considerations. The versatility and benefits offered by advanced sandwich panels make them ideal for contemporary industrial buildings. Notably, their ease of installation, thermal insulation properties, soundproofing capabilities, and fire protection attributes make them a preferred choice Ding et al. [2013].

Moreover, in recent decades we can also find other miscellaneous interests in composite sandwich structures. An excellent example is the growing interest of marine industry toward sandwich constructions, which also arises out of weight-saving objectives, whose consequences are beneficial to the whole life cycle of marine structures. They are commonly used in boat hulls and decks to provide us with strength and stiffness while reducing weight. These structures are also employed to create bulkheads and partitions within the interior of boats. In cabin interiors of

marine vehicle, composite sandwich panels can be used for walls, ceilings, and floors, offering acoustic and thermal insulation properties.

Moreover, these panels can be used in the fabrication of doors and hatches, providing rigidity, and resistance to marine environments. Furthermore, they find applications in floating structures such as pontoons and buoys because of their lightweight nature and corrosion resistance. Also, they have applications to the fabrication of ramps, walkways, and platforms for easy access to boats and ships, offering high strength and anti-slip properties to ensure safety during embarkation and disembarkation. So, composite sandwich materials can benefit the modern design stage of marine structures that will consequently lead to: fuel consumption reduction, speed increase for a specified power, easy building procedure, improving stability and maneuverability, mass reduction of building materials resulting cost and time savings (e.g. see Palomba et al. [2022]).

# Appendix B

## Some results of updating

In the subsequent illustrations, we present additional outcomes derived from the updating procedures detailed in Chapter 5. Specifically, these figures depict the sound pressure levels measured at distances of 20cm and 100cm from the center of the plate, comparing simulations before and after the updating procedures. As illustrated, similar to the preceding findings discussed in Chapter 5, these figures effectively demonstrate the impact of the updating procedures on the simulations regarding the composite sandwich, laminate, aluminum, and steel plates.

Hence, the following visuals depict the spectra of sound pressure levels emitted by radiating panels across the frequency range of [0, 2 kHz]. Specifically, Figures B.1 and B.2 showcase these spectra for the composite sandwich panel at distances of 20cm and 100cm, respectively. For the composite laminate panel, Figures B.3 and B.4 display the corresponding spectra at distances of 20cm and 100cm, respectively. Similarly, Figures B.5 and B.6 exhibit these spectra for the aluminum panel, again at distances of 20cm and 100cm, respectively. Lastly, Figures B.7 and B.8 present the spectra for the steel panel at distances of 20cm and 100cm, respectively.

It's noteworthy that consistency in the updated results is apparent across all of these results.

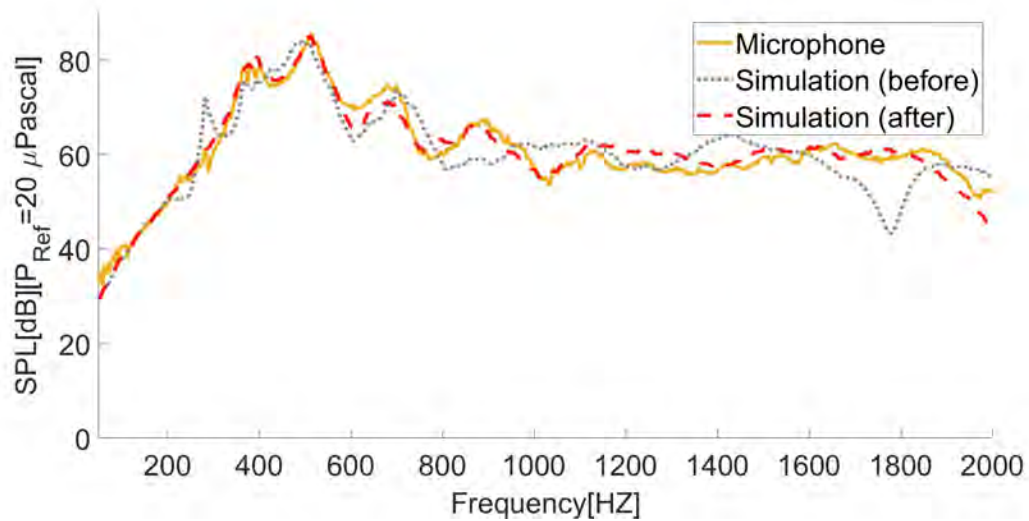


Figure B.1: Comparison of Sound Pressure Levels (SPL) for the composite sandwich plate: Simulations (before and after updating) vs. Microphone Measurements at a 20cm Distance

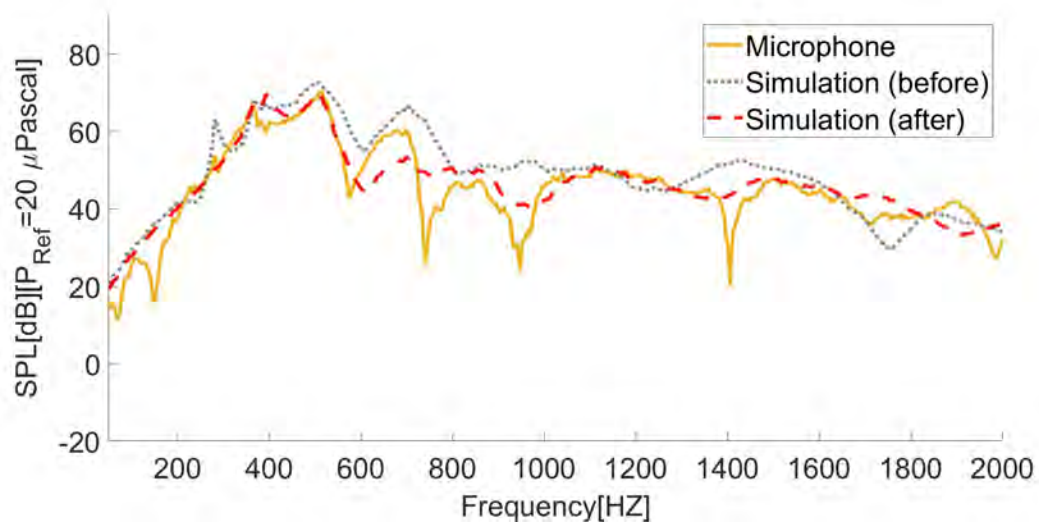


Figure B.2: Comparison of Sound Pressure Levels (SPL) for the composite sandwich plate: Simulations (before and after updating) vs. Microphone Measurements at a 100cm Distance

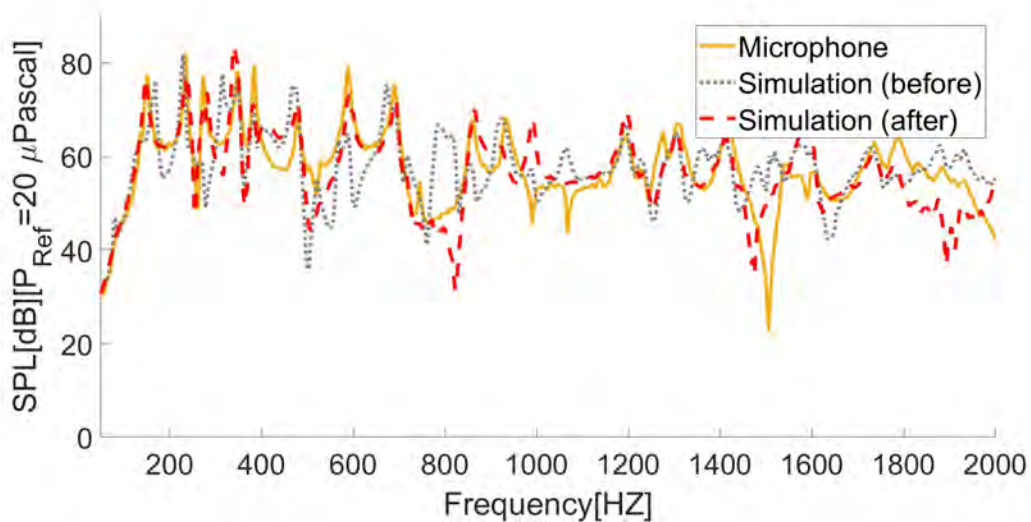


Figure B.3: Comparison of Sound Pressure Levels (SPL) for the composite laminate plate: Simulations (before and after updating) vs. Microphone Measurements at a 20cm Distance

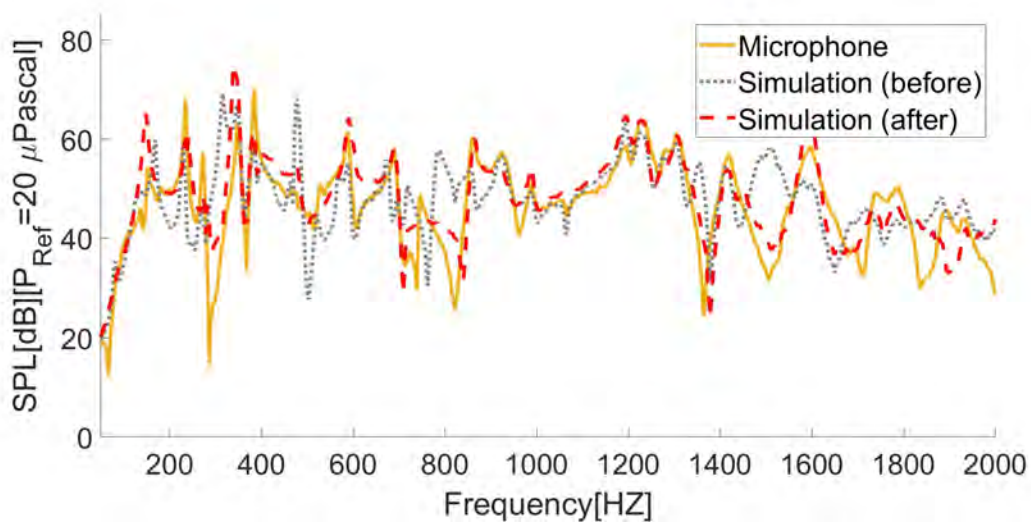


Figure B.4: Comparison of Sound Pressure Levels (SPL) for the composite laminate plate: Simulations (before and after updating) vs. Microphone Measurements at a 100cm Distance

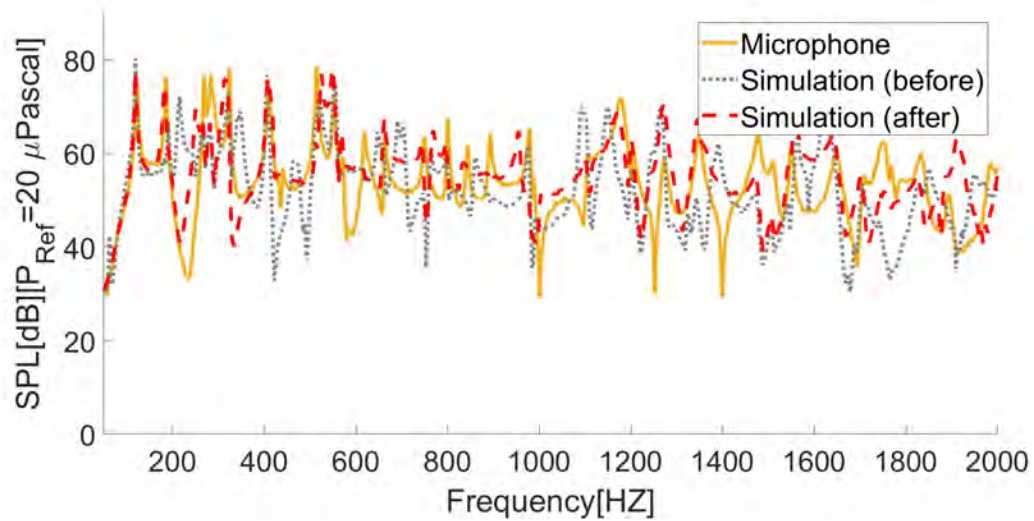


Figure B.5: Comparison of Sound Pressure Levels (SPL) for the Aluminium plate: Simulations (before and after updating) vs. Microphone Measurements at a 20cm Distance

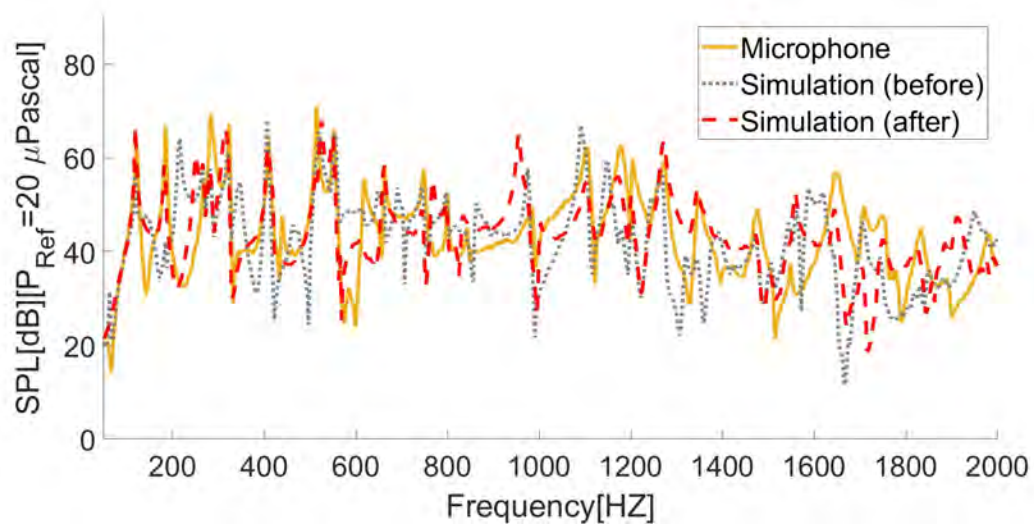


Figure B.6: Comparison of Sound Pressure Levels (SPL) for the Aluminium plate: Simulations (before and after updating) vs. Microphone Measurements at a 100cm Distance

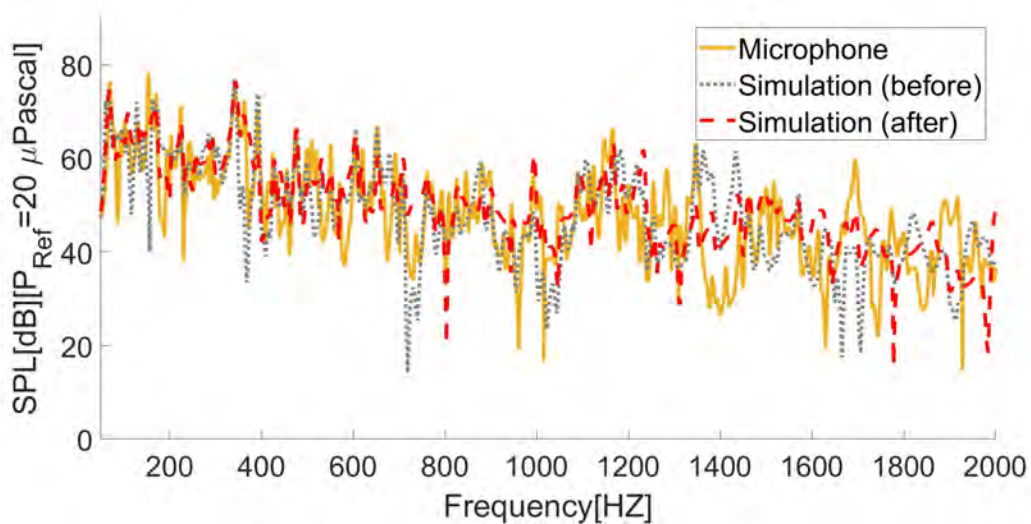


Figure B.7: Comparison of Sound Pressure Levels (SPL) for the steel plate: Simulations (before and after updating) vs. Microphone Measurements at a 20cm Distance

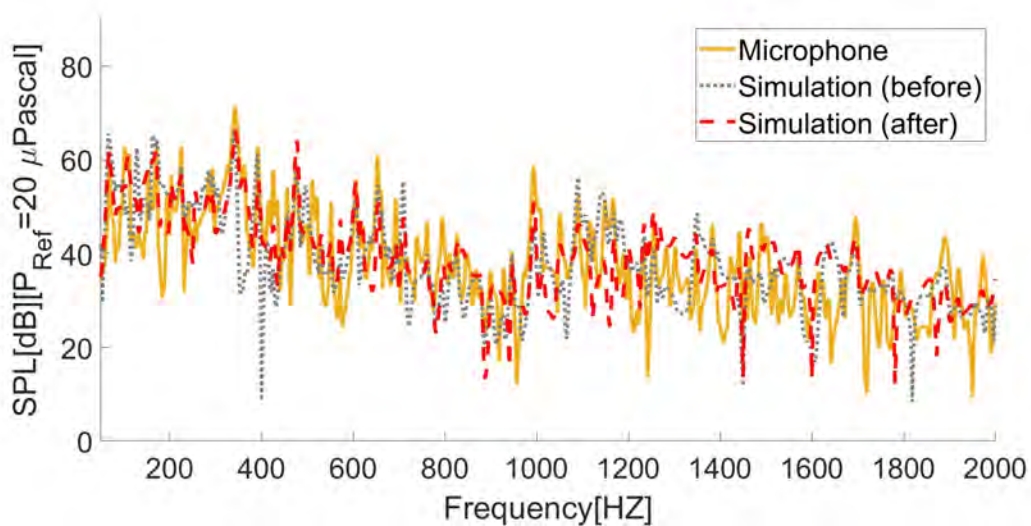


Figure B.8: Comparison of Sound Pressure Levels (SPL) for the steel plate: Simulations (before and after updating) vs. Microphone Measurements at a 100cm Distance





# Appendix C

## Statistical analysis of the design and optimization

In the following visual depictions, we illustrate distinct results derived from the statistical analysis detailed in Chapter 7 for the ten designs.

The statistical analysis has been conducted for sessions involving both mechanical and acoustic excitation. It encompasses the analysis of dimensions of the perceptual space, preference, and three psychoacoustic indices: loudness, sharpness, and SC, alongside a mechanical parameter, the stiffness-to-mass ratio. The analysis entails a linear regression with a 95% confidence interval, correlation coefficient  $r$ , and the  $p$  value.

Figures C.1 to C.5 depict the analysis between perceptual dimensions and other parameters for sessions featuring mechanical excitation. Additionally, Figure C.6 showcases the statistical relationship between loudness and preference within this session. Similarly, Figures C.7 to C.10 illustrate the analysis between perceptual dimensions and other parameters for sessions with acoustic excitation. Furthermore, Figures C.11 and C.12, respectively, display the statistical correlation of the preference with loudness and the mechanical parameter stiffness-to-mass ratio, in the acoustic excitation session.

Furthermore, regarding the perceptual space in both sessions, Figures C.13 and C.14 demonstrate the spectra of the sound pressure level for certain designs, closely aligned along the 1st dimension of the perceptual space. These figures also reveal the impact of the stiffness-to-mass ratio on the SPL spectra of stimuli in both mechanical and acoustic excitation sessions (refer to Sections 7.3.6 and 7.3.7).

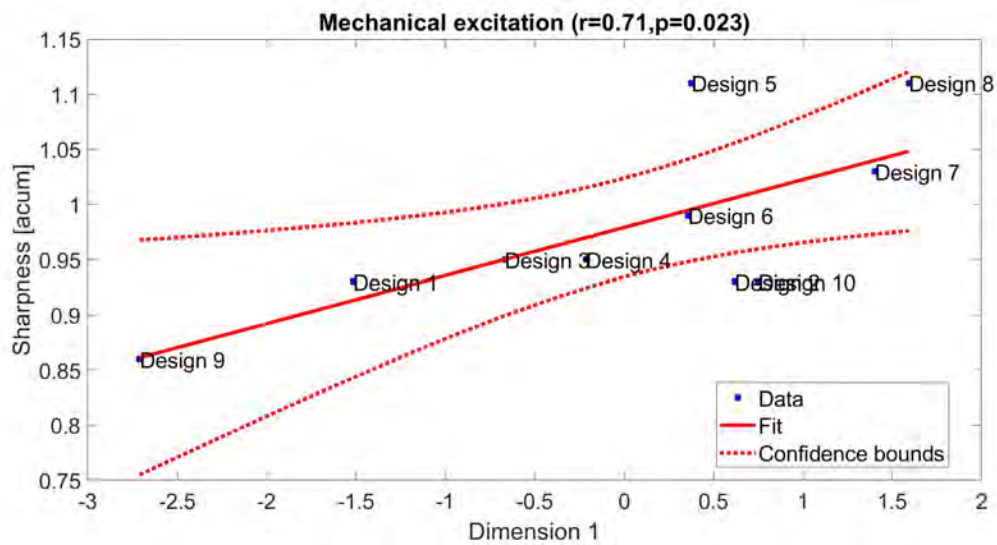


Figure C.1: The statistical analysis between the sharpness and dimension 1 of the perceptual space, corresponding to the session with the mechanical excitation

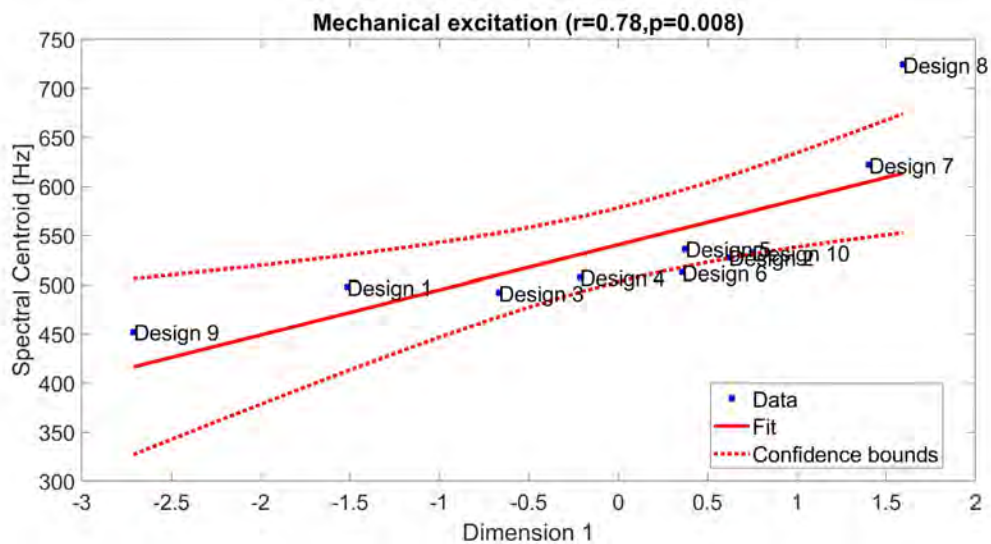


Figure C.2: The statistical analysis between the SC and dimension 1 of the perceptual space, corresponding to the session with the mechanical excitation

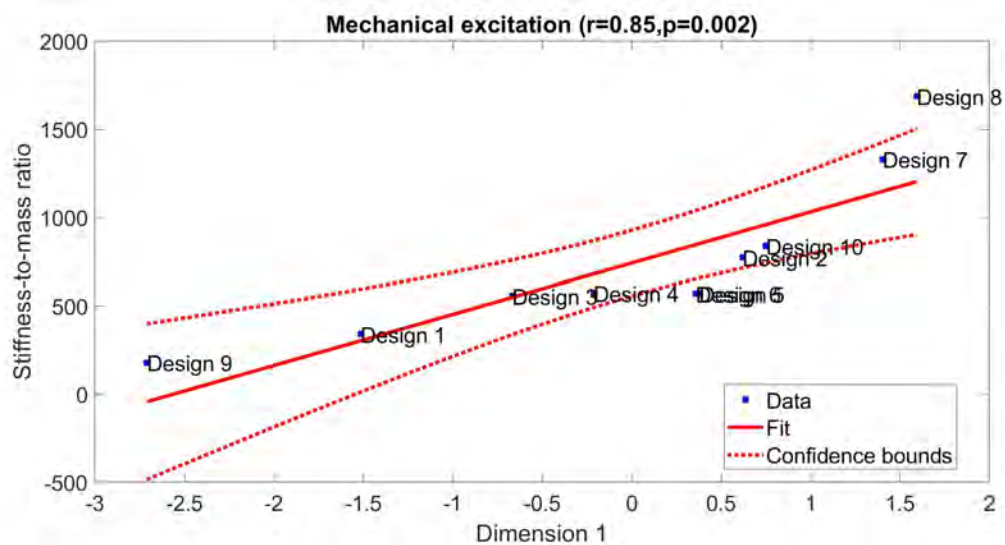


Figure C.3: The statistical analysis between the stiffness-to-mass ratio and dimension 1 of the perceptual space, corresponding to the session with the mechanical excitation

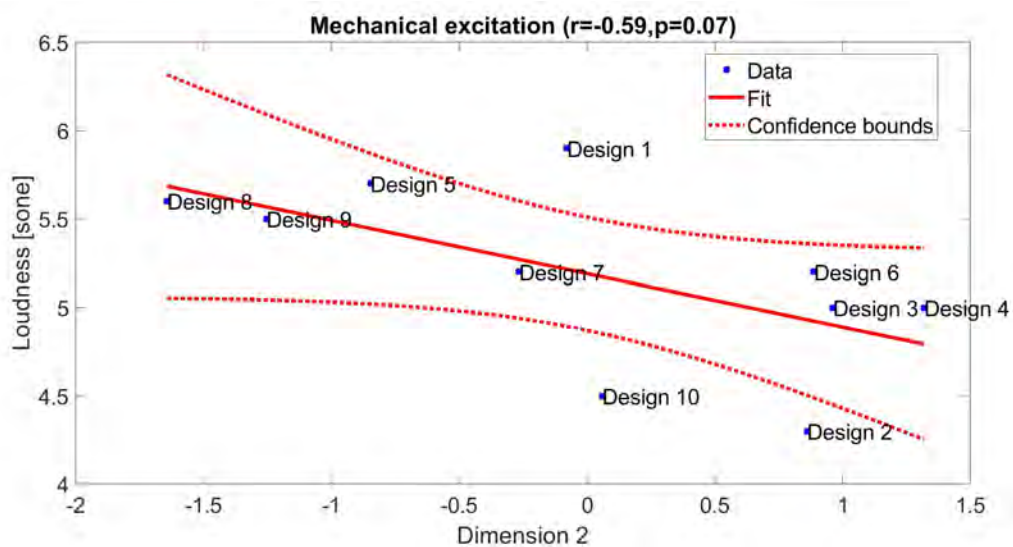


Figure C.4: The statistical analysis between the loudness and dimension 2 of the perceptual space, corresponding to the session with the mechanical excitation

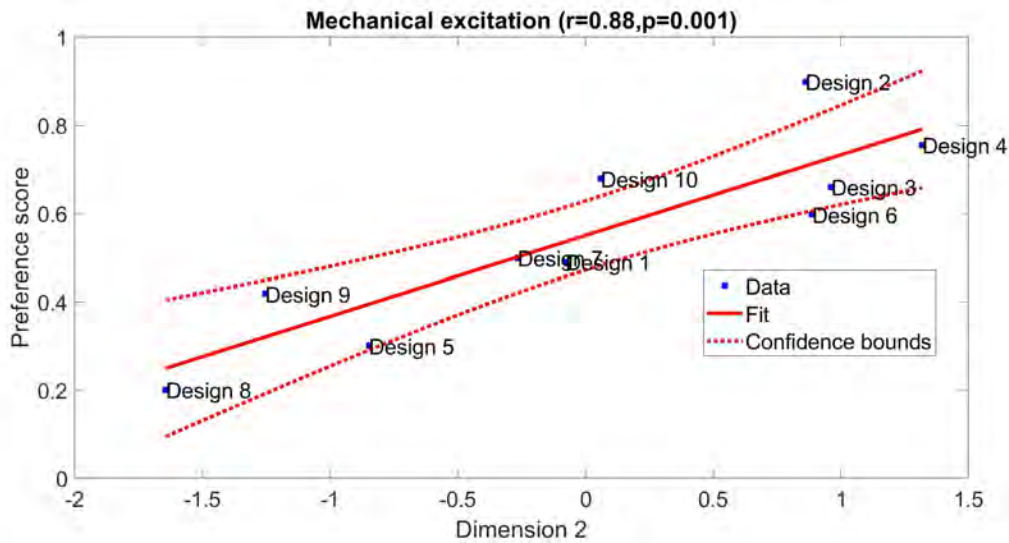


Figure C.5: The statistical analysis between the preference and dimension 2 of the perceptual space, corresponding to the session with the mechanical excitation

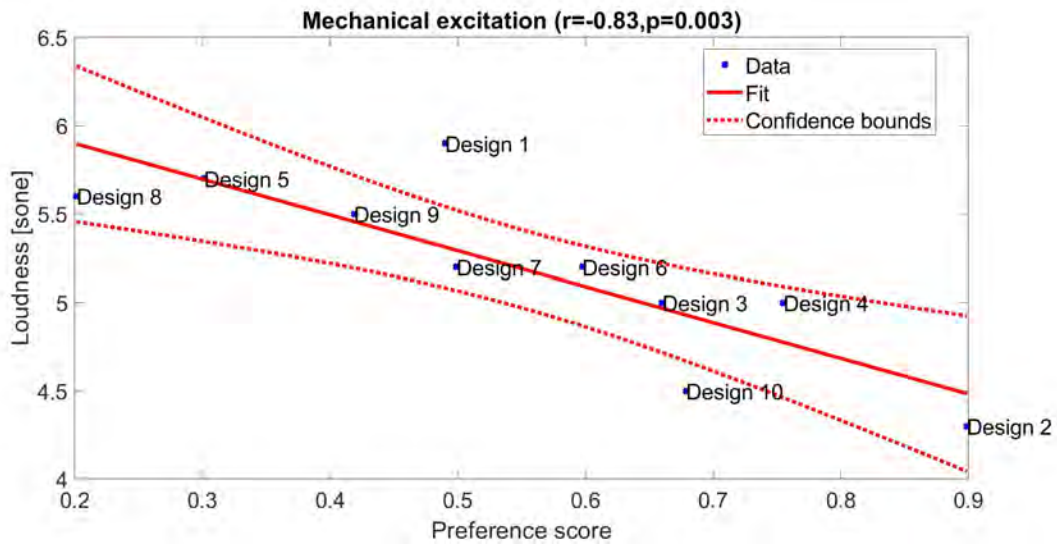


Figure C.6: The statistical analysis between the preference and loudness, corresponding to the session with the mechanical excitation

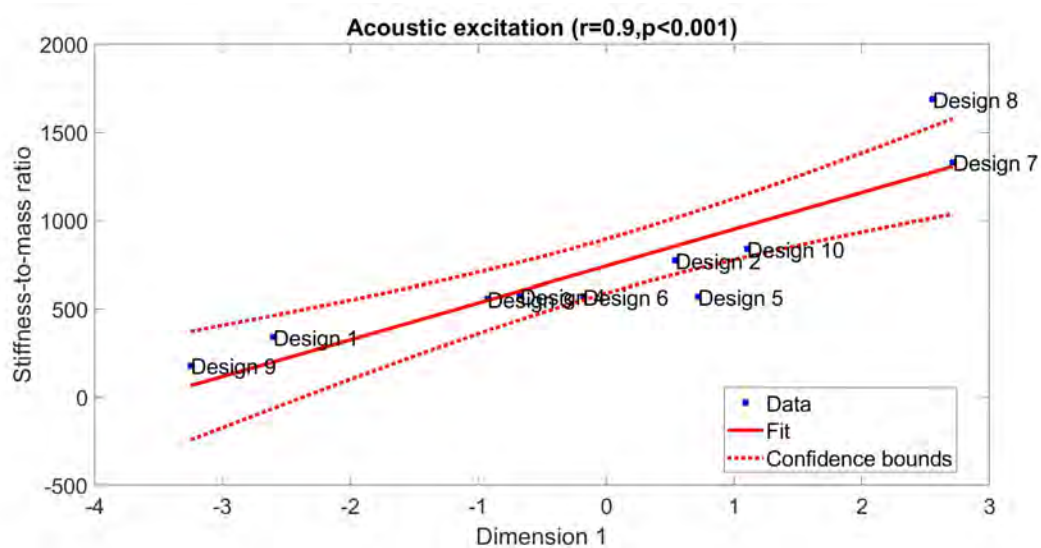


Figure C.7: The statistical analysis between the stiffness-to-mass ratio and dimension 1 of the perceptual space, corresponding to the session with the acoustic excitation

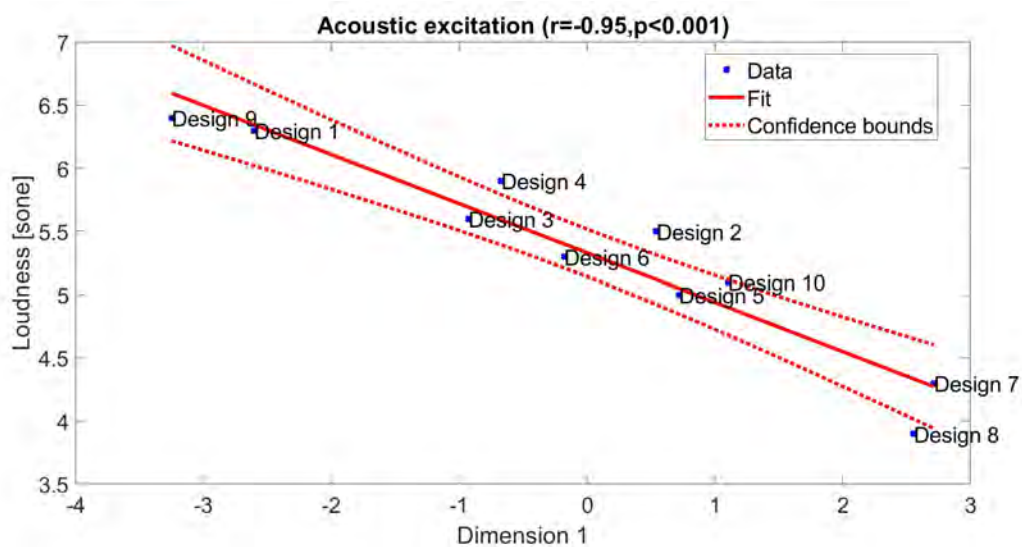


Figure C.8: The statistical analysis between the loudness and dimension 1 of the perceptual space, corresponding to the session with the acoustic excitation

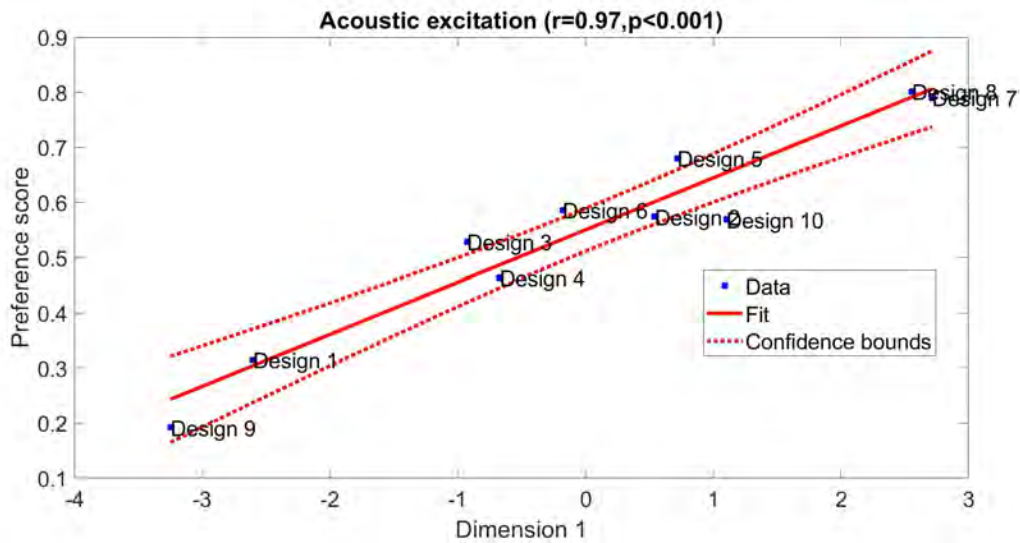


Figure C.9: The statistical analysis between the preference and dimension 1 of the perceptual space, corresponding to the session with the acoustic excitation

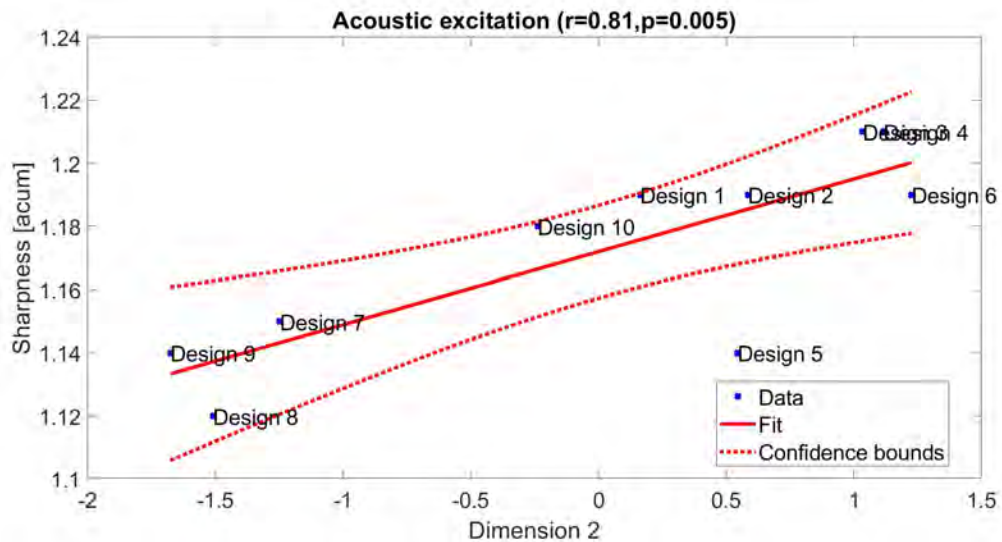


Figure C.10: The statistical analysis between the sharpness and dimension 2 of the perceptual space, corresponding to the session with the acoustic excitation

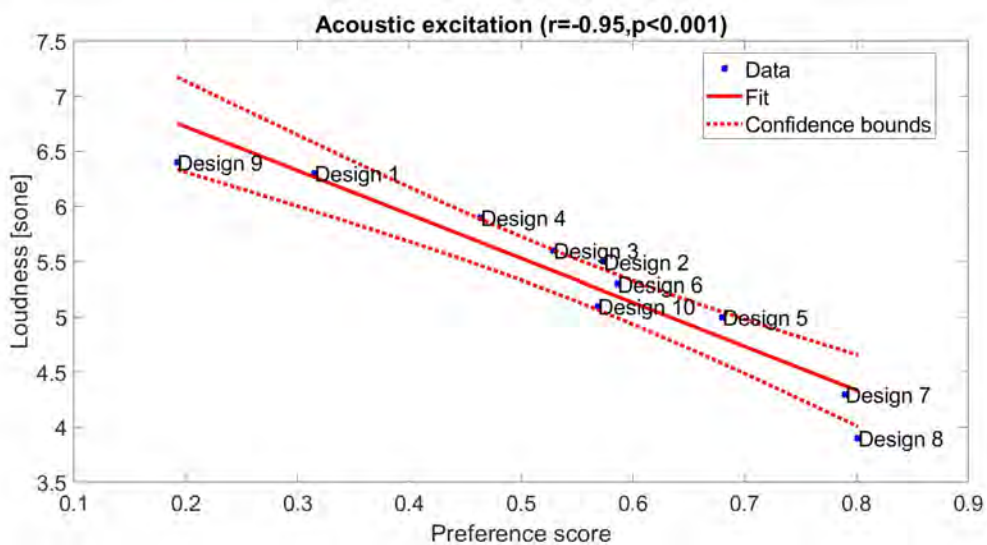


Figure C.11: The statistical analysis between the preference and loudness, corresponding to the session with the acoustic excitation

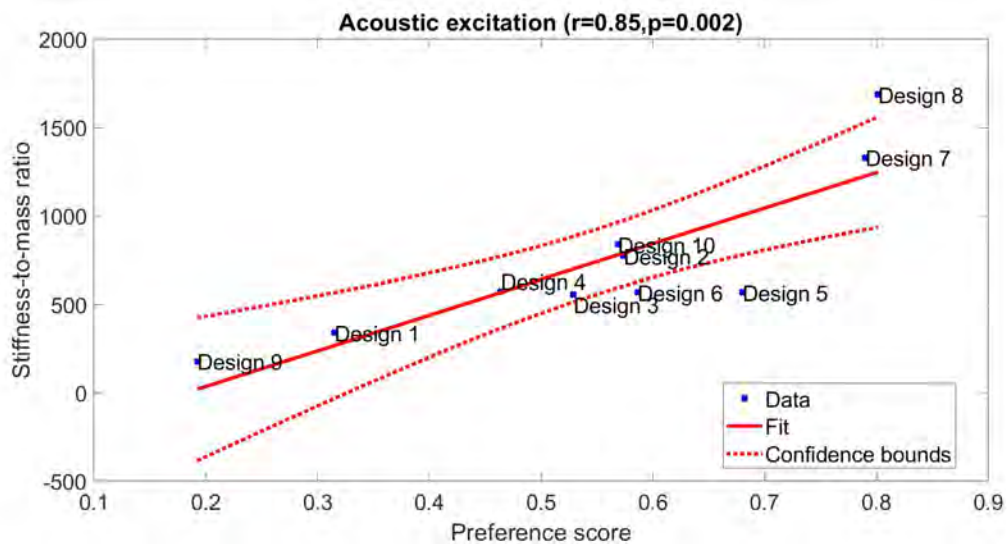


Figure C.12: The statistical analysis between the preference and stiffness-to-mass ratio, corresponding to the session with the acoustic excitation



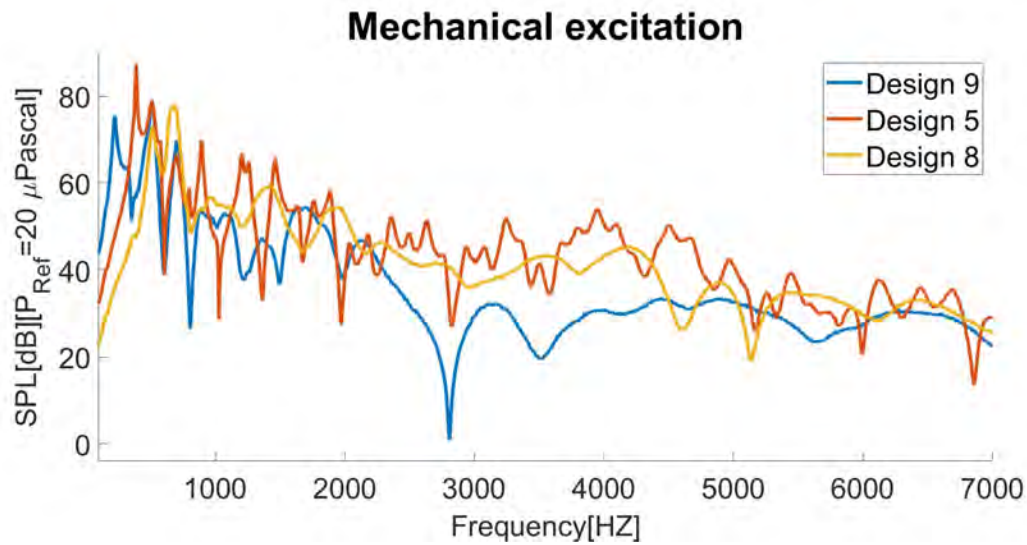


Figure C.13: SPL associated with Designs 5, 8, and 9 in the session with mechanical excitation. Designs 8 and 9 exhibit the highest and lowest stiffness-to-mass ratios, respectively, while Design 5 falls in the middle. The transition from the lowest to highest stiffness-to-mass ratio corresponds to a shift from the lowest to highest values along the 1st dimension of the perceptual space (see Figure 7.9 and Table 7.3)

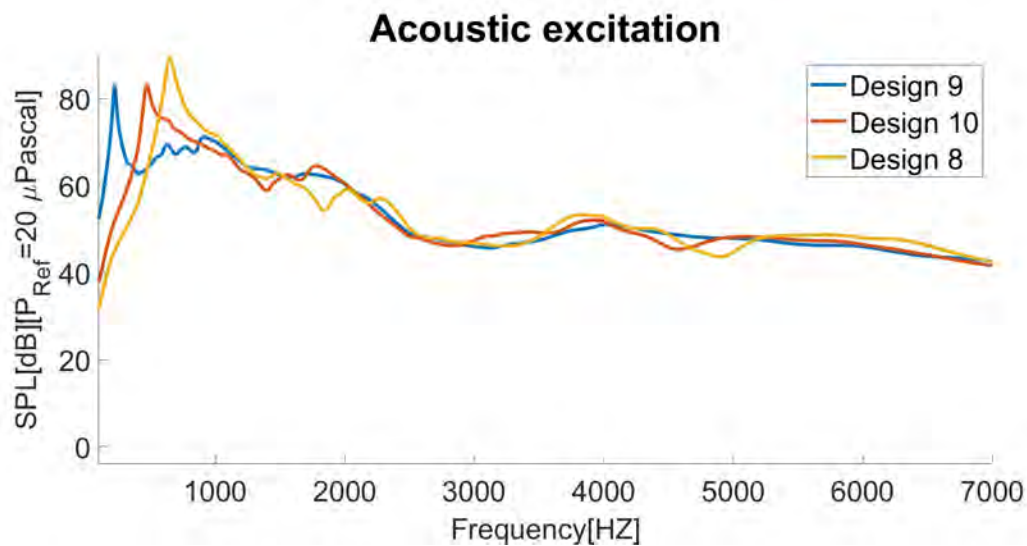


Figure C.14: SPL associated with Designs 8, 9, and 10 in the session with acoustic excitation. Designs 8 and 9 exhibit the highest and lowest stiffness-to-mass ratios, respectively, while Design 10 falls in the middle. The transition from the lowest to highest stiffness-to-mass ratio corresponds to a shift from the lowest to highest values along the 1st dimension of the perceptual space (c.f. Figure 7.10 and Table 7.3)